FEDERAL UNIVERSITY OF SAO CARLOS
CENTER OF EXACT SCIENCES AND TECHNOLOGY
GRADUATE PROGRAM IN PHYSICS

CHARGE CARRIER DYNAMICS AND OPTOELECTRONIC PROPERTIES IN QUANTUM TUNNELING HETEROSTRUCTURES

EDGAR DAVID GUARIN CASTRO

DOCTORAL THESIS

SÃO CARLOS - SP
BRAZIL
2021

FEDERAL UNIVERSITY OF SAO CARLOS
CENTER OF EXACT SCIENCES AND TECHNOLOGY
GRADUATE PROGRAM IN PHYSICS

CHARGE CARRIER DYNAMICS AND OPTOELECTRONIC PROPERTIES IN QUANTUM TUNNELING HETEROSTRUCTURES

Edgar David Guarin Castro

Thesis presented to the Graduate Program in Physics of the Federal University of São Carlos in partial fulfillment of the requirements for the degree of Doctor of Philosophy in the subject of Physics

Advisor: Prof. Dr. Victor Lopez-Richard

SÃO CARLOS - SP
BRAZIL
2021

UNIVERSIDADE FEDERAL DE SÃO CARLOS

Centro de Ciências Exatas e de Tecnologia
Programa de Pós-Graduação em Física

Folha de Aprovação

Defesa de Tese de Doutorado do candidato Edgar David Guarin Castro, realizada em 17/09/2021.

Comissão Julgadora:

Prof. Dr. Victor Lopez Richard (UFSCar)

Prof. Dr. Marcio Peron Franco de Godoy (UFSCar)

Profa. Dra. Mariama Rebello de Sousa Dias (RICHMOND)

Prof. Dr. Gerald Bastard (ENS Université PSL)

Prof. Dr. Iouri Poussep (USP)

O presente trabalho foi realizado com apoio da Coordenação de Aperfeiçoamento de Pessoal de Nível Superior - Brasil (CAPES) - Código de Financiamento 001.
O Relatório de Defesa assinado pelos membros da Comissão Julgadora encontra-se arquivado junto ao Programa de Pós-Graduação em Física.

To my family, who has
always supported my dreams,
and to my wife Helena,
with whom we reach
the unimaginable.

Acknowledgments

This work represents the materialization of a dream powered by the curiosity and fascination that generates in me the intriguing phenomena of this infinite universe, always motivated by the invaluable work of my professors. This work is also proof that the biggest goals in life only can be achieved with the support and company of wonderful people, without whom it would not have been possible to overcome the inherent obstacles in research.

That is why I am very grateful to God, my treasured parents, Judith and Edgar, and my cherished siblings, Vanessa and Sebastian, for their unconditional love, warm companion, and wholehearted support that encouraged me to pursue my dreams with the most genuine affection and jubilance. This thesis is yours.

I would like to express a special thanks from the bottom of my heart and soul to my precious and beloved wife, Helena. By her side, the entire world harmonizes, fears are defeated, and everything conjugates in the most surprising and unsuspected ways to give color and meaning to life. With her, not only do I share this existence, but also my love for science. This thesis is also for you.

My most sincere gratitude to my advisor Professor Dr. Victor Lopez Richard for his exceptional guidance, impressive expertise, and devoted dedication along with this entire research. His ingenious and relevant ideas enriched and shaped this work, unveiling the fundamental ingredients to understand the quantum universe. Professor Victor has become a respectable model of professionalism that will surely guide my entire career. I am very grateful for his teachings, for the opportunity to contribute to the construction of knowledge alongside him, and for the trust placed in me.

This thesis was also possible thanks to the outstanding support from Professor Dr. Marcio Daldin Teodoro, who enforced this research with his expertness, geniality, and dynamism in the lab, always providing encouragement and enthusiastic assistance in every aspect of this work. Thank you so much for having me in the group.

Thanks to Professor Dr. Gilmar Eugenio Marques for his help and contributions to this research. I am also grateful to all the professors from the Semiconductor Nanostructures Group and the Graduate Program in Physics of UFSCar, who directly or indirectly contributed to this work and my professional preparation.

I would also like to express my gratitude to the group of researchers, technical staff, and professors from TEP-Uni Würzburg, for providing the samples investigated in this thesis and guiding me during my doctoral stay in Würzburg. With special thanks to Professor Dr.

Sven Höfling for welcoming me into the group, and Dr. Fabian Hartmann and Dr. Andreas Pfenning for the reception, cordiality, and motivating discussions regarding the physics of semiconductor heterostructures that oriented my work.

A special thank you to Professor Dr. Gerald Bastard for the fruitful discussions, stimulating questions, and invaluable contributions to this research.

I would like to say a big thank you to my friend Dr. Andrea Naranjo for opening the doors of her life, for her truthful personal and professional support, and for her candid friendship.

Traveling this way was easy thanks to the splendid company and friendship from Joshua Morales and his family. Their unconditional support and companionship were an incentive to continue walking this path.

Many thanks to my folks and colleagues in Brazil: Yina, Vanderli, Verô, Edson, Leonardo, Chico, Natalia, Fernando, and in Europe: Harold, Kirill, Thamara, Yaksh, for introducing me into their cultures, for sharing their knowledge with me, for the coffee-breaks and dinners, and for opening my mind to an entirely new world.

I cannot stop thanking my professors at UnB and UPN for their unforgettable teachings that placed me in this time and place. With special thanks to Professors Dr. Leticia Coelho, Dr. Paulo Souza, Dr. Rosa Pedreros, and Nestor Mendez.

I am indebted to German Figueroa for his willingness to impart his knowledge and for inspiring me to study Physics. Thanks to him, I started this marvelous adventure.

Finally but no less important, I acknowledge the assistance from the technical and administrative staff of the UFSCar, and the financial support offered by the Coordenação de Aperfeiçoamento de Pessoal de Nível Superior-Brasil (CAPES)-Finance Code 001.

Abstract

Semiconductor quantum tunneling heterostructures offer a wide range of applications as photosensors, lasers, and circuit elements. However, fundamental questions related to energy transfer mechanisms and the correlation between some electrical and optical responses remain challenging. In order to provide insights into these problems, the nature of the carrier dynamics in these structures has been investigated by exploring the role of majority and minority carriers in the optoelectronic responses and the limiting factors responsible for their modulation. Thus, the transport and optical properties of different n-type samples built on Sb- and As-based double-barrier quantum well architectures have been analyzed using transport measurements and luminescence spectroscopies in continuous- and pulsed-wave mode. The characterization has been carried out by tuning various external parameters such as temperature, illumination, and magnetic fields.

Our observations revealed resonant tunneling of carriers from cryogenics up to room temperature. The inclusion of III-V quaternary alloys enhances the photodetection of infrared wavelengths. Quaternary layers serve as absorbers that allow a thorough tuning of the photosensor capabilities. The optical response of the devices allowed unveiling complex dynamics of non-equilibrium carriers, pointing out the formation of independent electron and hole populations that do not thermalize. This characteristic enables the mapping of thermalization mechanisms of hot carriers along with the structures. In all cases, it was found that the optoelectronic characteristics of the devices are strongly intertwined. In this regard, bistable optical and transport characteristics associated with an intrinsic magnetoresistance of some samples can be modulated simultaneously with temperature and magnetic fields. Models were proposed to simulate the charge dynamics, discerning the main ingredients that control the electrical response and, in some cases, the photosensor abilities. These models were complemented considering coherent and incoherent transport channels, which demonstrates how the transport and optical attributes correlate to produce the peculiar quantum response. This approach allows discussing the role of minority carriers in the overall dynamics of the systems, the segmentation of the relaxation mechanisms, and the optimization of the optoelectronic properties. The results are intended to offer a comprehensive theoretical and experimental analysis of the complex quantum phenomena behind these quantum tunneling systems.

Keywords: Semiconductor, Heterostructures, Resonant Tunneling Diodes, Photosensors, Optoelectronic Properties, Carrier Dynamics, Non-Equilibrium Carriers, Magnetoresistance.

Resumo

Heteroestruturas semicondutoras com tunelamento quântico oferecem diversas aplicações como fotossensores, lasers e elementos de circuitos lógicos. Porém, questões fundamentais relacionadas aos mecanismos de transferência de energia e à correlação entre algumas das suas propriedades optoeletrônicas, ainda são desafiadoras. Com o objetivo de decifrar estes problemas neste tipo de estruturas, a natureza da dinâmica de portadores tem sido pesquisada, explorando o papel dos portadores de carga nas respostas optoeletrônicas além dos fatores limitantes responsáveis pela sua modulação. Para essa finalidade as propriedades ópticas e de transporte em amostras tipo n, com arquiteturas de poço quântico de dupla barreira baseadas em Sb e As, foram analisadas por meio de medidas de transporte combinadas com espectroscopia de luminescência em modo contínuo e pulsado. A caracterização foi realizada controlando parâmetros como temperatura, iluminação e campos magnéticos. As observações revelaram tunelamento ressonante desde temperaturas criogênicas até temperatura ambiente. Além disso, a inclusão de ligas quaternárias III-V melhorou a fotodetecção no infravermelho, pois elas servem como regiões de absorção que permitem controlar as capacidades dos fotossensores. A resposta óptica dos dispositivos permitiu também desvendar dinâmicas complexas de portadores fora do equilíbrio, apontando para a formação de populações independentes que não termalizam entre si. Esta característica possibilita o mapeamento dos mecanismos de termalização dos portadores quentes ao longo das heteroestruturas. Em todos os casos, verificou-se que as características optoeletrônicas dos dispositivos estão entrelaçadas. Nesse sentido, as características optoeletrônicas associadas à magnetorresistência intrínseca de algumas amostras podem ser moduladas simultaneamente com temperatura e campos magnéticos. Assim, modelos foram propostos para simular a dinâmica de portadores, discernindo os principais ingredientes que controlam a resposta elétrica e, em alguns casos, a fotossensibilidade. Estes modelos foram complementados considerando canais de transporte coerentes e incoerentes, demostrando com isto como a correlação entre as propriedades ópticas e de transporte produz a peculiar resposta quântica. Essa abordagem permite discutir o papel dos portadores minoritários na dinâmica geral dos sistemas, a segmentação dos mecanismos de relaxamento e a otimização das propriedades optoeletrônicas. Os resultados buscam oferecer uma análise experimental e teórica abrangente dos complexos fenômenos quânticos por trás do funcionamento dos sistemas de tunelamento quântico.

Palavras-chave: Semicondutor, Heteroestruturas, Diodos de Tunelamento Ressonante, Fotosensores, Dinâmica de Portadores, Portadores Fora do Equilíbrio, Magnetorresistência.

Contents

List of Figures

Introduction

Technological advances in electronics and photonics require the creation of devices that work at high speeds and high frequencies with a minimum of applied voltages, ensuring not only circuits miniaturization but also an enhancement of the electrical currents and optical emissions produced during their operation. In this regard, *semiconductor heterostructures* constitute the building blocks for the development of nanodevices with these characteristics, since they allow controlling and tuning the charge carrier dynamics at the nanoscale. Thanks to the interfaces present in these systems, the electronic structure suffers energy discontinuities, due to differences in the bandgaps and the energy band edges of the materials, responsible for the appearance of confinement effects. In particular, heterostructures presenting discontinuities that produce potential energy barriers with thicknesses of a few nanometers, like in resonant tunneling diode (RTD) architectures, are of special interest. This kind of structure has been widely used as a test-bed to investigate quantum transport, carriers excitation, and relaxation dynamics, thermalization and recombination processes, as well as material parameters. In fact, the applicability and basic physics phenomena already demonstrated in RTDs, make them a countless source of interesting physical problems, related to the competition of several energy transfer mechanisms, and the strong correlation between electrical and optical responses.

The main goal of the present work is to investigate the nature of the carrier dynamics in unipolar n-type quantum tunneling heterostructures, exploring the role of majority and minority carriers in the optoelectronic properties of antimony (Sb-) and arsenic (As-) based systems. Understanding the carrier dynamics in these structures is paramount to improve the performance of nanoelectronic devices operating at infrared wavelengths, where energy relaxation mechanisms appear intertwined during the carrier transport and optical recombination. Thus, a quest for methods to thoroughly characterize these mechanisms and the conversion processes between electrical, optical, and thermal energies is a current scientific challenge. With the aim of addressing these problems, the following specific objectives were outlined:

- to provide insights on the main mechanisms for charge carrier transport, buildup, relaxation, thermalization, and recombination in different III-V semiconductor quantum-tunneling heterostructures, and to elucidate how they modulate the electrical and optical responses at the infrared spectral range, by changing external parameters such as temperature, illumination, and electromagnetic fields;

- to inquire about the underlying generation mechanisms of minority carriers (holes),

building up explanations on the origin of the optical emission produced at different regions within these devices;

- to study how minority carriers can buildup and escape through the active region of RTDs, in order to understand their role on the overall carrier dynamics of the systems;

- to explore the contribution of different carrier transport channels on the electrical response, as well as their relative weights on the generation of minority carriers, discerning their correlation with the optical properties of the devices;

- to contrast the optoelectronic characteristics of the studied samples to unveil the influence of band parameters and structural design on their transport and optical properties;

- to determine how the thermalization dynamics among majority and minority carrier populations is affected by internal and external factors at different regions of the heterostructures, to provide evidence on the influence of transport and excitation mechanisms in both the dynamics of non-equilibrium carriers and the segmentation of the energy relaxation mechanisms;

- to assess the weight of various carrier relaxation mechanisms present in Sb-based double-barrier quantum wells and to demonstrate how they compete with different relaxation rates to comprehend the temporal evolution of the carrier dynamics in quasi-bi-dimensional quantized states;

- to elucidate the effect of the intrinsic magnetoresistance in the transport and optical properties in some heterostructures, offering insights on how to tune the electrical and optical characteristics with external factors, based on the understanding of the intertwining between optoelectronic channels;

- to predict electrical and optical responses under different operating regimes, as a function of external stimuli, to offer clues about intrinsic and extrinsic factors that can improve the performance and photosensitivity of devices.

In order to achieve these objectives, different RTDs built on Sb- and As-based double-barrier quantum well structures have been studied. The samples were designed and grown via molecular beam epitaxy by the staff of both the Microstructure Laboratory (*Gottfried-Landwehr-Labor für Nanotechnologie*, GLLN) at the Chair of Technical Physics (*Technische Physik*, TEP) from Universität Würzburg (Uni Würzburg, Würzburg, Germany) and nanoplus Nanosystems and Technologies GmbH (Gerbrunn, Germany). The structural

quality, crystallinity, composition, and doping levels were verified by the staff of the GLLN through scanning electron microscopy, high-resolution X-ray diffraction, and time-of-flight secondary ion mass spectroscopy measurements. Subsequently, members from the Nanoelectronics Group at TEP-Uni Würzburg prepared several micrometric mesa diameters for the RTDs using chemical etching and lithography, complemented by the deposition of gold ring contacts on top of the mesas.

The electrical and optical characterization of the samples was performed during the present work, using electronic transport measurements, jointly with electro- and photoluminescence spectroscopies in continuous- and pulsed-wave mode. Experiments were performed in a wide range of temperatures from 4 up to 300 K, controlling various external parameters such as applied voltages, incident infrared light wavelengths, optical power densities, and magnetic fields from 0 up to 8 T. Part of the transport and photoluminescence measurements were carried out at the Nanoelectronics Group and the Laboratory for Optical Spectroscopy of Nanostructures from TEP-Uni Würzburg. Likewise, transport, magneto-transport and continuous- and pulsed-wave mode spectroscopy measurements were completed at the multi-user laboratory of the Semiconductor Nanostructures Group (*Grupo de Nanoestruturas Semicondutoras*, GNS) at the Physics Department of the Federal University of São Carlos (UFSCar, São Carlos, Brazil). The experimental analysis presented here was complemented by theoretical models developed at the GNS-UFSCar, through which the carrier dynamics inside the heterostructures were investigated. This study was supported by computational simulations of the electronic band profiles and optoelectronic responses for each sample.

The obtained results reveal outstanding transport and optical properties that open the path to optoelectronic applications covering the infrared wavelength region. This is possible thanks to the inclusion of lattice-matched III-V quaternary alloys into the heterostructures, which enhances the photodetection by increasing the absorption capabilities of the devices at energies between ~ 370 meV ($\lambda \approx 3.3$ μm) and ~ 1.00 eV ($\lambda \approx 1.2$ μm). Moreover, the dependence of band parameters on the material composition allows modulating the energy detection range and resonant tunneling characteristics, shining light on important material parameters such as band offsets and energy bandgaps. The photosensitivity properties in this type of heterostructures respond to complex dynamics of majority and minority carriers that tune the efficiency of drift, accumulation, and escape of generated carriers. It influences the electrostatic modulation of the electrical response and allows controlling their sensing abilities with voltage and illumination. In this sense, the proposed models indicate that the role of minority carriers can be correlated to both the trapping efficiency and quantum transmission of generated carriers at the double barrier structure and the tuning of these effects with external parameters.

The spatially-resolved correlation between electronic band structures and light emission also permitted ascribing the optical spectra to the site at the nanostructures where the optical recombination takes place. It facilitates the study of their interdependence with the transport characteristics and the temporal evolution of the carrier dynamics inside the quantum wells. By extracting the effective temperature from the spectrum components, a rich picture of the segmentation of the energy relaxation mechanisms has been unveiled along some heterostructures. The fundamental insights on the nature of non-equilibrium carriers thermalization have been provided by correlating the transport and optical characteristics under different conditions of illumination and applied voltage. This method demonstrates the unexpected non-thermalization between minority and majority non-equilibrium carriers, allowing the construction of a temperature gradient map for both electrons and holes. Moreover, time-resolved experiments disclose a clear voltage dependence of the effective lifetimes in Sb-based systems in clear contrast with As-based ones. Here, increased tunneling times at the sub-nanosecond scale due to high band offsets and the competition between escape, interband scattering, and optical recombination times in Sb-based systems induce slow dynamics (of the order of nanoseconds) at the resonance condition, determined by the filling process of the quasi-bi-dimensional quantum states.

The intriguing correlation between the optoelectronic properties that produce the peculiar quantum response of these devices can not be completely understood without considering the contribution of the coherent and incoherent channels to the transport characteristics of the systems. These channels not only redistribute the carriers along the heterostructures but also are efficient in the generation of holes, mainly via impact ionization processes. Generated holes are responsible for the electroluminescence emission. In As-based systems with bistable transport characteristics, for instance, these channels are also strongly affected by external magnetic fields which produce an unexpected pinched transport hysteresis, while keeping the qualitative shape of the optical bistability unchanged. The observations and models presented in this thesis offer clear evidence of the existence of an intrinsic magnetoresistance, tunable with temperature and magnetic fields, where the Zener tunneling through the narrow gap of the quaternary layer has a fundamental role in the carrier dynamics of the device.

Thus, this thesis has been organized into six chapters to offer a comprehensive theoretical and experimental analysis of the complex quantum phenomena pointed above. In Chapter 1, the fundamental ideas and models regarding the electronic structure, effective mass approximation, transport properties, and optical recombination mechanisms in semiconductor heterostructures are discussed following the $\mathbf{k}\cdot\mathbf{p}$ approach and elemental carrier statistics, that enable defining concepts such as carriers effective temperature and

lifetimes. Chapter 2 focuses on the foundation of the transport and optical properties of RTDs, presenting the proposed models for charge generation, accumulation, and transport of carriers in this kind of system, based on transfer matrix calculations for quantum tunneling. Chapter 3 presents the layered and electronic structure of each sample, jointly with the growth, microfabrication, and optoelectronic characterization techniques employed for the experimental work. Afterward, the results of the experimental and theoretical investigations of this thesis are exposed in the subsequent chapters. Thus, in Chapter 4, the basic transport and optical properties, as well as the photoresponse capabilities of Sb-based RTDs with GaInAsSb absorption layers are demonstrated, pointing out the electrostatic origin of these properties. Chapter 5 is devoted to studying non-equilibrium carriers in Sb-based RTDs and the mechanisms that modulate their thermalization dynamics as a function of external parameters. The picture is complemented with the temporal evolution of the carrier dynamics inside the quantum well, which is explicitly correlated with the transport characteristics, in contrast with As-based quantum wells. Finally, Chapter 6 contrasts the magneto-transport and magneto-optical bistabilities in As-based RTDs, establishing the interdependence between coherent and incoherent channels, intrinsic magnetoresistances, and electroluminescence emission. The main conclusions of this work are summarized in the final part of the thesis.

Given the scientific and technological relevance of controlling the carrier dynamics in semiconductor nanostructures, the findings presented here are intended to contribute to the development of the investigations of quantum tunneling devices. This thesis offers tools to improve their performance as fast response devices in the infrared spectral region from the understanding of the quantization effects. In this sense, the results attained in this work have been condensed in the following publications:

[1] E. R. Cardozo de Oliveira, A. Pfenning, E. D. Guarin Castro, M. D. Teodoro, E. C. dos Santos, V. Lopez-Richard, G. E. Marques, L. Worschech, F. Hartmann, and S. Höfling, "Electroluminescence on-off ratio control of n−i−n GaAs/AlGaAs-based resonant tunneling structures," Phys. Rev. B, **98**, p. 075302, 2018.

[2] E. D. Guarin Castro, F. Rothmayr, S. Krüger, G. Knebl, A. Schade, J. Koeth, L. Worschech, V. Lopez-Richard, G. E. Marques, F. Hartmann, A. Pfenning, and S. Höfling, "Resonant tunneling of electrons in AlSb/GaInAsSb double barrier quantum wells," AIP Adv., **10**, 5, p. 055024, 2020.

[3] E. D. Guarin Castro, A. Pfenning, F. Hartmann, G. Knebl, M. D. Teodoro, G. E. Marques, S. Höfling, G. Bastard, and V. Lopez-Richard, "Optical Mapping of Nonequilibrium Charge Carriers," J. Phys. Chem. C, **125**, 27, p. 14741–14750, 2021.

[4] F. Rothmayr, E. D. Guarin Castro, A. Pfenning, F. Hartmann, S. Höfling, J. Koeth, G. Knebl, A. Schade, S. Krüger, L. Worschech, and V. Lopez-Richard, "Resonant tunnelling diodes: Mid-infrared sensing at room temperature." 2021 (*submitted to Advanced Optical Materials*).

[5] E. D. Guarin Castro, A. Pfenning, F. Hartmann, M. D. Teodoro, L. Worschech, G. E. Marques, S. Höfling, and V. Lopez-Richard, "Tuning magneto-transport and magneto-electroluminescence bistabilities in resonant tunneling diodes." 2021 (*in preparation for submission*).

Additionally, the findings of this thesis complemented the collaborations indicated below:

[1] M. D. Teodoro, B. G. M. Tavares, E. D. Guarin Castro, R. R. LaPierre, and Yu. A. Pusep, "Recombination dynamics of Landau levels in an InGaAs/InP quantum well" Phys. Rev. B, **98**, p. 155431, 2018.

[2] V. Laurindo Jr., E. D. Guarin Castro, G. M. Jacobsen, E. R. C. de Oliveira, J. F. M. Domenegueti, B. Alén, Y. I. Mazur, G. J. Salamo, G. E. Marques, E. Marega Jr., M. D. Teodoro, and V. Lopez-Richard, "Pathway to excitonic coherence," 2021 (*submitted to Physical Review B*).

Chapter 1

Semiconductor Heterostructures

Semiconductor heterostructures are layered systems built by the deposition of crystalline films made of different materials. The deposition is performed on a semiconductor substrate employing highly accurate growth techniques such as Molecular Beam Epitaxy (MBE) [1, 2] or Metalorganic Chemical Vapor Deposition (MOCVD) [3]. These techniques allow for the fabrication of low-roughness layers with thicknesses ranging from one monolayer (~ 3 Å) to hundreds of nanometers, with extraordinary control nowadays. In the case of high-quality depositions carried out with high-purity materials, the growth process leads to the emergence of abrupt interfaces or *heterojunctions* across which the chemical composition changes at an atomic level [2]. The formation of the heterojunction is also favored by choosing two semiconductor alloys with an appropriate *lattice matching*: similar lattice constants that reduce the strain and interface defects. Some examples include heterojunctions conformed by III-V compounds such as GaAs/AlGaAs, GaSb/AlAsSb, or GaInAsSb/AlSb.

Heterostructures built on III-V compounds have been widely used due to their optoelectronic properties, relevant for commercial technologies based on high-mobility carriers and optical devices operating in the visible and infrared spectral regions such as light detectors [4, 5], lasers [6, 7], solar cells [8, 9], among others. These materials can be combined in binary, ternary, or quaternary alloys, extending the miscellany of heterostructure configurations and potential applications. In this chapter, fundamental concepts, and models that allow a comprehensive study of the transport and optical properties in semiconductor heterostructures will be discussed. They also set the grounds for the theoretical and experimental analyses carried out on the III-V heterostructures explored in this work.

1.1 Electronic Structure and the Effective Mass Approximation

The optical and transport properties of a semiconductor heterostructure depend essentially on the *electronic structure* of the constituent materials, which determines how charge carriers interact among them, with the lattice and with external factors (applied fields and temperature, for instance). To understand this dependence, let us first consider the movement of a free electron in a bulk semiconductor material, which is assumed as a perfect crystal characterized by a periodic potential, U, produced by the ion cores.

In three dimensions and at stationary conditions (neglecting the spin-orbit coupling), the position-dependent Schrödinger equation for the electron is given by [10, 11],

$$\left[\frac{\mathbf{p}^2}{2m_0} + U(\mathbf{r})\right]\psi(\mathbf{r}) = E\psi(\mathbf{r}), \tag{1.1}$$

where m_0 is the free electron mass, $\mathbf{p} = -i\hbar\nabla$ is the linear momentum operator, E is the electron energy, and $\psi(\mathbf{r})$ is the position-dependent electronic wavefunction. Due to the periodicity of the atoms in the semiconductor crystals, the potential $U(\mathbf{r})$ is expected to be a periodic function of the form $U(\mathbf{r}) = U(\mathbf{r}+\mathbf{R})$, where $\mathbf{R}$ is a translation vector, dependent on the lattice constant of the semiconductor. Consequently, the probability density must be also periodic, since every atom in a lattice is assumed to be identical. This implies that $\left|\psi(\mathbf{r})\right|^2 = \left|\psi(\mathbf{r}+\mathbf{R})\right|^2$. Consequently, the solutions must be of the form $\psi(\mathbf{r}) = \psi_{n\mathbf{k}}(\mathbf{r}) = \varphi_{n\mathbf{k}}(\mathbf{r})\exp(i\mathbf{k}\cdot\mathbf{r})$, with n as the number of the energy band and $\mathbf{k}$ as the wave vector. Here, $\varphi_{n\mathbf{k}}(\mathbf{r}) = \varphi_{n\mathbf{k}}(\mathbf{r}+\mathbf{R})$, as stated by the *Bloch's theorem* [12, 13]. This allows introducing the effective mass concept and the parabolic band approximation that will permeate this work.

Taking advantage of the translational symmetry, eq. 1.1 can be rewritten in the $\mathbf{k}\cdot\mathbf{p}$ representation as [10, 14, 15],

$$\left[\frac{\mathbf{p}^2}{2m_0} + U(\mathbf{r}) + \frac{\hbar^2k^2}{2m_0} + \frac{\hbar}{m_0}\mathbf{k}\cdot\mathbf{p}\right]|\varphi_{n\mathbf{k}}\rangle = \left[\hat{H}(\mathbf{k}=0) + \frac{\hbar^2k^2}{2m_0} + \frac{\hbar}{m_0}\mathbf{k}\cdot\mathbf{p}\right]|\varphi_{n\mathbf{k}}\rangle = E_{n\mathbf{k}}|\varphi_{n\mathbf{k}}\rangle, \tag{1.2}$$

where $\hat{H}(\mathbf{k}=0)$ is the Hamiltonian of the crystal with eigenvectors $|\varphi_{n0}\rangle$, such that $\hat{H}(\mathbf{k}=0)|\varphi_{n0}\rangle = E_{n0}|\varphi_{n0}\rangle$ [10] which is useful for the description of the electronic structure around certain band extremum. According to this representation, the solutions for wave

numbers close to the Γ-point have the form,

$$|\varphi_{n\mathbf{k}}\rangle = \sum_m C_m(\mathbf{k})\,|\varphi_{m0}\rangle\,. \tag{1.3}$$

Substituting these solutions into eq. 1.2, then multiplying by the complex conjugated, and integrating over the volume of the unitary cell volume, the Schrödinger equation transforms into,

$$\sum_m \left[\left(E_{n0} - E_{n\mathbf{k}} + \frac{\hbar^2 k^2}{2m_0}\right)\delta_{nm} + \frac{\hbar k}{m_0}\langle\varphi_{n0}|\mathbf{p}|\varphi_{m0}\rangle\right] C_m(\mathbf{k}) = 0, \tag{1.4}$$

where $\langle\varphi_{n0}|\mathbf{p}|\varphi_{m0}\rangle \equiv \int_{\Omega_0}\varphi^*_{n0}\mathbf{p}\varphi_{m0}d^3r = \mathbf{p}_{nm}(\mathbf{k}=0)$, with Ω_0 as the unitary cell volume [10]. Eq 1.4 can be diagonalized to obtain the dispersion relation for $E_{n\mathbf{k}}$, as well as the coefficients $C_m(\mathbf{k})$ for all the wave vectors, $\mathbf{k}$, at every single energy band, n. Assuming that the n^{th} energy band with energy E_{n0} is non-degenerated, it is possible to use a perturbation approach for small values of $\mathbf{k}$ in order to obtain $E_{n\mathbf{k}}$. As a result, one has $C_n \sim 1$ and taking into account that $C_m(0) = \delta_{nm}$, then

$$C_m = \frac{\hbar}{2m_0}\frac{\mathbf{k}\cdot\mathbf{p}_{nm}}{E_{n0} - E_{m0}}. \tag{1.5}$$

Introducing the values of C_n and C_m into eq. 1.4, the dispersion relation for $E_{n\mathbf{k}}$ with the second order correction for E_{n0} takes the form [10, 16],

$$E_{n\mathbf{k}} = E_{n0} + \frac{\hbar^2 k^2}{2m_0} + \frac{\hbar^2}{m_0^2}\sum_{m\neq n}\frac{|\langle\varphi_{n0}|\mathbf{k}\cdot\mathbf{p}|\varphi_{m0}\rangle|^2}{E_{n0} - E_{m0}}, \tag{1.6}$$

which gives the non-degenerated parabolic dispersion for $\mathbf{k} \to 0$, near to the Γ-point. Eq. 1.6 is usually expressed as [16, 17],

$$E_{n\mathbf{k}} = E_{n0} + \frac{\hbar^2 k^2}{2m_n^*}, \tag{1.7}$$

with,

$$\frac{1}{m_n^*} = \frac{1}{m_0} + \frac{2}{m_0^2 k^2}\sum_{m\neq n}\frac{|\langle\varphi_{n0}|\mathbf{k}\cdot\mathbf{p}|\varphi_{m0}\rangle|^2}{E_{n0} - E_{m0}}, \tag{1.8}$$

as the *carrier effective mass* of the n^{th} energy band, which in three dimensions corresponds to a tensor with components [10],

$$\frac{1}{m_n^{ij}} = \frac{1}{m_0}\delta_{ij} + \frac{2}{m_0^2}\sum_{m\neq n}\frac{p^i_{n,m}p^j_{m,n}}{E_{n0} - E_{m0}}, \tag{1.9}$$

being $i, j = x, y, z$ the Cartesian coordinates. This picture can be complemented by intro-

ducing relativistic corrections, *e.g.*, due to spin-orbit interaction [10]. The effective mass, as expressed by eq. 1.8 implies that in a semiconductor crystal, electrons can be treated as "free" carriers, but with a mass different from that of a free electron. The value of this effective mass depends on both the coupling between electronic states at different energy bands, n and m, which is determined by the $\mathbf{k}\cdot\mathbf{p}$ term, and the energy band separation $E_{n0} - E_{m0}$ characteristic of each type of semiconductor. According to the relative energy positions of the dominant contributions to the second term in eq. 1.9, the resulting effective mass can either be positive or negative [16, 17].

The $\mathbf{k}\cdot\mathbf{p}$ approximation summarized in eq. 1.4 also allows obtaining the band dispersion beyond the parabolic band approximation [15–19]. However, experiments have demonstrated that many optoelectronic phenomena occur at the vicinity of the Γ-point, where the parabolic approximation can be valid [10]. In this way and according to eq. 1.7, the conduction band (CB) in a semiconductor near to the center of the Brillouin zone ($\mathbf{k} = 0$) is described in this thesis as,

$$E_{\mathrm{CB}}(\mathbf{k}) = E_{\mathrm{g}} + \frac{\hbar^2 k^2}{2m_{\mathrm{e}}^*}, \tag{1.10}$$

with E_{g} as the band gap energy and m_{e}^* as the isotropic effective electron mass. The parabolic approximation is also reasonable for the valence band (VB) for describing effects where the anisotropy of the effective mass and coupling between light and heavy hole sub-bands play no significant role. In that case, the top valence band close to the center of the Brillouin zone ($\mathbf{k} = 0$) is assumed in the form,

$$E_{\mathrm{VB}}(\mathbf{k}) = -\frac{\hbar^2 k^2}{2m_{\mathrm{h}}^*}, \tag{1.11}$$

with an isotropic effective mass, m_{h}^*, that can be associated to holes when describing the charge dynamics of partially filled valence band. Their response is similar to a carrier with the same electron charge but opposite sign ($h = +e$) [10].

1.1.1 Electronic Structure in a Heterojunction

The $\mathbf{k}\cdot\mathbf{p}$ method discussed before, can be extended to the case of heterojunctions between two semiconductor materials. In this case, the electronic structure of one material aligns with another to form a *band profile* along the growth direction, z, characterized by discontinuities caused by the differences between the CB, VB, and bandgaps of the materials and their relative offsets. These discontinuities and the differences between effective masses and the bulk properties of the semiconductors are responsible for changes in the kinetic energy of the charge carriers when they travel from one material to another.

Depending on the materials of the heterojunction, the discontinuities can produce three types of alignments: straddling-gap, staggered-gap, and broken-gap alignments [16, 20, 21], as sketched in figures 1.1 (a), (b), and (c), respectively. In heterojunctions formed by III-V semiconductor alloys, for example, the most common alignment is the straddling profile. It can be found in interfaces such as GaAs/$Al_xGa_{1-x}As$, GaSb/AlSb, $Ga_xIn_{1-x}As_ySb_{1-y}$/GaSb, $In_xGa_{1-x}As/In_xAl_{1-x}As$, etc. The staggered configuration can also be obtained in III-V heterojunctions as $InP/In_xAl_{1-x}As$ or InAs/AlSb, or by changing the x, y compositions in ternary or quaternary alloys [22, 23]. The broken-gap alignment is not that common but can be observed in GaSb/InAs interfaces [21, 22].

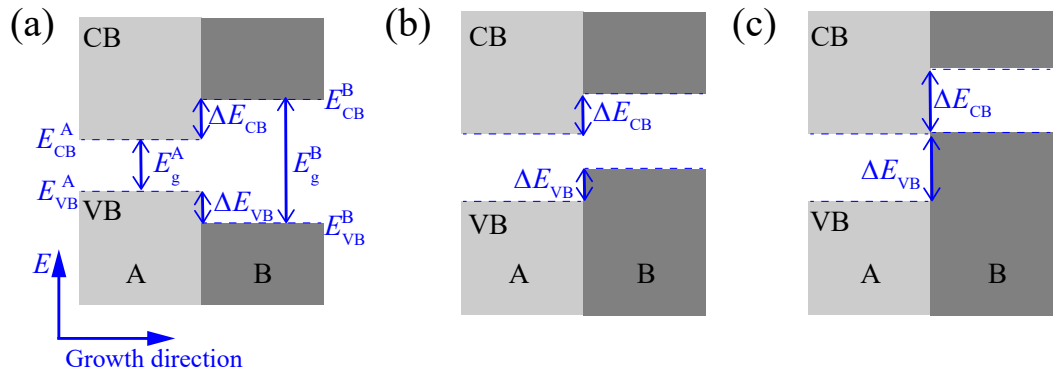

Figure 1.1 – Schematic band profiles of semiconductor heterojunctions formed by two different materials A and B. Depending on the materials employed, the heterojunction can present three types of band alignment: (a) Type I or straddling gap, (b) type II or staggered gap, and (c) type III or broken gap. The CB and VB offsets are depicted as ΔE_{CB} and ΔE_{VB}, respectively.

In all cases, the discontinuities between the energy bands induce *band offsets*, given by $\Delta E_j = E_j^B - E_j^A$, with j =CB, VB, g. From these relations, it is easy to see that the bandgap offset is the sum of the CB and VB offsets, $\Delta E_g = \Delta E_{CB} + \Delta E_{VB}$. Since the bandgap is usually a well-defined parameter, ΔE_g can be obtained straightforwardly, but the determination of ΔE_{CB} or ΔE_{VB} is a complex task depending on the fundamental properties of the semiconductors employed to form the heterojunction. Their definition is also crucial to tune their transport and optical properties of heterostructures, as well as to exploit the quantum confinement of charge carriers in technological applications.

The representation shown in figure 1.1 assumes perfectly abrupt interfaces at the heterojunction. Moreover, electronic states are not expected at the interfaces. Under these assumptions and considering a perfect lattice-matching between materials A and B, the *envelope function model* can be implemented to describe the electronic structure of a heterostructure presenting any of the foregoing band alignments. According to this model, the wavefunctions inside each material can be expressed as [10, 11, 24–26],

$$\psi_i(\mathbf{r}) = \sum_n \mathcal{F}_n^i(\mathbf{r})\varphi_{n0}^i(\mathbf{r}), \tag{1.12}$$

where $\mathcal{F}_n^i(\mathbf{r})$ are the *envelope functions*, which vary slowly over the lattice period, and i =A,B. In turn, the Bloch functions at $k=0$, $\varphi_{n0}^i(\mathbf{r})$, vary rapidly over the lattice period, and they are assumed to be the same in each material, so that: $\varphi_{n0}^{\mathrm{A}} \equiv \varphi_{n0}^{\mathrm{B}}$. Thus, a potential energy, $\mathcal{U}(\mathbf{r})$, can be considered to take into account the abrupt change of the electronic kinetic energy at the interface. In this way, according to eq. 1.4 and integrating around the volume of the interface, the Schrödinger equation for the heterostructure can be written as,

$$\int_\Omega d^3r \mathcal{F}_n(\mathbf{r}) \sum_m \left[\left(E_{m0} + \frac{\hbar^2 k^2}{2m_0} + \mathcal{U}(\mathbf{r}) - E_{n\mathbf{k}} \right) \delta_{nm} + \frac{1}{m_0} \mathbf{p}\cdot\mathbf{p}_{nm}(\mathbf{k}=0) \right] \mathcal{F}_m(\mathbf{r}) = 0, \tag{1.13}$$

where $\hbar\mathbf{k}$ has been transformed into the operator $\mathbf{p} = -i\hbar\nabla$ and $\mathbf{p}_{nm}(\mathbf{k}=0) = \langle \varphi_{n0}|\mathbf{p}|\varphi_{m0}\rangle$. Eq. 1.13 corresponds to an eigenvalue problem that can be expressed as,

$$[\hat{H}(\mathbf{k}=0) + \mathcal{U}(\mathbf{r})]\,|\mathcal{F}(\mathbf{r})\rangle = E\,|\mathcal{F}(\mathbf{r})\rangle\,, \tag{1.14}$$

where $\hat{H}(\mathbf{k}=0)$ is the Hamiltonian of the crystal as indicated in eq. 1.2, and $|\mathcal{F}(\mathbf{r})\rangle$ contains information about the finite energy band-edges considered in the heterostructure.

In this approach, to guarantee the continuity of the wavefunctions at the heterojunction, the envelope functions are continuous at the interface. Moreover, the electron states inside each material are assumed to be described by the Kane model [10, 27]. Under these assumptions, the boundary conditions can be obtained by considering the z axis along the growth direction, such that the heterojunction is located at $z=0$. Then, the interface potential, $\mathcal{U}$, can be supposed to be a shift in the CB and VB edges (at the center of the Brillouin zone) in material B with respect to A. Thus, taking the bottom of the CB of material A as the energy origin, the potential energy along the heterostructure becomes z-dependent and of the form,

$$\mathcal{U}(z) = \begin{cases} 0 & \text{if } z \le 0 \\ \mathcal{U}_0 & \text{if } z > 0. \end{cases} \tag{1.15}$$

As a consequence, the motion of electrons inside materials A and B can be described by k_z^{A} and k_z^{B}, respectively, while the lattice matching assumed for the system makes the heterostructure translationally invariant in the xy-plane. This implies that the transverse wavevector $k_\perp = (k_x, k_y)$ is conserved across the heterojunction and the envelope functions in a specific band edge take the form [10, 26],

$$\mathcal{F}_n(\mathbf{r}_\perp, z) = S\exp(i\mathbf{k}_\perp\cdot\mathbf{r}_\perp) f_n(z), \tag{1.16}$$

with S as a constant. Multiplying by its conjugate and integrating over space, one obtains a new set of eigenvalue equations given by,

$$\mathscr{H}_0 f_m(z) = E f_n(z), \tag{1.17}$$

where the matrix elements of $\mathscr{H}_0$ are [10],

$$D_{nm}\left(z, \frac{\partial}{\partial z}\right) = \left(E_{n0} + \mathcal{U}_0 + \frac{\hbar^2 k_\perp^2}{2m_0} - \frac{\hbar^2}{2m_0}\frac{\partial^2}{\partial z^2}\right)\delta_{nm} + \frac{\hbar \mathbf{k}_\perp}{m_0}\langle n|\mathbf{p}_\perp|m\rangle - \frac{i\hbar}{m_0}\langle n|p_z|m\rangle \frac{\partial}{\partial z}. \tag{1.18}$$

The effect of remote bands on the envelope functions can be taken into account only up to the second order in $\mathbf{p}$, which introduces the effective matrix [10],

$$\mathscr{H} = \mathscr{H}_0 - \frac{\hbar^2}{2}\sum_{\alpha,\beta}\frac{\partial}{\partial r_\alpha}\frac{1}{\widetilde{M}^{\alpha\beta}}\frac{\partial}{\partial r_\beta}, \tag{1.19}$$

with $\alpha, \beta = x, y, z$ and $\widetilde{M}^{\alpha\beta}$ a matrix with elements given by the effective mass tensor [10],

$$\frac{m_0}{M_{nm}^{\alpha\beta}} = \frac{2}{m_0}\sum_\nu \langle n|p_\alpha|\nu\rangle \frac{1}{\bar{E} - E_{\nu 0} - \mathcal{U}_\nu(z)}\langle n|p_\beta|\nu\rangle, \tag{1.20}$$

where ν refers to the remote edges and $\bar{E}$ is the average energy of the lowest Γ edges. The envelope functions are then the solutions of

$$\mathscr{H} f_m(z) = E f_n(z). \tag{1.21}$$

By integrating this expression across the heterojunction, where $f(z=0)$ is supposed continuous, a set of boundary conditions can be established as,

$$\mathscr{A}_{nm}^{\mathrm{A}} f_m^{\mathrm{A}}(z=0) = \mathscr{A}_{nm}^{\mathrm{B}} f_m^{\mathrm{B}}(z=0), \tag{1.22}$$

where the matrix elements are of the form [10],

$$\mathscr{A}_{nm} = -\frac{\hbar^2}{2m_0}\left[\left(\delta_{nm} + \frac{m_0}{M_n^{zz}}\right)\frac{\partial}{\partial z} + \frac{2i}{\hbar}\langle n|p_z|m\rangle + i\sum_{\alpha=x,y}\frac{m_0}{M_{nm}^{z\alpha}}k_\alpha\right]. \tag{1.23}$$

In the isotropic and non-degenerate parabolic approximation for the lowest energy bands, and for materials with different effective masses, $m_{\mathrm{A}}^* \neq m_{\mathrm{B}}^*$, eq. 1.21 can be simplified by assuming quantum states belonging to a single parabolic band. This model is known as the *BenDaniel-Duke model* [28], which for the case of a conduction band gives as a

result [10],

$$\left[E_s + \mathcal{U}_s(z) - \frac{\hbar^2}{2}\frac{\partial}{\partial z}\frac{1}{\mathcal{M}(z)}\frac{\partial}{\partial z} + \frac{\hbar^2 k_\perp^2}{2\mathcal{M}(z)}\right] f(z) = Ef(z), \tag{1.24}$$

with $\mathcal{U}_s(z)$ defined by eq. 1.15 and,

$$\mathcal{M}(z) = \begin{cases} m_A^* & \text{if } z \leq 0 \\ m_B^* & \text{if } z > 0. \end{cases} \tag{1.25}$$

Considering again the continuity condition for f at the heterojunction, the following boundary condition can be established,

$$\frac{1}{m_A^*}\frac{df^A(z)}{dz} = \frac{1}{m_B^*}\frac{df^B(z)}{dz}. \tag{1.26}$$

The above-presented expressions make it possible the description of the propagation of electronic waves along a heterostructure, as it is discussed in § 2.1 for tunneling structures, as well as the electronic structure at the interface, which produces the band profiles that guided the study of the heterostructures explored in this work. The band offsets, $\mathcal{U}(z)$, are of critical importance, once the energy levels in a quantum heterostructure are strongly dependent on this parameter, as presented in § 2.1 for the quantum wells in double-barrier structures. Several approaches have been reported in the literature for the theoretical determination of band offsets [20]. They cover methods based on the Anderson's rule [29], gap-state models [30], ab-initio pseudopotential calculations [31, 32], average bond energy theory [33], and tight-binding scheme [22], among others. However, each model has its limitations which can sometimes generate significant discrepancies between experimental data and predictions. Therefore, much care must be taken when choosing the predicted parameters for a specific heterojunction.

1.2 Transport Properties of Semiconductor Heterostructures

The transport of carriers inside a semiconductor heterostructure can be described using the parabolic band and the isotropic effective mass approximations to treat the carriers as approximately "free" charges under the action of an external field. To study their movement, let us consider conduction band electrons, such that the interactions among them and local field effects due to ionic charges are neglected. As a first approximation, we also assume electrons as plane waves traveling along z-direction so that $k_\perp^2$ has a negligible contribution allowing for a decoupling of the z components of the motion in eq 1.4. In this

sense, effects caused by scattering due to defects or sidewall interfaces are unconsidered. Then, the time evolution of an electron in one dimension (1D) in a heterostructure is given by,

$$\left[-\frac{\hbar^2}{2m^*}\frac{\partial^2}{\partial z^2}+U_0(z)\right]\Psi = i\hbar\frac{\partial\Psi}{\partial t}, \tag{1.27}$$

with $U_0(z)$ as the band profile of the heterojunction. The 3D case will be taken over in eq. 1.37. In the case of a sequence of step-like profiles (with flat bands), the stationary solution for this equation are of the form $\Psi = \psi(z)\exp(-i\omega t)$, being $\psi(z) = \mathcal{A}(z)\exp(ik(z)z) + \mathcal{B}(z)\exp(-ik(z)z)$ and $\omega = E/\hbar$. Here, $\mathcal{A}$ and $\mathcal{B}$ are constant amplitude coefficients within each layer, with positive (negative) exponent in $\psi(z)$ indicating to a wave propagation along positive (negative) z-direction. In this sense, the group velocity can be defined as $v_g \equiv \partial\omega/\partial k = \hbar k/m^*$, the wavevector, also constant within each layer, defined as $k(z) \equiv \sqrt{2m^*(E-U_0(z))}/\hbar$. Being the probability density given by $\rho \equiv |\psi|^2$ and following the continuity equation, $-\nabla\cdot\tilde{\mathbf{J}} = \partial\rho/\partial t$, the probability flux in 1D is,

$$\tilde{J}_z \equiv \frac{i\hbar}{2m^*}\left(\psi\frac{d\psi^*}{dz}-\psi^*\frac{d\psi}{dz}\right), \tag{1.28}$$

Lets assume flat band conditions at both left (emitter) and right (collector) ends of a layered structure so that the corresponding incoming and outgoing wavefunction components are $\psi_{L(R)}(z) = \mathcal{A}_{\mathcal{L}(\mathcal{R})}\exp(ik_{L(R)}z)$, then the corresponding fluxes take the form,

$$\tilde{J}_z^{L(R)} = \frac{\hbar k_{L(R)}}{m^*_{L(R)}}|\mathcal{A}_{\mathcal{L}(\mathcal{R})}|^2. \tag{1.29}$$

Therefore, when an electron reach a heterojunction, traveling from the left-hand side of it, one can define the *flux transmission coefficient*, $\mathcal{T}$, as the ratio between the electronic flux transmitted into the right-hand side of the heterojunction, $\tilde{J}_R$, and the incoming flux from the left-hand side, $\tilde{J}_\mathrm{L}$, so that [34]

$$\mathcal{T} \equiv \frac{\tilde{J}_R}{\tilde{J}_\mathrm{L}} = \frac{k_\mathrm{R}m^*_\mathrm{L}}{k_\mathrm{L}m^*_\mathrm{R}}\left|\frac{\mathcal{A}_\mathrm{R}}{\mathcal{A}_\mathrm{L}}\right|^2, \tag{1.30}$$

Thus, the contribution to the charge current density of a single electron in a given state with an incoming momentum k_L becomes

$$J_z^R = e\mathcal{T}\frac{\hbar k_L}{m^*_L}|\mathcal{A}_\mathcal{L}|^2. \tag{1.31}$$

Then, considering the normalization condition $\psi_L(z) = \exp(ik_Lz)/\sqrt{(L)}$ so that each state can occupy a volume in k space defined by $dk = 2\pi/L$ and the twofold spin degeneracy of

each given electronic state, the element of current density can be written as

$$dJ_z^R = 2e\mathscr{T}\frac{\hbar k}{m_L^*}\frac{dk_L}{2\pi}, \tag{1.32}$$

By considering that the source of electrons that contribute to the current on the left side is thermalized, then the electronic state occupation must be included and for this reason it is necessary to multiply the last expression by the local Fermi distribution $f(E,\mu_L)$, so that

$$dJ_z^R = 2e\mathscr{T} f(E,\mu_L)\frac{\hbar k}{m_L^*}\frac{dk}{2\pi}, \tag{1.33}$$

with μ as a chemical potential, also known as *quasi-Fermi level* that can be defined if the system is not strongly disturbed [34]. By integrating eq. 1.33 and taking $dE = \hbar^2 k dk/m^*$, the contribution to the current density of the flux from the left side to the right becomes

$$J_z^R = \frac{2e}{h}\int_0^\infty \mathscr{T} f(E,\mu_L)dE. \tag{1.34}$$

Consider, for instance, a single barrier with thermalized contacts, as sketched in figure 1.2 (a). This situation corresponds to an intrinsic material sandwiched by two highly doped semiconductors, for instance. The latter can be characterized by a distribution of electrons with chemical potentials μ_L and μ_R for the left- and right-hand sides, respectively. If a forward bias voltage, V, is applied, the right-hand side is shifted to lower energies regarding the left-hand side, and the difference between their energetic positions is simply $\mu_\mathrm{L} - \mu_\mathrm{R} = eV$.

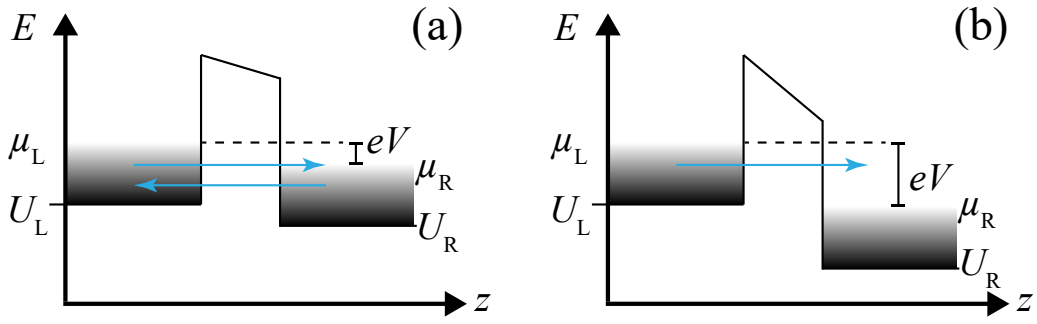

Figure 1.2 – Schematic representation of 1D-transport through a single potential barrier surrounded by a Fermi sea of electrons for (a) low and (b) high applied forward voltages, V. Blue horizontal arrows represents the electronic current contributions from both sides. In (b), high applied voltages prevent electronic currents from the right. Adapted from ref. [34]

To obtain the total current density, it is necessary to calculate the electronic current

flowing also from right to the left,

$$J_{\mathrm{L}} = -\frac{2e}{h}\int_{U_{\mathrm{R}}}^{\infty} \mathscr{T} f(E,\mu_{\mathrm{R}})dE, \tag{1.35}$$

where we have used the symmetry of the transmission coefficient. Thus the total current is $J = J_{\mathrm{R}} + J_{\mathrm{L}}$, which gives as a result

$$J = \frac{2e}{h}\int_{U_{\mathrm{L}}}^{\infty} \mathscr{T}\left[f(E,\mu_{\mathrm{L}}) - f(E,\mu_{\mathrm{R}})\right]dE, \tag{1.36}$$

where the lower limit corresponds to the higher value between U_{L} and U_{R}, since there are no propagating waves in the range from U_{R} to U_{L} [34].

Eq. 1.36 can be extended to three-dimensions taking advantage of the decoupling assumed between the in-plane and the z-component of the transport. Accordingly, the current differential from the left-hand side can be expressed as

$$dJ_{\mathrm{R}} = 2e\mathscr{T}(z) f(E,\mu_{\mathrm{L}})\frac{\hbar k_z}{m^*}\frac{dk_x}{2\pi}\frac{dk_y}{2\pi}\frac{dk_z}{2\pi}. \tag{1.37}$$

Taking $k_\perp^2 = k_x^2 + k_y^2$, integrating the last expression and rearranging terms, one has

$$J_{\mathrm{R}} = e\int_0^{\infty}\frac{dk_z}{2\pi}\mathscr{T}(z)\frac{\hbar k_z}{m^*}\left[2\int\frac{d^2k_\perp}{(2\pi)^2} f(E,\mu_{\mathrm{L}})\right]. \tag{1.38}$$

In a similar way, the total energy is given by $E = E_z + E_\perp$, where $E_z = U_{\mathrm{L}} + \hbar^2 k_z^2/2m^*$ and $E_\perp = \hbar^2 k_\perp^2/2m^*$. Hence, $dE_z = \hbar^2 k_z dk_z/m^*$ and the current from the left turns into

$$J_{\mathrm{R}} = \frac{e}{2\pi\hbar}\int_{U_{\mathrm{L}}}^{\infty}\mathscr{T}(z)dE_z\left[2\int\frac{d^2k_\perp}{(2\pi)^2} f(E_z+E_\perp,\mu_{\mathrm{L}})\right]. \tag{1.39}$$

If thermal equilibrium among carriers is assumed, Fermi-Dirac functions of the form $f(E,\mu) = \left\{1+\exp[(E-\mu)/k_{\mathrm{B}}T]\right\}^{-1}$ can be used as occupation functions. In such a case, it is easy to show that $f(E_z+E_\perp,\mu_{\mathrm{L}}) = f(E_\perp,\mu_{\mathrm{L}}-E_z)$ and eq. 1.39 results in

$$J_{\mathrm{L}} = \frac{e}{2\pi\hbar}\int_{U_{\mathrm{L}}}^{\infty}\mathscr{T}(z)dE_z\left[2\int\frac{d^2k_\perp}{(2\pi)^2} f(E_\perp,\mu_{\mathrm{L}}-E_z)\right]. \tag{1.40}$$

The expression in square brackets, with the factor of 2 for spin, represents the electron density in a two-dimensional electron gas, $n_{2\mathrm{D}}(\mu)$, in the xy-plane, with the band edge raised to $E_z = U_{\mathrm{L}} + \hbar^2 k_z^2/2m^*$. This density can be rewritten as

$$n_{2\mathrm{D}}(\mu) = 2\int_{-\infty}^{\infty}\frac{d^2k_\perp}{(2\pi)^2} f(E_\perp,\mu) = 4\int_0^{\infty}\frac{2\pi k_\perp dk_\perp}{(2\pi)^2} f(E_\perp,\mu), \tag{1.41}$$

where $dE_\perp = \hbar^2 k_\perp dk_\perp / m^*$ and consequently,

$$n_{2D}(\mu) = \frac{2m^*}{\hbar^2 \pi} \int_0^\infty f(E_\perp, \mu) dE_\perp. \tag{1.42}$$

For thermal equilibrium conditions and making the variable change $\varrho \equiv \exp[-(E_\perp - \mu)/k_B T]$ in eq. 1.42, the integral on the right-hand side transforms into,

$$\int_0^\infty f(E_\perp, \mu) dE_\perp = k_B T \int_0^{\varrho_0} \frac{1}{1+\varrho} d\varrho = k_B T \ln\left(1+\varrho_0\right), \tag{1.43}$$

where $\varrho_0 = \exp(\mu/k_B T)$. Thus, the 2D carrier density at equilibrium has the form

$$n_{2D}(\mu) = \frac{2m^* k_B T}{\hbar^2 \pi} \ln\left[1 + \exp\left(\frac{\mu}{k_B T}\right)\right]. \tag{1.44}$$

The results presented above allow expressing the current densities from the left- and right-hand sides, in 3D as

$$\begin{aligned} J_R &= \frac{e}{2\pi\hbar} \int_{U_L}^\infty \mathcal{T}(z) n_{2D}(\mu_L - E_z) dE_z, \\ J_L &= -\frac{e}{2\pi\hbar} \int_{U_R}^\infty \mathcal{T}(z) n_{2D}(\mu_R - E_z) dE_z, \end{aligned} \tag{1.45}$$

and the total current density in 3D takes the form

$$J = \frac{e}{2\pi\hbar} \int_{U_L}^\infty \mathcal{T}(E_z) \left[n_{2D}(\mu_L - E_z) - n_{2D}(\mu_R - E_z)\right] dE_z, \tag{1.46}$$

which has a similar structure to the Tsu-Esaki equation [35]. This is an important result, since it allows to characterize coherent transport channels along the growth direction of quantum tunneling heterostructures, by choosing an appropriate transmission coefficient. This constitutes the basis for the discussion of the transport properties in resonant tunneling diode presented in § 2.3 and throughout the results of this work.

1.3 Optical Recombination Mechanisms

When a semiconductor system is subjected to a *continuous* external excitation that promotes electrons in the CB and holes in the VB, different *recombination* mechanisms can be triggered, thus leading to the subsequent carriers annihilation. Such a process can be *radiative*, as happens during luminescence emissions, or *non-radiative*, as occurs in the Auger recombination process, for example. In both cases, electrons and holes disappear after recombination, and the excess energy given by the excitation source can be transferred into photons, phonons, or both. Although radiative and non-radiative

processes can be simultaneously present in the optical dynamics of semiconductors, only the former is considered in this section since it gives rise to the optical spectra observed during experiments that will be described in Chapters 4, 5, and 6, where the effects of non-radiative processes in the optical response of the samples is negligible.

Prior to recombination, *generation* processes must be triggered to promote carriers to high energy levels that recombine after a certain characteristic time. It is achieved, for example, by exciting the semiconductor with high-enough applied electric fields that inject carriers into the system, leading to an electroluminescence (EL) emission, or with incident light, whose photons usually have energy equal or greater than the bandgap of the materials, $\hbar\omega \geq E_g$, to guarantee light absorption and the subsequent photoluminescence (PL) emission.

During EL emission, the supplied electrical energy is converted into radiation, in a process defined by the structural parameters of the sample [36]. Although various transport mechanisms in a semiconductor can promote carriers into states suitable for radiative recombination [36, 37], the *impact ionization process* prevails in the generation of EL emissions under certain conditions. In this process, electrons driven by high-applied electric fields can travel along with the CB until colliding with electrons in the VB or donor activator centers. This collision promotes the latter into the CB states, transferring kinetic energy, which is conserved jointly with the linear momentum [38, 39]. The excitation of VB electrons toward the CB leaves empty states or holes at the former band, that become available for radiative recombination processes. In order to trigger this process, electrons responsible for ionization must achieve a minimum energy. This threshold energy for ionization, assuming the parabolic approximation and a process without emission of phonons, is given by [40],

$$E_{\text{th}} = E_g\left(\frac{2+\theta}{1+\theta}\right), \tag{1.47}$$

where $\theta = m_h^*/m_e^*$. Although the threshold energy can also depend on temperature, electric fields and the crystallographic direction [40–43], it is mainly determined by characteristic parameters of the semiconductor. Thus, for GaAs and GaSb at room temperature, E_{th} must be $\sim 1.1E_g$. Then, the impact ionization rate, as a function of the kinetic energy, can be obtained according to the generalized Keldysh model as [44, 45],

$$\Pi(E) = C\left(\frac{E-E_{\text{th}}}{E_{\text{th}}}\right)^a, \tag{1.48}$$

with C and a as characteristic parameters of the semiconductor material.

On the other hand, during PL emission, the generation rate is ruled by *light absorption*. Here, the excited electron gains energy without changing its momentum once the momentum transferred from the incoming photon can be neglected [46]. In semiconductors with

direct gap, the absorbed photon promotes the electron from an initial state with energy E_i to a final state with energy E_f, such that $\hbar\omega = E_f - E_i$ with $E_f > E_i$. Consequently, the absorption coefficient can be calculated as [46],

$$\alpha = \mathscr{C} \sum_{i,f} f(E_i)[1 - f(E_f)]P_{if}, \tag{1.49}$$

where $\mathscr{C}$ is a constant, $f(E_i)$ is the occupancy of electrons in the initial state, $[1 - f(E_f)]$ characterizes the availability of the empty final states, and P_{if} is the transition probability from the initial to the final state that can be obtained by the Fermi Golden Rule for time-dependent perturbations as [47],

$$P_{if} = \frac{2\pi}{\hbar} \left|\langle \varphi_f | V | \varphi_i \rangle\right|^2 \delta(E_f - E_i - \hbar\omega), \tag{1.50}$$

where, $\langle \varphi_f | V | \varphi_i \rangle \equiv V_{if} \propto \epsilon \cdot \langle \varphi_f | \mathbf{p} | \varphi_i \rangle$, with ϵ as the polarization vector of the incident photon [18].

After excitation by electric fields or light, carriers might lose energy due to scattering processes, until reaching states closer to the CB or VB edges, where radiative recombination is most likely to take place. In case of *band-to-band recombination*, where $|\varphi_i\rangle = |\varphi_C\rangle$ and $|\varphi_f\rangle = |\varphi_V\rangle$ (with C and V indicating CB and VB), the optical emission rate is given by,

$$Q \propto \sum_{C,V} |V_{CV}|^2 f(E_C)[1 - f(E_V)]\delta(E_C - E_V - \hbar\omega), \tag{1.51}$$

with $E_C > E_V$, both defined by eqs. 1.10 and 1.11, respectively. As a consequence, one has contributions of both conduction and valence band states, and the summation must be performed along different combinations between these states. This can be done by introducing the *joint density of states*, $\rho_{JDS}(\omega)$ [18], such that $Q \propto |V_{C,V}|^2 \rho_{JDS}(\omega)$. Here, under the approximation of direct transitions, with no change in the linear momentum after recombination ($k_C = k_V = k$), the perturbation V_{CV} can be considered as $|V_{CV}|^2 \propto |\epsilon \cdot \mathbf{p}|^2 \delta_{k_C,k_V}$. In turn, $\rho_{JDS}(\omega)$, is given by,

$$\rho_{JDS}(\omega) = \frac{2}{(2\pi\hbar)^3} \int d^3p\, f(E_C)[1 - f(E_V)]\delta(E_C - E_V - \hbar\omega), \tag{1.52}$$

with $p = \hbar k$. This expression can be integrated in the parabolic band approximation for E_C and E_V yielding,

$$\rho_{JDS}(\omega) = \frac{\sqrt{2{m_r^*}^3(\hbar\omega - E_g)}}{(\pi^2\hbar)^3} f_\mu\left(E_g + \frac{m_r^*}{m_e^*}(\hbar\omega - E_g)\right)\left[1 - f_\mu\left(-\frac{m_r^*}{m_h^*}(\hbar\omega - E_g)\right)\right], \tag{1.53}$$

with μ as a common chemical potential within the bandgap and $m_{\mathrm{r}}^{*\,-1} = m_{\mathrm{e}}^{*\,-1} + m_{\mathrm{h}}^{*\,-1}$ as a reduced effective mass.

In this sense, eq. 1.53 enables the calculation of the optical recombination rate in direct band-to-band recombination processes, as $Q \propto |\epsilon \cdot \mathbf{p}|^2 \delta_{k_{\mathrm{C}},k_{\mathrm{V}}} \rho_{\mathrm{JDS}}(\omega)$. This is possible as long as the occupation function for electrons is conveniently defined, according to the carrier dynamics at the CB and VB, as examined in the next section.

1.4 Electrons and Holes Statistics and the Concept of Effective Temperature

In order to use the optical emission rate as defined in the preceding section, it is imperative to define appropriate distribution functions for the electronic states in the CB and VB. Although this is not an easy task, one can assume, as an initial approach, that carriers in each band are in thermal equilibrium among themselves, following Fermi-Dirac distributions. Accordingly, the valence band vacancy probability can be rewritten in terms of the hole occupation as,

$$1 - f_{\mu}\left(-\frac{m_{\mathrm{r}}^{*}}{m_{\mathrm{h}}^{*}}(\hbar\omega - E_{\mathrm{g}}), T\right) = f_{-\mu}\left(\frac{m_{\mathrm{r}}^{*}}{m_{\mathrm{h}}^{*}}(\hbar\omega - E_{\mathrm{g}}), T\right). \tag{1.54}$$

Hence, substituting eq. 1.54 into eq. 1.53 one can obtain the band-to-band optical emission intensity, according to eq. 1.51, as

$$Q \propto \sqrt{2m_{\mathrm{r}}^{*\,3}(\hbar\omega - E_{\mathrm{g}})}\, f_{\mu}\left(E_{\mathrm{g}} + \frac{m_{\mathrm{r}}^{*}}{m_{\mathrm{e}}^{*}}(\hbar\omega - E_{\mathrm{g}}), T\right) f_{-\mu}\left(\frac{m_{\mathrm{r}}^{*}}{m_{\mathrm{h}}^{*}}(\hbar\omega - E_{\mathrm{g}}), T\right). \tag{1.55}$$

Figure 1.3 (a) illustrates the optical emission intensity obtained with eq. 1.55 as a function of $\hbar\omega/E_{\mathrm{g}}$, for different values of $k_{\mathrm{B}}T$. As expected for this model, the emission is triggered at energies above the bandgap $\hbar\omega/E_{\mathrm{g}} \geq 1$, with an increasing intensity as the temperature rises. We should point out that additional effects, not considered in this simulation, may counterbalance such an increase.

In thermal-equilibrium conditions and taking the non-degenerate limit of the optical emission rate, which corresponds to the high-energy spectral tail where $(E-\mu)/k_{\mathrm{B}}T \gg 0$, the Fermi-Dirac distributions can be approximated by Boltzmann's functions of the form $f_{\mu}(E,T) \propto \exp[-(E-\mu)/k_{\mathrm{B}}T]$. In this limit, the optical emission rate is $Q \propto \exp(-\hbar\omega/k_{\mathrm{B}}T)$, as indicated in figure 1.3 (b) by dashed lines.

It is worth noting that, the relative contribution of each band to the occupation probability in terms of the photon energy is also dependent of the carriers effective mass. Thus, an effective chemical potential, μ^{*}, can be assigned to both type of carriers, and the

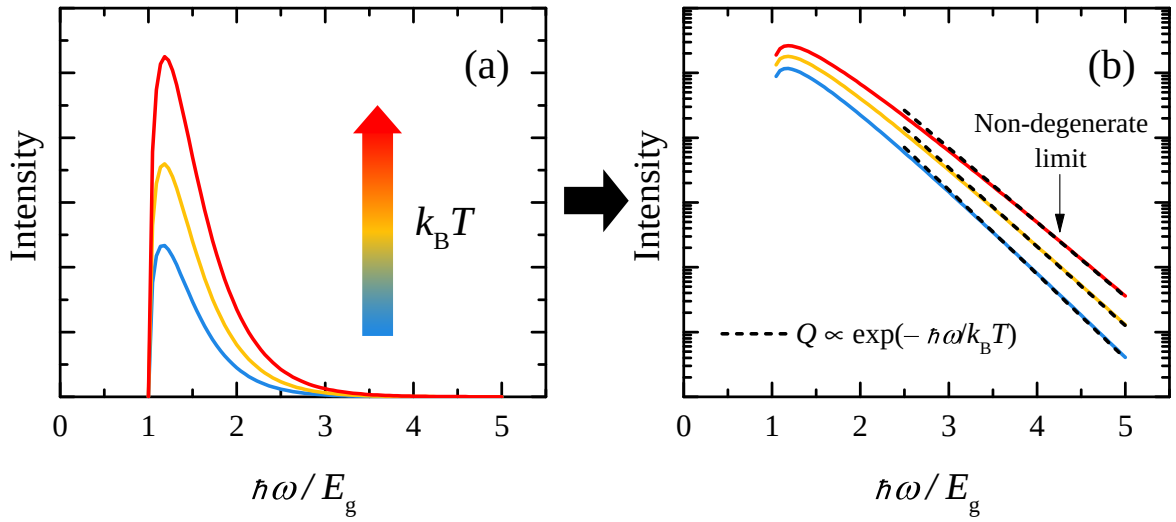

Figure 1.3 – (a) Optical emission intensity in a semiconductor as a function of $\hbar\omega/E_g$, for different values of $k_B T$ (color lines), according to eq. 1.55. (b) Same situation as in (a) plotted in a semi-logarithmic scale to illustrate the non-degenerate limit, $(E-\mu)/k_B T \gg 0$, where $Q \propto \exp(-\hbar\omega/k_B T)$ (dashed lines).

distribution functions can be transformed in the following way,

$$f_\mu\left(E_g + \frac{m_r^*}{m_e^*}(\hbar\omega - E_g), T\right) f_{-\mu}\left(\frac{m_r^*}{m_h^*}(\hbar\omega - E_g), T\right) = f_{\mu_e^*}\left(\hbar\omega - E_g, \frac{m_e^*}{m_r^*}T\right) f_{\mu_h^*}\left(\hbar\omega - E_g, \frac{m_h^*}{m_r^*}T\right). \quad (1.56)$$

In eq. 1.56, effective chemical potential for electrons is $\mu_e^* = m_e^*(\mu_e - E_g)/m_r^*$, and for holes is $\mu_h^* = m_h^*\mu_h/m_r^*$, with μ_i representing the chemical potential for each carrier population. Note that for a stationary condition, under an applied electric field, continuous wave optical excitation, or both, the thermal equilibrium is not reached. Thus, within the more general picture, electrons and holes can be considered as independent subsystems and their probability distributions ruled by Fermi-like functions with independent chemical potentials (μ_e, μ_h) and temperatures (T_e, T_h) [48]. As a result, the optical emission rate for uncoupled e-h pairs in stationary conditions takes the form,

$$Q \propto \sqrt{2m_r^{*\,3}(\hbar\omega - E_g)}\, f_{\mu_e^*}\left(\hbar\omega - E_g, \frac{m_e^*}{m_r^*}T_e\right) f_{\mu_h^*}\left(\hbar\omega - E_g, \frac{m_h^*}{m_r^*}T_h\right). \quad (1.57)$$

Given the finite time for energy exchange between carriers and the lattice, which is assumed in equilibrium with the environment at a temperature, T_L, the mean energy excess with respect to the equilibrium energy can be characterized by the carriers temperature, T_i (i =e,h). In the energy relaxation time approximation, the mean variation of energy over

time is given by [49]

$$\left\langle \frac{dE_i}{dt} \right\rangle \approx \frac{\frac{2}{3}\langle E_i \rangle - k_B T_L}{\tau_i^{\varepsilon}}, \tag{1.58}$$

being the energy relaxation time represented by τ_i^{ε}, and the average carrier energy defined by $\langle E_i \rangle \equiv 3/2 k_B T_i$. Thus, T_i is a parameter that depends on both external fields and scattering mechanisms. Based on these approximations, in the non-degenerate limit for photon energies above the bandgap, eq. 1.57 can be expressed as,

$$Q \propto \sqrt{2 m_r^{*\,3} (\hbar\omega - E_g)} \exp\left[\frac{(\mu_e - E_g) + \frac{m_r^*}{m_e^*} E_g}{k_B\, T_e} + \frac{-\mu_h + \frac{m_r^*}{m_h^*} E_g}{k_B\, T_h} \right] \exp\left[-\frac{\hbar\omega}{k_B T_{eff}^{e\text{-}h}} \right], \tag{1.59}$$

where the last exponential term in eq. 1.59, which depends on the energy of the emitted photons, $\hbar\omega$, represents the Boltzmann's exponential decay ruled by the *e-h effective temperature* given by,

$$\frac{1}{T_{eff}^{e\text{-}h}} = \frac{m_r^*}{m_e^*}\frac{1}{T_e} + \frac{m_r^*}{m_h^*}\frac{1}{T_h}, \tag{1.60}$$

Despite this expression being valid for bulk materials, an analogous energy decay can also be obtained for 2D e-h pairs [10]. Thus, disregarding the effect of slow-varying terms with $\hbar\omega$, one may approximate, $\ln Q(\hbar\omega) \approx -\hbar\omega/(k_B T_{eff}^{e\text{-}h}) + C$, with C as a constant. The latter can be used to fit the high-energy spectral tails of the emission bands, yielding the corresponding value of $T_{eff}^{e\text{-}h}$, as discussed in Chapter 5, where the physical meaning of $T_{eff}^{e\text{-}h}$ will be clarified.

The effective temperature obtained from this procedure has contributions from the temperature of both electrons and holes, which are not necessarily thermalized with the lattice. These *hot carriers* are mainly present in heterostructures subjected to high energy excitations, where the energy gained from the excitation source causes an increase of the charge carrier mean energy above its thermal equilibrium value, $3k_B T_L/2$ [50, 51]. Consequently, $T_{eff}^{e\text{-}h}$ is expected to vary for changing optical excitation conditions and applied voltage. The optical and electrical heating of non-equilibrium carriers has been the focus of various studies using analogous approaches to the one presented here [52, 53]. Besides the characterization of the thermalization of hot carriers, optical and electrical heating has been used, for instance, to unveil the nature of energy relaxation mechanisms in heterostructures [54], and even to characterize the localization dynamics of photogenerated carriers [55].

Note that, according to eq. 1.60, the weights of electron or hole contributions to the e-h effective temperature depend on their effective masses. For example, if $m_e^* \ll m_h^*$, one has

that $m_r^* \rightarrow m_e^*$ and the e-h effective temperature can be approximated to,

$$T_{eff}^{e\text{-}h} \approx T_e \frac{1}{1+\frac{m_e^* T_e}{m_h^* T_h}}, \tag{1.61}$$

implying that the assumption $T_{eff}^{e\text{-}h} \approx T_e$ is not straightforward for the independent thermalization of electrons and holes.

The relative effect of varying individual temperatures can be evaluated by examining the derivative,

$$\frac{dT_{eff}^{e\text{-}h}}{dT_i} = \frac{m_i^*}{m_r^*}\left(1+\frac{m_i^* T_i}{m_i^* T_i}\right)^{-2}, \tag{1.62}$$

as a function of the ratio between carriers temperature, T_h/T_e, as depicted in figure 1.4. The derivative with respect to the holes temperature (black solid line) shows that when $T_h/T_e \rightarrow \infty$, $T_{eff}^{e\text{-}h}$ is not affected by changes of T_h, but when $T_h/T_e \rightarrow 0$, $T_{eff}^{e\text{-}h}$ is strongly influenced by varying T_h. For the derivative with respect to the electrons temperature (blue solid line), the opposite is expected. In both cases, the variation of the carriers effective temperature is limited by the ratios m_h^*/m_r^* (black dashed line) and m_e^*/m_r^* (blue dashed line) for holes and electrons, respectively. This dependence indicates that fluctuations in holes temperature can also be detected by measuring $T_{eff}^{e\text{-}h}$, if T_h is low compared with T_e.

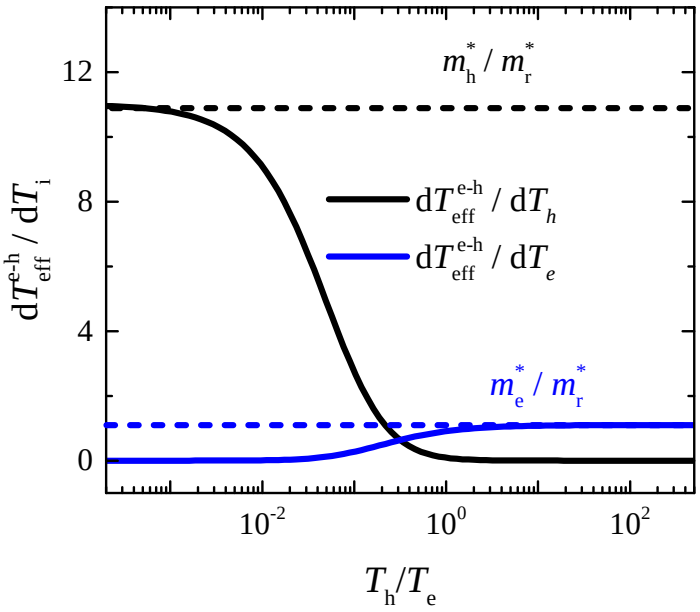

Figure 1.4 – Calculated derivative of $T_{eff}^{e\text{-}h}$ with respect to T_i for i =h (black line), and i =e (blue line) as a function of the ratio T_h/T_e. Horizontal dashed lines indicate the limits where changes in T_h/T_e produce the greatest variations in $T_{eff}^{e\text{-}h}$. Adapted from ref. [56].

The non-thermalization of different kinds of hot carriers is an old prediction [49, 57, 58] grounded on the difference between carriers population and carriers effective masses. These differences control the balance between the efficiency of the carrier-carrier scatter-

ing process and the strength of the coupling of the carriers with the lattice that leads to potential energy losses [52, 53, 59]. Thus, thermalization maps may also discern temperature profiles according to the carrier type, as presented in § 5.4.

1.5 Time-resolved Carrier Dynamics

The generation and recombination dynamics can be better understood by analyzing the temporal response of the system when subjected to a *pulsed excitation*. In the case of Time-Resolved Photoluminescence (TRPL) measurements, a pulse of light is provided, which is assumed infinitely short in time (concerning the intrinsic time scales of the studied dynamics) and with energy enough to generate a population of carriers in excited states of the semiconductor or heterostructure [60]. When the pulse is turned off, this excited-state population starts to *decay* due to different scattering and energy relaxation processes. As a result, carriers do not recombine at the same time. The time distribution of emitted photons translates into a transient response, with an optical emission intensity decaying in time, characterized by a *lifetime* [60].

To unveil the main ingredients of these dynamics and gain an understanding of the meaning of the observed lifetimes, a three-level model can be assumed as a first approximation for a quantized system, as sketched in figure 1.5 (a). The excitation pulse pumps carriers into an excited state (red arrow), thus generating a population of electron-hole pairs, n_{exc}. Subsequently, this population relaxes to a ground state (straight arrow) with a decay time τ_{in}, producing the population n_0. There, carriers can relax in two ways: by recombining radiatively with a rate characterized by a time τ_1 (wavy arrow), or by recombining (or escaping) non-radiatively (curved arrow) in a process determined by a time τ_{d}.

Then, a system of rate equations can be set as,

$$\begin{aligned} \frac{dn_{\text{exc}}}{dt} &= -\frac{n_{\text{exc}}}{\tau_{\text{in}}} \\ \frac{dn_0}{dt} &= \frac{n_{\text{exc}}}{\tau_{\text{in}}} - \frac{n_0}{\tau_1} - \frac{n_0}{\tau_{\text{d}}}, \end{aligned} \tag{1.63}$$

with τ_{in}, τ_1, and τ_{d} assumed as constants. Herein, positive terms on the right refer to generation of carriers in a specific quantum state, while negative terms indicate relaxation of carriers population along different lifetimes. Under these circumstances, at the instant $t = 0$ the initial population in the excited state is $n_{\text{exc}}(0) = N_0$, while the ground state is void, $n_0(0) = 0$. Introducing the total dephasing time as $\tau_2^{-1} = \tau_1^{-1} + \tau_{\text{d}}^{-1}$, which must be

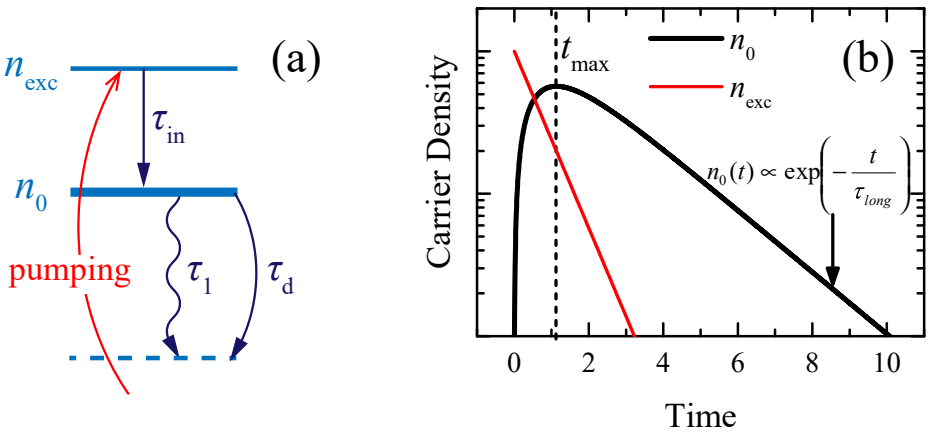

Figure 1.5 – (a) Representation of a three-level model illustrating the carrier dynamics in a quantized system. The excited population, n_{exc}, generated after pumping (red arrow) with a pulsed source, relaxes into the population n_0 at a fundamental state (straight arrow). Therein, carriers can recombine radiatively (wavy arrow) or non-radiatively (curved arrow). (b) Carrier density as a function of time, obtained for n_0 (black line) and n_{exc} (red line), according to eqs. 1.64 and 1.65. After injection from the excited state, the maximum of n_0 is achieved at t_{max}. At long times, the exponential decay is ruled by τ_{long}.

closer to the lowest time between τ_1 and τ_d, the solutions for the system in eq. 1.63 are,

$$n_{exc}(t) = N_0 \exp\left(-\frac{t}{\tau_{in}}\right) \tag{1.64}$$

$$n_0(t) = N_0 \frac{\tau_2}{|\tau_2 - \tau_{in}|}\left[1 - \exp\left(-t\frac{|\tau_2 - \tau_{in}|}{\tau_2\tau_{in}}\right)\right]\exp\left(-\frac{t}{\tau_{long}}\right), \tag{1.65}$$

with $\tau_{long} = \max(\tau_2, \tau_{in})$.

Figure 1.5 (b) shows the time evolution of both carrier populations in a semi-logarithmic scale, according to eqs. 1.64 and 1.65. Here, n_0 defines the optical transient emission of the system, since the optical intensity is proportional to the carrier population involved in radiative recombination processes, as discussed in the previous section. In the first moments, n_0 rises due to injection from the excited state, attaining a maximum value at,

$$t_{max} = \frac{\tau_2\tau_{in}}{|\tau_2 - \tau_{in}|}\ln\left(\frac{\tau_2}{\tau_{in}}\right), \tag{1.66}$$

after which the carrier population decreases. The transient response at long times, $n_0(t) \propto \exp(-t/\tau_{long})$, is determined by the competition between τ_2 and τ_{in}, or in other words, by the competition between radiative/non-radiative recombination and intraband relaxation processes [10].

We should note that for very fast dynamics, the assumption of an instantaneous pumping might fail. In such a case the experimental excitation signal must be deconvoluted in order to distinguish the characteristic lifetimes of the system at this regime [10]. Also, TRPL experiments may produce non-monoexponetial decays, preventing the deconvolution of

the signal. Thus, the transient response is characterized by an effective lifetime given by,

$$\tau_{\text{eff}}(t) = -\left(\frac{d}{dt}\ln \mathcal{I}\right)^{-1}, \tag{1.67}$$

with $\mathcal{I}$ being the intensity of the emitted light. This time may differ from the limit lifetime τ_{long}, which corresponds to,

$$\tau_{\text{long}}(t) = \lim_{t\to\infty} \tau_{\text{eff}}(t). \tag{1.68}$$

Eq. 1.67 implies that the estimations of the lifetimes are unavoidably dependent on the temporal window chosen for the extraction of τ_{eff}, and, consequently, the experimental results must be carefully analyzed and interpreted in the light of the specific properties of the system, as considered in § 5.5, for the study of the carrier dynamics in Sb-based double-barrier quantum wells.

References

[1] R. J. Matyi, "Ch. 2. Growth of Quantum Confined Structures by Molecular Beam Epitaxy," in *Heterostructures and Quantum Devices* (N. G. Einspruch and W. R. Frensley, eds.), vol. 24 of *VLSI Electronics Microstructure Science*, pp. 25–61, Elsevier, 1994.

[2] J. R. Arthur, "Molecular beam epitaxy," *Surf. Sci.*, vol. 500, no. 1, pp. 189–217, 2002.

[3] P. D. Dapkus, "Chapter 3 - Metalorganic Chemical Vapor Deposition for the Fabrication of Nanostructure Materials," in *Heterostructures and Quantum Devices* (N. G. Einspruch and W. R. Frensley, eds.), vol. 24 of *VLSI Electronics Microstructure Science*, pp. 63–106, Elsevier, 1994.

[4] A. Pfenning, J. Jurkat, A. Naranjo, D. Köck, F. Hartmann, and S. Höfling, "Resonant tunneling diode photon number resolving single-photon detectors," in *Infrared Remote Sensing and Instrumentation XXVII* (M. Strojnik and G. E. Arnold, eds.), vol. 11128, pp. 47 – 56, International Society for Optics and Photonics, SPIE, 2019.

[5] X. Wang, D. Pan, M. Sun, F. Lyu, J. Zhao, and Q. Chen, "High-Performance Room-Temperature UV-IR Photodetector Based on the InAs Nanosheet and Its Wavelength- and Intensity-Dependent Negative Photoconductivity," *ACS Appl. Mater. Interfaces*, vol. 13, no. 22, pp. 26187–26195, 2021. PMID: 34032402.

[6] J. R. Meyer, W. W. Bewley, C. L. Canedy, C. S. Kim, M. Kim, C. D. Merritt, and I. Vurgaftman, "The Interband Cascade Laser," *Photonics*, vol. 7, no. 3, 2020.

[7] A. Bader, A. Pfenning, A. Schade, G. Knebl, R. Weih, Y. Rawal, L. Worschech, F. Hartmann, and S. Höfling, "Progress on mid-infrared optoelectronic devices: interband

cascade lasers, interband cascade detectors, and resonant tunneling diodes," in *Infrared Remote Sensing and Instrumentation XXVIII* (M. Strojnik, ed.), vol. 11502, pp. 114 – 123, International Society for Optics and Photonics, SPIE, 2020.

[8] G. Moses, X. Huang, Y. Zhao, M. Auf der Maur, E. A. Katz, and J. M. Gordon, "InGaN/GaN multi-quantum-well solar cells under high solar concentration and elevated temperatures for hybrid solar thermal-photovoltaic power plants," *Prog. Photovoltaics*, vol. 28, no. 11, pp. 1167–1174, 2020.

[9] A. Raman, C. Chaturvedi, and N. Kumar, "Multi-Quantum Well-Based Solar Cell," in *Electrical and Electronic Devices, Circuits, and Materials*, pp. 351–372, John Wiley & Sons, Ltd, 2021.

[10] G. Bastard, *Wave Mechanics Applied to Semiconductor Heterostructures*. Paris: les éditions de physique, 1990.

[11] F. T. Vasko and A. V. Kuznetsov, *Electronic States and Optical Transitions in Semiconductor Heterostructures*. Graduate Texts in Contemporary Physics, New York: Springer, 1st ed., 1999.

[12] A. F. Ioffe, *Physics of Semiconductors*. New York: Academic Press, Inc., 1st ed., 1960.

[13] C. Kittel, *Introduction to Solid State Physics*. New Jersey: John Wiley & Sons, Inc., 8th ed., 2005.

[14] J. M. Luttinger and W. Kohn, "Motion of Electrons and Holes in Perturbed Periodic Fields," *Phys. Rev.*, vol. 97, pp. 869–883, Feb 1955.

[15] M. R. d. S. Dias, *Transport phenomena in quasi-one-dimensional heterostructures*. PhD thesis, Universidade Federal de São Carlos, SSão Carlos, SP, 2014.

[16] P. Yu and M. Cardona, *Fundamentals of Semiconductors: Physics and Materials Properties*. Graduate Texts in Physics, Berlin: Springer, 4th ed., 2010.

[17] O. Manasreh, *Semiconductor Heterojunctions and Nanostructures*. New York: McGraw-Hill Education, 2005.

[18] M. Grundmann, *The Physics of Semiconductors: An Introduction Including Devices and Nanophysics*. Berlin: Springer Berlin Heidelberg, 2006.

[19] D. M. Meneses Gustin, *Electronic and optical properties of Quasi-2D nanostructures and exfoliated systems*. PhD thesis, Universidade Federal de São Carlos, SSão Carlos, SP, 2017.

[20] E. T. Yu, J. O. McCaldin, and T. C. McGill, "Band Offsets in Semiconductor Heterojunctions," vol. 46 of *Solid State Physics*, pp. 1–146, Academic Press, 1992.

[21] W. R. Frensley, "Chapter 1 - Heterostructure and Quantum Well Physics," in *Heterostructures and Quantum Devices* (N. G. Einspruch and W. R. Frensley, eds.), vol. 24 of *VLSI Electronics Microstructure Science*, pp. 1–24, Elsevier, 1994.

[22] K. Shim, "Composition dependence of band alignments in $Ga_xIn_{1-x}As_ySb_{1-y}$ heterojunctions lattice matched to GaSb and InAs," *J. Appl. Phys.*, vol. 114, no. 20, p. 203703, 2013.

[23] E. D. Guarin Castro, F. Rothmayr, S. Krüger, G. Knebl, A. Schade, J. Koeth, L. Worschech, V. Lopez-Richard, G. E. Marques, F. Hartmann, A. Pfenning, and S. Höfling, "Resonant tunneling of electrons in AlSb/GaInAsSb double barrier quantum wells," *AIP Adv.*, vol. 10, no. 5, p. 055024, 2020.

[24] S. R. White and L. J. Sham, "Electronic Properties of Flat-Band Semiconductor Heterostructures," *Phys. Rev. Lett.*, vol. 47, pp. 879–882, Sep 1981.

[25] G. Bastard, "Superlattice band structure in the envelope-function approximation," *Phys. Rev. B*, vol. 24, pp. 5693–5697, Nov 1981.

[26] G. Bastard, "Theoretical investigations of superlattice band structure in the envelope-function approximation," *Phys. Rev. B*, vol. 25, pp. 7584–7597, Jun 1982.

[27] E. O. Kane, "Ch. 3. The $\mathbf{k}\cdot\mathbf{p}$ Method," in *Physics of III-V Compounds* (R. Willardson and A. Beer, eds.), vol. 1 of *Physics of III-V Compounds*, pp. 75–100.

[28] D. J. BenDaniel and C. B. Duke, "Space-Charge Effects on Electron Tunneling," *Phys. Rev.*, vol. 152, pp. 683–692, Dec 1966.

[29] R. L. Anderson, "Germanium-Gallium Arsenide Heterojunctions," *IBM J. Res. Dev.*, vol. 4, no. 3, 1960.

[30] J. Tersoff, "Theory of semiconductor heterojunctions: The role of quantum dipoles," *Phys. Rev. B*, vol. 30, pp. 4874–4877, Oct 1984.

[31] C. G. Van de Walle and R. M. Martin, "Theoretical study of band offsets at semiconductor interfaces," *Phys. Rev. B*, vol. 35, pp. 8154–8165, May 1987.

[32] R. Resta, S. Baroni, and A. Baldereschi, "Theory of band offsets at semiconductor heterojunctions: An ab-initio linear response approach," *Superlattices Microstruct.*, vol. 6, no. 1, pp. 31–37, 1989.

[33] H.-Q. Wang, J.-C. Zheng, R.-Z. Wang, Y.-M. Zheng, and S.-H. Cai, "Valence-band offsets of III–V alloy heterojunctions," *Surf. Interface Anal.*, vol. 28, no. 1, pp. 177–180, 1999.

[34] J. H. Davies, *The Physics of Low-dimensional Semiconductors. An Introduction.* London: Cambridge University Press, 1st ed., 1998.

[35] R. Tsu and L. Esaki, "Tunneling in a finite superlattice," *Appl. Phys. Lett.*, vol. 22, no. 11, pp. 562–564, 1973.

[36] H. K. Henisch, *Electroluminescence.* Oxford: Pergamon Press, 1st ed., 1962.

[37] J. I. Pankove, *Electroluminescence.* Berlin: Springer-Verlag, 1st ed., 1977.

[38] C. R. H. White, M. S. Skolnick, L. Eaves, and M. L. Leadbeater, "Electroluminescence and impact ionization phenomena in a double-barrier resonant tunneling structure," *Appl. Phys. Lett.*, vol. 58, no. 11, pp. 1164–1166, 1991.

[39] E. R. Cardozo de Oliveira, A. Pfenning, E. D. Guarin Castro, M. D. Teodoro, E. C. dos Santos, V. Lopez-Richard, G. E. Marques, L. Worschech, F. Hartmann, and S. Höfling, "Electroluminescence on-off ratio control of $n-i-n$ GaAs/AlGaAs-based resonant tunneling structures," *Phys. Rev. B*, vol. 98, p. 075302, Aug 2018.

[40] C. L. Anderson and C. R. Crowell, "Threshold Energies for Electron-Hole Pair Production by Impact Ionization in Semiconductors," *Phys. Rev. B*, vol. 5, pp. 2267–2272, Mar 1972.

[41] P. T. Landsberg, *Recombination in Semiconductors.* Cambridge: Cambridge University Press, 1st ed., 1991.

[42] J. Bude, K. Hess, and G. J. Iafrate, "Impact ionization in semiconductors: Effects of high electric fields and high scattering rates," *Phys. Rev. B*, vol. 45, pp. 10958–10964, May 1992.

[43] I. C. Sandall, J. S. Ng, S. Xie, P. J. Ker, and C. H. Tan, "Temperature dependence of impact ionization in InAs," *Opt. Express*, vol. 21, pp. 8630–8637, Apr 2013.

[44] L. Keldysh, "Kinetic theory of impact ionization in semiconductors," *Sov. Phys. JETP*, vol. 37, no. 10, pp. 509–518, 1960.

[45] R. Redmer, J. R. Madureira, N. Fitzer, S. M. Goodnick, W. Schattke, and E. Schöll, "Field effect on the impact ionization rate in semiconductors," *J. Appl. Phys.*, vol. 87, no. 2, pp. 781–788, 2000.

[46] S. Perkowitz, *Optical characterization of semiconductors: Infrared, Raman, and Photoluminescence Spectroscopy*. London: Academic Press, 1st ed., 1993.

[47] A. Messiah, *Quantum Mechanics*. Amsterdam: North Holland Publishing Company, 1st ed., 1961.

[48] K. Hess, "Phenomenological Physics of Hot Carriers in Semiconductors," in *Physics of Nonlinear Transport in Semiconductors* (D. K. Ferry, J. R. Barker, and C. Jacoboni, eds.), (Boston, MA), pp. 1–42, Springer US, 1980.

[49] V. L. Bonch-Bruevich and S. G. Kalashnikov, "XVI - Hot Electrons," in *The Physics of Semiconductors - Russian Edition*, (Moscow), pp. 523–524, Nauka, 1977.

[50] G. Bauer, "Determination of electron temperatures and of hot electron distribution functions in semiconductors," in *Solid-State Physics*, (Berlin, Heidelberg), pp. 1–106, Springer Berlin Heidelberg, 1974.

[51] L. Reggiani, "General Theory," in *Hot-Electron Transport in Semiconductors* (L. Reggiani, ed.), (Berlin, Heidelberg), pp. 7–86, Springer Berlin Heidelberg, 1985.

[52] R. A. Höpfel, J. Shah, and A. C. Gossard, "Nonequilibrium electron-hole plasma in GaAs quantum wells," *Phys. Rev. Lett.*, vol. 56, pp. 765–768, Feb 1986.

[53] H. M. van Driel, X. Zhou, W. W. Rühle, J. Kuhl, and K. Ploog, "Photoluminescence from hot carriers in low-temperature-grown gallium arsenide," *Appl. Phys. Lett.*, vol. 60, no. 18, pp. 2246–2248, 1992.

[54] S. Lyon, "Spectroscopy of hot carriers in semiconductors," *J. Lumin.*, vol. 35, no. 3, pp. 121–154, 1986.

[55] J. Tang, V. R. Whiteside, H. Esmaielpour, S. Vijeyaragunathan, T. D. Mishima, M. B. Santos, and I. R. Sellers, "Effects of localization on hot carriers in InAs/AlAs$_x$Sb$_{1-x}$ quantum wells," *Appl. Phys. Lett.*, vol. 106, no. 6, p. 061902, 2015.

[56] E. D. Guarin Castro, A. Pfenning, F. Hartmann, G. Knebl, M. D. Teodoro, G. E. Marques, S. Höfling, G. Bastard, and V. Lopez-Richard, "Optical Mapping of Non-equilibrium Charge Carriers," *J. Phys. Chem. C*, vol. 125, no. 27, p. 14741–14750, 2021.

[57] J. Shah, A. Pinczuk, A. C. Gossard, and W. Wiegmann, "Energy-loss rates for hot electrons and holes in GaAs quantum wells," *Phys. Rev. Lett.*, vol. 54, pp. 2045–2048, May 1985.

[58] J. Shah, "IV.1 - Ultrafast luminescence studies of carrier relaxation and tunneling in semiconductor nanostructures," in *Hot Carriers in Semiconductor Nanostructures: Physics and Applications*, (San Diego), pp. 279–312, AT&T, Academic Press, 1992.

[59] H. L. Cui, X. L. Lei, and N. J. M. Horing, "Negative minority-electron mobility in a nonequilibrium electron-hole plasma," *Phys. Rev. B*, vol. 37, pp. 8223–8227, May 1988.

[60] J. R. Lakowicz, *Principles of Fluorescence Spectroscopy*. Boston: Springer, 3rd ed., 2006.

Chapter 2

Resonant Tunneling Diodes

First studied in the early 70s [1, 2], *resonant tunneling diodes* (RTDs) are among the most investigated semiconductor heterostructures of the last four decades. Their electrical and optical response can be modulated by external parameters such as temperature, illumination, or applied fields, allowing for their application as elementary units of photodetectors [3–5], optical switches [6], and terahertz oscillators [7, 8]. Thus, in this chapter, the description of basic RTDs functionalities that includes the correlation between the quantum transport of charge carriers and optical processes is introduced.

2.1 Quantum Tunneling in an RTD

Figures 2.1 (a) and (b) show, respectively, the schematic representation of an n-type RTD heterostructure and the corresponding band profile of the active region at zero applied voltage. The heterostructure is grown on an n-doped substrate (gray region), and it is usually composed of two highly doped regions at the ends of the device (blue regions), as illustrated in figure 2.1 (a). High doping profiles allow raising the Fermi level above the CB, creating accessible states for electrons. Between these regions, an undoped nanometric active region, known as the *double-barrier structure* (DBS), is grown by depositing two high-bandgap materials (orange layers), sandwiching a low-bandgap semiconductor (yellow layer) [9]. On both sides of the DBS, undoped *spacer layers* are deposited to avoid structural defects during the growth process of the DBS [10]. Metallic contacts at the bottom and top of the heterostructure allow for the electrical functionalities and characterization to be performed.

The band profile in figure 2.1 (b) reveals that along the growth direction, z, the band offsets between the materials at the DBS can produce energetic potential barriers at the CB (black) and VB (red) with heights U_{CB} and U_{VB}, respectively. Between them, a finite *quantum well* (QW) is created. As the quasi-confinement occurs in z-direction, given translational invariance of the heterostucture along (x, y) directions, one can assume that

the in-plane components of the wavevector, $\vec{k}_\perp = (k_x, k_y)$, are conserved. Then, the total carriers energy have an in-plane, $E_\perp$ and a vertical component, E_z: $E = E_\perp + E_z$, with $E_\perp = \hbar^2 k_\perp^2 / 2m^*(z)$, and $E_z = U(z) + \hbar^2 k_z / 2m^*(z) k_z$, as defined in § 1.2 (see eq. 1.39) [9].

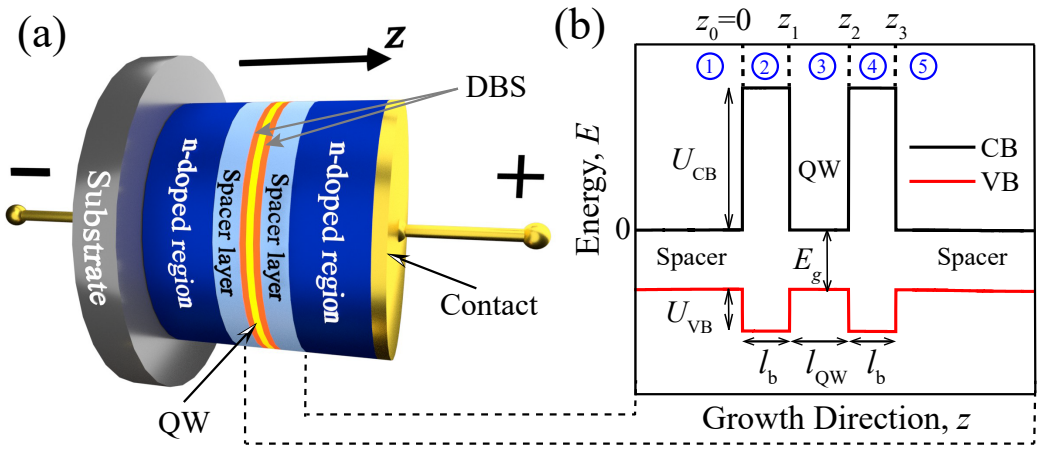

Figure 2.1 – (a) Illustration of an RTD heterostructure, where z represents the growth direction. (b) Schematic band profile of the DBS at zero bias voltage. Blue numbers label the regions of the DBS. The zero-energy corresponds to the bottom of the spacer layers CB. The thickness, l_b, is assumed the same for both barriers.

Let us consider now the transmission of a *coherent* wave through the DBS at the CB, taking the zero energy as the CB edge of the spacer layers as indicated in figure 2.1 (b). The DBS can be divided into five regions and we used as reference for $z_0 = 0$ the position of the heterojunction between regions 1 and 2. Considering an incident wavefunction coming from region 1, the solutions of the Schrödinger equation at each region, take the general form

$$\psi_r(z) = \mathcal{A}_r \exp(i k_r z) + \mathcal{B}_r \exp(-i k_r z), \tag{2.1}$$

with $r = 1,2,3,4,5$ representing the regions in the DBS. The first term on the right side of Eq. 2.1, corresponds to the wavefunction component transmitted from left to right. The second term represents the reflected wavefunctions at the heterojunctions. In the symmetrical DBS presented in figure 2.1 (b), regions 1, 3, and 5 are made of the same semiconductor, then the effective masses and the wavevectors in these regions are the same: $k_1 = k_3 = k_5 = \sqrt{2m_1^* E}/\hbar$. In regions 2 and 4, the change in the material leads to $k_2 = k_4 = \sqrt{2m_2^*(E - U_{CB})}/\hbar$. To guarantee the continuity of the solutions at every heterojunction, the wavefunctions must satisfy

$$\mathcal{A}_r \exp(i k_r z_h) - \mathcal{B}_r \exp(-i k_r z_h) = \mathcal{A}_{r+1} \exp(i k_{r+1} z_h) - \mathcal{B}_{r+1} \exp(-i k_{r+1} z_h), \tag{2.2}$$

whilst their first derivative must fulfill Eq. 1.26, yielding

$$\mathcal{A}_r \frac{ik_r}{m_r^*}\exp(ik_r z_h) - \mathcal{B}_r \frac{ik_r}{m_r^*}\exp(-ik_r z_h) = \mathcal{A}_{r+1}\frac{ik_{r+1}}{m_{r+1}^*}\exp(ik_{r+1}z_h) - \mathcal{B}_{r+1}\frac{ik_{r+1}}{m_{r+1}^*}\exp(-ik_{r+1}z_h). \quad (2.3)$$

The subscript h represents the position of each interface, such that $z_0 = 0$, $z_1 = l_b$, $z_2 = l_b + l_{QW}$, and $z_3 = 2l_b + l_{QW}$, with l_b and l_{QW} representing the barrier and QW thicknesses, respectively, as indicated in figure 2.1 (b). The system of eqs. 2.2 and 2.3 can be rewritten in the representation of the *transfer matrix method* [11] as

$$\begin{bmatrix} \exp(ik_r z_h) & \exp(-ik_r z_h) \\ \frac{ik_r}{m_r^*}\exp(ik_r z_h) & \frac{ik_r}{m_r^*}\exp(-ik_r z_h) \end{bmatrix} \begin{bmatrix} \mathcal{A}_r \\ \mathcal{B}_r \end{bmatrix} = \begin{bmatrix} \exp(ik_{r+1} z_h) & \exp(-ik_{r+1} z_h) \\ \frac{ik_{r+1}}{m_{r+1}^*}\exp(ik_{r+1} z_h) & \frac{ik_{r+1}}{m_{r+1}^*}\exp(-ik_{r+1} z_h) \end{bmatrix} \begin{bmatrix} \mathcal{A}_{r+1} \\ \mathcal{B}_{r+1} \end{bmatrix}. \quad (2.4)$$

The matrices on the left and on the right of Eq. 2.4 can be labeled as $\mathbf{M}_\alpha$ and $\mathbf{M}_{\alpha+1}$, respectively, with $\alpha = 2h+1$ as an index used to identify the matrices. Thus, using the inverse matrix of $\mathbf{M}_\alpha$, for the four heterojunctions in the DBS shown in figure 2.1 (b), and from Eq. 2.4, we have four matrix equations of the form

$$\begin{bmatrix} \mathcal{A}_r \\ \mathcal{B}_r \end{bmatrix} = \mathbf{M}_\alpha^{-1}\mathbf{M}_{\alpha+1}\begin{bmatrix} \mathcal{A}_{r+1} \\ \mathcal{B}_{r+1} \end{bmatrix}, \quad (2.5)$$

linking the amplitudes of the incident and transmitted wavefunctions as

$$\begin{bmatrix} \mathcal{A}_1 \\ \mathcal{B}_1 \end{bmatrix} = \mathbf{M}_1^{-1}\mathbf{M}_2\mathbf{M}_3^{-1}\mathbf{M}_4\mathbf{M}_5^{-1}\mathbf{M}_6\mathbf{M}_7^{-1}\mathbf{M}_8\begin{bmatrix} \mathcal{A}_5 \\ \mathcal{B}_5 \end{bmatrix}. \quad (2.6)$$

The number of matrices is always twice the number of heterojunctions considered, and they can be operated to form a single matrix $\mathbf{M}$, called the *transfer matrix*. If we also consider that there is no incoming wavefunction from the right at region 5, then Eq. 2.6 becomes

$$\begin{bmatrix} \mathcal{A}_1 \\ \mathcal{B}_1 \end{bmatrix} = \mathbf{M}\begin{bmatrix} \mathcal{A}_5 \\ 0 \end{bmatrix} \quad (2.7)$$

where $\mathcal{A}_1 = \mathbf{M}_{11}\mathcal{A}_5$. Taking into account Eq. 1.30, the transmission coefficient for a DBS is given by

$$\mathcal{T}(E) = \frac{k_5}{m_5^*}\frac{m_1^*}{k_1}\left|\frac{\mathcal{A}_5}{\mathcal{A}_1}\right|^2 = \frac{k_5}{m_5^*}\frac{m_1^*}{k_1}\frac{1}{|\mathbf{M}_{11}|^2}. \quad (2.8)$$

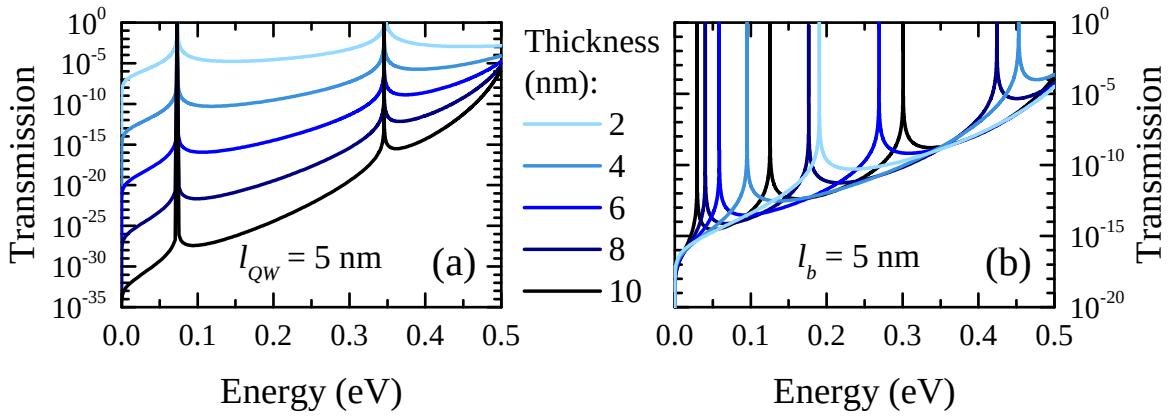

Figure 2.2 – Calculated CB transmission coefficient as a function of the electron energy for a symmetrical GaAs/$Al_{0.6}Ga_{0.4}As$ DBS with (a) different barrier thicknesses (l_{QW} = 5 nm), and (b) different QW thicknesses (l_b = 5 nm). In these calculations, U_{CB} = 0.50 eV.

In a symmetrical DBS like the structure presented in figure 2.1 (b), $k_1 = k_5$ and $m_1^* = m_5^*$, as mentioned before. Consequently, the transmission coefficient can be reduced to $\mathscr{T}(E) = 1/|\mathbf{M}_{11}|^2$. Figures 2.2 (a) and (b) show the CB transmission coefficients as a function of the electron energy calculated via the transfer matrix method, for a GaAs/$Al_{0.6}Ga_{0.4}As$ DBS with different barrier and QW thicknesses, respectively. We assumed a CB offset of U_{CB} = 0.50 eV [6, 12]. The positions of the transmission peaks correspond to the energies necessary for resonant tunneling through the DBS.

Taking l_{QW} = 5 nm, figure 2.2 (a) shows two transmission peaks ($\mathscr{T}$ = 1) at 73 meV and 347 meV, which is a signature of the quantum interference nature of this effect. By increasing l_b, the transmission between peaks drops several orders of magnitude without significantly changing the position of the peaks. On the other hand, for barriers with l_b = 5 nm, figure 2.2 (b) shows that the thicker the QW, the greater the number of resonant energy states at the DBS. The strength of the quasi-confinement in the QW makes the first transmission peak appear at high energies in narrow QWs, as compared with wide QWs, and affects the energy spacing between resonances. The first peak is associated with a *fundamental quasi-bound* state in the QW, while the more energetic peaks correspond to *excited quasi-bound* states.

2.2 The Effect of Charge Carrier Accumulation

When a forward bias voltage, V, is applied to an RTD along the z-direction, as indicated by the +/− signs in figure 2.3 (a), electrons, e^-, from the emitter travel across the heterostructure until reaching the collector side. However, during their journey through the heterostructure, electrons interact with the DBS, accumulating before it and producing a potential energy drop, $-eV_{DBS}$, along an effective length, l_{DBS}. Under stationary conditions, the applied electric field can ionize part of the doped regions at the collector side,

producing a depletion region of length l_1, contributing to the total potential energy drop, $-eV$, that electrons must undergo when reaching the collector contact, compensated by the externally applied bias voltage.

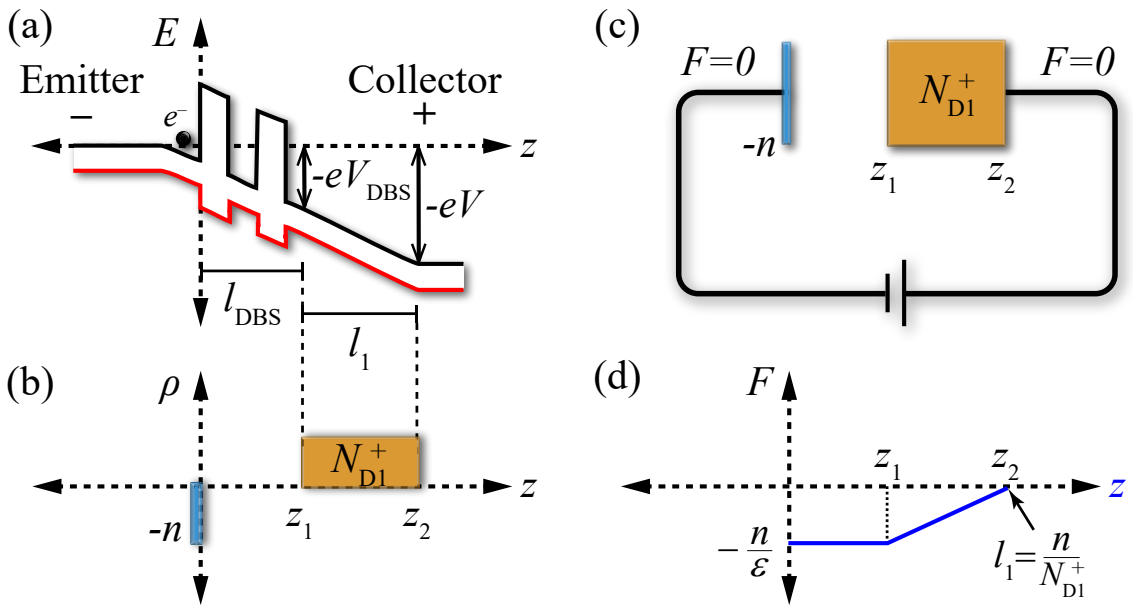

Figure 2.3 – (a) Schematic RTD band profile under an applied forward voltage, indicating the depletion produced by the accumulation of electrons, e^-, close to the DBS. (b) Representation of the charge density, ρ, distribution along with the RTD. (c) The DBS and the depleted doped region can be considered as a capacitor so that the electric field outside it is zero ($F = 0$). (d) Electric field inside the RTD as a function of the growth direction. The area under the graph gives the voltage drops inside the heterostructure.

Some assumptions can be made to estimate the voltage drop inside the biased heterostructure. First of all, electrons accumulating near the DBS form a *2D-sheet*, with density $-n$, whilst the charge at the collector side corresponds to ionized donors with a constant *3D donor density*, N_{D1}^{+}, between $z_2 - z_1 = l_1$, as illustrated by the charge density (ρ) distribution as a function of the growth direction in figure 2.3 (b). Secondly, the emitter side and the outermost layers at the collector side can be assumed as quasi-metallic due to their high doping profiles. As a consequence, there is no depletion caused by the applied voltage in these regions, and the electric field is $F = 0$. Thus, the system can be represented as a capacitor as depicted in figure 2.3 (c) with the neutrality condition, $N_{D1}^{+} l_1 = n$.

For a diode with diameter much larger than its height (along z-direction), the effect of the lateral surface can be neglected. Then using Gauss's law, $\nabla \cdot \vec{F} = \rho/\varepsilon$, and cylindrical

symmetry, the electric field inside the heterostructure has the form,

$$F = \begin{cases} 0 & \text{if } z < 0 \\ -\frac{n}{\varepsilon} & \text{if } 0 \le z < z_1 \\ -\frac{n}{\varepsilon} + \frac{N_{D1}^+}{\varepsilon}(z - z_1) & \text{if } z_1 \le z < z_2 \\ 0 & \text{if } z \ge z_2. \end{cases} \tag{2.9}$$

The electric field as a function of z is represented in figure 2.3 (d). Then, the total voltage drop inside the heterostructure can be now assessed by integrating $\nabla V = -\vec{F}$, which is equivalent to calculating the area under the $F(z)$ plot. Thus, we have,

$$V = -\frac{n}{\varepsilon} l_{\text{DBS}} - \frac{n^2}{2\varepsilon N_{D1}^+} = V_{\text{DBS}} + V_{\text{D1}}, \tag{2.10}$$

where the voltage drop along the DBS is $V_{\text{DBS}} = -n/\varepsilon l_{\text{DBS}}$ while $V_{D1} = -n^2/(2\varepsilon N_{D1}^+)$ corresponds to the voltage drop due to the ionized donors. The dependence between V_{DBS} and V is clearer by expressing V_{D1} in terms of V_{DBS}, which results in,

$$|V_{\text{DBS}}(V)| = V_0 \left(1 - \sqrt{1 + \frac{2|V|}{V_0}}\right), \tag{2.11}$$

where $V_0 = l_{\text{DBS}}^2 N_{D1}^+/\varepsilon$. Figure 2.4 (a) shows the $V_{\text{DBS}}(V)$ dependence according to Eq. 2.11 and for various values of V_0. The higher the applied voltage, V, the higher the electrons accumulation and the voltage drop at the DBS, which is also proportional to V_0. This accumulation is affected by the quantum tunneling of charge carriers, responsible for the characteristic RTD electrical response, as discussed in § 2.3.

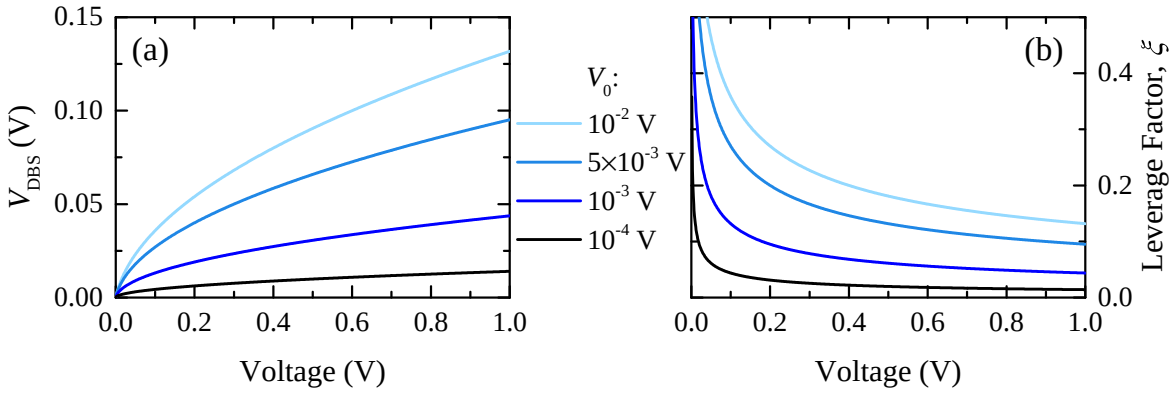

Figure 2.4 – Bias voltage dependence of (a) the voltage drop at the DBS V_{DBS}, and (b) the leverage factor, ξ, according to Eq. 2.11. Color gradient represent the cases for different values of $V_0 = l_{\text{DBS}}^2 N_{D1}^+/\varepsilon$.

The voltage drop at the DBS is a fraction of V, and this relation is usually presented as,

$$V_{\mathrm{DBS}}(V) = \xi V \tag{2.12}$$

where ξ is a voltage-dependent *leverage factor*, that can be obtained by dividing Eq. 2.11 by V. It results in the dependence presented in figure 2.4 (b) for different values of V_0. By increasing the applied voltage, the leverage factor is reduced. Although this relationship is not linear, ξ can be considered constant within certain voltage ranges that depend on the composition and structural parameters of the sample, such as the barrier/QW thicknesses and the charge buildup along the heterostructure [13, 14].

2.3 RTD Transport Properties

The depletion of the DBS under an applied voltage due to the distribution and accumulation of charge carriers allows tuning the alignment between the electronic states from the emitter side and the QW quasi-bond states. This alignment also modulates the current passing through the heterostructure. In this approximation, the electric field is assumed uniform inside the RTD, and V_{DBS} drops along $l_{\mathrm{DBS}} = 2l_b + l_{QW}$, due to the accumulation of electrons at region 1. Then, the potential energy drop along the DBS can be obtained as,

$$U(z) = -\frac{eV_{\mathrm{DBS}}}{l_{\mathrm{DBS}} - z_0}(z - z_0). \tag{2.13}$$

For narrow enough layers, the simplest possible approximation consists in step-like drops as indicated in figure 2.5 (a), for the case of the CB of a symmetrical DBS. Taking the first heterojunction as reference at $z_0 = 0$, the electric potential energy at the QW and after the DBS is $U_1 = -eV_{\mathrm{DBS}} l_b / l_{\mathrm{DBS}}$ and $U_2 = -eV_{\mathrm{DBS}}$, respectively. Following these assumptions, the wavevectors for each region become,

$$\begin{gathered} k_1 = \frac{\sqrt{2m^*E}}{\hbar}, \qquad k_2 = \frac{\sqrt{2m_b^*(E - U_{\mathrm{CB}})}}{\hbar}, \qquad k_3 = \frac{\sqrt{2m^*(E - U_1)}}{\hbar}, \\ k_4 = \frac{\sqrt{2m_b^*(E - U_{\mathrm{CB}} - U_1)}}{\hbar}, \qquad k_5 = \frac{\sqrt{2m^*(E - U_2)}}{\hbar}, \end{gathered} \tag{2.14}$$

with m^* as the electron effective mass at regions 1, 3, and 5, and m_b^* as the effective mass at the barriers (regions 2 and 4). The expressions 2.14, allow establishing a dependence between the transmission coefficient and V_{DBS}, according to Eq. 2.8.

Figure 2.5 (b) presents the calculated transmission according to the transfer matrix method introduced in § 2.1, for different V_{DBS} along a GaAs / $Al_{0.6}Ga_{0.4}As$ RTD with L_b = 3.5 nm, L_{QW} = 4.0 nm, and U_{CB} = 0.50 eV [6]. At V_{DBS} = 0 V (gray line), two transmission

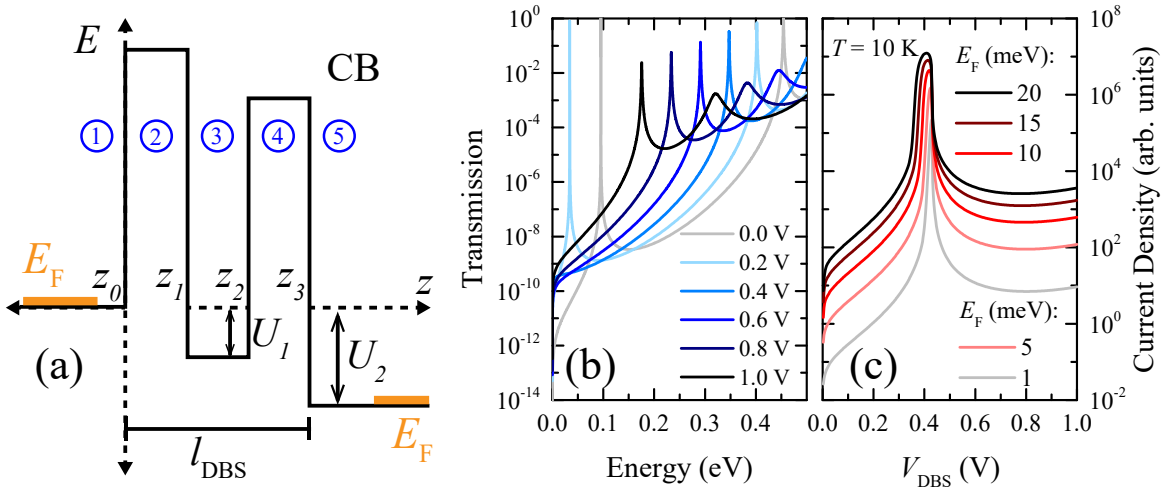

Figure 2.5 – (a) The depletion of the DBS at the CB due to V_{DBS} can be assumed as a step-like deformation where the QW and the second barrier (regions 3 and 4) drop a potential energy U_1, while region 5 drops an energy U_2. Calculated (b) transmission for different V_{DBS}, and (c) current density as a function of V_{DBS}, for different Fermi levels, E_{F} and for a GaAs/$Al_{0.6}Ga_{0.4}$As RTD. Calculations were made using $L_b = 3.5$ nm, $L_{QW} = 4.0$ nm, and $U_{\mathrm{CB}} = 0.50$ eV [6].

peaks appear at 95 and 454 meV. By increasing V_{DBS}, the transmission peaks are shifted to lower energies, implying that electronic states near the CB edge of the emitter side ($E = 0$) can be easily aligned with the fundamental quasi-bond state at the QW. For $V_{\mathrm{DBS}} > 0.20$ V, the first excited quasi-bond state remains at relative high energies, and its intensity sinks with voltage, making resonant tunneling through this state difficult. The high-energy peak after the first excited quasi-bond state is a consequence of the constructive interference of wavefunctions produced by the heterojunctions, for energies above U_{CB}.

Based on these results, the current density can be now obtained according to Eq. 1.46, assuming the same Fermi level, E_{F}, at both sides of the DBS. Thus, it is easy to show that the current density through the DBS, due to transmission of *coherent* waves from the emitter side (J_{co}), takes the form predicted by Tsu & Esaki [1]

$$J_{\mathrm{co}}(V_{\mathrm{DBS}}) = \frac{em^* k_{\mathrm{B}} T}{2\pi^2 \hbar^3} \int_0^\infty \mathscr{T}(E_z, V_{\mathrm{DBS}}) \ln \left[\frac{1 + \exp\left(\frac{E_F - E_z}{k_{\mathrm{B}} T}\right)}{1 + \exp\left(\frac{E_F - E_z - eV_{\mathrm{DBS}}}{k_{\mathrm{B}} T}\right)} \right] dE_z. \tag{2.15}$$

Using the transmission coefficient obtained by the transfer matrix method, the integration in Eq. 2.15 can be performed numerically to get the coherent current density as a function of V_{DBS}, which has been depicted in figure 2.5 (c) for the same GaAs/$Al_{0.6}Ga_{0.4}$As RTD [6]. The simulations are presented for $T = 10$ K and various Fermi levels above the CB edge. The calculated current density has a peak at $V_{\mathrm{DBS}} \approx 0.43$ V, and by increasing E_{F}, both the intensity and the width of the current density peak grows, corresponding to more electrons tunneling resonantly through the DBS.

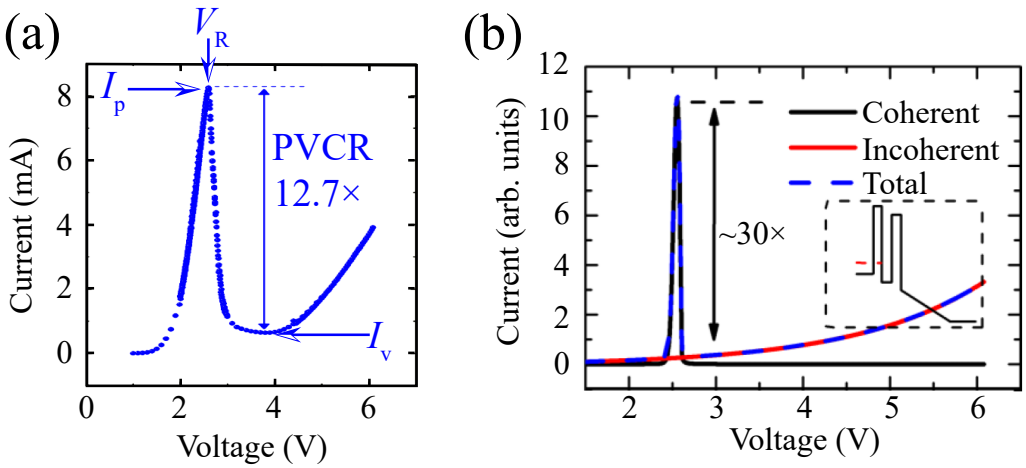

Figure 2.6 – (a) $I(V)$ characteristic of a GaAs/$Al_{0.6}Ga_{0.4}$As RTD at $T = 10$ K. (b) Calculated coherent and incoherent currents for the same RTD. (a) and (b) were adapted from Ref. [6].

The model presented above allows a simplified description of the coherent transport of carriers in a DBS. Thus, similarities and differences emerge when comparing calculated and observed current-voltage, $I(V)$, characteristics of real systems. Figure 2.6 (a) displays the experimental $I(V)$ characteristic of a GaAs/$Al_{0.6}Ga_{0.4}$As RTD as reported in Ref. [6]. The result of the simulated contribution of coherent transport according to the model described above is represented in Figure 2.6 (b) with a black curve. The peak current, I_p, is followed by a drop-down to the valley current, I_v, in both experiment and theory. It is a distinctive signature of RTDs, known as the *negative differential resistance* (NDR) region. The quality of the performance of RTDs is characterized by the *peak-to-valley current ratio* (PVCR) defined as PVCR= I_p/I_v, and there is a discrepancy between the experiment and the model. Another contrast with the coherent transport simulation is that, after surpassing I_v, the current measured experimentally increases again exponentially with the applied voltage.

It points to the need of consider the contribution of *incoherent* channels, I_{inco}, originated by thermionic emission, sidewall leakage, and non-resonant transport of hot carriers [15–17]. Thermionic emission is suppressed at cryogenic temperatures, while sidewall leakage can be prevented by the formation of smooth RTD sidewalls and avoiding oxidation of the device, using appropriate passivation materials [4]. This kind of transport can be represented by an exponential function given by,

$$J_{inco}(V) = J_0 \left[\exp\left(\frac{\eta V}{k_B T} \right) - 1 \right], \tag{2.16}$$

where J_0 is the saturation current density and η an efficiency parameter [18, 19].

The calculated $I(V)$ characteristic (dashed blue line) obtained by summing up Eqs. 2.15 (black line) and 2.16 (red line) is displayed in Figure 2.6 (b). Furthermore, by taking the

resonance voltage of the calculated coherent channel ($V_{\mathrm{DBS}}^{\mathrm{R}} = 0.43$ V) and the experimental curve ($V_R = 2.60$ V), a leverage factor of $\xi = 0.163$ was obtained, according to Eq. 2.12. This factor accounts not only for the additional voltage drops produced in the RTD due to charge buildup but also for the voltage drops produced in the circuit by the resistance of the contacts and the experimental setup. With this, the calculated voltages were adjusted to the experimental ones.

The results depicted in Figure 2.6 (b) indicate that near the resonance condition, the coherent channel is dominant. However, for higher voltages, the incoherent channel prevails, generating a PVCR ($\sim 30\times$) of the same order of magnitude as observed during experiments ($12.7\times$). Since the calculated current was obtained within a completely coherent picture, the simulated current peak is narrower than the experimental peak. Inelastic scattering processes, not consider in our approximation, are responsible for the broadening of the measured current-peak and the reduction of the PVCR [18, 20, 21].

2.3.1 RTD Bistability

The NDR region in an RTD can be turned into a *bistable* conductive state, where two conductivity levels emerge for the same applied voltage. This condition is evidenced as an hysteresis in the $I(V)$ characteristic, that can be produced by extrinsic conditions [22–27] or charge buildup processes intrinsically caused [28–32]. The hysteresis is obtained by sweeping up the voltage from $V = 0$ V up to a finite voltage after resonance, and then sweeping it down to zero, as shown in figure 2.7 (a), for a GaAs/AlGaAs RTD with a GaInNAs absorption layer at room temperature, taken from Ref. [26]. The resulting $I(V)$ characteristic presents a peak current of $I_{\mathrm{p}} = 2.6$ mA, and a valley current of $I_{\mathrm{v}} = 0.9$ mA with a PVCR of 2.9 and two threshold voltages, one at $V_{\mathrm{u}} = 6.83$ V for the up-sweep, and the other at $V_{\mathrm{d}} = 5.86$ V for the down-sweep. Color dots indicate two tunneling conditions with currents I_{u} and I_{d} for the same applied voltage, V.

The observed bistability can be ascribed to a *total resistance*, R, originating from extrinsic load and intrinsic contributions. The latter can be originated by the presence of the metallic contacts and by momentum scattering processes occurring along the entire heterostructure, where the segmentation of the architecture with several interfaces can reduce the coherence of the carriers transported via resonant channels. In order to assess the effect of this resistance, we depicted in figure 2.7 (b) the simulated $I(V)$ characteristic for an RTD analogous to the one used for generating panel (a) but by assuming $R = 0$. Here, the current density was obtained as $J = J_{\mathrm{co}} + J_{\mathrm{inco}}$, with J_{co} and J_{inco} defined by eqs. 2.15 and 2.16, respectively. Calculations were performed using the approximation proposed by Schulman *et al.* [18] for the transmission in the coherent transport channel. In this case, we take $m^* = 0.63 m_e$ as the effective electron mass for the GaAs QW, $\Gamma = 0.07$ meV as the

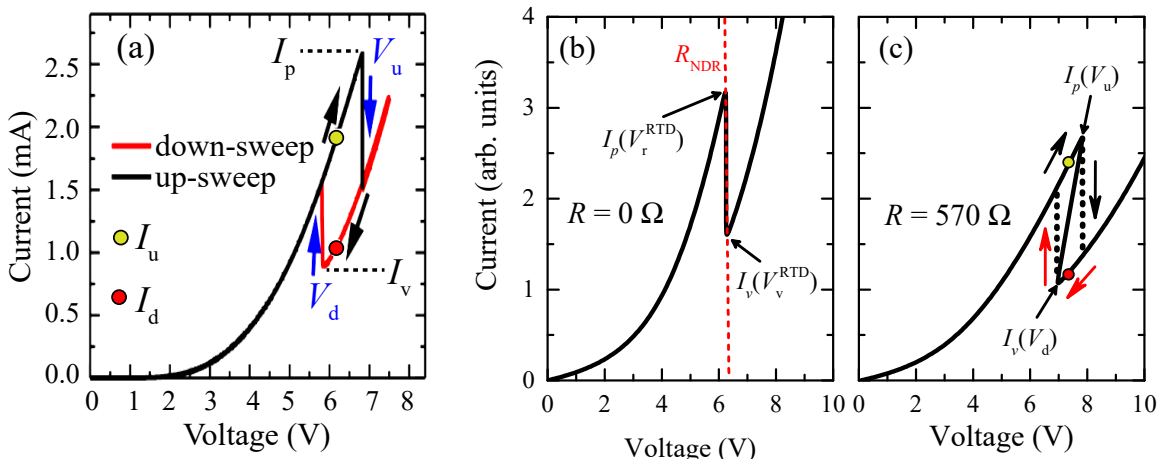

Figure 2.7 – (a) Experimental $I(V)$ characteristic for a GaAs/AlGaAs RTD with a GaInNAs absorption layer at room temperature. Adapted from Ref. [26]. Simulated $I(V)$ characteristics for the same RTD taking (b) $R = 0$, and (c) $R = 570\ \Omega$. In (c), the up- and down-sweep voltage directions are represented by black and red arrows, respectively.

broadening of the transmission peak, $E_F = 50$ meV as the Fermi level, and $E_r = 150$ meV as the the resonant energy level in the QW. For the incoherent transport channel, $\eta = 0.009$ and $J_0 = 1.32 \times 10^{-4}$ were employed. Then, the total current is calculated as $I(V) = A\,J(V)$, with A being the RTD's cross sectional area. When $R = 0$, there is no bistability and the NDR region can be characterized by a resistance, R_{NDR} (red dashed line) given by

$$R_{NDR} = \frac{V_r^{RTD} - V_v^{RTD}}{I_p - I_v} < 0, \tag{2.17}$$

where V_r^{RTD} and V_v^{RTD} correspond to the resonance and valley voltages at the RTD, respectively. It is clear that in this case $R_{NDR} \to 0$.

If the coherent and incoherent channels coexist with a total resistance, $R \neq 0$, then, according to the Kirchhoff's voltage law, the total voltage can be expressed as

$$V = V_{RTD} + R\,I(V_{RTD}), \tag{2.18}$$

where V_{RTD} is the voltage drop at the RTD and the second term on the right corresponds to the voltage drop caused by the intrinsic resistance. Consequently, the threshold voltages are $V_{u(d)} = V_{r(v)}^{RTD} + R\,I_{p(v)}$. Subtracting V_d from V_u and solving for R, we obtain that the total resistance is

$$R = \frac{V_u - V_d}{I_p - I_v} - R_{NDR}. \tag{2.19}$$

If $R_{NDR} \to 0$, then the total resistance can be obtained from the ratio between the hysteresis width and height, such that $R = (V_u - V_d)/(I_p - I_v)$. This gives a total resistance of $R = 570\ \Omega$ for the case depicted in figure 2.7 (a). Using this value, the total current was

calculated again as a function of the voltage defined by eq. 2.18, as shown in figure 2.7 (c). The bistability, as observed in the experiments, is represented by dotted lines. Black and red arrows indicate the up- and down-sweep directions, indicating a clockwise bistability. The simulated characteristic presents a Z-shaped NDR region in line with some theoretical models [29, 31]. Nevertheless, the electrical response of the RTD inside the bistability can present more complex paths, sometimes inaccessible to conventional measuring techniques, where a voltage source is connected in series with the RTD [33].

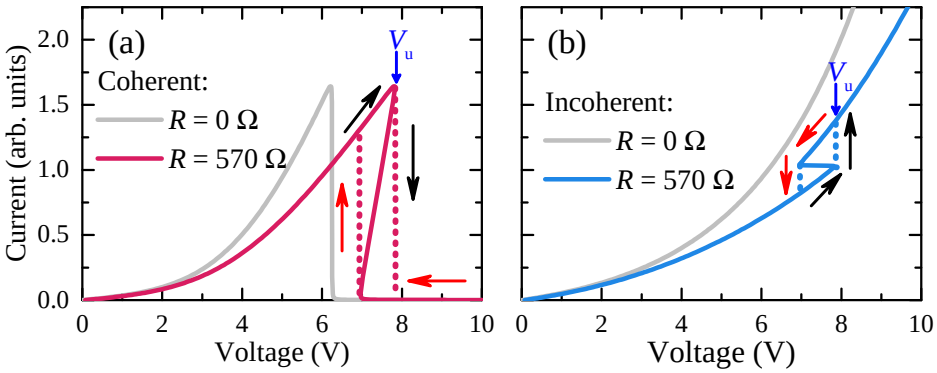

Figure 2.8 – Simulated (a) coherence and (b) incoherence transport channels with a total load resistance, R. Calculations of the transport channels for $R = 0\ \Omega$ are displayed as gray lines. The up- and down-sweep voltage directions are represented by black and red arrows, respectively.

The influence of the total resistance on each transport channel is presented in figure 2.8 (a) and (b), for the coherent and incoherent contributions, respectively. The simulated currents for $R = 0\ \Omega$ (gray lines) are also shown as reference. Note that the resistance not only shifts the current channels to higher voltages but it also produces two qualitatively different hysteretic patterns, depending on the current component. During an up-sweep of the voltage, the current contribution through the coherent channel sharply drops at V_u, leading to a clockwise bistability, which prevails in the $I(V)$ characteristic, since the coherent current is dominant at this voltage regime. On the contrary, the incoherent channel increases at V_u, producing an anticlockwise hysteresis. The modulation of the total resistance with temperature or external magnetic fields can change the relative contribution of each current channel, and with this, the qualitative shape of the bistability, as discussed in Ch. 4.

2.4 Charge Buildup Under Illumination and RTD Photoresponse

The photogeneration of carriers in an RTD by an incident light also produces electrostatic effects responsible for band bending and modulation of the electrical response. The first suggestion of charge accumulation as the origin of the RTD photoresponse was re-

ported in Ref. [34]. This response was associated with the accumulation of photogenerated holes at the depletion region of the collector side, near the DBS. Afterward, different experimental [35–37] and theoretical works [38, 39] have demonstrated that the modulation of the photocurrent is a consequence of the accumulation of photogenerated minority carriers. This accumulation provokes a *photoinduced voltage shift*, ΔV_{ph}, in the $I(V)$ characteristic under illumination. Recent experimental works have corroborated these findings using both continuous and time-resolved photoresponse as reported in Refs. [3, 40, 41].

In order to unveil the voltage dependence of ΔV_{ph}, we have developed a model that includes the charge distribution along the heterostructure and the interplay of various transport channels within the same framework. Let us consider an RTD with an absorption region and an optical window (OW), both with high n-doped profiles, as sketched in figure 2.9 (a). The absorber enhances the photocreation of carriers, while the high-bandgap OW enables optical access to the active region. When incident photons are absorbed within an RTD biased by an applied voltage, electron-hole pairs are generated and spatially separated due to the action of the applied electric field. The photogenerated electrons can then accumulate at the heterojunction with the OW, while holes buildup close to the collector barrier at the DBS in a forward voltage configuration.

A charge density distribution, ρ, along the growth direction, can be set as depicted in figure 2.9 (b). The photogenerated holes and electrons produce 2D-carrier distributions, p_{ph} and $-n_{\mathrm{ph}}$, at the collector barrier (z_1) and at the heterojunction with the OW (z_4), respectively. We have also considered the presence of a spacer layer of length l_0, between the holes accumulated near the DBS and the doped region within the absorber. Additionally, the absorption layer and the OW can be partially depleted along l_1 and l_2, with 3D charge densities, N_{D1}^{+} and N_{D2}^{+}, respectively. Usually, $N_{D2}^{+} > N_{D1}^{+}$. Thus, the electric field calculated by means of Gauss's law is given by,

$$F = \begin{cases} 0 & \text{if } z < 0 \\ -\frac{n}{\varepsilon} & \text{if } 0 \le z < z_1 \\ -\frac{n}{\varepsilon} + \frac{p_{\mathrm{ph}}}{\varepsilon} & \text{if } z_1 \le z < z_2 \\ -\frac{n}{\varepsilon} + \frac{p_{\mathrm{ph}}}{\varepsilon} + \frac{N_{D1}^{+}}{\varepsilon}(z - z_2) & \text{if } z_2 \le z < z_3 \\ 0 & \text{if } z_3 \le z < z_4 \\ -\frac{n_{\mathrm{ph}}}{\varepsilon} + \frac{N_{D2}^{+}}{\varepsilon}(z - z_4) & \text{if } z_4 \le z < z_5 \\ 0 & \text{if } z \ge z_5 \end{cases} \tag{2.20}$$

as illustrated in figure 2.9 (c). According to the neutrality conditions $p_{\mathrm{ph}} + N_{D1}^{+} l_1 = n$ and

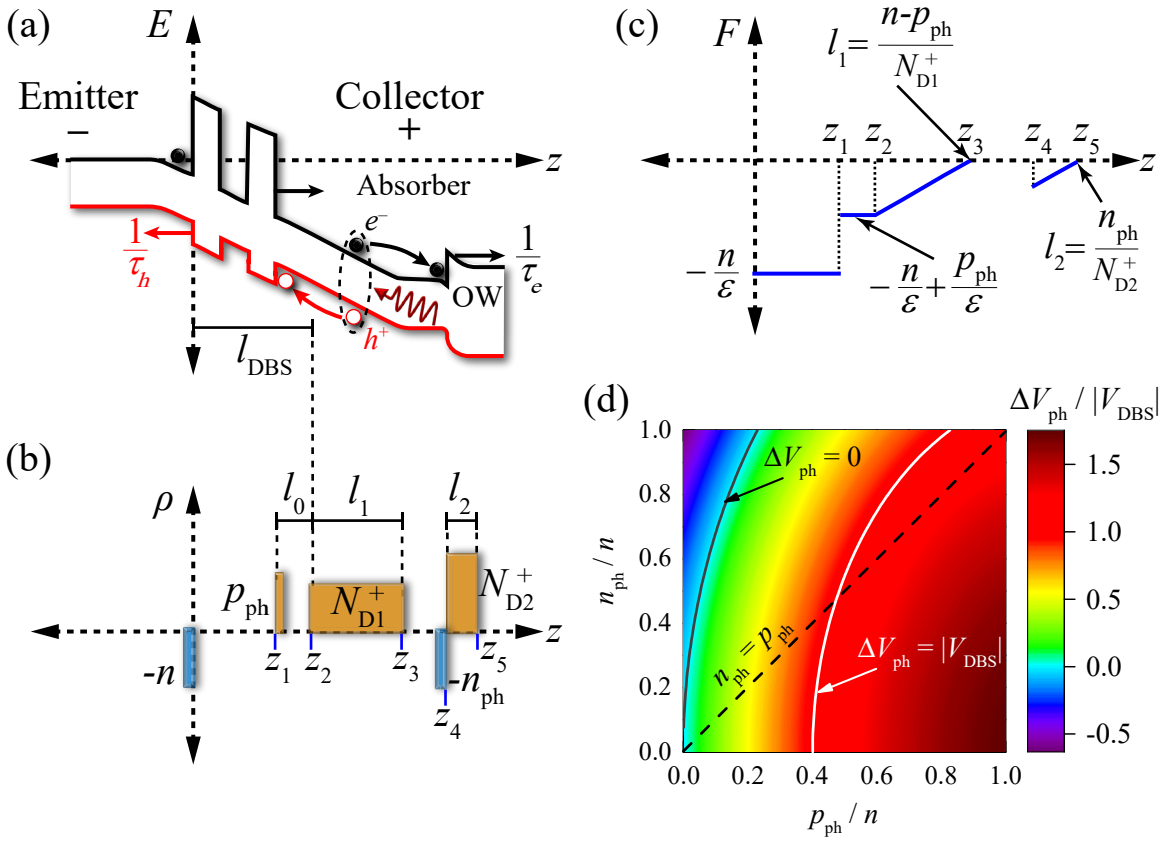

Figure 2.9 – Illustration of the (a) band profile, (b) charge density distribution, and (c) electric field inside a voltage-biased RTD under illumination, as a function of the growth direction. (d) Normalized voltage shift with respect to $|V_{\mathrm{DBS}}|$ as a function of the normalized photogenerated carriers accumulated at the absorption layers, according to Eq. 2.22. Contour lines show the cases for zero voltage shift (black line) and $\Delta V_{\mathrm{ph}} = |V_{\mathrm{DBS}}|$ (white line). The case of the same amount of photocreated electrons and holes accumulated at the absorber is indicated with a dashed line. Calculations were carried out taking $N_{D1}^{+}/N_{D2}^{+} = 0.5$, $l_0/l_{\mathrm{DBS}} = 0.5$, and $n/(2N_{D1}^{+}l_{\mathrm{DBS}}) = 1.25$.

$N_{D2}^{+}l_2 = n_{\mathrm{ph}}$, the solution of the Poisson equation results in a total voltage drop given by,

$$V = V_{\mathrm{DBS}} + V_{D1} + \Delta V_{\mathrm{ph}}, \tag{2.21}$$

with $V_{\mathrm{DBS}} + V_{D1}$ defined by Eq. 2.10 and ΔV_{ph} as the photoinduced voltage shift produced by buildup of photogenerated carriers and defined as,

$$\Delta V_{\mathrm{ph}} = \frac{p_{\mathrm{ph}} l_0}{\varepsilon} + \frac{1}{2\varepsilon N_{D1}^{+}}\left(2np_{\mathrm{ph}} - p_{\mathrm{ph}}^2 - n_{\mathrm{ph}}^2 \frac{N_{D1}^{+}}{N_{D2}^{+}}\right). \tag{2.22}$$

Figure 2.9 (d) shows a color-gradient map of the relative voltage shift, $\Delta V_{\mathrm{ph}}/|V_{\mathrm{DBS}}|$ as a function of the relative trapped electrons, n_{ph}/n, and holes, p_{ph}/n, at the absorber, according to Eq. 2.22. Here, $|V_{\mathrm{DBS}}|$ and n were assumed constant. The calculations were performed by taking $N_{D1}^{+}/N_{D2}^{+} = 0.5$, $l_0/l_{\mathrm{DBS}} = 0.5$, and $n/(2N_{D1}^{+}l_{\mathrm{DBS}}) = 1.25$. Under these conditions, the photogenerated carriers at the absorber mainly produce a positive shift,

implying a reduction of the total voltage drop, V (assumed negative in our reference system). If the photogenerated electrons, n_{ph}, are trapped efficiently at the absorber while keeping p_{ph} low, then ΔV_{ph} can be zero ($\Delta V_{\mathrm{ph}} = 0$ contour line) or assume negative values (cyan-blue regions), as depicted in figure 2.9 (d). By increasing the number of photogenerated holes trapped near the DBS at the absorber region, ΔV_{ph} becomes positive even for high values of n_{ph}. Thus, the higher the p_{ph}, the higher the ΔV_{ph}. The case when the voltage shift compensates the voltage drop at the DBS is also presented in figure 2.9 (d), with the $\Delta V_{\mathrm{ph}} = |V_{\mathrm{DBS}}|$ contour line.

2.4.1 Voltage Dependence of the Photoinduced Voltage Shift

The voltage dependence of the trapped photogenerated carrier densities at the absorber can be obtained by considering the dynamics illustrated in figure 2.10. The incoming photons, with energy $\hbar\omega$, generate electron-hole pairs within the depleted absorber. The local electric field spatially separates the photogenerated electron (hole) populations, n_0 (p_0), which after drifting through the absorber, can be trapped with a rate, $1/\tau_{\mathrm{tr}}^{\mathrm{e(h)}}$, at the interface with the OW and close to the DBS, forming the n_{ph} and p_{ph}, 2D carrier distributions, respectively. Moreover, these carriers can drift and escape without trapping with a rate, $1/\tau_{\mathrm{esc}}^{\mathrm{e(h)}}$.

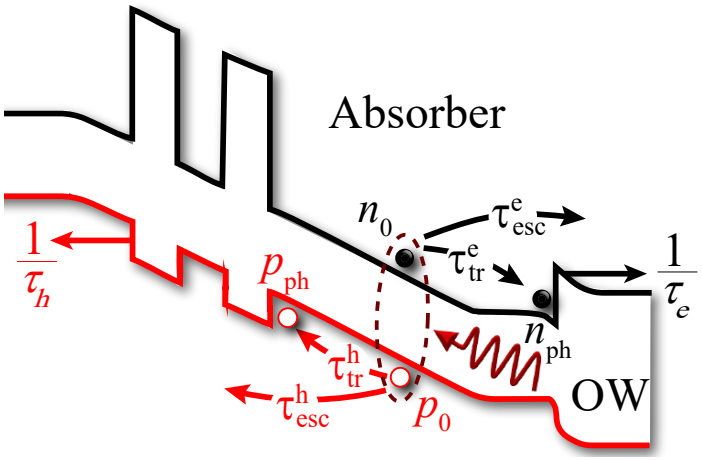

Figure 2.10 – Representation of the photogeneration, drifting, escaping, and trapping of carriers in the absorber. The escaping and trapping processes for electrons, e, and holes, h, take place with characteristic times $\tau_{\mathrm{esc}}^{\mathrm{e(h)}}$ and $\tau_{\mathrm{tr}}^{\mathrm{e(h)}}$, respectively. Trapped electrons, n_{ph}, and holes, p_{ph}, can tunnel through the heterojunctions with a rate $1/\tau_{\mathrm{e(h)}}$.

In this way, the time evolution of the initial photogenerated carriers can be described as

$$\begin{aligned}\frac{dn_0}{dt} &= \mathrm{F}\,\alpha(\hbar\omega, V) - \frac{n_0}{\tau_{\mathrm{tr}}^{\mathrm{e}}} - \frac{n_0}{\tau_{\mathrm{esc}}^{\mathrm{e}}} - \frac{n_0}{\tau_{\mathrm{los}}^{\mathrm{e}}},\\ \frac{dp_0}{dt} &= \mathrm{F}\,\alpha(\hbar\omega, V) - \frac{p_0}{\tau_{\mathrm{tr}}^{\mathrm{h}}} - \frac{p_0}{\tau_{\mathrm{esc}}^{\mathrm{h}}} - \frac{p_0}{\tau_{\mathrm{los}}^{\mathrm{h}}},\end{aligned} \tag{2.23}$$

where $\mathrm{F} = fP/\hbar\omega$ is the incoming photon flux density, with P as the optical power density and f the fraction of this power transmitted to the device, α is the absorption ratio between the absorbed and the incident light, and $\tau_{\mathrm{los}}^{\mathrm{e(h)}}$ is a characteristic time due to radiative and non-radiative recombination processes, as well as other losses that prevent trapping. Analogously, changes in the population of the trapped carriers at the interfaces, can be expressed as

$$\begin{aligned}\frac{dn_{\mathrm{ph}}}{dt} &= \frac{n_0}{\tau_{\mathrm{tr}}^{\mathrm{e}}} - \frac{n_{\mathrm{ph}}}{\tau_{\mathrm{e}}},\\ \frac{dp_{\mathrm{ph}}}{dt} &= \frac{p_0}{\tau_{\mathrm{tr}}^{\mathrm{h}}} - \frac{p_{\mathrm{ph}}}{\tau_{\mathrm{h}}},\end{aligned} \tag{2.24}$$

where τ_{e} and τ_{h} are the electron and hole lifetimes, respectively, which characterize the carriers tunneling processes by means of the transmission rates, $\mathcal{T}$, such that, $1/\tau_{\mathrm{e(h)}} \propto \mathcal{T}_{\mathrm{e(h)}}$. In the stationary condition, $dn_0/dt = dp_0/dt = dn_{\mathrm{ph}}/dt = dp_{\mathrm{ph}}/dt = 0$, then the initial density of photogenerated carriers, according to eqs. 2.23, is given by

$$\begin{aligned}n_0(V) &= \mathrm{F}\,\alpha(\hbar\omega, V)\,\frac{\tau_{\mathrm{tr}}^{\mathrm{e}}\tau_{\mathrm{esc}}^{\mathrm{e}}\tau_{\mathrm{los}}^{\mathrm{e}}}{\tau_{\mathrm{tr}}^{\mathrm{e}}\tau_{\mathrm{esc}}^{\mathrm{e}} + \tau_{\mathrm{tr}}^{\mathrm{e}}\tau_{\mathrm{los}}^{\mathrm{e}} + \tau_{\mathrm{los}}^{\mathrm{e}}\tau_{\mathrm{esc}}^{\mathrm{e}}},\\ p_0(V) &= \mathrm{F}\,\alpha(\hbar\omega, V)\,\frac{\tau_{\mathrm{tr}}^{\mathrm{h}}\tau_{\mathrm{esc}}^{\mathrm{h}}\tau_{\mathrm{los}}^{\mathrm{h}}}{\tau_{\mathrm{tr}}^{\mathrm{h}}\tau_{\mathrm{esc}}^{\mathrm{h}} + \tau_{\mathrm{tr}}^{\mathrm{h}}\tau_{\mathrm{los}}^{\mathrm{h}} + \tau_{\mathrm{los}}^{\mathrm{h}}\tau_{\mathrm{esc}}^{\mathrm{h}}},\end{aligned} \tag{2.25}$$

and substituting eqs. 2.25 into eqs. 2.24, for the same condition, we obtain

$$\begin{aligned}n_{\mathrm{ph}}(V) &= \mathrm{F}\,\alpha(\hbar\omega, V)\,\frac{\tau_{\mathrm{e}}}{1 + \tau_{\mathrm{tr}}^{\mathrm{e}}/\tau_{\mathrm{esc}}^{\mathrm{e}} + \tau_{\mathrm{tr}}^{\mathrm{e}}/\tau_{\mathrm{los}}^{\mathrm{e}}},\\ p_{\mathrm{ph}}(V) &= \mathrm{F}\,\alpha(\hbar\omega, V)\,\frac{\tau_{\mathrm{h}}}{1 + \tau_{\mathrm{tr}}^{\mathrm{h}}/\tau_{\mathrm{esc}}^{\mathrm{h}} + \tau_{\mathrm{tr}}^{\mathrm{h}}/\tau_{\mathrm{los}}^{\mathrm{h}}},\end{aligned} \tag{2.26}$$

that can be rewritten as

$$\begin{aligned}n_{\mathrm{ph}}(V) &= \mathrm{F}\,\alpha(\hbar\omega, V)\,\tau_{\mathrm{e}}(V)\,\eta_{\mathrm{e}}(V),\\ p_{\mathrm{ph}}(V) &= \mathrm{F}\,\alpha(\hbar\omega, V)\,\tau_{\mathrm{h}}(V)\,\eta_{\mathrm{h}}(V).\end{aligned} \tag{2.27}$$

Here, the light absorption ratio can be simulated as a step-like function of the form [42],

$$\alpha(\hbar\omega, V) = \alpha_0\left\{1 + \frac{1}{2}\sum_{j=1}^{2}\mathrm{erf}\left(\frac{\hbar\omega - E_{\mathrm{g},j} + \gamma V^2}{\sqrt{2}\sigma_\alpha}\right)\right\}, \tag{2.28}$$

that considers the absorption of photons with energy $\hbar\omega$ above the bandgap of the absorption layer, $E_{\mathrm{g},1}$ and the optical window, $E_{\mathrm{g},2}$; γ is a parameter that accounts for the Stark shift under an applied bias voltage [43], σ_α defines the broadening of the absorption lines due to homogeneous or inhomogeneous contributions, and α_0 is an intensity ratio.

On the other hand, the *trapping quantum efficiency* for electrons and holes, i =e,h,

is given by the term $\eta_{\rm i} = 1/\left(1+\tau^{\rm i}_{\rm tr}/\tau^{\rm i}_{\rm esc}+\tau^{\rm i}_{\rm tr}/\tau^{\rm i}_{\rm los}\right)$ in eqs. 2.27. The quantum efficiency weights the ability of the conversion of the incoming light power into effective trapped charges, which are detectable in the current-voltage read-out. Quantum efficiencies hold relevant insights about device performance [44, 45] and can be expressed in terms of ratios of concomitant types of decay rates [46], as we proposed in this model. In this sense, the quantum efficiency can be obtained by assuming the trapping and escape rates dependence on the applied voltage in the form of an activation probability rate,

$$\begin{aligned}\frac{1}{\tau^i_{\rm tr}(V)} &= \frac{1}{\tau^i_{\rm tr,0}}\exp\left(\frac{-\Delta E_\eta+\xi eV}{k_{\rm B}T_i}\right),\\ \frac{1}{\tau^i_{\rm esc}(V)} &= \frac{1}{\tau^i_{\rm esc,0}}\exp\left(\frac{-\Delta E_\eta+\xi eV}{k_{\rm B}T_i}\right),\end{aligned} \tag{2.29}$$

being $\tau^i_{\rm tr,0}$ and $\tau^i_{\rm esc,0}$ characteristic trapping and escape times, respectively, that must depend on the layer length and the carriers velocity (mobility and local electric field); ξ is the leverage factor, T_i is the carrier temperature, and $\Delta E_\eta = \Delta E_0/[1+\chi(N)]$ is an intrinsic barrier due to changes in the absorber composition or internal electric fields. Here, ΔE_0 is the maximum height of the intrinsic barrier, and χ is the electric susceptibility, which within the Claussius-Mossoti approximation [47] can be expressed as $\chi(N) = {\rm p_{exc}}N/(1-{\rm p_{exc}}N/3)$, where $\rm p_{exc}$ is the exciton polarizability, proportional to the exciton volume, and $N = F\,\alpha(\hbar\omega, V)$ is the density of photogenerated excitons. Consequently, the quantum efficiency can be expressed as

$$\eta_i(V) = \frac{\eta^i_0}{1+\frac{\tau^i_{\rm tr,0}}{\tau^i_{\rm los}\left(1+\tau^i_{\rm tr,0}/\tau^i_{\rm esc,0}\right)}\exp\left(\frac{\Delta E_\eta-\xi eV}{k_{\rm B}T_i}\right)} \equiv \frac{\eta^i_0}{1+\exp\left(-\frac{V-V^i_{\rm th}}{\sigma^i_\eta}\right)}, \tag{2.30}$$

with $\eta^i_0 \equiv 1/\left(1+\tau^i_{\rm tr,0}/\tau^i_{\rm esc,0}\right) < 1$ as the maximum trapping quantum efficiency. Thus, the quantum efficiencies are expressed as logistic functions with a steepness defined by $\sigma^i_\eta \equiv k_{\rm B}T_i/\xi e$, and onsets at

$$V^i_{\rm th} = \sigma^i_\eta \ln\left(\eta^i_0\frac{\tau^i_{\rm tr,0}}{\tau^i_{\rm los}}\right)+\frac{\Delta E_\eta}{\xi e}, \tag{2.31}$$

Note that the threshold voltages, $V^i_{\rm th}$, as defined by eq. 2.31 depend on structural parameters of the RTD (first term on the right) and on the parameters that characterize the charge dynamics at the absorber (second term). The former has a significant contribution when the parameters in the argument of the logarithm diverge by orders of magnitude, making the argument positive or negative regarding their relative values. Accordingly, efficient losses (smaller $\tau^i_{\rm los}$) or slower drifting (larger $\tau^i_{\rm tr,0}$) can induce an increase of $V^i_{\rm th}$.

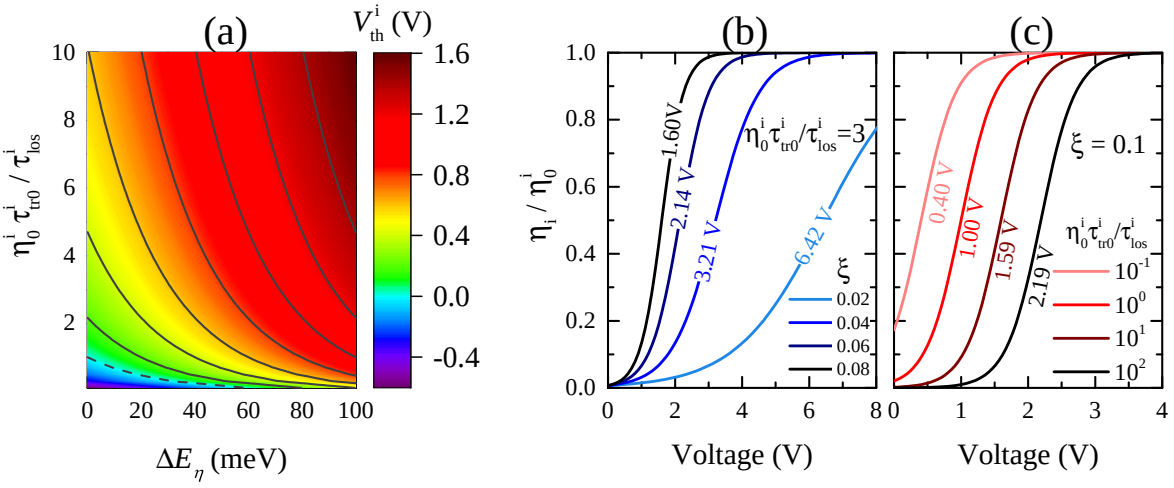

Figure 2.11 – (a) Calculated threshold voltage as a function of $\eta_0 \tau^i_{tr,0}/\tau^i_{los}$ and ΔE_η for $\xi = 0.1$, according to eq. 2.31. Contour lines show the threshold voltage at every 0.2 V, starting at $V^i_{th} = 0$ V (dashed line). Simulated trapping quantum efficiency as a function of the applied voltage for different (b) leverage factors and (c) $\eta_0 \tau^i_{tr,0}/\tau^i_{los}$ ratios, taking $\Delta E_\eta = 0.1$ eV. The voltage values on each curve correspond to their respective threshold voltages. All the calculations were carried out for $T_i = 300$ K.

Figure 2.11 (a) shows a color-gradient map of the threshold voltage obtained from eq. 2.31, as a function of $\eta_0 \tau^i_{tr,0}/\tau^i_{los}$ and ΔE_η, for $\xi = 0.1$. The higher the $\eta_0 \tau^i_{tr,0}/\tau^i_{los}$ ratio or ΔE_η, the higher the threshold voltage, and higher applied voltages are required to reach high trapping efficiencies. This is depicted in figures 2.11 (b) and (c), where the quantum efficiency as a function of the applied voltage is plotted for different leverage factors and $\eta_0 \tau^i_{tr,0}/\tau^i_{los}$ ratios, respectively. Voltage values on the curves indicate the corresponding threshold voltages. According to this model, a decrease (increase) of the leverage factor, previously discussed, affects both the growth rate of the efficiency and the threshold voltage, while the tuning of $\eta_0 \tau^i_{tr,0}/\tau^i_{los}$, linked to the carriers mobility, modulates just V^i_{th}.

Based on these expressions, and taking appropriate voltage-dependent escape times for trapped electrons and holes, eqs. 2.11 and 2.27 can be introduced in eq. 2.22 to obtain the voltage dependence of ΔV_{ph}. This model is applied in Chapter 4 to emulate the functionalities of an RTD photosensor.

References

[1] R. Tsu and L. Esaki, "Tunneling in a finite superlattice," *Appl. Phys. Lett.*, vol. 22, no. 11, pp. 562–564, 1973.

[2] L. L. Chang, L. Esaki, and R. Tsu, "Resonant tunneling in semiconductor double barriers," *Appl. Phys. Lett.*, vol. 24, no. 12, pp. 593–595, 1974.

[3] A. Pfenning, F. Hartmann, R. Weih, M. Emmerling, L. Worschech, and S. Höfling,

"p-Type Doped AlAsSb/GaSb Resonant Tunneling Diode Photodetector for the Mid-Infrared Spectral Region," *Adv. Opt. Mater.*, vol. 6, no. 24, p. 1800972, 2018.

[4] F. Rothmayr, A. Pfenning, C. Kistner, J. Koeth, G. Knebl, A. Schade, S. Krueger, L. Worschech, F. Hartmann, and S. Höfling, "Mid-infrared GaSb-based resonant tunneling diode photodetectors for gas sensing applications," *Appl. Phys. Lett.*, vol. 112, no. 16, p. 161107, 2018.

[5] A. Pfenning, J. Jurkat, A. Naranjo, D. Köck, F. Hartmann, and S. Höfling, "Resonant tunneling diode photon number resolving single-photon detectors," in *Infrared Remote Sensing and Instrumentation XXVII* (M. Strojnik and G. E. Arnold, eds.), vol. 11128, pp. 47 – 56, International Society for Optics and Photonics, SPIE, 2019.

[6] E. R. Cardozo de Oliveira, A. Pfenning, E. D. Guarin Castro, M. D. Teodoro, E. C. dos Santos, V. Lopez-Richard, G. E. Marques, L. Worschech, F. Hartmann, and S. Höfling, "Electroluminescence on-off ratio control of $n-i-n$ GaAs/AlGaAs-based resonant tunneling structures," *Phys. Rev. B*, vol. 98, p. 075302, Aug 2018.

[7] K. Kasagi, S. Suzuki, and M. Asada, "Large-scale array of resonant-tunneling-diode terahertz oscillators for high output power at 1 THz," *J. Appl. Phys.*, vol. 125, no. 15, p. 151601, 2019.

[8] S. Iwamatsu, Y. Nishida, M. Fujita, and T. Nagatsuma, "Terahertz coherent oscillator integrated with slot-ring antenna using two resonant tunneling diodes," *Appl. Phys. Express*, vol. 14, p. 034001, jan 2021.

[9] H. Mizuta and T. Tanoue, *The Physics and Applications of Resonant Tunnelling Diodes*. Cambridge Studies in Semiconductor Physics and Microelectronic Engineering, Cambridge: Cambridge University Press, 1995.

[10] F. Hartmann, F. Langer, D. Bisping, A. Musterer, S. Höfling, M. Kamp, A. Forchel, and L. Worschech, "GaAs/AlGaAs resonant tunneling diodes with a GaInNAs absorption layer for telecommunication light sensing," *Appl. Phys. Lett.*, vol. 100, no. 17, p. 172113, 2012.

[11] O. Manasreh, *Semiconductor Heterojunctions and Nanostructures*. New York: McGraw-Hill Education, 2005.

[12] E. T. Yu, J. O. McCaldin, and T. C. McGill, "Band Offsets in Semiconductor Heterojunctions," vol. 46 of *Solid State Physics*, pp. 1–146, Academic Press, 1992.

[13] H. B. de Carvalho, Y. Galvão Gobato, M. J. S. P. Brasil, V. Lopez-Richard, G. E. Marques, I. Camps, M. Henini, L. Eaves, and G. Hill, "Voltage-controlled hole spin injection in nonmagnetic GaAs/AlAs resonant tunneling structures," *Phys. Rev. B*, vol. 73, p. 155317, Apr 2006.

[14] V. G. Popov, V. G. Krishtop, O. N. Makarovskii, and M. Henini, "Magnetotunneling spectroscopy of polarons in a quantum well of a resonant-tunneling diode," *J. Exp. Theor. Phys.*, vol. 111, no. 2, p. 220–224, 2010.

[15] J. J. L. Rascol, K. P. Martin, R. E. Carnahan, R. J. Higgins, L. A. Cury, J. C. Portal, B. G. Park, E. Wolak, K. L. Lear, and J. S. Harris, "Influence of ballistic electrons on the device characteristics of vertically integrated resonant tunneling diodes," *Appl. Phys. Lett.*, vol. 58, no. 14, pp. 1482–1484, 1991.

[16] G. Ternent and D. J. Paul, "SPICE Modeling of the Scaling of Resonant Tunneling Diodes and the Effects of Sidewall Leakage," *IEEE Transactions on Electron Devices*, vol. 59, no. 12, pp. 3555–3560, 2012.

[17] A. Yangui, M. Bescond, T. Yan, N. Nagai, and K. Hirakawa, "Evaporative electron cooling in asymmetric double barrier semiconductor heterostructures," *Nat. Commun.*, vol. 10, no. 1, p. 4504, 2019.

[18] J. Schulman, H. De Los Santos, and D. Chow, "Physics-based RTD current-voltage equation," *IEEE Electron Device Lett.*, vol. 17, no. 5, pp. 220–222, 1996.

[19] S. Sze and K. N. Kwok, *Physics of Semiconductor Devices*. New Jersey: John Wiley & Sons, Inc., 3rd ed., 2007.

[20] K. L. Jensen and F. A. Buot, "The effects of scattering on current-voltage characteristics, transient response, and particle trajectories in the numerical simulation of resonant tunneling diodes," *J. Appl. Phys.*, vol. 67, no. 12, pp. 7602–7607, 1990.

[21] D. Z. Ting, S. K. Kirby, and T. C. McGill, "Interface roughness effects in resonant tunneling structures," *Appl. Phys. Lett.*, vol. 64, no. 15, pp. 2004–2006, 1994.

[22] H. C. Liu, "Circuit simulation of resonant tunneling double-barrier diode," *J. Appl. Phys.*, vol. 64, no. 9, pp. 4792–4794, 1988.

[23] T. J. Foster, M. L. Leadbeater, L. Eaves, M. Henini, O. H. Hughes, C. A. Payling, F. W. Sheard, P. E. Simmonds, G. A. Toombs, G. Hill, and M. A. Pate, "Current bistability in double-barrier resonant-tunneling devices," *Phys. Rev. B*, vol. 39, pp. 6205–6207, Mar 1989.

[24] J. Iñarrea and G. Platero, "Photoinduced current bistabilities in a semiconductor double barrier," *Europhys. Lett.*, vol. 33, pp. 477–482, feb 1996.

[25] P. Orellana, F. Claro, E. Anda, and S. Makler, "Self-consistent calculation of resonant tunneling in asymmetric double barriers in a magnetic field," *Phys. Rev. B*, vol. 53, pp. 12967–12972, May 1996.

[26] F. Hartmann, A. Pfenning, M. Rebello Sousa Dias, F. Langer, S. Höfling, M. Kamp, L. Worschech, L. K. Castelano, G. E. Marques, and V. Lopez-Richard, "Temperature tuning from direct to inverted bistable electroluminescence in resonant tunneling diodes," *J. Appl. Phys.*, vol. 122, no. 15, p. 154502, 2017.

[27] A. Pfenning, E. D. Guarin Castro, F. Hartmann, M. D. Teodoro, L. Worschech, , S. Höfling, G. E. Marques, and V. Lopez-Richard, "Tuning magneto-transport and magneto-electroluminescence bistabilities in GaAs-based resonant tunneling diodes." 2021.

[28] V. J. Goldman, D. C. Tsui, and J. E. Cunningham, "Observation of intrinsic bistability in resonant tunneling structures," *Phys. Rev. Lett.*, vol. 58, pp. 1256–1259, Mar 1987.

[29] F. W. Sheard and G. A. Toombs, "Space-charge buildup and bistability in resonant-tunneling double-barrier structures," *Appl. Phys. Lett.*, vol. 52, no. 15, pp. 1228–1230, 1988.

[30] N. Kluksdahl, A. Kriman, D. Ferry, and C. Ringhofer, "Intrinsic bistability in the resonant tunneling diode," *Superlattices Microstruct.*, vol. 5, no. 3, pp. 397–401, 1989.

[31] D. D. Coon, K. M. S. V. Bandara, and H. Zhao, "Is intrinsic bistability really intrinsic tristability?," *Appl. Phys. Lett.*, vol. 54, no. 21, pp. 2115–2117, 1989.

[32] J. G. Chen, J. Chen, R. A. Wilson, W. Johnson, and C. H. Yang, "On the intrinsic bistability in resonant tunneling structures: Observation of area and temperature dependence of hysteresis," *J. Appl. Phys.*, vol. 70, no. 4, pp. 2473–2475, 1991.

[33] A. D. Martin, M. L. F. Lerch, P. E. Simmonds, and L. Eaves, "Observation of intrinsic tristability in a resonant tunneling structure," *Appl. Phys. Lett.*, vol. 64, no. 10, pp. 1248–1250, 1994.

[34] P. England, J. E. Golub, L. T. Florez, and J. P. Harbison, "Optical switching in a resonant tunneling structure," *Appl. Phys. Lett.*, vol. 58, no. 9, pp. 887–889, 1991.

[35] H. S. Li, Y. W. Chen, K. L. Wang, D. S. Pan, L. P. Chen, and J. M. Liu, "Photocontrolled double-barrier resonant-tunneling diode," *J. Vac. Sci. Technol., B: Microelectron. Nanometer Struct.–Process., Meas., Phenom.*, vol. 12, no. 2, pp. 1269–1272, 1994.

[36] P. W. Park, H. Y. Chu, S. G. Han, Y. W. Choi, G. Kim, and E. Lee, "Optical switching mechanism based on charge accumulation effects in resonant tunneling diodes," *Appl. Phys. Lett.*, vol. 67, no. 9, pp. 1241–1243, 1995.

[37] T. S. Moise, Y. Kao, L. D. Garrett, and J. C. Campbell, "Optically switched resonant tunneling diodes," *Appl. Phys. Lett.*, vol. 66, no. 9, pp. 1104–1106, 1995.

[38] V. Duez, M. Chaubet, O. Vanbésien, and D. Lippens, "Optical switching of resonant interband tunnelling diodes induced by heavy hole space charge effects," *Electron. Lett.*, vol. 36, pp. 974–975(1), May 2000.

[39] I. J. S. Coêlho, J. F. Martins-Filho, J. M. L. Figueiredo, and C. N. Ironside, "Modeling of light-sensitive resonant-tunneling-diode devices," *J. Appl. Phys.*, vol. 95, no. 12, pp. 8258–8263, 2004.

[40] A. Pfenning, F. Hartmann, M. Rebello Sousa Dias, F. Langer, M. Kamp, L. K. Castelano, V. Lopez-Richard, G. E. Marques, S. Höfling, and L. Worschech, "Photocurrent-voltage relation of resonant tunneling diode photodetectors," *Appl. Phys. Lett.*, vol. 107, no. 8, p. 081104, 2015.

[41] A. Pfenning, F. Hartmann, F. Langer, M. Kamp, S. Höfling, and L. Worschech, "Sensitivity of resonant tunneling diode photodetectors," *Nanotechnology*, vol. 27, p. 355202, jul 2016.

[42] R. A. Morgan, "Improvements in self electro-optic effect devices: toward system implementation," in *Devices for Optical Processing* (D. M. Gookin, ed.), vol. 1562, pp. 213 – 227, International Society for Optics and Photonics, SPIE, 1991.

[43] J. A. Brum and G. Bastard, "Electric-field-induced dissociation of excitons in semiconductor quantum wells," *Phys. Rev. B*, vol. 31, pp. 3893–3898, Mar 1985.

[44] J.-I. Shim and D.-S. Shin, "Measuring the internal quantum efficiency of light-emitting diodes: towards accurate and reliable room-temperature characterization," *Nanophotonics*, vol. 7, no. 10, pp. 1601–1615, 2018.

[45] O. Almora, C. I. Cabrera, J. Garcia-Cerrillo, T. Kirchartz, U. Rau, and C. J. Brabec, "Quantifying the Absorption Onset in the Quantum Efficiency of Emerging Photovoltaic Devices," *Adv. Energy Mater.*, vol. 11, no. 16, p. 2100022, 2021.

[46] M. S. Skolnick, P. E. Simmonds, D. G. Hayes, A. W. Higgs, G. W. Smith, A. D. Pitt, C. R. Whitehouse, H. J. Hutchinson, C. R. H. White, L. Eaves, M. Henini, and O. H. Hughes, "Excitation mechanisms of photoluminescence in double-barrier resonant-tunneling structures," *Phys. Rev. B*, vol. 42, pp. 3069–3076, Aug 1990.

[47] A. Matveev, *Electricity and Magnetism.* Moscow: MIR Publishers, 1st ed., 1986.

Chapter 3

Experimental Methods

The experimental component of this Thesis is devoted to the investigation of the transport and optical properties of n-type RTDs composed of III-V semiconductor materials. Particular attention was given to antimony (Sb)-based n-type RTDs from the 6.1-Å family [1], due to their distinctive type-I band alignment with large band offsets at the CB and VB [2], similar or even higher than the offsets present in conventional GaAs/AlGaAs RTDs [3–5]. This property gives Sb-based RTDs notable advantage in their resonant tunneling transport characteristics at cryogenic temperatures, which can be extended to room temperatures by the addition of ternary semiconducting *emitter prewells* [6, 7], or by employing the GaInAsSb quaternary compound at both sides of the DBS, as reported in Ref. [8]. These methods have been proven crucial for the enhancement of the PVCR in this type of RTDs.

The use of Sb-based semiconductors also offers widely tunable direct bandgaps, covering the mid- (MIR) and near-infrared (NIR) spectral regions, in contrast with the narrow light emission/absorption range observed in As-based RTDs (typically between 1.37 and 1.55 eV) [9, 10]. Moreover, Sb-based alloys have a spin-orbit interaction energy comparable with its bandgap (~ 0.80 eV), which makes the ionization coefficient of holes to be relatively high, thus producing an improvement in the signal-to-noise ratio at photon energies lower than 0.95 eV, for GaAlSb avalanche photodetectors grown on GaSb [11]. For these reasons, Sb-based RTDs constitute optically active elements, suitable for the development of high-performance infrared optoelectronic devices such as photodetectors [12, 13] and quantum cascade lasers [14].

In addition to the Sb-based RTDs, the outstanding optoelectronic response under applied magnetic fields of a typical n-type GaAs/AlGaAs RTD with a GaInNAs absorption layer was also explored. The modulation of the current-voltage *bistability* with temperature and magnetic fields in this kind of heterostructure provided further clues about the complex quantum transport physics present in these RTDs.

In the following sections, the fabrication process and the structural characteristics of

each sample are described. The characterization techniques used to unveil the carrier dynamics in these heterostructures are also detailed. All the samples were designed, fabricated, and processed by the Microstructure Laboratory (*Gottfried-Landwehr-Labor für Nanotechnologie*, GLLN) at the Chair of Technical Physics (*Technische Physik*, TEP) of Universität Würzburg (Uni Würzburg, Würzburg, Germany) and nanoplus Nanosystems and Technologies GmbH (Gerbrunn, Germany). The transport and optical characterization were performed at the Nanoelectronics Group and the Laboratory for Optical Spectroscopy of Nanostructures of TEP-Uni Würzburg, and the Semiconductor Nanostructures Group (*Grupo de Nanoestruturas Semicondutoras*, GNS) at the Physics Department of Federal University of São Carlos (UFSCar, São Carlos, Brazil).

3.1 Sample Growth and Electronic Structure Engineering

The studied RTDs were grown through *molecular beam epitaxy* (MBE), a technique that employs localized beams of atoms or molecules in an ultra-high vacuum environment to provide low levels of contamination and avoid oxidation of the materials [15–17]. The RTD growing process starts with an n-type crystalline substrate wafer mounted on the heater block of the MBE growth chamber. In there, group-III elements and dopants are supplied by solid-state evaporation cells, whereas group-V elements are provided by valved cracking cells [6]. In the case of Sb-based compounds, the n-type doping profile is achieved by using column-VI elements as donors, like Te in our case, while for the As-based system, Si was chosen as a doping material.

When the atoms provided by the fast-source evaporation cells arrive at the crystalline substrate, they can migrate to lattice sites, a process activated by the thermal energy transferred by the substrate, which is kept at a moderately elevated temperature [17]. In these conditions, the beam of atoms or molecules travels in nearly collision-free paths until arriving at the substrate, where they condense and form crystalline or *epitaxial* surfaces with nanometric or even atomic control of the roughness.

With the help of shutters, it is possible to interrupt the beam quickly and efficiently, giving the possibility of changing the composition, doping profiles, or even the material of the subsequent layer. Thus, defects during the deposition process are reduced and abrupt heterojunctions between different semiconductor materials can be formed [17]. To prevent having a concentration gradient along the substrate, the wafer is continuously rotated during the growth process. At the same time, the quality of the deposition, the vacuum conditions, and the growth rate are monitored *in situ* employing techniques such as reflection high energy electron diffraction [17].

The RTD heterostructures grown via MBE are presented in figure 3.1 for each of the four studied samples, indicating the function, doping profile, thickness, and composition of each layer. In all cases, high electron concentrations at the contacts ($\sim 10^{18}$ cm^{-3}) are necessary for improving resonant tunneling through the high CB barriers. This also ensures good carrier mobilities and 2D electron densities of around $\sim 10^{12}$ cm^{-2} close to the DBS under an applied voltage [1]. Undoped buffer or spacer layers were incorporated on each side of the DBSs to reduce both oxidation and diffusion of dopants into the tunneling structure. Capping layers finalize the heterostructures to seal off the sample.

(a)

Function	Doping (cm^{-3})	Width (nm)	Material
Cap	2×10^{18}	50	GaSb
Contact	1×10^{18}	120	
Absorption Layer	1×10^{18}	50	$Ga_{0.64}In_{0.36}As_{0.33}Sb_{0.67}$
	5×10^{17}	25	
	1×10^{17}	130	
Buffer	Undoped	25	
Double Barrier Structure (DBS)		4	AlSb
		5	$Ga_{0.64}In_{0.36}As_{0.33}Sb_{0.67}$
		4	AlSb
Buffer		25	$Ga_{0.64}In_{0.36}As_{0.33}Sb_{0.67}$
Absorption Layer	1×10^{17}	130	
	5×10^{17}	50	
Contact	1×10^{18}	120	GaSb
	2×10^{18}	300	
n GaSb-substrate			

(b)

Function	Doping (cm^{-3})	Width (nm)	Material
Cap	2×10^{18}	10	GaSb
Contact	1×10^{18}	150	
Absorption Layer	5×10^{17}	50	$Ga_{0.64}In_{0.36}As_{0.33}Sb_{0.67}$
	1×10^{17}	130	
Buffer	Undoped	20	
Double Barrier Structure (DBS)		5	GaSb
		4	AlSb
		5	$GaAs_{0.15}Sb_{0.85}$
		4	AlSb
Prewell		7	$GaAs_{0.15}Sb_{0.85}$
Buffer		20	GaSb
Contact	5×10^{17}	120	
	2×10^{18}	300	
n GaSb-substrate			

(c)

Function	Doping (cm^{-3})	Width (nm)	Material
Cap	1×10^{18}	10	GaSb
Optical Window	1×10^{18}	220	$Al_{0.3}Ga_{0.7}As_{0.03}Sb_{0.97}$
Contact	5×10^{17}	120	GaSb
Buffer	Undoped	27	
Double Barrier Structure (DBS)		4.5	$AlAs_{0.08}Sb_{0.92}$
		5	$GaAs_{0.15}Sb_{0.85}$
		4.5	$AlAs_{0.08}Sb_{0.92}$
Prewell		7	$GaAs_{0.15}Sb_{0.85}$
Buffer		20	GaSb
Contact	5×10^{17}	120	
	1×10^{18}	300	
n GaSb-substrate			

(d)

Function	Doping (cm^{-3})	Width (nm)	Material
Cap	1×10^{18}	556	GaAs
Absorption Layer	1×10^{17}	144	$Ga_{0.89}In_{0.11}N_{0.04}As_{0.96}$
		5	
Buffer	Undoped	10	GaAs
Double Barrier Structure (DBS)		3	$Al_{0.4}Ga_{0.6}As$
		4	GaAs
		3	$Al_{0.4}Ga_{0.6}As$
Buffer		15	GaAs
Contact	1×10^{17}	300	
	1×10^{18}		
n GaAs-substrate			

Figure 3.1 – Representation of the MBE-grown layered structures for (a) RTD-A, (b) RTD-B, (c) RTD-C, and (d) RTD-D. RTDs A-C are based on the GaSb system, whilst RTD-D is a GaAs-based structure. All the samples are n-i-n RTDs, with n-type highly doped materials at the emitter and collector sides, and intrinsic DBSs. A pseudomorphically $GaAs_{0.15}Sb_{0.85}$ emitter prewell was integrated into the RTDs B and C DBS to favor room temperature resonant tunneling.

RTDs A-C, illustrated in figures 3.1 (a)-(c), respectively, are Sb-based samples grown on n-type GaSb(100) substrates, with n-type GaSb contacts. RTD-D is an As-based structure with n-type GaAs substrate and contacts, as sketched in figure 3.1 (d). The fundamental properties of these samples were initially reported in Refs. [8], [13], [6], and [18], respectively. The RTD-C sample was referred in Ref. [6] as RTD 3.

The semiconductor compounds employed to build the heterostructures have similar crystal lattice constants: $a = 6.10$ Å for the Sb-based systems [19], and $a = 5.65$ Å for the As-based system [20]. This guarantees *lattice-matched commensurate* growth. Only in the case of the layers forming $GaAs_{0.15}Sb_{0.85}$ prewells (RTDs B and C), the growth is *pseudomorphic*, which means that due to the ~ 3 % lattice-constant mismatching between $GaAs_{0.15}Sb_{0.85}$ ($a \approx 5.90$ Å) [19] and GaSb or AlSb ($a = 6.10$ Å), the prewell adopts the 2D lattice structure of the previous layer, inducing an strain or an uniaxial distortion along the growth direction [17].

Figures 3.2 (a)-(d) show the calculated CB minimum (black lines) and VB maximum (red lines) profiles along the growth direction, close to the DBS for every sample. The calculations were performed at zero applied voltage with the *nextnano* simulation tool [21] and the offsets of the $Ga_{0.64}In_{0.36}As_{0.33}Sb_{0.67}$/GaSb heterojunctions were corrected after Shim [2].

A brief description of the DBS present in each RTD is given as follows:

- RTD-A contains AlSb barriers and $Ga_{0.64}In_{0.36}As_{0.33}Sb_{0.67}$ as emitter/collector and quantum well material. This quaternary alloy reduces the bandgap considerably ($E_g = 374$ meV), as observed in figure 3.2 (a). It allows to cover the CH_4, NO_2, and NH_3 absorption lines [22] that can be useful for sensing applications. It also enables the combination of the excellent transport properties of InAs, a consequence of its low effective electron mass, with the optoelectronic capabilities of GaSb-based RTDs, enhanced by the pronounced type-I band alignment. Due to its higher bandgap ($E_g = 812$ meV) [23], the top contact GaSb layer also works as an optical window (OW) for MIR wavelengths.

- RTD-B takes advantage of the resonant tunneling properties of the $GaAs_{0.15}Sb_{0.85}$/AlSb DBS with a $GaAs_{0.15}Sb_{0.85}$ emitter prewell, which is necessary to keep the quality of resonant tunneling transport at room temperature. The inclusion of small concentrations of As in the GaSb compound increases the Γ-L valley separation by lowering the Γ-valley. As a consequence, the *L*-valley states in the emitter prewell are depopulated with respect to the bulk GaSb, thus favoring resonant transport through the Γ-valley states [6, 7]. A $Ga_{0.64}In_{0.36}As_{0.33}Sb_{0.67}$ layer was also deposited at the collector side, as presented in figure 3.2 (b), to act as an absorption region, similarly to RTD-A.

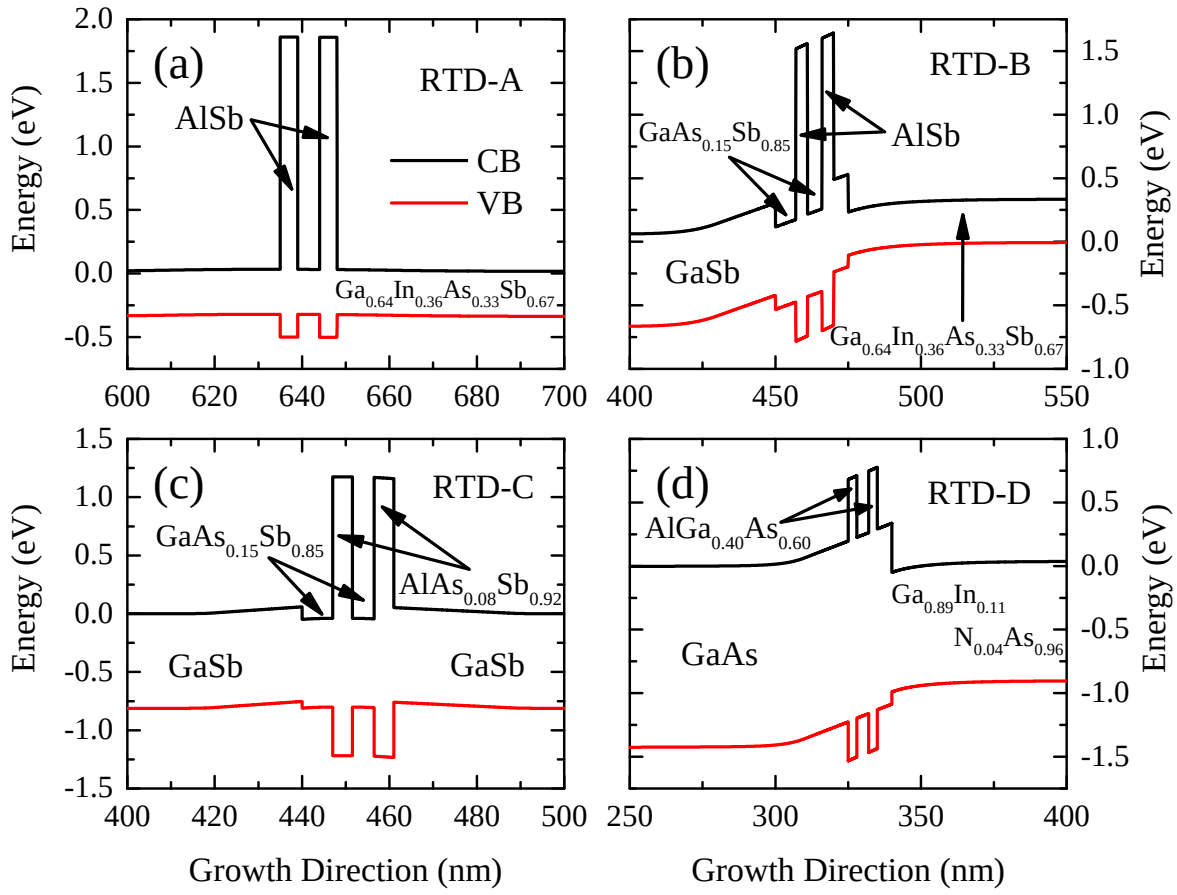

Figure 3.2 – Simulated CB minimum (black lines) and VB maximum (red lines) profiles close to the DBS for (a) RTD-A, (b) RTD-B, (c) RTD-C, and (d) RTD-D, at zero applied voltage. The Sb-based systems (RTDs A-C) present lower emitter/collector and QW bandgaps, as well as higher CB barriers than the As-based system (RTD-D). All the DBSs present type-I band alignment.

- RTD-C incorporates the same DBS as in RTD-B, but with GaSb absorption layers, as displayed in figure 3.2 (c). The insertion of As atoms into the AlSb barriers (As< 10%) increases the bandgap and results in a marked type-I alignment. The combination with an $Al_{0.30}Ga_{0.70}As_{0.03}Sb_{0.97}$ OW allows for the optical operation in the NIR spectral region [24].

- RTD-D integrates a conventional GaAs/$Al_{0.40}Ga_{0.60}As$ DBS with a $Ga_{0.89}In_{0.11}N_{0.04}As_{0.96}$ absorption layer, as indicated in figure 3.2 (d). The quaternary system also enables light emission and detection in the NIR region, with a high-temperature performance thanks to the relative-high band offset (above 500 meV), formed at the heterojunction with the GaAs layer. This results in an enhanced confinement of electrons at the CB [20, 25–30].

After deposition, the doping profiles and width of the different semiconductor layers are verified *ex situ* by time-of-flight secondary ion mass spectroscopy and cross-sectional scanning electron microscopy, respectively. Figure 3.3 illustrates an electron microscopy

image of RTD-A as reported in Ref. [8]. Layers with high Al concentrations are observed as the darkest regions, indicating the position of the AlSb barriers. They allow assessing the thickness and position of the DBS. The $Ga_{0.64}In_{0.36}As_{0.33}Sb_{0.67}$/GaSb heterojunctions are also clearly observed.

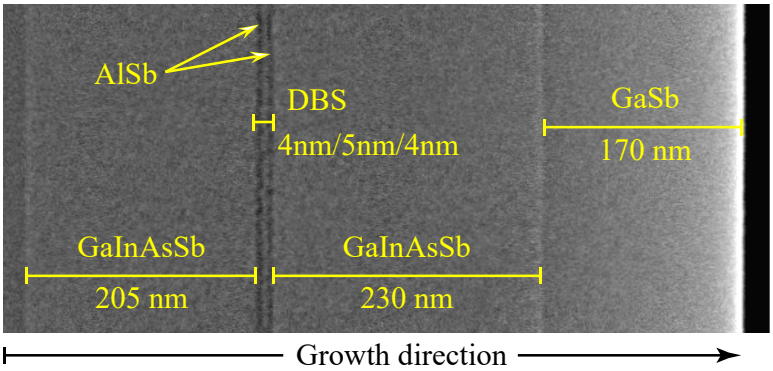

Figure 3.3 – Cross-sectional scanning electron microscopy image of RTD-A. Darkest regions indicate the presence of layers with high Al concentration. The $Ga_{0.64}In_{0.36}As_{0.33}Sb_{0.67}$/GaSb heterojunctions are also observed [8].

The electron microscopy images also indicate good crystal quality and lattice-matched crystal growth with no apparent dislocations or defects. It is corroborated with high-resolution X-ray diffraction measurements as exemplified in Ref. [6] for RTD-C. In that case, compressive and tensile strain secondary patterns are also present in the measured spectrum of RTD-C due to the incorporation of the pseudomorphic GaAsSb layers.

3.2 Device Microfabrication

To characterize the transport and optical properties of the samples, circular RTD mesa structures with different diameters are fabricated from the MBE-grown heterostructures. The aim is to produce cylindrical diodes with ring-shaped metallic contacts to gain optical access to the heterostructure. This process is known as *microfabrication*, and it is carried out in a *clean room* in which the air is heavily filtered, to avoid defects that can be transferred to the heterostructure. The microfabrication process is summarized in figure 3.4.

Initially, the wafer with the heterostructure is cleaned out by removing the native oxides with a solution of NH_4OH and deionized water. Subsequently, a 200-nm thick AuGe/Ni/Au contact is deposited by electron beam evaporation on the bottom of the substrate. Then, a 10×10 mm^2 piece is cleaved out of the wafer, and the top of the heterostructure is coated by a $\sim 5-$nm thick layer of *photoresist* using the spin-coating technique. With this technique, a drop of photoresist is dipped on the center of the sample and spread out uniformly over the surface by subjecting the sample to fast rotations. A photomask with circular

transparent patterns and different diameters is placed on the sample's top to form a coating pattern after a *photolitography* process, as sketched in figure 3.4 (a).

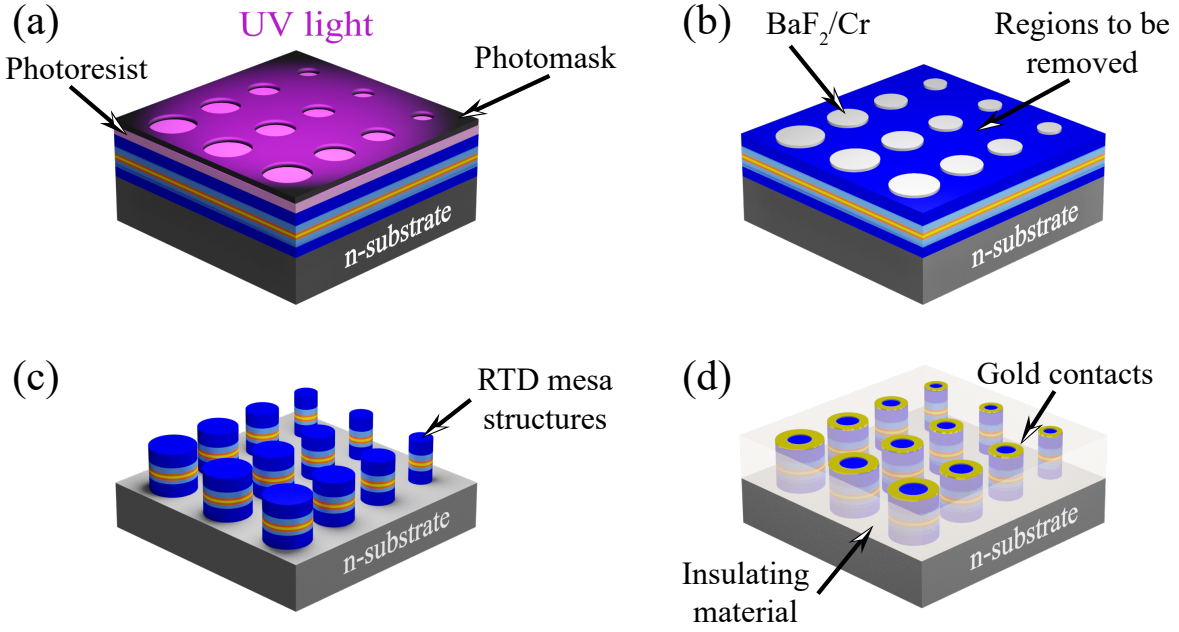

Figure 3.4 – Illustration of the RTD microfabrication process: (a) Sample pieces of 10×10 mm^2 are coated with photoresist and then masked to form a coating pattern via photolithography with ultra-violet light. (b) The photoresist is lifted off, and the pattern of circles with different diameters is protected with a thin layer of BaF_2/Cr. (c) Circular RTD mesas are formed by reactive ion etching and the BaF_2/Cr layer is removed. (d) An insulating material is deposited on the sample to bring electrical isolation and sidewalls passivation. Finally, ring-shaped gold-based contacts are deposited on top of the mesas.

During photolithography, the unmasked regions of the sample's surface are exposed to ultra-violet light, leading to a degradation of the photoresist material. Thus, the regions that were not exposed to light can be removed by *dry-chemical etching*. This removal is performed after *metallization* of the surface by deposition of a BaF_2/Cr layer of 5 nm on the top of the sample, necessary to protect the circular patterns from etching. Using N-Methylpyrrolidone, the excess of photoresist is *lifted-off* to expose the regions that will be removed, as indicated in figure 3.4 (b). Afterward, employing Cr_2/Ar reactive ion etching at 200°C and with a depth of about 50 nm below the DBS, the uncovered regions are attacked to reveal the *mesas* or the cylindrical structures depicted in figure 3.4 (c). The BaF_2/Cr layers are then removed with deionized water.

To electrically isolate the diodes and passivate the sidewall mesas, an insulating material is deposited over the entire sample. This passivation process hampers sidewall leakage by avoiding the formation of semi-metallic conductive layers at the sidewalls due to oxidation after the etching process. In this way, RTDs A and B were passivated using a technique developed at nanoplus Nanosystems and Technologies GmbH. This technique consists of depositing ~ 1 µm of Silicon Nitride (Si_3N_4/SiO_2) via sputtering on the etched

heterostructure. Then, using photolithography and reactive ion etching, the excess of Silicon Nitride is removed. Finally, Ti/Pt/Au ring-shaped contacts are grown via galvanic deposition on top of each mesa. On the other hand, RTDs C and D were passivated at the GLLN-TEP-Uni Würzburg, with the polymer *BenzoCycloButene*, which was cured at 200°C for two hours. Ti/Au ring-shaped contacts were deposited via sputtering on the top. Figure 3.4 (d) sketches a sample after passivation and top contacts deposition. Gold pads are also deposited and connected to each contact to facilitate the welding process.

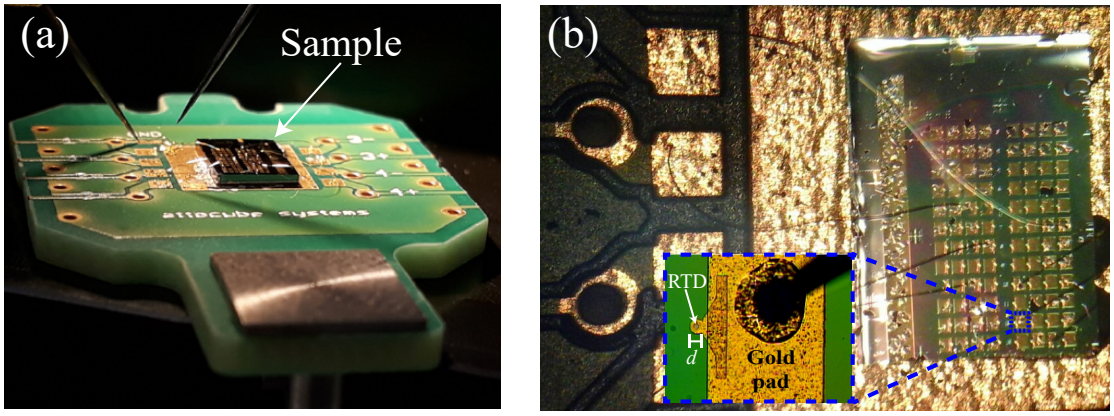

Figure 3.5 – (a) Picture of the sample attached to the gold-based chip carrier, obtained with a digital camera. Adapted from ref. [31]. (b) Optical microscope image of the sample with several diodes of different diameters, d, on top of the chip carrier. Gold threads can be seen as black curved lines connecting chip contacts and sample gold pads. The inset shows the magnified image of one of the RTDs.

The final step in the microfabrication process is to attach the sample to a gold-based chip carrier using silver paint and *micro-welding*. Figure 3.5 (a) shows a picture of the sample sitcked on top of the chip carrier with silver paint, which is used to connect (thermal and electrically) the bottom of the sample to the chip. Needles in the picture correspond to the wedges of the bonding machine employed for micro-welding. In this process, the tips of a micrometric gold thread are pressed and rubbed by the wedges at ultrasonic frequencies on the sample gold pads and the chip-carrier contacts to connect them. Figure 3.5 (b) depicts an optical microscope image of the sample with the top-contact gold pads of the RTDs connected to the chip contacts by the gold threads (thin black lines). The inset also shows a magnified image of one of the RTDs with diameter d, after the micro-welding process.

3.3 Transport Characterization

The RTDs' $I(V)$ characteristics were obtained by transport measurements, conducted by placing the chip-carriers on contact terminal blocks connected to a SourceMeter (Keithley 2400), operated remotely through an in-house developed data acquisition software.

The DC bias voltages were applied in forward and reverse directions, by following complete cycles starting at zero bias voltage, sweeping up to a finite absolute voltage value, and then sweeping down the applied voltage to zero, with the aim to unveil bistabilities in the systems.

The measurements were performed in helium cryostats to explore the RTD electronic properties at temperatures between 4 and 300 K. RTD-A was characterized in the dark using a cryostat (Oxford) connected to a proportional-integral-derivative temperature controller and a resistive heater. The transport characteristics of RTDs C and D were assessed by employing an ultra-low vibration cryostat (Attocube AttoDRY1000), which incorporates a heater stage with a calibrated temperature sensor. This cryostat also allows for the transport characterization under illumination conditions via a top-fused silica window, and under applied magnetic fields up to 9 T in Faraday configuration (magnetic field parallel to light propagation), thanks to its integrated superconducting magnets. RTD-B was characterized at room temperature, making the use of cryostats unnecessary.

3.4 Optical Characterization

The fundamental optical properties of GaInAsSb lattice-matched to GaSb in RTDs A and B were investigated via PL measurements at room temperature, using *Fourier-transform infrared* spectroscopy. This technique enables the acquisition of a wide emission spectral range at infrared (IR) wavelengths [32, 33]. The spectrometer receives the emitted signal from the sample after radiation with a beam composed of different frequencies of light and detects which of those frequencies are absorbed by the sample, using *interferometry* techniques [33]. Subsequently, the associated software applies a Fourier transform to the interferogram to obtain the intensity of the emission, as a function of the photon energy.

Similarly, the optical properties of RTDs C and D were explored via luminescence spectroscopies utilizing a *confocal microscope* associated with an ultra-low vibration He cryostat (Attocube AttoDRY1000). Compared to conventional microscopy, the confocal technique increases the optical resolution of the detected luminescence spectra by rejecting out-of-focus light [34, 35]. It is realized by external optomechanical components positioned outside the cryostat, as sketched in figure 3.6.

In the case of PL excitation, a *continuous-wave* infrared laser beam produced by a diode laser and conducted by a single-mode optical fiber coupled to the excitation arm of the confocal microscope is collimated by an aspherical lens L1 in figure 3.6. The beam is then directed (white arrows) to a beam splitter (BS) that reflects part of the beam to the sample inside the cryostat. Therein, the sample is located in a xyz piezo nanopositioner with a resolution of up to 10 nm, and the laser beam is focused onto the sample by changing its position in z and by using an objective lens L2 of numerical aperture NA= 0.64. In this way,

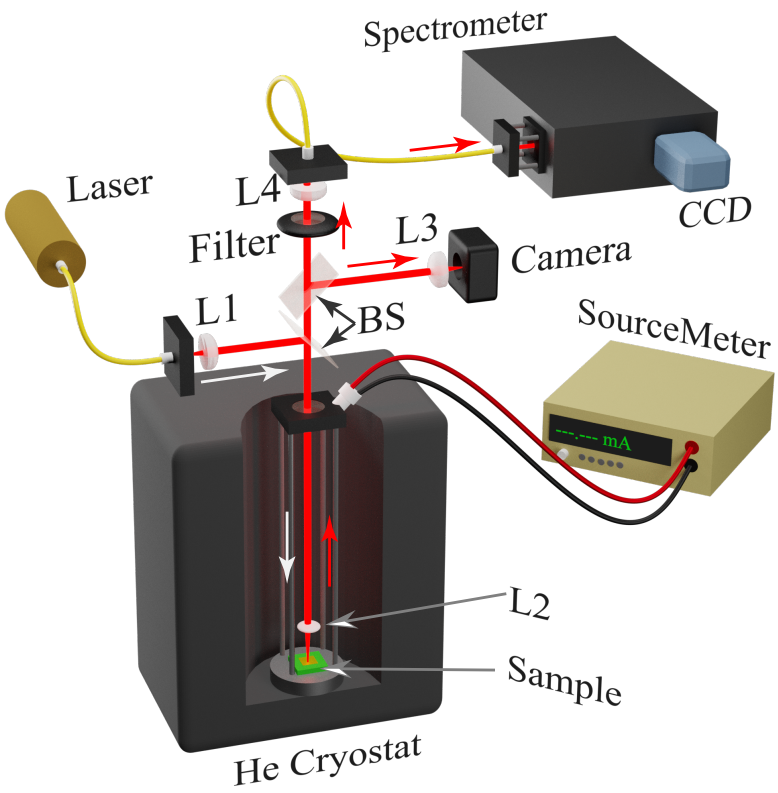

Figure 3.6 – Schematic representation of the experimental setup used for the RTDs electro-optical characterization. In the case of PL excitation, the laser beam is collimated by the lens L1 and redirected to the sample (white arrows) by the lowest beam splitter, BS. Before reaching the sample, the beam is focused on L2. The sample's emission (red arrows) travels outside the cryostat and a second BS reflects a fraction of the light to a camera (after focusing with L3), while the rest continues to the collector optical fiber (focused by L4). The collected signal is analyzed with a spectrometer and a Charge-Coupled Device (CCD).

the optical excitation is restricted to a small laser spot with a diameter of about 1 µm to increase the illumination efficiency.

The emitted light from the sample after excitation and the reflected laser beam travels back out of the cryostat (red arrows in figure 3.6), reaching a second BS where a fraction of the light is reflected onto the imaging arm of the microscope, and the rest is transmitted, filtered, and focused through the collector arm. In the imaging arm, the incoming light is focused by lens L3 onto an imaging camera used to align the excitation and collection signals as well as to find and position the laser spot on top of the sample by adjusting the samples position and the orientation of the optomechanical components, prior to measurement. In turn, a long pass filter in the collector arm blocks the reflected laser beam from the cryostat and lets the sample emission through lens L4, which is responsible for focusing the sample emission on the collector fiber. This fiber works as a blocking pinhole, eliminating any out-of-focus information in the collection path to increase the spectral resolution. The fiber also transports the in-focus sample emission toward a

spectrometer (Andor Shamrock) with a high-resolution Charge-Coupled Device, which detects the optical signal to produce emission spectra.

The EL or EL+PL emission can be also detected with the same setup by connecting a SourceMeter in the electrical terminals of the cryostat. The observed spectra can then be obtained as a function of the applied voltage. Magneto-PL measurements in the Faraday configuration are also available. Additionally, the intensity and the resolution of the spectral lines can be enhanced by lowering the temperature, which reduces the probability of scattering and non-radiative recombination processes, resulting in sharper and stronger spectral lines.

3.4.1 Time-Resolved PL Measurements

The RTD-C carrier dynamics was also explored through *time-resolved PL* (TRPL) measurements. In this technique, the sample is excited with a light pulse of a width preferably shorter than the effective lifetime, τ, of the optically active states in the sample [36]. The carriers are then excited for a short time (~ 100 ps), after which they start to decay due to different relaxation mechanisms, emitting light during the process, as discussed in § 1.5. The intensity of the randomly emitted light, which is proportional to the photoexcited carrier density at a given time, is also time-dependent, and gradually decreases [36].

Figure 3.7 (a) sketches the situation for a mono-exponential decay. Here, the effective lifetime of the sample can be extracted from the slope of a plot of the light intensity as a function of t (blue line) in a semi-logarithmic scale. Changes in the lifetimes can also be studied as a function of external parameters such as temperature, optical power, voltage, or magnetic fields. However, many luminescent decays are more complex, and special care must be taken in the case of multi-exponential decays because different multi-exponential functions can result in similar intensity decay curves, as exposed in Ref. [37]. Moreover, depending on the sample characteristics and the type of excitation, non-exponential decays can emerge. For these reasons, the decay spectra have to be analyzed in detail, taking into account the contribution of the most likely decay mechanisms in the sample that can reveal additional information about the system.

In turn, the fast and low-intensity emission of the samples produces additional detection challenges that can be handled by using amplifiers as photomultiplier tubes (PMTs) to increase the signal levels for timing [38], and a Time-Correlated Single Photon Counting (TCSPC) electronics [39], that measures the time between the excitation pulse and the observed photon with a detection rate of around 1 photon per 100 excitation pulses [36]. The measurement is used to construct a histogram of the photon distribution as a function of time, as represented in figure 3.7 (a), obtained after counting the emitted photons (red dots) in a time range Δt, which gives the decay curve observed during the experiments.

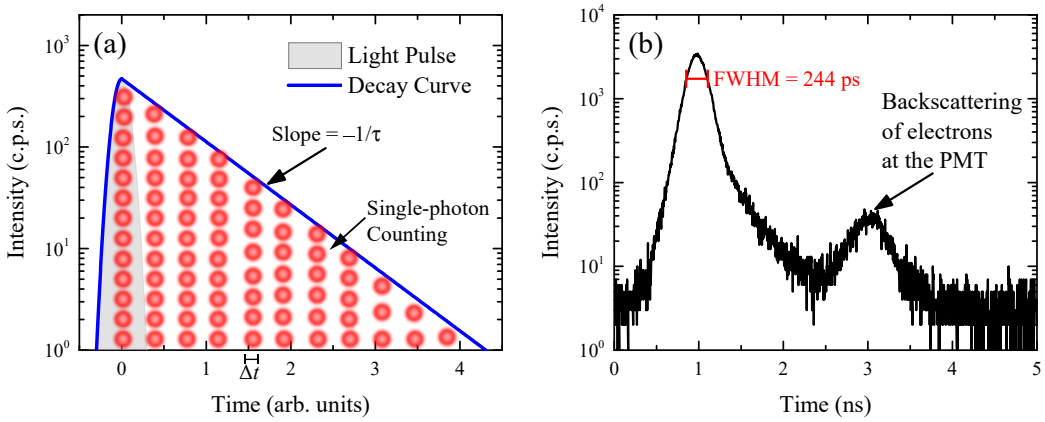

Figure 3.7 – (a) Representation of a mono-exponential decay curve (blue solid line) as a function of time, after excitation with a light pulse (gray shadow). The decay curve is the result of a single-photon counting histogram (red dots), which gives an intensity in counts per second (c.p.s.). The slope of the decay curve also gives the effective lifetime of the sample, τ. (b) Measured IRF in our experiments, showing its respective FWHM, for a pulsed laser of $\lambda = 1080$ nm and a frequency of $f = 80$ MHz.

Note that the use of these provisions must take into account the non-ideal instrument response function (IRF) that must be deconvoluted from the detected signal since it affects the observed effective lifetimes. The IRF refers to the response of the instrument to a zero-lifetime sample and depends on the shape of the excitation pulse and the way the signal is detected by the instruments [36]. Figure 3.7 (b) shows the measured IRF for our experiments as an example. The main peak determines the shortest time that can be measured by the instrument that, according to a manufacturer technical note [40], corresponds to the 1/10 of its full width at half maximum (FWHM). Under these conditions, the time-resolved analysis can be achieved via iterative reconvolution of the detected signal. An afterpulse at 3 ns can be produced due to elastic backscattering of electrons at the first dynode of the PMT [38]. However, the intensity of this peak only constitutes 0.01% of the counts in the peak channel and can, in general, be neglected.

In this way, the RTD-C characterization was conducted in the setup presented in the last section by coupling a 1080-nm diode laser in *pulsed mode* to the confocal microscope, with a pulse width of about 100 ps and a frequency of 80 MHz. In this type of measurement, the sample's emission is collected by a PMT (Hamamatsu) coupled to a spectrometer and a TCSPC electronics (PicoHarp 300) with a resolution of $\Delta t = 4$ ps and a maximum measurement rate of 10^7 counts/sec. This configuration offers an IRF FWHM$\approx$ 244 ps, as presented in figure 3.7 (b), which allows the detection of lifetimes of at least 24.4 ps.

References

[1] H. Kroemer, "The 6.1 Å family (InAs, GaSb, AlSb) and its heterostructures: a selective review," *Phys. E (Amsterdam, Neth.)*, vol. 20, no. 3, pp. 196–203, 2004. Proceedings of the 11th International Conference on Narrow Gap Semiconductors.

[2] K. Shim, "Composition dependence of band alignments in $Ga_xIn_{1-x}As_ySb_{1-y}$ heterojunctions lattice matched to GaSb and InAs," *J. Appl. Phys.*, vol. 114, no. 20, p. 203703, 2013.

[3] R. Beresford, L. F. Luo, and W. I. Wang, "Resonant tunneling of holes in AlSb/GaSb/AlSb double-barrier heterostructures," *Appl. Phys. Lett.*, vol. 55, no. 7, pp. 694–695, 1989.

[4] J. L. Jimenez, X. Li, and W. I. Wang, "Resonant tunneling in AlSb-GaSb-AlSb and AlSb-InGaSb-AlSb double barrier heterostructures," *Appl. Phys. Lett.*, vol. 64, no. 16, pp. 2127–2129, 1994.

[5] F. Hartmann, A. Pfenning, G. Knebl, R. Weih, A. Bader, M. Emmerling, M. Kamp, S. Höfling, and L. Worschech, "Antimonide-based resonant tunneling photodetectors for mid infrared wavelength light detection," in *Infrared Remote Sensing and Instrumentation XXV* (M. Strojnik and M. S. Kirk, eds.), vol. 10403, pp. 32 – 38, International Society for Optics and Photonics, SPIE, 2017.

[6] A. Pfenning, G. Knebl, F. Hartmann, R. Weih, A. Bader, M. Emmerling, M. Kamp, S. Höfling, and L. Worschech, "Room temperature operation of GaSb-based resonant tunneling diodes by prewell injection," *Appl. Phys. Lett.*, vol. 110, no. 3, p. 033507, 2017.

[7] A. Pfenning, G. Knebl, F. Hartmann, R. Weih, M. Meyer, A. Bader, M. Emmerling, L. Worschech, and S. Höfling, "GaSb/AlAsSb resonant tunneling diodes with GaAsSb emitter prewells," *Appl. Phys. Lett.*, vol. 111, no. 17, p. 171104, 2017.

[8] E. D. Guarin Castro, F. Rothmayr, S. Krüger, G. Knebl, A. Schade, J. Koeth, L. Worschech, V. Lopez-Richard, G. E. Marques, F. Hartmann, A. Pfenning, and S. Höfling, "Resonant tunneling of electrons in AlSb/GaInAsSb double barrier quantum wells," *AIP Adv.*, vol. 10, no. 5, p. 055024, 2020.

[9] C. R. H. White, M. S. Skolnick, L. Eaves, and M. L. Leadbeater, "Electroluminescence and impact ionization phenomena in a double-barrier resonant tunneling structure," *Appl. Phys. Lett.*, vol. 58, no. 11, pp. 1164–1166, 1991.

[10] C. Van Hoof, J. Genoe, R. Mertens, G. Borghs, and E. Goovaerts, "Electroluminescence from bipolar resonant tunneling diodes," *Appl. Phys. Lett.*, vol. 60, no. 1, pp. 77–79, 1992.

[11] H. Law, K. Nakano, and L. Tomasetta, "III-V alloy heterostructure high speed avalanche photodiodes," *IEEE J. Quantum Electron.*, vol. 15, no. 7, pp. 549–558, 1979.

[12] A. Pfenning, F. Hartmann, R. Weih, M. Emmerling, L. Worschech, and S. Höfling, "p-Type Doped AlAsSb/GaSb Resonant Tunneling Diode Photodetector for the Mid-Infrared Spectral Region," *Adv. Opt. Mater.*, vol. 6, no. 24, p. 1800972, 2018.

[13] F. Rothmayr, A. Pfenning, C. Kistner, J. Koeth, G. Knebl, A. Schade, S. Krueger, L. Worschech, F. Hartmann, and S. Höfling, "Mid-infrared GaSb-based resonant tunneling diode photodetectors for gas sensing applications," *Appl. Phys. Lett.*, vol. 112, no. 16, p. 161107, 2018.

[14] A. Bader, A. Pfenning, A. Schade, G. Knebl, R. Weih, Y. Rawal, L. Worschech, F. Hartmann, and S. Höfling, "Progress on mid-infrared optoelectronic devices: interband cascade lasers, interband cascade detectors, and resonant tunneling diodes," in *Infrared Remote Sensing and Instrumentation XXVIII* (M. Strojnik, ed.), vol. 11502, pp. 114 – 123, International Society for Optics and Photonics, SPIE, 2020.

[15] A. Cho and J. Arthur, "Molecular beam epitaxy," *Prog. Solid State Chem.*, vol. 10, pp. 157–191, 1975.

[16] R. J. Matyi, "Ch. 2. Growth of Quantum Confined Structures by Molecular Beam Epitaxy," in *Heterostructures and Quantum Devices* (N. G. Einspruch and W. R. Frensley, eds.), vol. 24 of *VLSI Electronics Microstructure Science*, pp. 25–61, Elsevier, 1994.

[17] J. R. Arthur, "Molecular beam epitaxy," *Surf. Sci.*, vol. 500, no. 1, pp. 189–217, 2002.

[18] F. Hartmann, F. Langer, D. Bisping, A. Musterer, S. Höfling, M. Kamp, A. Forchel, and L. Worschech, "GaAs/AlGaAs resonant tunneling diodes with a GaInNAs absorption layer for telecommunication light sensing," *Appl. Phys. Lett.*, vol. 100, no. 17, p. 172113, 2012.

[19] O. Madelung, *Semiconductors: Data Handbook*. Berlin: Springer, 3rd ed., 2004.

[20] M. Kondow, K. Uomi, A. Niwa, T. Kitatani, S. Watahiki, and Y. Yazawa, "GaInNAs: A Novel Material for Long-Wavelength-Range Laser Diodes with Excellent High-Temperature Performance," *Jpn. J. Appl. Phys.*, vol. 35, pp. 1273–1275, feb 1996.

[21] S. Birner, T. Zibold, T. Andlauer, T. Kubis, M. Sabathil, A. Trellakis, and P. Vogl, "nextnano: General purpose 3-D simulations," *IEEE Trans. Electron Devices*, vol. 54, no. 9, pp. 2137–2142, 2007.

[22] I. Gordon, L. Rothman, C. Hill, R. Kochanov, Y. Tan, P. Bernath, M. Birk, V. Boudon, A. Campargue, K. Chance, B. Drouin, J.-M. Flaud, R. Gamache, J. Hodges, D. Jacquemart, V. Perevalov, A. Perrin, K. Shine, M.-A. Smith, J. Tennyson, G. Toon, H. Tran, V. Tyuterev, A. Barbe, A. Császár, V. Devi, T. Furtenbacher, J. Harrison, J.-M. Hartmann, A. Jolly, T. Johnson, T. Karman, I. Kleiner, A. Kyuberis, J. Loos, O. Lyulin, S. Massie, S. Mikhailenko, N. Moazzen-Ahmadi, H. Müller, O. Naumenko, A. Nikitin, O. Polyansky, M. Rey, M. Rotger, S. Sharpe, K. Sung, E. Starikova, S. Tashkun, J. V. Auwera, G. Wagner, J. Wilzewski, P. Wcisło, S. Yu, and E. Zak, "The HITRAN2016 molecular spectroscopic database," *J. Quant. Spectrosc. Radiat. Transfer*, vol. 203, pp. 3–69, 2017. HITRAN2016 Special Issue.

[23] I. Vurgaftman, J. R. Meyer, and L. R. Ram-Mohan, "Band parameters for III–V compound semiconductors and their alloys," *J. Appl. Phys.*, vol. 89, no. 11, pp. 5815–5875, 2001.

[24] E. D. Guarin Castro, A. Pfenning, F. Hartmann, G. Knebl, M. D. Teodoro, G. E. Marques, S. Höfling, G. Bastard, and V. Lopez-Richard, "Optical Mapping of Non-equilibrium Charge Carriers," *J. Phys. Chem. C*, vol. 125, no. 27, p. 14741–14750, 2021.

[25] T. Kitatani, M. Kondow, S. Nakatsuka, Y. Yazawa, and M. Okai, "Room-temperature lasing operation of GaInNAs-GaAs single-quantum-well laser diodes," *IEEE J. Sel. Top. Quantum Electron.*, vol. 3, no. 2, pp. 206–209, 1997.

[26] E. D. Jones, N. A. Modine, A. A. Allerman, I. J. Fritz, S. R. Kurtz, A. F. Wright, S. T. Tozer, and X. Wei, "Optical properties of InGaAsN: a new 1-eV bandgap material system," in *Light-Emitting Diodes: Research, Manufacturing, and Applications III* (E. F. Schubert, I. T. Ferguson, and H. W. Yao, eds.), vol. 3621, pp. 52 – 63, International Society for Optics and Photonics, SPIE, 1999.

[27] H. Riechert, A. Ramakrishnan, and G. Steinle, "Development of InGaAsN-based 1.3 μm VCSELs," *Semicond. Sci. Technol.*, vol. 17, pp. 892–897, jul 2002.

[28] Q. Han, X. H. Yang, Z. C. Niu, H. Q. Ni, Y. Q. Xu, S. Y. Zhang, Y. Du, L. H. Peng, H. Zhao, C. Z. Tong, R. H. Wu, and Q. M. Wang, "1.55 μm GaInNAs resonant-cavity-enhanced photodetector grown on GaAs," *Appl. Phys. Lett.*, vol. 87, no. 11, p. 111105, 2005.

[29] W. K. Loke, S. F. Yoon, K. H. Tan, S. Wicaksono, and W. J. Fan, "Improvement of GaInNAs p-i-n photodetector responsivity by antimony incorporation," *J. Appl. Phys.*, vol. 101, no. 3, p. 033122, 2007.

[30] F. Hartmann, A. Pfenning, M. Rebello Sousa Dias, F. Langer, S. Höfling, M. Kamp, L. Worschech, L. K. Castelano, G. E. Marques, and V. Lopez-Richard, "Temperature tuning from direct to inverted bistable electroluminescence in resonant tunneling diodes," *J. Appl. Phys.*, vol. 122, no. 15, p. 154502, 2017.

[31] E. R. Cardozo de Oliveira, *Contraste entre propriedades optoeletrônicas em estruturas de tunelamento ressonante n-i-n baseadas em GaAs*. PhD thesis, Universidade Federal de São Carlos, SSão Carlos, SP, 2019.

[32] S. Perkowitz, *Optical characterization of semiconductors: Infrared, Raman, and Photoluminescence Spectroscopy*. London: Academic Press, 1st ed., 1993.

[33] J. A. D. H. Peter Griffiths, *Fourier Transform Infrared Spectrometry*. Chemical Analysis: A Series of Monographs on Analytical Chemistry and Its Applications, Wiley-Interscience, 2nd ed., 2007.

[34] T. Wilson, "Ch. 7. Confocal Microscopy," in *Microanalysis of Solids* (B. Yacobi, D. Holt, and K. L.L., eds.), Springer Science + Business Media, (New York), pp. 219–232, Springer, 1994.

[35] P. Conn, ed., *Techniques in Confocal Microscopy: Reliable Lab Solutions*. Oxford: Academic Press - Elsevier, 1st ed., 2010.

[36] J. R. Lakowicz, *Principles of Fluorescence Spectroscopy*. Boston: Springer, 3rd ed., 2006.

[37] A. Grinvald and I. Z. Steinberg, "On the analysis of fluorescence decay kinetics by the method of least-squares," *Anal. Biochem.*, vol. 59, no. 2, pp. 583–598, 1974.

[38] Hamamatsu, *Photomultiplier Tubes: Basics and Applications*. Hamamatsu Photonics K. K., Hamamatsu, 3rd ed., 2007.

[39] D. O'Connor, *Time-correlated Single Photon Counting*. London: Academic Press - Elsevier Science, 1st ed., 1984.

[40] M. Wahl, *Time-Correlated Single Photon Counting - Technical Note*. PicoQuant GmbH, Berlin, Germany, 2014.

Chapter 4

Combining Optical and Transport Properties of RTDs for Optical Sensing

The transport and optical properties, as well as the intertwining between them in Sb-based RTDs, are presented in the following sections. The experimental characterization is supported with simulations of the transport and optoelectronic response based on the theoretical models for the charge buildup and quantum tunneling presented and discussed in Chapter 2. Our results suggest that, although the samples are n-type RTDs, the role of the minority carriers (holes) in the carrier dynamics is crucial to understand the quantum processes and the optical sensing abilities of these devices.

The correlation between the charge carrier dynamics and the optical response exposed here and the way it is affected by external factors such as temperature, incident light, and applied voltages offers fundamental insights into the physics of carriers excitation, transport, and accumulation in semiconductor heterostructures in general. This knowledge can be advantageous to improve nanodevices performance and their functionalities, with potential applications as photosensors within the MIR spectral region (25 meV - 0.4 eV).

4.1 Basic Transport and Optical Properties of Sb-Based RTDs

Lattice-matched $(GaSb)_x(InAs_{0.91}Sb_{0.09})_{1-x}$ heterojunctions, as those incorporated in RTDs A and B (see figures 3.2 (a) and (b)), are versatile semiconductor structures that allow for a wide modulation of the RTDs optical and electronic properties, thanks to the range of band offsets that can be achieved just by changing the alloy composition x [1]. In this regard, the CB barrier heights ($2\ \text{eV} \geq U_{CB} \geq 1\ \text{eV}$), bandgap energy ($0.2\ \text{eV} \leq E_g \leq 0.7\ \text{eV}$), and Γ-L energy separation ($0.7\ \text{eV} \geq \Delta E_{\Gamma L} \geq 25\ \text{meV}$), can be tuned across a broad interval.

In our case, a composition with $x = 0.64$ was chosen to form $Ga_{0.64}In_{0.36}As_{0.33}Sb_{0.67}$ absorption layers in RTDs A and B, as we reported in refs. [2]. The normalized room-

temperature PL spectra of this quaternary layer from RTD-A is presented in figure 4.1 (a), on a semilogarithmic scale. A similar response was obtained for RTD-B. Using a Boltzmann's distribution function, $Q \propto \exp\left(\hbar\omega / k_B T_{eff}^{e\text{-}h}\right)$, the mono-exponential decay of the high-energy tail of the spectra was fitted (blue dashed line) as described in Chapter 1. This approach is also tackled in Chapter 5. In the present case, an electron-hole effective temperature of $T_{eff}^{e\text{-}h} = 290$ K $\left(k_B T_{eff}^{e\text{-}h} = 25 \text{ meV}\right)$ was extracted, matching with the nominal values and indicating a carrier thermalization with the lattice at room temperature.

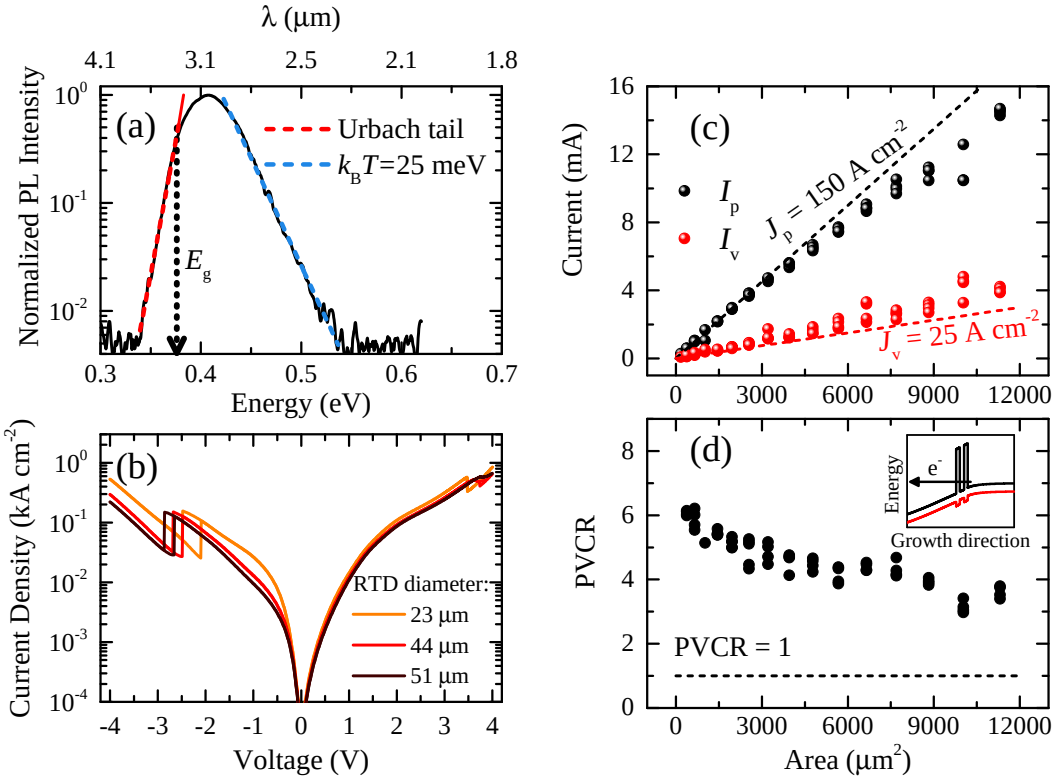

Figure 4.1 – Fundamental optical and transport properties of RTD-A. (a) Normalized PL spectra of the $Ga_{0.64}In_{0.36}As_{0.33}Sb_{0.67}$ layers lattice matched to GaSb. (b) Current density as a function of the applied voltage for different mesa diameters. (c) Peak current, I_p (black spheres), valley current, I_v (red spheres), and (d) PVCR (black dots) as a function of the RTDs' cross-sectional area for reverse bias voltages. An schematic representation of the band profile under a reverse bias voltage is illustrated in the inset of panel (d). All the measurements were performed at $T = 295$ K. Adapted from ref. [2].

In turn, the Urbach's rule [3] was employed to characterize the low-energy side of the spectra, since this rule describes the absorption or emission spectrum at energies below the bandgap of a semiconductor ($\hbar\omega < E_g$) [4–7]. At this regime, the emission of light is attributed to the effect of phonons, impurities, and defects, and it can be described by an exponential function, $P \propto \exp(\hbar\omega / E_U)$ [5, 7, 8]. Here, $E_U \propto k_B T$ is the Urbach parameter that measures the thermal and structural disorder within a crystal [5, 8–10]. The higher the lattice disorder, the higher E_U. Thus, an Urbach parameter of $E_U = 10$ meV was obtained, in good agreement with the parameters reported for p-type GaInAsSb grown via

MBE [11] and GaInAsSb grown by liquid phase epitaxy [12]. This value is even close to that reported for n-type GaAs grown by MBE at room temperature [8]. It also demonstrates an excellent sample quality, since undoped GaAs samples present an Urbach parameter of $E_U \approx 7$ meV [8, 13, 14], whereas amorphous semiconductors with a high degree of disorder, exhibit an E_U >50 meV [9] or even on the order of 10^2 meV [15, 16]. Bearing in mind that Urbach's rule does not allow the description of the spectra for $\hbar\omega > E_g$, then the bandgap energy of the quaternary layer can be approximately determined as the point at which the emission line starts to deviate from the exponential Urbach fit function [11]. This point coincides with the spectral position at which the emission intensity is ~ 0.6 of its maximum, according to ref. [7]. This point is indicated by the dotted black arrow in figure 4.1 (a). The obtained bandgap energy was $E_g = 376$ meV, corresponding to a cut-off wavelength of $\lambda \approx 3.3$ µm, in agreement with Shim's model [1].

The electronic transport properties of RTD-A were investigated in the dark, at room temperature, by measuring the current density-voltage, $J(V)$, characteristics for different mesa diameters, ranging from $d = 16$ up to 121 µm. Figure 4.1 (b) exemplifies the $J(V)$ characteristics for three different diameters. The symmetric design of RTD-A, as presented in the band profile in figure 3.2 (a), induces an electrical response with NDR regions for both forward and reverse bias voltages with similar conditions for resonances.

The reproducibility of the diode's response was studied by analyzing the peak (black spheres) and valley (red spheres) currents, as well as the PVCR (black dots), obtained at reverse bias conditions, as a function of the cross-sectional area of the mesas, as presented in figures 4.1 (c) and (d), respectively. The inset in panel (d) shows a representation of the band profile at this voltage regime, with a black arrow indicating tunneling of electrons. The best response (best resolution of the resonance), corresponding to the largest value of the PVCR= 6.0, has been attained for the RTD with $d = 23$ µm. It represents an improvement regarding the PVCRs reported for other GaSb-based RTDs [11, 17, 18], but it is still lower than the PVCR= 11.0 reported for AlSb/InAs RTDs [19]. By using as reference the values of the peak and valley current densities for this diode, the lines corresponding to $J_p = 150$ A cm^{-2}, and $J_v = 25$ A cm^{-2} are represented in panel (c) by the black and red dashed lines, respectively, to indicate the ideal response. Note that diodes with larger diameters deviate from these ideal values, presenting lower (higher) peak (valley) currents, and thereby, lower PVCRs≈ 3.5. We ascribed this response to an increasingly inhomogeneous current spreading from the top ring contact. On the other hand, peak and valley current densities of $J_p \approx 575$ A cm^{-2} and $J_v \approx 334$ A cm^{-2}, respectively, were measured for the same RTD at forward bias voltages, producing a PVCR≈ 1.7. For RTDs with higher diameters, the NDR region vanishes at this voltage regime.

The resonant tunneling properties of the RTD with $d = 23$ µm were also character-

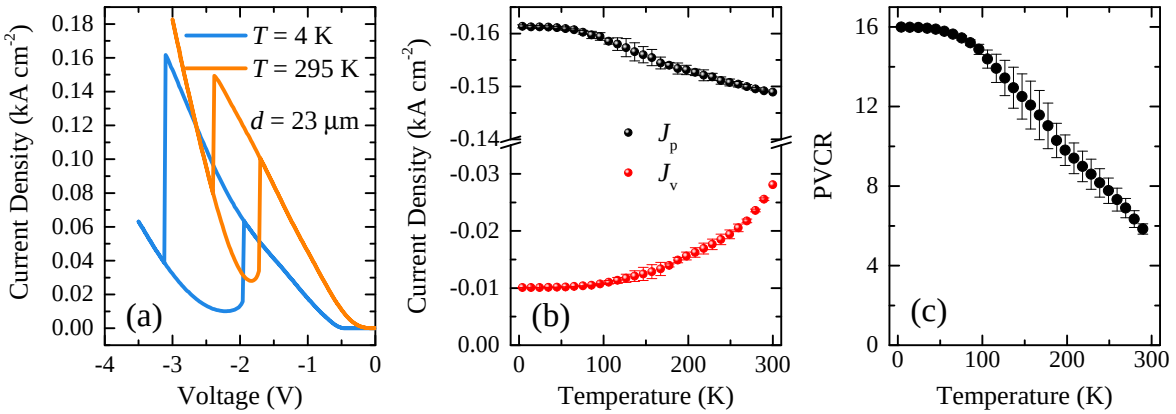

Figure 4.2 – Temperature dependence of resonant tunneling in RTD-A, for a diode diameter of $d = 23$ µm. (a) $J(V)$ characteristic at room temperature (orange line) and cryogenics temperature (blue line). (b) Peak (J_p, black spheres), valley (J_v, red spheres) current densities, and (c) PVCR (black dots) as a function of temperature. Adapted from ref. [2].

ized by varying the temperature. Figure 4.2 (a) displays the $J(V)$ characteristics at room ($T = 295$ K) and cryogenic temperature ($T = 4$ K). Since the temperature sensor and the RTD were located at slightly different positions within the cryostat, the $J(V)$ characteristics were measured for both the cooling-down and heating-up sweeps to account for temperature deviations between the sensor and the sample. As expected, J_p increases, whereas J_v decreases by lowering the temperature. This is corroborated by the temperature dependence of the averaged J_p (black spheres) and J_v (red spheres) in figure 4.2 (b). The enhancement of J_p at low temperatures is a consequence of the reduced inelastic scattering [20, 21], which could be dominated by the interaction with acoustic phonons in this regime [22, 23]. Conversely, the decrease of J_v, as the temperature is lowered, is attributed to the reduction of thermally activated tunneling [20, 24, 25]. It results in the growth of the PVCR when the temperature decreases, as shown in figure 4.2 (c), where a maximum of PVCR= 16.0 is observed at cryogenic temperatures. Note that for temperatures below 50 K, the peak and valley current densities and the PVCR stabilizes at $J_p = 161$ A cm^{-2}, $J_v = 10$ A cm^{-2}, and PVCR=16.0, respectively, suggesting an activation temperature for scattering mechanisms via phonon interaction, as well as for thermally activated transport channels.

The above-presented results demonstrate resonant tunneling of electrons for MIR optically active AlSb/GaInAsSb double-barrier quantum well RTDs within a wide temperature range, from $T = 4$ K up to room temperature. This kind of RTDs manifests a good reproducibility and peak-to-valley current ratios of up to PVCR=16.0 at cryogenic temperatures and a PVCR=6.0 at room temperature. Thus, AlSb/GaInAsSb RTDs can open opportunities for applications as MIR optoelectronic devices, complemented by great design flexibility.

4.2 Sb-Based RTDs as MIR Photosensors

The interest in MIR high-performance optoelectronic devices for optical molecule and gas spectroscopy applications has increased in the last few years [26–29] since several strong absorption lines of gases such as CO_2 (618 meV), CH_4 (535 meV), CO (532 meV), and H_2O (462 meV) are found in this optical region [30]. Thus, RTD-B has been recently proposed as a photosensor with excellent reproducibility for room temperature operation [18]. Its simple architecture, described in figure 3.2 (b), combines the resonant tunneling properties of a $GaAs_{0.15}Sb_{0.85}$/AlSb DBS [17] with an optically active $Ga_{0.64}In_{0.36}As_{0.33}Sb_{0.67}$ absorption layer at the collector side. This design allows a thorough tuning of the sensor selectivity at different operation regimes for optical sensing.

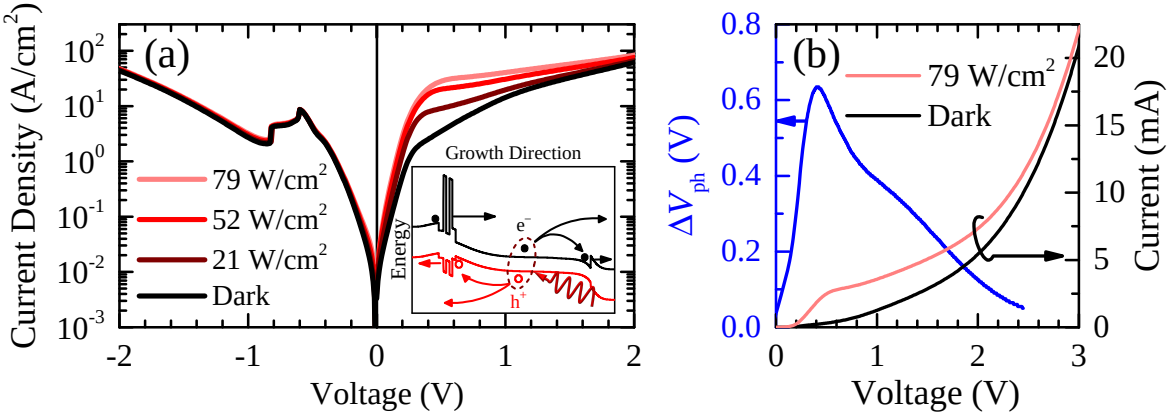

Figure 4.3 – (a) Room-temperature $J(V)$ characteristics of RTD-B in the dark (black line) and under illumination for different optical power densities (red gradient), and an incident laser energy of $\hbar\omega = 620$ meV. The inset shows a schematic representation of the band profile under a forward bias voltage and illumination, and the carrier dynamics, according to figure 2.10. (b) At forward bias voltages, a photoinduced voltage shift (ΔV_{ph}, blue line) is observed, as exemplified for the $I(V)$ characteristics in the dark and under illumination with the highest power.

The room temperature photoresponse of RTD-B with a diameter of $d = 106\,\mu$m is displayed in figure 4.3 (a), where the $J(V)$ characteristics are shown in the dark (black line) and under illumination for various optical power densities (red gradient lines), using an excitation laser with an energy of $\hbar\omega = 620$ meV. An asymmetric response that depends on the incident optical power is clearly seen. At reverse bias voltages, we observe an NDR region with peak and valley current densities of $J_p = 8.71$ and $J_v = 2.07$ A cm^{-2}, respectively, but no appreciable photoresponse is detected at this voltage regime. At forward bias voltages, the enhanced current density produces a breakdown of the RTD caused by Joule heating, hampering the observation of an NDR region, which is only observable for voltages above 3 V and diode diameters below 15 µm [18]. Nevertheless, a photoresponse is detected at forward voltages between 0 and 3 V, where a photoinduced voltage shift, ΔV_{ph}, of the current density under illumination is observed. The voltage shift of the $I(V)$ characteristic

obtained with the higher excitation optical power density with respect to the $I(V)$ response in the dark has been displayed in figure 4.3 (b) as a blue line. A maximum $\Delta V_{ph} = 0.63$ V is observed at $V = 0.41$ V.

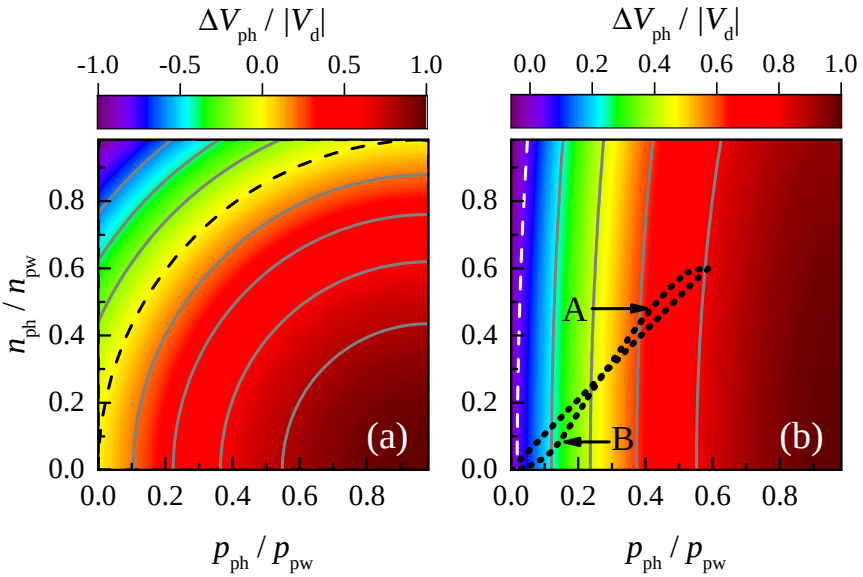

Figure 4.4 – Mapping of the relative voltage shift, $\Delta V_{ph}/|V_{D1}|$, as a function of the relative trapped carrier densities n_{ph}/n and p_{ph}/n for: (a) $N^+_{D1} = N^+_{D2}$ and (b) $N^+_{D1} < N^+_{D2}$. Dashed contour lines represent $\Delta V_{ph} = 0$. The black dotted line in (b) represents the carrier densities evolution for the conditions discussed in figure 4.5 (c) and (d).

The photosensor capabilities of RTD-B can be understood by taking into account the proposed charge buildup model under illumination, presented in § 2.4. In accordance with it, we can consider a 2D electron density accumulated in the prewell, n, at the left from the DBS, as sketched in the inset of figure 4.3 (a), and according with figures 2.9 (a) and (b). At the depletion regions in the quaternary layer and the GaSb optical window, 3D charge densities, N^+_{D1} and N^+_{D2}, are produced by electric field ionization, along the lengths l_1 and l_2, respectively. Under illumination, the photogenerated electron-hole pairs in the absorption layer of length l_{ab}, can drift in opposite directions, inducing a 2D accumulation of electrons, n_{ph}, and holes, p_{ph}, at the GaInAsSb/GaSb interface and close to the DBS, respectively, where both type of carriers can eventually escape, as indicated in the inset of panel (a), in line with figure 2.10. The relative contribution of the photogenerated trapped carriers to ΔV_{ph} is depicted in figures 4.4 (a) and (b), where the maps of $\Delta V_{ph}/|V_{D1}|$ as a function of the relative trapped carrier densities n_{ph}/n and p_{ph}/n are depicted for $N^+_{D1} = N^+_{D2}$ and $N^+_{D1} < N^+_{D2}$, respectively. These maps were generated by employing eq. 2.22. Here, in compliance with the RTD-B structural parameters, the term dependent of l_0 was neglected, because of its insignificant contribution to ΔV_{ph}. Based on this approximation, it is worth noting that a positive shift, corresponding to lower absolute values of V, is a consequence of the relative increase of trapped holes. This is reinforced for $N^+_{D1} < N^+_{D2}$

because the effect of photogenerated electrons is weighted as $n_{\mathrm{ph}}^2 N_{D1}^+ / N_{D2}^+$ in eq. 2.22. The contours corresponding to $\Delta V_{\mathrm{ph}} = 0$ have also been added as reference.

Following the proposed model, the voltage dependence of the photoinduced voltage shift can be emulated by considering the relation between trapped carrier densities and the applied voltage, as presented in eqs. 2.27. In accordance with them, the absorption coefficient, defined in eq. 2.28, was simulated taking the bandgap energies of the quaternary absorption layer as $E_{\mathrm{g},1} = 376$ meV, and for the GaSb optical window as $E_{\mathrm{g},2} = 727$ meV. Furthermore, we assume $\gamma = 20$ and $\sigma_\alpha = 20$ meV. Conversely, the hole and electron lifetimes, $\tau_{\mathrm{h}}(V)$ and $\tau_{\mathrm{e}}(V)$, were determined in terms of their transmission probabilities. In the former case, the transport of holes through the DBS for forward bias voltages is essential to obtain $\tau_{\mathrm{h}}(V)$. For this reason, we calculated the contribution of resonant transport channels for holes as a function of the voltage drop at the DBS, V_{DBS}, by using the transfer matrix approximation (see § 2.1).

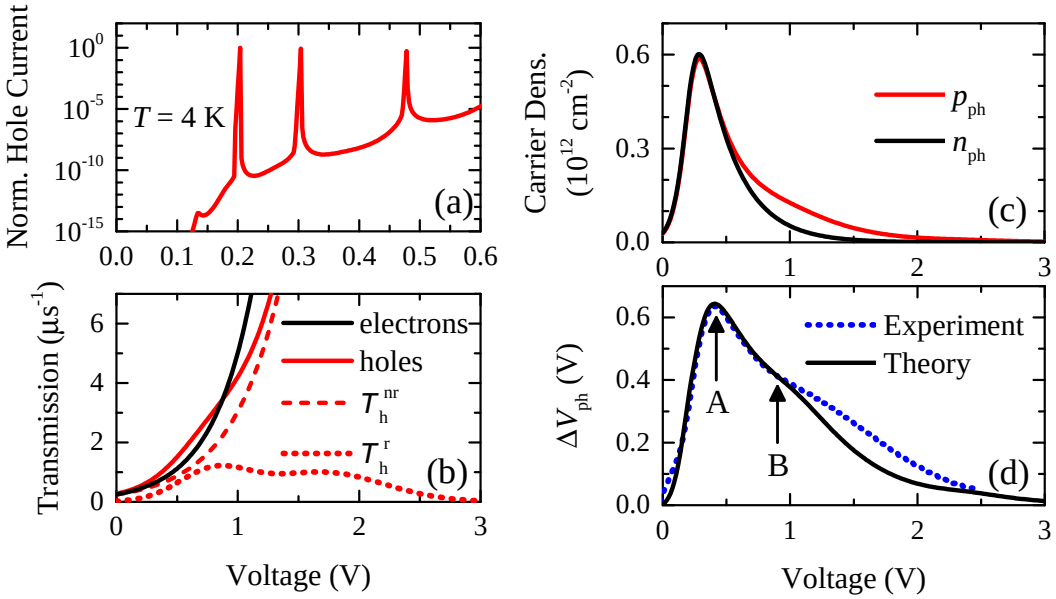

Figure 4.5 – (a) Calculated hole current as a function of the bias voltage at the DBS, V_{DBS}. Emulated applied-voltage dependence of: (b) electron ($\mathcal{T}_{\mathrm{e}}$, black line) and hole ($\mathcal{T}_{\mathrm{h}}$, red line) total transmission rates, as well as non-resonant ($\mathcal{T}_{\mathrm{h}}^{\mathrm{nr}}$, dashed line) and resonant ($\mathcal{T}_{\mathrm{h}}^{\mathrm{r}}$, dotted line) hole transmissions; (c) trapped electron (black line) and hole (red line) densities; and (d) photoinduced voltage shift (black solid line), as compared with the observed ΔV_{ph} (blue dotted line), as shown in figure 4.3 (b). Points A and B indicate the positions of the ΔV_{ph} maximum and first hole transmission peak at $V = 0.44$ and 0.92 V, respectively.

Figure 4.5 (a) shows the results of the calculation for $T = 4$ K. The low temperature used in the simulations allows determining the positions of the first two hole resonant channels at $V_{\mathrm{DBS}}^{\mathrm{res1}} = 0.20$ V and $V_{\mathrm{DBS}}^{\mathrm{res2}} = 0.30$ V. Thus, according to eq. 2.21 and assuming effective values for $l_{\mathrm{DBS}} = 21.5$ nm, $l_0 = 2.5$ nm, $\epsilon = 15\epsilon_0$, and $N_{D1}^+ = 6 \times 10^{16}$ cm^{-3}, these voltages correspond to total applied voltages of $V_1 = 0.80$ V and $V_2 = 1.65$ V. The values of these and other parameters presented here, were employed in the calculations in order to obtain

simulations closer to the observed responses, and they do not correspond to experimental nominal values. Using these results, the resonant hole transmission rate through the DBS can be simulated as

$$\mathcal{T}_{\mathrm{h}}^{\mathrm{r}}(V) = \mathrm{T}_{\mathrm{h}}^{\mathrm{r}} \sum_{j=1}^{2} \exp\left[-\frac{(V-V_j)^2}{2\sigma_j^2}\right], \tag{4.1}$$

while the non-resonant contribution can be described as

$$\mathcal{T}_{\mathrm{h}}^{\mathrm{nr}}(V) = \mathrm{T}_{\mathrm{h}}^{\mathrm{nr}} \exp\left(\beta_{\mathrm{h}} V\right), \tag{4.2}$$

so that the total hole transmission is $\mathcal{T}_{\mathrm{h}}(V) = \mathcal{T}_{\mathrm{h}}^{\mathrm{r}}(V) + \mathcal{T}_{\mathrm{h}}^{\mathrm{nr}}(V)$. In a similar way, trapped electrons at the GaInAsSb/GaSb heterojunction can escape via a non-resonant channel

$$\mathcal{T}_{\mathrm{e}}(V) = \mathrm{T}_{\mathrm{e}}^{\mathrm{nr}} \exp\left(\beta_{\mathrm{e}} V\right). \tag{4.3}$$

In the above expressions and for the case of RTD-B, we considered the transmission intensities as $\mathrm{T}_{\mathrm{h}}^{\mathrm{r}} = 1\ \mu\mathrm{s}^{-1}$ and $\mathrm{T}_{\mathrm{h}}^{\mathrm{nr}} = \mathrm{T}_{\mathrm{e}}^{\mathrm{nr}} = 0.25\ \mu\mathrm{s}^{-1}$, in accordance with the lifetimes reported in refs. [31, 32]. The transmission peak broadening for holes was assumed as $\sigma_1 = 0.29$ V and $\sigma_2 = 0.50$ V, and the escape rates of holes and electrons as $\beta_{\mathrm{h}} = 2.5\ \mathrm{V}^{-1}$ and $\beta_{\mathrm{e}} = 3.7\ \mathrm{V}^{-1}$, respectively. All these transmission channels are plotted in figure 4.5 (b). The total transmission rates for electrons (black) and holes (red) are displayed as solid lines. The resonant and non-resonant contributions for hole transmission rates are presented as dotted and dashed lines, respectively.

The trapping quantum efficiency was determined according to eq. 2.30 where, assuming carrier thermalization at room temperature ($T_{\mathrm{e}} = T_{\mathrm{h}} = 300$ K) and a local leverage factor of $\xi \approx 1/2$, the steepness of the function was estimated as $\sigma_\eta^i = 0.05$ V, with i =e,h. However, one must bear in mind that non-thermalization among electrons and holes, which depends on certain excitation conditions, makes the temperature of the transported carriers rise above the lattice temperature, as discussed in § 1.4 and § 5.3, as well as in ref. [33]. Consequently, the lowest possible effective temperature of hot carriers is expected in the absorber, close to the DBS. Additionally, to determine the threshold voltage, V_{th}^i, as defined by eq. 2.31, we assumed $\eta_0^i \tau_{\mathrm{tr},0}^i / \tau_{\mathrm{los},0}^i \approx 1$ since the screening of built-in electric fields, represented by the term $\Delta E_\eta/(\xi e)$, have been confirmed as the leading effect in the increment of V_{th}^i. Thus, we assumed $\Delta E_\eta/(\xi e) = 0.70$ V. For the simulations we also consider $N_{D2}^+ = 1 \times 10^{18}\ \mathrm{cm}^{-3}$, and for the case of high (low) optical power densities, $f\alpha_0\eta_0^i$ was estimated to be $\sim 10^{-5}$ (10^{-8}), while $\mathrm{p_{exc}}N$ was $\sim 10^{-2}$ (10^{-1}) Ω^{-1}.

The calculated trapped hole (red line) and electron (black line) densities as a function of the applied voltage are displayed in figure 4.5 (c). Both carrier densities increase at low voltages due to the onset of the photoconductivity at the absorption layer, which is

a combination of the absorption coefficient and the quantum efficiency. After reaching a maximum, the photoconductivity competes with the escape channels of the trapped charges, activated at higher voltages. It induces the reduction of the carrier densities, which, in this case, is more pronounced for electrons than for holes. The path followed by the relative values of the trapped charges as the applied voltage grows has been plotted in figure 4.4 (b) (dotted black line) over the contour color map of the relative voltage shift. Then, using these results, the corresponding voltage shift was calculated (black solid line) as a function of the applied voltage, as displayed in figure 4.5 (d), showing a good agreement with the experimental results (blue dotted line). Besides the maximum value at $V = 0.44$ V (point A), ΔV_{ph} exhibits a dip at $V \approx 0.90$ V (point B), ascribed to the position of the first resonant channel for holes. The same points are indicated in the path presented in figure 4.4 (b).

4.3 RTD Optical Read-Out and Photosensitivity

The interplay between buildup and escape of trapped carriers has also allowed defining low and high optical power regimes for RTD-B, where its sensor capabilities change, depending on the applied voltage, V, and the energy of the incident light, $\hbar\omega$. Figures 4.6 (a) and (b) show a mapping of the calculated ΔV_{ph} as a function of V and $\hbar\omega$, for high and low optical power densities, respectively. In both cases, a photoresponse is observed for excitation energies above 300 meV. At high optical powers, the photoinduced voltage shift is prominent at low applied voltages around $V = 0.50$ V, whereas, at low optical powers, the ΔV_{ph} maximum not only decreases but also shifts to higher voltages, close to $V = 1.00$ V, as indicated by white vertical dashed lines.

All the above-mentioned results are corroborated by experimental observations. For $\hbar\omega = 619$ meV and high optical powers, as illustrated by the upper horizontal dot-dashed line in (a), the calculated ΔV_{ph} presents a maximum at $V = 0.44$ V (peak A) and a shoulder at $V \approx 1.00$ V (peak B), as indicated in panel (c). Similarly, the experimental photocurrent in panel (f) exhibits these peaks at $V = 0.52$ and 1.30 V, respectively, for an optical power density of 67 W/cm^2. The photocurrent was normalized to allow for a comparison with the simulations. In the case of incident photon energies below the quaternary bandgap ($E_{\text{g},1} = 376$ meV), peak B is more pronounced than peak A, as exemplified for the calculated ΔV_{ph} and the measured photocurrent with $\hbar\omega = 365$ meV in panels (d) and (g), respectively. The peaks in ΔV_{ph} are a consequence of the photoconductivity onset at the absorption layer, which depends on the absorption coefficient and the steepness of the quantum efficiency discussed above. This dependence produces a fast increase in the voltage shift for low voltages. On the contrary, the slow decrease of the voltage shift for higher voltages is modulated by the escape rates of the holes through the DBS. Since the Stark effect reduces

the effective energy gap by increasing the applied voltage (see eq. 2.28), the absorption of photons with energies below the bandgap can be triggered at higher voltages, as sketched by the curved dotted line in (a).

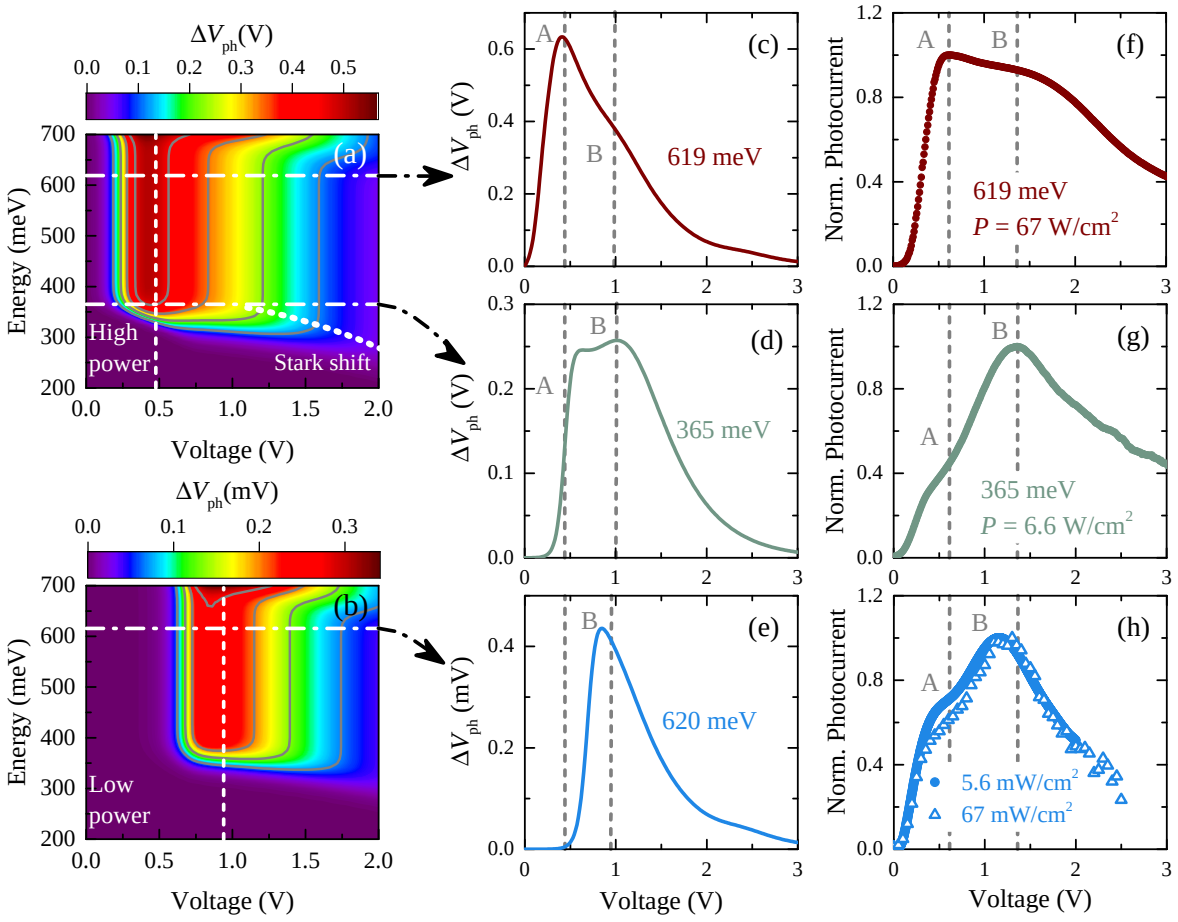

Figure 4.6 – Calculated ΔV_{ph} as a function of the applied voltage and incident photon energy for: (a) high- and (b)low-optical power regimes. Horizontal dot-dashed lines indicate the photon energies at which simulations and measurements were performed. Vertical dashed lines show the position of the maximum photoresponse at each regime. Simulated voltage shift for: (c) $\hbar\omega = 619$ meV and (d) $\hbar\omega = 365$ meV in the high-power regime, and (e) $\hbar\omega = 619$ meV in the low-power regime. Normalized photocurrent measured for: (f) $\hbar\omega = 619$ meV and (g) $\hbar\omega = 365$ meV in the high-power regime, and (h) $\hbar\omega = 619$ meV in the low-power regime, for different optical power densities.

On the other hand, at the low-power regime and for $\hbar\omega = 619$ meV (upper horizontal dot-dashed line in (b)), the simulation shows peak B at the same voltage position as for the high-power regime, with a noticeable reduction of peak A intensity, as displayed in figure 4.6 (e). The observed photocurrent obtained with power densities of 5.6×10^{-3} and 67×10^{-3} mW/cm^2, as depicted in panel (h) with blue dots and triangles, respectively, unveils the presence of peak A, but with an intensity lower than peak B. This photoresponse is the result of the reduced screening of the threshold voltage, $V_{th}^{i}(N)$, as the density of photogenerated excitons, N, decreases, which provokes an increment in the intrinsic barrier ($\Delta E_\eta \rightarrow \Delta E_0$). It modulates the quantum efficiency, increasing $V_{th}^{i}(N)$, according

to eqs. 2.30 and 2.31, and demands higher applied voltages to reach a maximum photoresponse.

After verifying the good agreement between the theory and experiments, the proposed model was implemented to characterize the sensor response in terms of its relative photosensitivity to changes in the incoming photon flux, F, and excitation energy light, $\hbar\omega$. In this sense, the sensitivity was defined as

$$S(x) = \frac{1}{V}\frac{\partial \Delta V_{\text{ph}}}{\partial x}, \tag{4.4}$$

with $x = \hbar\omega, \text{F}$. Figures 4.7 (a) and (b) present the simulated $S(\hbar\omega)$ at high- and low-optical power regimes, respectively, as functions of the applied voltage and photon energy. The device is highly sensitive to incoming photons with energies between 300 and 400 meV, as well as for energies between 600 and 700 meV, at these regimes. It depends on the position of the onset of the absorption, determined by the energy bandgaps of the absorber and the optical window, the applied voltage, and the Stark shift, as indicated by $E_{\text{g},j} - \gamma V^2$ with $j = 1, 2$, in eq. 2.28. The reduction of the sensitivity and its shift to higher voltages at the low-power regime (panel (b)) is due to the reduction in the quantum efficiency and the screening of the threshold voltage as the incident optical power decreases.

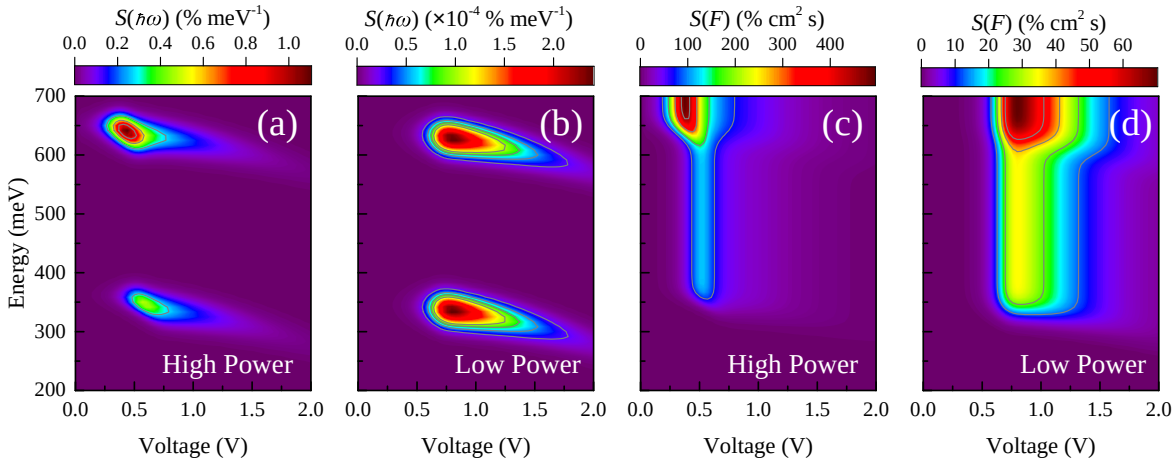

Figure 4.7 – Calculated relative photosensitivity as a function of the applied voltage and incident light energy, regarding changes in: the energy of the incoming photons, $S(\hbar\omega)$ for (a) high- and (b) low-optical power regimes; and the incoming photon flux, $S(F)$, for (c) high and (d) low optical powers.

In order to assess the quality of the device for resolving absorption lines within the spectral range determined by the energy profile of the absorber and the optical window, the simulated S(F) at high- and low-optical power regimes was calculated, as depicted in figures 4.7 (c) and (d), respectively. In the former case, a sharp increase in the photosensitivity can be observed for low voltages, ascribed to the steepness (reduction of σ_η^i, with i =e,h) of the quantum efficiency onset that modulates the photoconductivity of the absorber layer.

Take into account that this steepness is also dependent on the carrier temperature and local leverage factor. Moreover, the rise of the susceptibility at high optical power densities reduces ΔE_η and V_{th}^i, according to eq 2.31, and consequently shifts the position of the quantum efficiency onset to lower voltages. In contrast, at the low-power regime (panel (d)), the photosensitivity, now observed at higher applied voltages, spreads in a higher voltage range.

4.3.1 Optical Gas Sensing

The optical sensing abilities of the device, in presence of gas molecules such as H_2O, were also explored in the low power regime and for a varying excitation profile of the light source. In this case, the photon flux profile of the optical excitation source was reproduced using the expression

$$\mathrm{F_I}(\hbar\omega) = \frac{1}{2}\left[1 + \mathrm{erf}\left(\frac{\hbar\omega_c - \hbar\omega}{\Gamma}\right)\right], \tag{4.5}$$

where $\hbar\omega_c = 720$ meV is the cutoff energy and $\Gamma = 110$ meV the broadening of the emitted light. The absorption ratio for the H_2O line was emulated as

$$\alpha_{H_2O}(\hbar\omega) = \frac{1}{5}\exp\left[-\frac{(\hbar\omega - E_{H_2O})^2}{2\sigma_{H_2O}^2}\right], \tag{4.6}$$

with the water absorption line at $E_{H_2O} = 450$ meV and a broadening of $\sigma_{H_2O} = 25$ meV [30]. The profiles defined by eqs. 4.5 and 4.6 are plotted in figure 4.8 (a), as a red line and a light blue peak, respectively. The absorption profile of RTD-B, as obtained using eq. 2.28, is also depicted in dark blue.

Consequently, the effective incoming photon flux can be obtained as $\mathrm{F}(\hbar\omega) = \mathrm{F_I}(\hbar\omega) - \alpha_{H_2O}(\hbar\omega)$, and with it, the photoinduced voltage shift can be calculated as a function of the applied voltage and excitation photon energy, as shown in figure 4.8 (b).The absorption produced by H_2O vapor induces a dip in ΔV_{ph}, as indicated by the dashed line. In turn, the peak at $\hbar\omega = 710$ meV (dotted line) is caused by the absorption in the GaSb layer. These results were confirmed by experiments where the photocurrent, I_{ph}, was measured using a light source and a monochromator. The observed I_{ph} as a function of the applied voltage and excitation photon energy is displayed in figure 4.8 (c), showing a good agreement with the simulation in panel (b). This is affirmed by the cross-sectional views of the measured photocurrent for different applied voltages presented in figure 4.8 (d). The measured small dip at 329 meV is attributed to a reduction in the light power of the source (not included in the simulations). Changes in light power were also cross-checked with a commercially available photodiode.

These results explicitly demonstrate not only the optical selectivity in Sb-based RTD

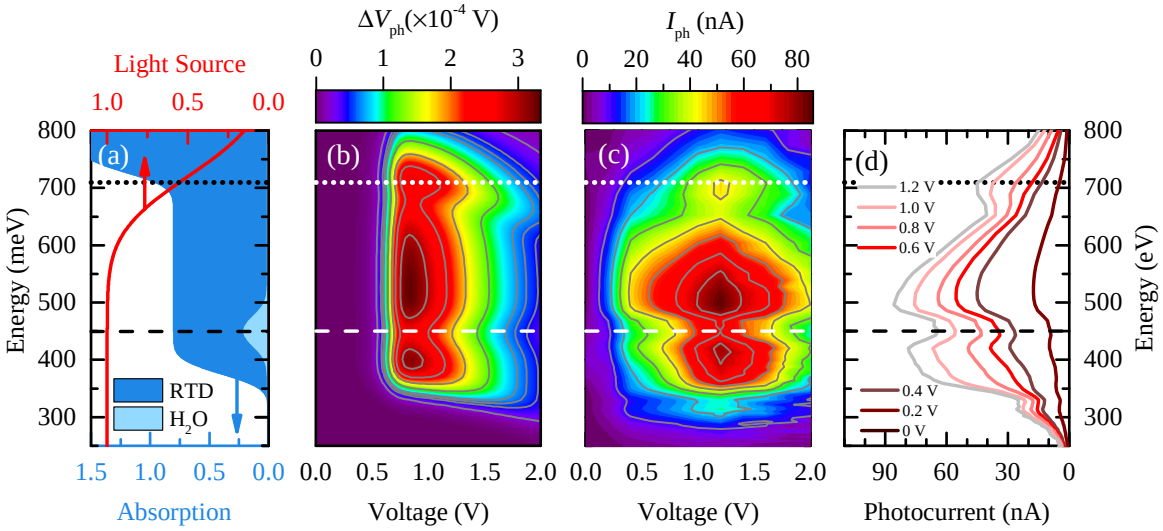

Figure 4.8 – (a) Optical photon flux profile of the excitation light (red line) and the light absorption ratios in the RTD (dark blue) and for the H_2O vapor (light blue). (b) Calculated ΔV_{ph} using the profiles of panel (a). (c) Experimental photocurrent within the same range of parameters of panel (b). (d) Photoresponse profiles for various voltages correlated to the optical power density of the excitation light.

photodetectors within the MIR spectral range, as indicated in figures 4.7 (a) and (b), but also the tunability of the photosensing capabilities as indicated in figures 4.7 (c) and (d). Experiments and models also corroborate the potential applications of this kind of RTDs in gas sensing at different optical and electrical regimes, as presented in figure 4.8. This photosensor response is closely dependent on the trapping efficiency and quantum transmission of the photogenerated carriers at the absorber, especially of the minority trapped carriers which enhances the sensor sensitivity.

References

[1] K. Shim, "Composition dependence of band alignments in $Ga_xIn_{1-x}As_ySb_{1-y}$ heterojunctions lattice matched to GaSb and InAs," *J. Appl. Phys.*, vol. 114, no. 20, p. 203703, 2013.

[2] E. D. Guarin Castro, F. Rothmayr, S. Krüger, G. Knebl, A. Schade, J. Koeth, L. Worschech, V. Lopez-Richard, G. E. Marques, F. Hartmann, A. Pfenning, and S. Höfling, "Resonant tunneling of electrons in AlSb/GaInAsSb double barrier quantum wells," *AIP Adv.*, vol. 10, no. 5, p. 055024, 2020.

[3] F. Urbach, "The long-wavelength edge of photographic sensitivity and of the electronic absorption of solids," *Phys. Rev.*, vol. 92, pp. 1324–1324, Dec 1953.

[4] T. H. Keil, "Theory of the Urbach Rule," *Phys. Rev.*, vol. 144, pp. 582–587, Apr 1966.

[5] J. D. Dow and D. Redfield, "Toward a Unified Theory of Urbach's Rule and Exponential Absorption Edges," *Phys. Rev. B*, vol. 5, pp. 594–610, Jan 1972.

[6] J. Takeda, T. Ishihara, and T. Goto, "Low energy tail of the exciton luminescence band in 2H-PbI2 and its relation to Urbach rule," *Solid State Commun.*, vol. 56, no. 1, pp. 101–103, 1985.

[7] J. Bleuse, S. Perret, Y. Curé, L. Grenet, R. André, and H. Mariette, "Optical determination of the band gap and band tail of epitaxial $Ag_2ZnSnSe_4$ at low temperature," *Phys. Rev. B*, vol. 102, p. 195205, Nov 2020.

[8] S. R. Johnson and T. Tiedje, "Temperature dependence of the Urbach edge in GaAs," *J. Appl. Phys.*, vol. 78, no. 9, pp. 5609–5613, 1995.

[9] G. D. Cody, T. Tiedje, B. Abeles, B. Brooks, and Y. Goldstein, "Disorder and the Optical-Absorption Edge of Hydrogenated Amorphous Silicon," *Phys. Rev. Lett.*, vol. 47, pp. 1480–1483, Nov 1981.

[10] P. Van Mieghem, "Theory of band tails in heavily doped semiconductors," *Rev. Mod. Phys.*, vol. 64, pp. 755–793, Jul 1992.

[11] A. Pfenning, F. Hartmann, R. Weih, M. Emmerling, L. Worschech, and S. Höfling, "p-Type Doped AlAsSb/GaSb Resonant Tunneling Diode Photodetector for the Mid-Infrared Spectral Region," *Adv. Opt. Mater.*, vol. 6, no. 24, p. 1800972, 2018.

[12] V. Rakovics, A. Tóth, B. Podör, C. Frigeri, J. Balázs, and Z. Horváth, "Liquid phase epitaxy growth and characterization of $Ga_{1-x}In_xAs_ySb_{1-y}$ quaternary alloys," *Mater. Sci. Eng. B*, vol. 91-92, pp. 83–86, 2002.

[13] M. D. Sturge, "Optical Absorption of Gallium Arsenide between 0.6 and 2.75 eV," *Phys. Rev.*, vol. 127, pp. 768–773, Aug 1962.

[14] M. B. Panish and H. C. Casey, "Temperature Dependence of the Energy Gap in GaAs and GaP," *J. Appl. Phys.*, vol. 40, no. 1, pp. 163–167, 1969.

[15] S. Coulibaly, F. De Chelle, J. Berger, J. Ferraton, A. Donnadieu, J. Magariño, and D. Kaplan, "Boron doping and post-hydrogenation effects on optical gaps and urbach tails of amorphous hydrogenated silicon films prepared by chemical vapour deposition," *Thin Solid Films*, vol. 115, no. 4, pp. 263–268, 1984.

[16] J. Melsheimer and D. Ziegler, "Band gap energy and Urbach tail studies of amorphous, partially crystalline and polycrystalline tin dioxide," *Thin Solid Films*, vol. 129, no. 1, pp. 35–47, 1985.

[17] A. Pfenning, G. Knebl, F. Hartmann, R. Weih, M. Meyer, A. Bader, M. Emmerling, L. Worschech, and S. Höfling, "GaSb/AlAsSb resonant tunneling diodes with GaAsSb emitter prewells," *Appl. Phys. Lett.*, vol. 111, no. 17, p. 171104, 2017.

[18] F. Rothmayr, A. Pfenning, C. Kistner, J. Koeth, G. Knebl, A. Schade, S. Krueger, L. Worschech, F. Hartmann, and S. Höfling, "Mid-infrared GaSb-based resonant tunneling diode photodetectors for gas sensing applications," *Appl. Phys. Lett.*, vol. 112, no. 16, p. 161107, 2018.

[19] J. Soderstrom, D. Chow, and T. McGill, "InAs/AlSb double-barrier structure with large peak-to-valley current ratio: a candidate for high-frequency microwave devices," *IEEE Electron Device Lett.*, vol. 11, no. 1, pp. 27–29, 1990.

[20] Y. Fu, Q. Chen, M. Willander, H. Brugger, and U. Meiners, "Influence of impurity and phonon scattering effects in resonant tunneling structures," *J. Appl. Phys.*, vol. 74, no. 3, pp. 1874–1878, 1993.

[21] N. Zou, Q. Chen, and M. Willander, "Effect of scattering on the resonant-tunneling current in double-barrier structures," *J. Appl. Phys.*, vol. 75, no. 3, pp. 1829–1831, 1994.

[22] R. Ulbrich, "Energy Relaxation of Photoexcited Hot Electrons in GaAs," *Phys. Rev. B*, vol. 8, pp. 5719–5727, Dec 1973.

[23] V. Laurindo Jr., E. D. Guarin Castro, G. M. Jacobsen, E. R. C. de Oliveira, J. F. M. Domenegueti, B. Alén, Y. I. Mazur, G. J. Salamo, G. E. Marques, E. Marega Jr., M. D. Teodoro, and V. Lopez-Richard, "Pathway to excitonic coherence," 2021.

[24] L. de Saint Pol, "Estimation of temperature limit for negative differential resistance using resonant tunnelling," *Electron. Lett.*, vol. 26, pp. 342–343(1), March 1990.

[25] K. J. P. Jacobs, B. J. Stevens, R. Baba, O. Wada, T. Mukai, and R. A. Hogg, "Valley current characterization of high current density resonant tunnelling diodes for terahertz-wave applications," *AIP Adv.*, vol. 7, no. 10, p. 105316, 2017.

[26] C. S. Goldenstein, R. Spearrin, J. B. Jeffries, and R. K. Hanson, "Infrared laser-absorption sensing for combustion gases," *Prog. Energy Combust. Sci.*, vol. 60, pp. 132–176, 2017.

[27] Z. Du, S. Zhang, J. Li, N. Gao, and K. Tong, "Mid-Infrared Tunable Laser-Based Broadband Fingerprint Absorption Spectroscopy for Trace Gas Sensing: A Review," *Appl. Sci.*, vol. 9, no. 2, 2019.

[28] Y. Wang, K. Zheng, F. Song, F. K. Tittel, and C. Zheng, "Mid-Infrared Absorption Spectroscopy for Gas Sensing and Application," in *2020 IEEE 5th Optoelectronics Global Conference (OGC)*, pp. 80–82, 2020.

[29] M. Vlk, A. Datta, S. Alberti, H. D. Yallew, V. Mittal, G. S. Murugan, and J. Jágerská, "Extraordinary evanescent field confinement waveguide sensor for mid-infrared trace gas spectroscopy," *Light: Sci. Appl.*, vol. 10, no. 1, pp. 2047–7538, 2021.

[30] I. Gordon, L. Rothman, C. Hill, R. Kochanov, Y. Tan, P. Bernath, M. Birk, V. Boudon, A. Campargue, K. Chance, B. Drouin, J.-M. Flaud, R. Gamache, J. Hodges, D. Jacquemart, V. Perevalov, A. Perrin, K. Shine, M.-A. Smith, J. Tennyson, G. Toon, H. Tran, V. Tyuterev, A. Barbe, A. Császár, V. Devi, T. Furtenbacher, J. Harrison, J.-M. Hartmann, A. Jolly, T. Johnson, T. Karman, I. Kleiner, A. Kyuberis, J. Loos, O. Lyulin, S. Massie, S. Mikhailenko, N. Moazzen-Ahmadi, H. Müller, O. Naumenko, A. Nikitin, O. Polyansky, M. Rey, M. Rotger, S. Sharpe, K. Sung, E. Starikova, S. Tashkun, J. V. Auwera, G. Wagner, J. Wilzewski, P. Wcisło, S. Yu, and E. Zak, "The HITRAN2016 molecular spectroscopic database," *J. Quant. Spectrosc. Radiat. Transfer*, vol. 203, pp. 3–69, 2017. HITRAN2016 Special Issue.

[31] A. Pfenning, F. Hartmann, M. Rebello Sousa Dias, F. Langer, M. Kamp, L. K. Castelano, V. Lopez-Richard, G. E. Marques, S. Höfling, and L. Worschech, "Photocurrent-voltage relation of resonant tunneling diode photodetectors," *Appl. Phys. Lett.*, vol. 107, no. 8, p. 081104, 2015.

[32] A. Pfenning, F. Hartmann, F. Langer, M. Kamp, S. Höfling, and L. Worschech, "Sensitivity of resonant tunneling diode photodetectors," *Nanotechnology*, vol. 27, p. 355202, jul 2016.

[33] E. D. Guarin Castro, A. Pfenning, F. Hartmann, G. Knebl, M. D. Teodoro, G. E. Marques, S. Höfling, G. Bastard, and V. Lopez-Richard, "Optical Mapping of Non-equilibrium Charge Carriers," *J. Phys. Chem. C*, vol. 125, no. 27, p. 14741–14750, 2021.

Chapter 5

Non-Equilibrium Carrier Dynamics in Semiconductor Heterostructures

Carrier excitation, transport, relaxation, and recombination can be exhaustively investigated in semiconductor heterostructures such as RTDs. They offer a simple architecture, where the intertwining between transport and optical properties enables a thorough characterization of the carrier dynamics, including the mapping of the thermalization mechanisms of non-equilibrium carriers as described in this chapter. The study of the thermalization dynamics of this type of carrier has attracted considerable attention in recent years [1–7] since its understanding is paramount for improving the performance of nanoelectronic devices. Here, heating and cooling processes are mediated by conversion mechanisms between electrical, optical, and thermal energies, whose characterization is a current scientific challenge.

By spatially resolving the correlation between the emitted light, charge transport, and buildup, as well as the electronic band structure of RTD-C, we have been able to perform such a characterization, as we reported in ref. [8]. The study is based on the extraction of the effective carrier temperature from the spectrum components observed at different regions of the heterostructure and under different conditions of illumination and applied voltage. In the present chapter, this characterization is described, offering clear evidence of an unexpected non-thermalization among minority and majority carriers, as well as the segmentation of the energy relaxation mechanisms along the entire heterostructure. This picture is enriched with the study of the temporal evolution of the carrier dynamics inside the QW, which discloses fundamental insights on the carrier relaxation dynamics under different transport regimes.

5.1 The Induced Electroluminescence

The transport and optical properties of RTD-C were initially investigated in the dark at $T = 4$ K. Figure 5.1 (a) shows the $I(V)$ characteristic of RTD-C, revealing the resonant

tunneling of majority carriers (electrons) at forward bias voltages, with a current peak of $I_p = 0.30$ mA at a resonance voltage of $V_R = 2.10$ V (dashed line). This resonant transport is enhanced by the presence of the pseudomorphically grown $GaAs_{0.05}Sb_{0.95}$ emitter prewell, as described in figure 3.2 (c) [9, 10].

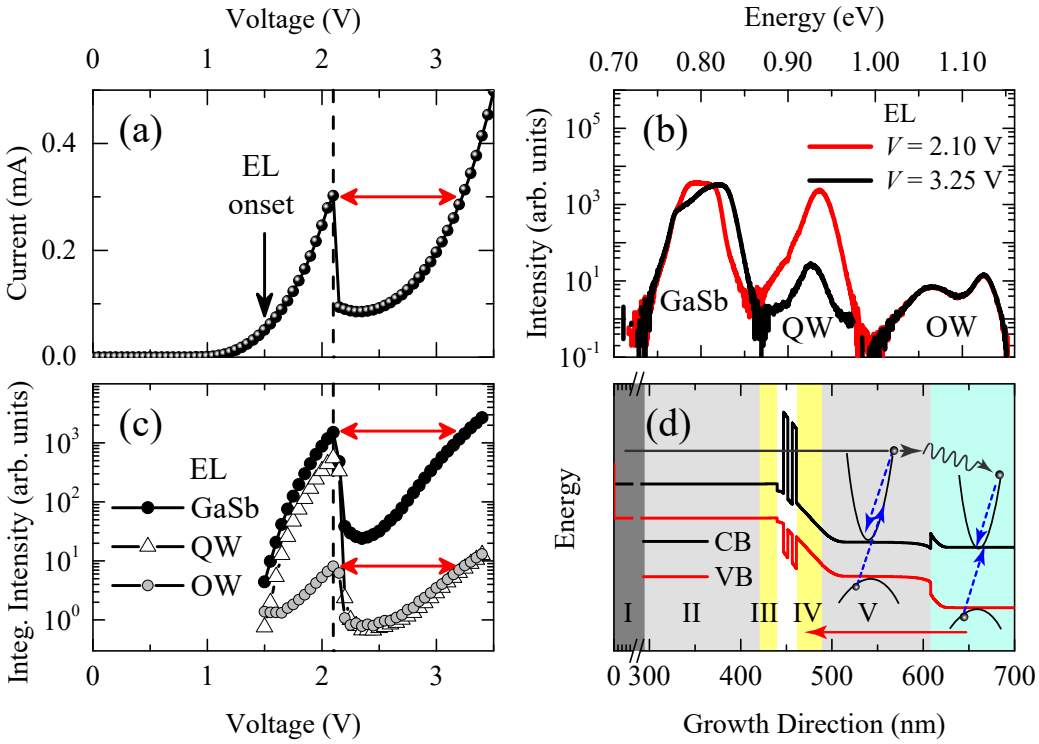

Figure 5.1 – (a) RTD-C $I(V)$ characteristic in the dark. The resonance condition (dashed line) and EL onset (vertical arrow) are detected at $V_R = 2.10$ V and $V_{EL} = 1.50$ V, respectively. (b) EL emission at resonance ($V = 2.10$ V, red line) and after resonance ($V = 3.25$ V, black line), where the same current condition is observed, as indicated by the horizontal double-arrow in (a). (c) Integrated intensity as a function of voltage for the GaSb (black dots), QW (open triangles), and OW (gray circles) EL emissions. (d) Illustration of the energy band profile and charge carrier dynamics under an applied voltage. GaSb layers were identified with roman numerals. Shaded color regions indicate different doping profiles. Holes produced after electron impact ionization (blue dashed arrows) at region V and the OW are transported toward region I (horizontal red arrow), accumulating in region IV, or recombining optically at intermediary regions. Adapted from ref. [8].

The applied voltage also induces an NIR electroluminescence (EL) emission, with an onset at $V_{EL} = 1.50$ V, pointed by the vertical arrow in figure 5.1 (a). Figure 5.1 (b) displays the EL spectra for $V = 2.10$ V and $V = 3.25$ V, corresponding to the on-resonance and out-of-resonance conditions. At these voltages, the current through the heterostructure is the same, as indicated in (a) by the double-horizontal arrow. The EL spectra unveils two high-energy emission bands at 1.12 eV and 1.06 eV, attributed to band-to-band [11] and donor-level transitions inside the $Al_{0.30}Ga_{0.70}As_{0.03}Sb_{0.97}$ optical window. These bands are labeled as OW. The interband optical recombination between the first confined levels in the double-barrier quantum well produces the emission observed at 0.93 eV, which is labeled

as QW. A low-energy band, ranging from 0.72 eV to 0.86 eV, is also detected, corresponding to combined emissions from the bulk GaSb layers [12, 13].

The integrated intensity of the GaSb, QW, and OW EL emissions as a function of the applied voltage, as presented in figure 5.1 (c), exposes the correlation between the transport and optical properties. At the EL onset (V_{EL} = 1.50 V), the EL emissions start to increase with the resonant current, reaching a peak at the resonance voltage, where the GaSb and QW emissions have almost the same intensities. However, for higher applied voltages, the EL intensities decrease to minimum values at the valley voltage (V_v = 2.35 V), and then they rise again due to the contribution of non-resonant currents, as we demonstrated in ref. 14. At voltages higher than V_R, the GaSb intensity is distinctly higher than the QW and OW intensities. Also, note that the GaSb and OW EL emissions attain the same intensities when the current condition is equivalent to the resonance, as denoted by the double-horizontal arrows, implying similar optical recombination efficiencies.

Although the EL emission in RTDs is usually observed in p-i-n heterostructures [15–18], where the doping profiles provide carriers with opposite charges that can eventually recombine, it has been demonstrated that in n-type RTDs, the EL emission can be also induced through impact ionization processes, which usually occur at the collector region [14, 19, 20]. This is the case of RTD-C, where the impact ionization process produces the holes necessary for optical recombination. The mechanism has been sketched in figure 5.1 (d), which illustrates the CB minimum (black line) and VB maximum (red line) under an applied forward voltage. Roman numerals serve to identify different GaSb layers, while color shaded regions have been used to distinguish different doping profiles, as presented in figure 3.1 (c): region I was doped with $n = 1 \times 10^{18}$ cm^{-3} (dark gray), regions II and V are doped with $n = 5 \times 10^{17}$ cm^{-3} (light gray), regions III and IV (yellow) and the DBS (white) are intrinsic layers, and the optical window was grown with $n = 1 \times 10^{18}$ cm^{-3} (cyan).

At resonance, majority charge carriers are transported in the CB from regions I and II, tunneling through the DBS, until reaching ballistically region V and the OW (black solid arrow) [21–23]. Therein, electrons can lose part of their energy by scattering processes (wavy arrow), but their energy is still enough to induce impact ionization processes, where CB ballistic electrons collide with electrons at the VB. The latter is then excited and promoted to the CB, conserving electrons energy and momentum (blue dashed arrows) [14, 19]. Subsequently, minority carriers (holes) are produced in the VB, where they can also be transported toward region I (red arrow) by the action of the applied voltage. These holes are responsible for the EL emission presented in figure 5.1 (b) since they can recombine optically at different regions of the heterostructure. Only the depletion of region IV and part of region V, close to the heterojunction with region IV, can hamper there the radiative recombination process.

The applied voltage also affects both the number of carriers available for optical recombination and the efficiency of this process in different parts of the heterostructure. This is why the QW emission intensity changes drastically between $V = 2.10$ V and $V = 3.25$ V, even though the current through the RTD remains the same, as depicted in figure 5.1 (c). In contrast, the intensity of both the GaSb and OW are almost unchanged at these voltages, unveiling the difference between resonant and non-resonant conditions. Moreover, the increase of the Fermi level at region III and in the prewell, caused by electrons accumulation [13], provokes the observed broadening of the high-energy side of the GaSb EL emission after resonance, as shown in figure 5.1 (b).

5.2 Photoluminescence emission and Photoresponse

The RTD-C optical response under illumination was also explored at cryogenic temperatures, employing two diode lasers as excitation sources. One of them offers an incident energy of $\hbar\omega_1 = 1.88$ eV, suitable for optically exciting the entire heterostructure, since the bandgap energies of the GaSb layers and the AlGaAsSb OW are expected to be 0.81 eV and 1.20 eV, respectively, as indicated in figure 3.1 (c). The other laser emits at $\hbar\omega_2 = 1.15$ eV, allowing the excitation just of the GaSb layers and the DBS, avoiding photogeneration of holes at the OW, and increasing light penetration. Both lasers were operated in continuous mode at an optical power density of 3.34×10^4 W /cm^2 and 1.25×10^4 W /cm^2, respectively.

Figures 5.2 (a) and (b) show the spectra obtained after illumination with the $\hbar\omega_1$ and $\hbar\omega_2$ lasers, respectively, and for different applied voltages. Below the EL onset ($V_{EL} <$ 1.5 V), pure PL emission can be studied, as exemplified by the PL1 and PL2 spectra (green lines) at zero-bias voltage, in (a) and (b), respectively. In the former, the most energetic emission at 1.12 eV is absent, and only appears for applied voltages above the EL onset. The low-efficient photogeneration of electron-hole (e-h) pairs in the OW prevents optical recombination at this energy. The reduction of this photogeneration efficiency is ascribed to a transition between direct- and indirect-energy-gap observed in the $Al_xGa_{1-x}As_ySb_{1-y}$ system when $x = 0.30$ [11, 24]. Consequently, only impact ionization processes can produce the holes necessary for recombination at this energy band. The presence of impurities in the OW due to the high doping profile makes the absorption of light from the high-energy laser more efficient, allowing for the detection of the less energetic OW emission, observed at 1.06 eV.

At voltages above the EL onset, the PL and EL emissions unavoidably overlap, and the corresponding EL+PL1 and EL+PL2 spectra are displayed in figures 5.2 (a) and (b) for the high- and low-energy lasers, respectively. Under illumination, holes can additionally be generated by light absorption, which occurs to a greater extent in the GaSb regions. This is supported by calculations using the Lambert-Beer law [25] for the low-energy laser.

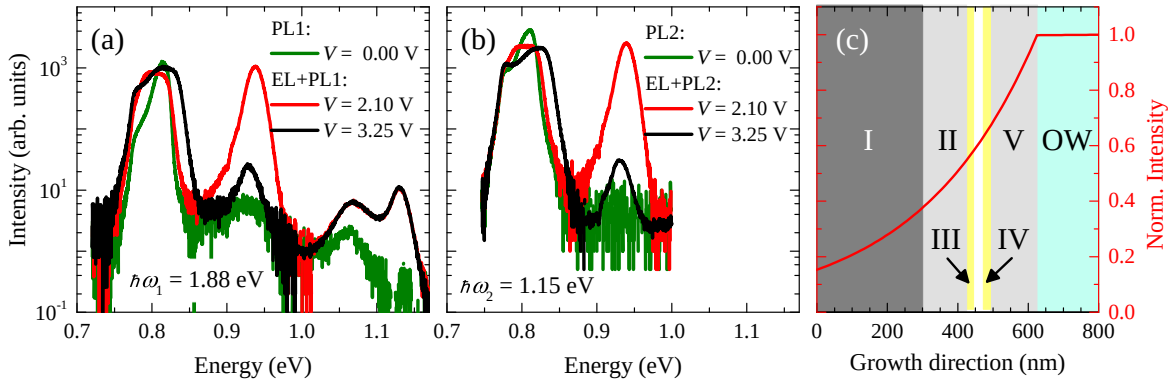

Figure 5.2 – Luminescence spectra under illumination detected after excitation with a laser of energy (a) $\hbar\omega_1 = 1.88$ eV and (b) $\hbar\omega_2 = 1.15$ eV. Green, red, and black lines correspond to spectra measured at $V = 0$, 2.10 V and 3.25 V, respectively. Adapted from ref. [8]. (c) Calculated intensity of the transmitted light through the heterostructure as a function of the growth direction. Quantum effects in the absorption have not been considered in this approximation.

According to that, absorption processes in bulk materials reduces the power, P, of the light transmitted through the structure, following an exponential decay: $P(l) = P_0 \exp(-\alpha l)$, where P_0 is the intensity of the incident light, α is the absorption coefficient, and l is the thickness of the material. Taking the absorption coefficients of GaSb and AlGaAsSb as $\alpha_{\text{GaSb}} = 10^4$ cm^{-1} and $\alpha_{\text{AlGaAsSb}} = 10^2$ cm^{-1}, respectively [26], corresponding to a laser energy of $\hbar\omega_2 = 1.15$ eV, the decay of the normalized intensity of the transmitted light across the RTD can be obtained as plotted in figure 5.2 (c). In this approximation, quantum effects on the absorption caused by the DBS have not been considered. This result shows that the OW does not absorb light with this energy, but GaSb layers can absorb around 80% of the transmitted light. Then, optical generation of e-h pairs under illumination is highly efficient at these regions, leading to the PL below the EL threshold and the combined EL+PL above it.

The correlation between the PL emission and the transport properties under illumination also offers important insights into the carrier dynamics, especially at low voltages, where there is no EL emission. Figure 5.3 (a) exposes, on a semi-logarithmic scale, the $I(V)$ characteristic under illumination (red line) with the $\hbar\omega_2$ laser. For applied voltages above $V = 1.20$ V, the illuminated $I(V)$ characteristic follows the response in the dark (black line). Nevertheless, for voltages between 0 and 1.20 V, the $I(V)$ characteristic is shifted to lower voltages. As discussed in the previous Chapter and § 2.4, this photoresponse is mainly a consequence of the balance between the accumulation of photogenerated holes in the depleted region IV near the DBS and their escape through resonant and non-resonant channels. It induces a voltage shift, ΔV_{ph} (blue line), proportional to the number of accumulated carriers. The observed ΔV_{ph} exhibits a maximum at $V = 0.50$ V, and it has a significant impact on the thermalization analysis exposed in the next section.

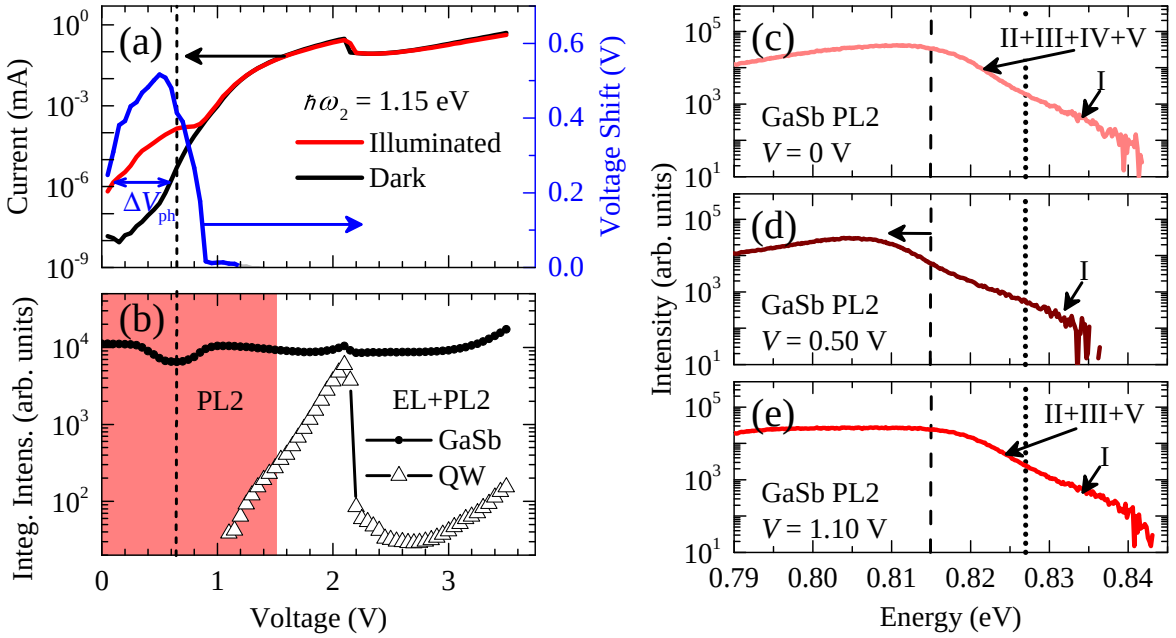

Figure 5.3 – (a) $I(V)$ characteristic under illumination with the $\hbar\omega_2$ laser (red line). At low applied voltages, the $I(V)$ characteristic presents a photoinduced voltage shift (ΔV_{ph}, blue line), with respect to the $I(V)$ characteristic in the dark (black line). (b) Integrated intensity as a function of the applied voltage for the EL+PL2 emissions, coming from the QW (open triangles) and GaSb layers (solid circles). The red-shaded region represents the bias voltage range where just PL emission is observed. A dip in the GaSb emission is detected at $V = 0.65$ V (dashed line). Adapted from ref. [8]. High-energy side of the GaSb PL2 spectra for applied voltages of (c) 0, (d) 0.50, and (e) 1.10 V, indicating the contributions of each GaSb region. Dashed and dotted lines denote energies of 815 and 827 meV, respectively, as reference

Figure 5.3 (b), shows the EL+PL2 integrated intensities for QW (open triangles) and GaSb (solid dots) emissions as functions of the applied voltage. The shaded region in red corresponds to the bias voltage range before the EL onset. Despite the QW and GaSb emissions peak at the resonance voltage with almost the same intensities, as in the case of the EL emission observed in figure 5.1 (c), the absorption of light in the GaSb layers (see figure 5.2 (c)) photogenerates carriers, which enhance the radiative recombination for the whole bias voltage range. As a result, the GaSb emission keeps an almost constant intensity, much higher than the QW emission, for out-resonance conditions. In contrast, the QW emission maintains a clear correlation with the $I(V)$ characteristic.

The stability of the intensity in the GaSb PL2 emission is interrupted at low applied voltages between $V = 0.30$ V and $V = 0.90$ V, where a reduction of 42% at $V = 0.65$ V, with respect to the intensity at zero-bias voltage, is detected. The intensity dip is denoted by the dashed line in figure 5.3 (b) and shows a correlation with the photoinduced ΔV_{ph} in (a). A closer look at the GaSb PL2 spectra at these voltages also reveals that the dip is produced by the shrinkage of the GaSb spectra. Figures 5.3 (c)-(e) exposes the high-energy side of the GaSb PL2 emission for $V = 0$, 0.50, and 1.10 V, respectively. At zero-bias

voltage, it is expected a contribution to the PL spectra from all the GaSb regions. Then, the emissions above 815 meV (dashed line) and 827 meV (dotted line) are ascribed to the high-energy tails produced by radiative recombination in regions II-V and region I, respectively [13]. Below $V = 0.50$ V, the accumulation of holes at region IV escalates and repels photogenerated holes at region III. Furthermore, around $V = 0.50$ V, the resonant tunneling of holes is triggered, minimizing both the accumulation of holes in region IV and the minority carriers population at region V. Consequently, the probability of band-to-band optical recombination in regions III-V is lowered, and the spectrum is shrunk, as pointed by the horizontal arrow in figure 5.3 (d). For $V > 0.50$ V, the emission at energies above 815 meV is detected again, as showed in panel (e), thanks to the reduction of the trapped holes in region IV, which vanishes close to $V = 0.90$ V, where ΔV_{ph} is almost zero (see panel (a)). However, at this voltage regime, emission from region IV is not expected due to its depletion, as mentioned before.

5.3 Non-Equilibrium Electrons and Holes

Based on the transport and optical characterization of the heterostructure, the hot carrier dynamics was explored in line with the effective temperature model proposed in § 1.4. This analysis allows investigating the mechanisms behind the modulation of the effective local temperature, such as Joule heating, optical heating, or the evaporative cooling of hot carriers. With this, the conditions for thermalization between minority and majority non-equilibrium carriers can be discerned and a thermalization map can be obtained to distinguish temperature profiles along the heterostructure, according to the carrier type.

Since the thermalization processes depend on the type of excitation, the analysis has been performed on the high-energy tails of the spectra for each type of emission. According to eq. 1.59, these tails can be fitted using a Boltzmann's function of the form $Q(\hbar\omega) \propto \exp[-\hbar\omega/(k_B T_{eff}^{e\text{-}h})]$, allowing for the extraction of the electron-hole (e-h) pair effective temperature, $T_{eff}^{e\text{-}h}$, which is defined by eq. 1.60. Despite this approximation being widely described in the scientific literature [27–31], special care must be taken in samples with non-uniform absorptivity at energies above the bandgap. In these cases, a non-mono-exponential decay of the high-energy tail can be observed, which can lead to an overestimation of the effective temperature [6, 7, 32].

Figure 5.4 (a) exposes the high-energy tails of the OW spectra, obtained from EL (top panel) and EL+PL1 (bottom panel) optical emissions, at $V = 2.10$ V (dark lines) and $V = 3.40$ V (light lines). The mono-exponential decays allowed the use of Boltzmann's functions for the fitting procedure, as indicated by blue dotted lines. From them, $T_{eff}^{e\text{-}h}$ was extracted as a function of the applied voltage, as presented in figure 5.4 (b) for temperatures obtained

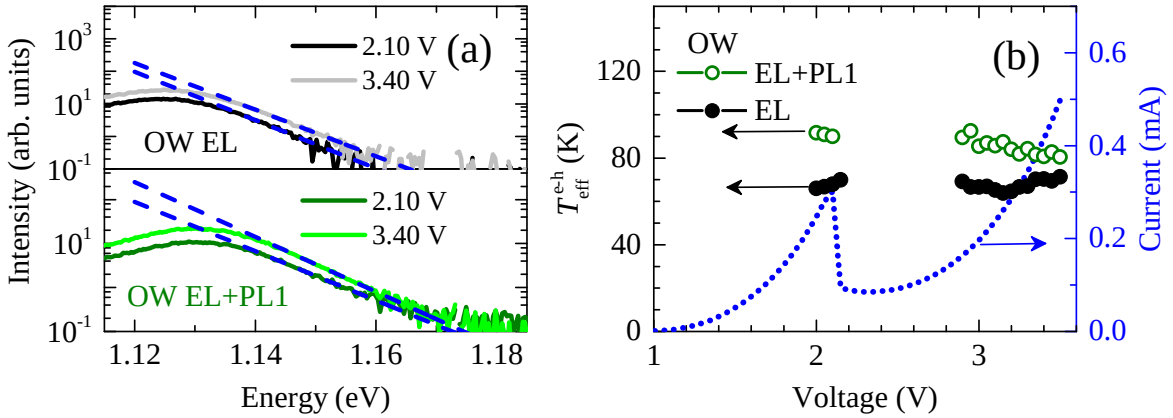

Figure 5.4 – (a) High-energy tails from the EL (dark lines, upper panel) and EL+PL1 (green lines, bottom panel) OW spectra, at resonance ($V = 2.10$ V) and out-of-resonance conditions ($V = 3.40$ V). The tails were fitted using Boltzmann functions (blue dashed lines). (b) Effective carrier temperature as a function of the applied voltage. T_{eff}^{e-h} was obtained from EL (black dots), and EL+PL1 (green dots) OW spectra. The $I(V)$-characteristic (blue dotted line) is presented as reference. Adapted from ref. [8].

from the EL (black dots) and EL+PL1 (green circles) OW emissions. The $I(V)$-characteristic has been added as a reference. At the valley condition, low currents reduce the intensity of the emitted light and impede the extraction of reliable values of T_{eff}^{e-h}. It is worth noting that the obtained T_{eff}^{e-h} is higher than the lattice temperature, $T_L = 4$ K, which is a signature of the presence of hot carriers in the OW. The results show that T_{eff}^{e-h} at the OW attains an almost constant value of around 68 K during EL. Under illumination, T_{eff}^{e-h} rises up to ~ 90 K, due to optical heating. Incoming photons provide an excess energy to a large fraction of carriers, exciting them to high energetic levels and increasing T_{eff}^{e-h} [31, 33]. Regardless this increment, for $V > 2.90$ V, T_{eff}^{e-h} drops to 80 K ascribed to an evaporative cooling of highly energetic holes from the OW [2], as explained below.

Figure 5.5 (a) shows the high-energy tails of the QW spectra, for the same conditions as in figure 5.4 (a) for the OW. The effective temperatures in the QW obtained from the Boltzmann's functions are presented in figure 5.5 (b) as a function of the applied voltage, for the case of the EL (black dots), EL+PL1 (green circles), and EL+PL2 (red triangles) QW emissions. Here, the extracted T_{eff}^{e-h} presents an increase with the applied voltage from $T \approx 37$ K before resonance, up to $T \approx 134$ K after resonance, depending on the type of excitation. The highest temperatures in the QW are achieved for the EL+PL1 emission, and a cooling process similar to the cooling observed in the OW is also detected under illumination above $V = 2.90$ V.

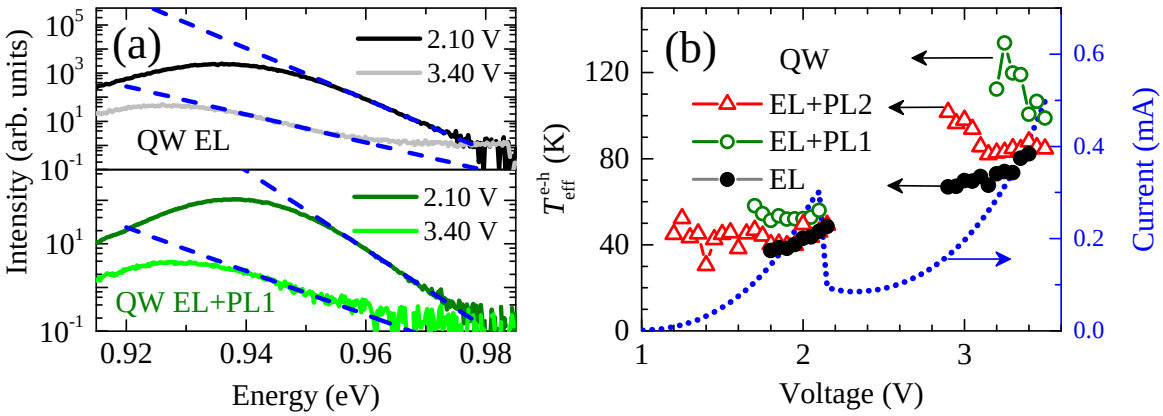

Figure 5.5 – (a) High-energy tails from the EL (dark lines, upper panel) and EL+PL1 (green lines, bottom panel) QW spectra, at resonance ($V = 2.10$ V) and out-of-resonance conditions ($V = 3.40$ V). The tails were fitted using Boltzmann functions (blue dashed lines). (b) Effective carrier temperature as a function of the applied voltage. $T_{\text{eff}}^{\text{e-h}}$ was obtained from EL (black dots), EL+PL1 (green dots), and EL+PL2 (red triangles) QW spectra. The $I(V)$-characteristic (blue dotted line) is presented as reference. Adapted from ref. [8].

The cooling process observed in both the OW and QW can be explained as the result of the *evaporation* of highly energetic carriers when they are extracted from a specific region, driven by the applied voltage [2, 34]. This process is illustrated in figures 5.6 (a) and (b) for dark and illumination conditions, respectively. In stationary conditions, the population distribution can be characterized by $\rho(E)f(E)$, with $\rho(E)$ the density of states and $f(E)$ the distribution function characterized by $T_{\text{eff}}^{\text{e-h}}$. In the dark, most energetic electrons from regions I and II are removed by the applied electric field (horizontal black arrow) and transported until region V and the OW, where they can produce holes by impact ionization (dashed arrows), as explained in figure 5.1 (d).

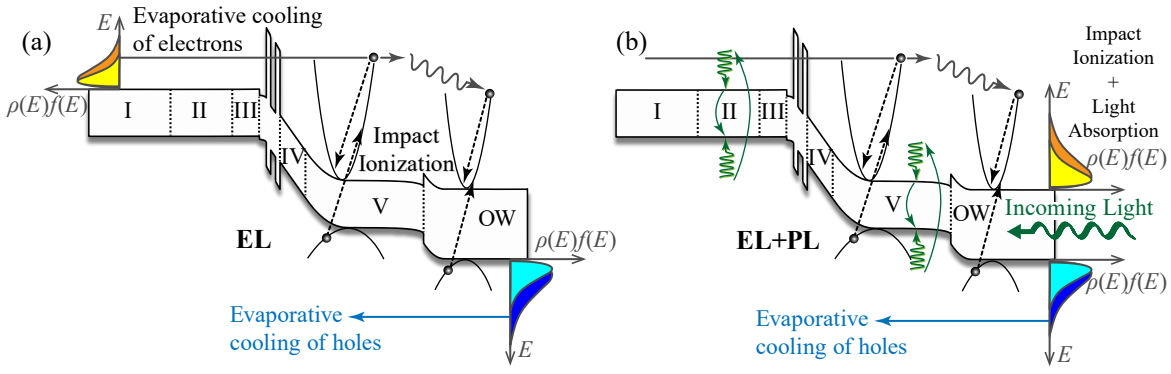

Figure 5.6 – Illustration of the energy band profile and the hot carrier dynamics under an applied forward voltage. (a) In the dark, electrons from regions I and II travel ballistically until region V and the OW where they produce holes by impact ionization (dashed arrows). The carrier population distribution, $\rho(E)f(E)$ is represented at region I and the OW. These distributions relax towards colder distributions due to the evaporative cooling of hot carriers [2]. (b) PL excitation gives additional energy to the carriers due to light absorption (green arrows), broadening $\rho(E)f(E)$ towards hotter distributions.Adapted from ref. [8].

Holes can also be removed from the OW and region V by the action of the applied electric field. As a consequence, the local states relax toward "colder" distributions (light color distributions), reducing the local carriers temperature, as exemplified by the schematic population distributions in region I for electrons and in the OW for holes. One must consider that the extraction of local hot carriers may occur through different channels both resonantly [2] and non-resonantly [35]. Under illumination, a similar picture is expected, but in this case, the absorption of light contributes to the broadening of the local states to "hotter" distributions, reflected by the increment of $T_{\text{eff}}^{\text{e-h}}$.

Figure 5.7 (a) depicts the high-energy tails of the GaSb EL spectra. As discussed in § 5.2, the high energy side of the GaSb emission presents two tails, observable at voltages below the resonance condition: one related to the emission from region I, and another related to the emission from regions II, III, and V, as presented in figure 5.3 (e). After resonance, the emissions from regions II, III, and V broaden towards higher energies, masking the spectral tail from region I. This response enables the extraction of $T_{\text{eff}}^{\text{e-h}}$ as a function of the applied voltage, for both tails at voltages between 1.85 V and 2.15 V, as displayed in figure 5.7 (b), for the I-tail (open circles) and the II+III+V-tail (solid circles). In both cases, $T_{\text{eff}}^{\text{e-h}}$ increases with the applied voltage ranging from 27 K up to 46 K for the II+III+V-tail, and from 60 K up to 76 K for the I-tail. The overall rise in $T_{\text{eff}}^{\text{e-h}}$ with the applied voltage, as observed in the GaSb regions and the QW, is a consequence of the Joule heating under high electric fields during the drift of hot carriers toward the outermost regions of the heterostructure [21, 30, 36, 37].

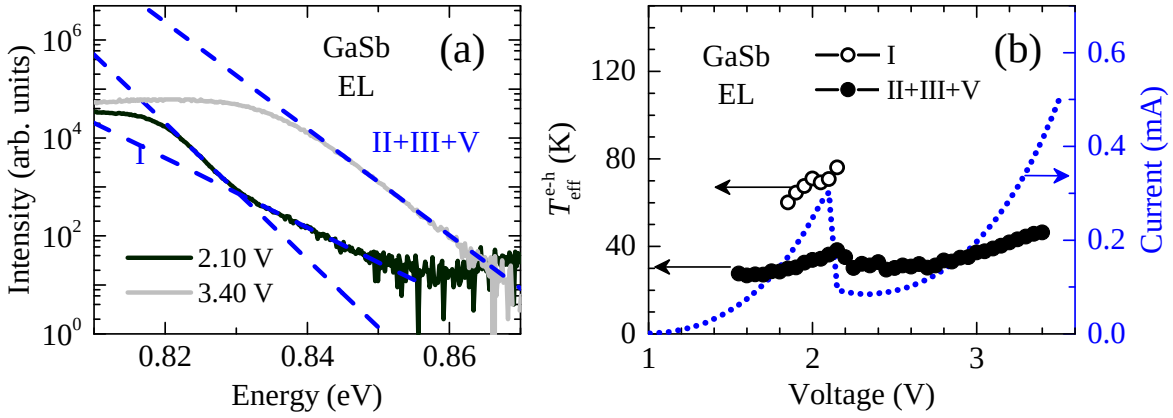

Figure 5.7 – (a) High-energy tails from the GaSb EL spectra, at resonance (V = 2.10 V) and out-of-resonance conditions (V = 3.40 V). The tails were fitted using Boltzmann functions (blue dashed lines). Two tails are observed: one coming from region I and the other from regions II, III, and V. (b) Effective carrier temperature as a function of the applied voltage, for the I-tail (open circles) and the II+III+V-tail (solid circles). The $I(V)$-characteristic (blue dotted line) is presented as a reference. Adapted from ref. [8].

When the heterostructure is illuminated, the effective carrier temperature of the hot carriers at the GaSb regions can be also extracted at low voltages. Figures 5.8 (a) and (b)

show the PL1 and PL2 high-energy tails of the GaSb spectra, close to the PL dip ($V = 0.50$ V, top panels) and at voltages above it (bottom panels). The spectral narrowing at $V = 0.50$ V (indicated by vertical arrows) caused by holes accumulation in region IV, as discussed in § 5.2, only permits the extraction of the effective temperature from the I-tail. At higher voltages, when the accumulation of holes is reduced, the emission from regions II, III, and V is restored, allowing the extraction of $T_{\text{eff}}^{\text{e-h}}$ from that tail.

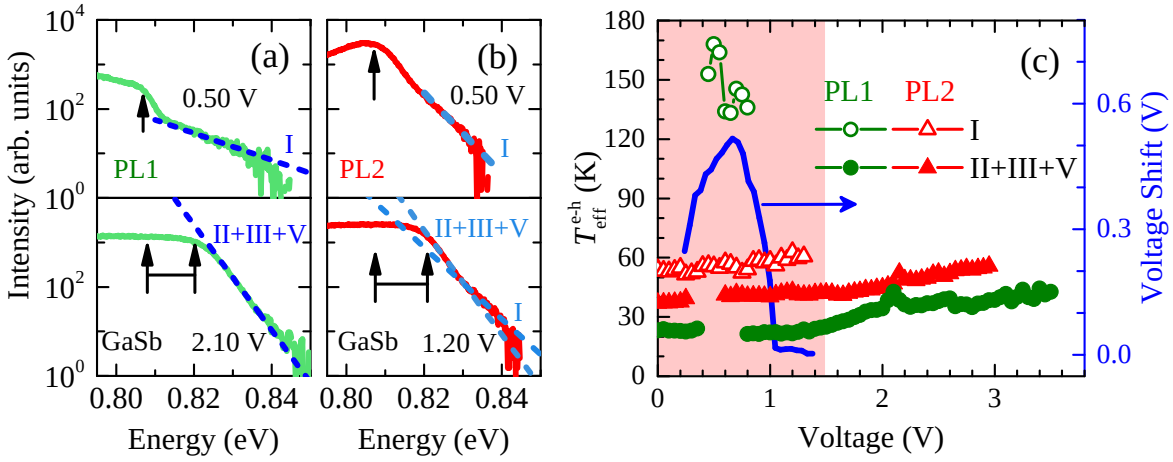

Figure 5.8 – High-energy tails from the GaSb (a) PL1 and (b) PL2 emissions, at the PL dip ($V = 0.50$ V, top panels) and voltages above the PL dip (bottom panels). The tails were fitted using Boltzmann functions (blue dashed lines). Black arrows indicate the broadening of the spectra after the PL dip. (c) Effective carrier temperature obtained from each tail as a function of the applied voltage for the PL1 (green symbols) and PL2 (red symbols) emissions. The $\Delta V_{\text{ph}}(V)$ (blue line) is presented as reference. Adapted from ref. [8].

The voltage dependence of the effective temperature derived from each spectral tail is plotted in figure 5.8 (c) for the PL1 (green symbols) and PL2 (red symbols) emissions. The photoinduced voltage shift, as shown in figure 5.2 (a), has been added in the background. The extracted e-h pair effective temperatures rise with the applied voltage due to Joule heating induced by the electric field. Values of $T_{\text{eff}}^{\text{e-h}}$ for the II+III+V-tail, at voltages close to the PL dip ($0.4\text{ V} < V < 0.8\text{ V}$), cannot be resolved, as ΔV_{ph} increases and the II+III+V emission shrinks. It hampers an adequate fitting. Note also that the values of $T_{\text{eff}}^{\text{e-h}}$ for the I-tail from the PL1 emission (open green circles) can only be obtained for voltages between 0.45 V and 0.80 V. Outside this range, the broadening of the GaSb spectra masks the I-tail, as exemplified in the bottom panel of figure 5.8 (a). In contrast, the I-tail from the PL2 emission intensifies, widening the detection range (red open triangles) from $V = 0$ up to 1.30 V, as presented in panel (c). The intensification of the I-tail for the low-energy excitation laser is the result of the photogeneration of carriers in the deepest regions, I and II, due to the higher penetration of this laser.

Surprisingly, our results indicate that the effective temperatures obtained from the II+III+V-tail of the PL1 emission (green solid circles), which are similar to the EL tempera-

tures presented in figure 5.7 (b), are lower than the PL2 temperatures (red solid triangles). The PL1 temperatures were expected to be higher than the PL2 temperatures since the effective temperature can increase for higher excitation energies, as reported in ref. [31]. By weighting the effects of hot-carriers local cooling and heating in terms of the excitation energy, this apparent anomaly will be addressed in the next section.

5.4 Thermalization of Non-Equilibrium Carriers

The singular results presented at the end of the last section can be understood by means of a proposed model, as we reported in ref. [8]. This model considers the dependence of the e-h pair effective temperature on the carriers dynamics and the experimental conditions. Thus, the thermalization between electrons and holes can be assessed [29, 38, 39]. Under electrical and optical excitations, the averaged carriers energy-loss rate per unit volume in a particular region of the heterostructure can be expressed as

$$n_i \left\langle \frac{\partial E_i}{\partial t} \right\rangle = j_i F_{\text{local}} + n_i \frac{\Delta\mu_i^{\text{in}}}{\tau_i^{\text{in}}} - n_i \frac{\Delta\mu_i^{\text{out}}}{\tau_i^{\text{out}}} \tag{5.1}$$

where n_i (i = e,h) is the carriers density. The volumetric electrical power density dissipated by a certain heterostructure region is represented by the first term on the right, where j_i is the current density and F_{local} is the local electric field. The heating/cooling powers, $\Delta\mu_i^{\text{in/out}}/\tau_i^{\text{in/out}}$, are produced by other sources, such as optical excitation or evaporative processes, respectively. Here, $\Delta\mu_i$ corresponds to variations in the effective chemical potential, and τ_i is the carriers relaxation time. By substituting eq. 1.58 into eq. 5.1, the carriers temperature can be expressed as

$$T_i = T_{\text{L}} + \Delta T_i^{\text{exc}} + \frac{\tau_i^{\varepsilon}}{k_{\text{B}} n_i} j_i F_{\text{local}} \tag{5.2}$$

with $\Delta T_i^{\text{exc}} = \left(\tau_i^{\varepsilon}/k_{\text{B}}\right)\left[\left(\Delta\mu_i^{\text{in}}/\tau_i^{\text{in}}\right) - \left(\Delta\mu_i^{\text{out}}/\tau_i^{\text{out}}\right)\right]$ representing the balance in the carriers temperature provoked by carrier excitation or evaporation, which also depends on the excitation energy. If the energy of the incoming photons increases, the chances for local extraction of high energetic carriers can be enhanced, reducing the average local excess energy, and lowering the effective temperatures. This explains the seeming anomaly of the PL1 temperatures of the II+III+V-tail, pointed out in figure 5.8 (c).

In order to assess the thermalization among electrons and holes, it is necessary to examine the dependence of the e-h pair effective temperature on the applied electrical power, P_{el}. In this sense, P_{el} can be correlated with the volumetric electrical power density by means of the relation $j_i F_{\text{local}} \approx \xi P_{\text{el}}/\mathcal{V}_{\text{local}}$, being ξ a leverage factor and $\mathcal{V}_{\text{local}}$ the local

volume of the considered region. Then, eq. 5.2 can be expressed as

$$T_i = T_L + \Delta T_i^{exc} + \kappa_i P_{el} \tag{5.3}$$

where $\kappa_i = \xi \tau_i^{\varepsilon} / (k_B n_i \mathcal{V}_{local})$ symbolizes a temperature variation rate per power unit. Hence, according to eq. 1.60, if carriers thermalize among them during external excitation, then $T_{eff}^{e\text{-}h} = T_e = T_h$, and a linear dependence with P_{el} is expected for $T_{eff}^{e\text{-}h}$.

Figures 5.9 (a) and (b) show the effective temperatures obtained from the II+III+V-tail of the GaSb EL (black squares) and PL1 (green dots) emissions, respectively, as a function of the applied electrical power. This power was obtained as the product between the measured current and the applied voltage, $P_{el} = IV$. According to eq. 5.3 and considering that during EL there are no external excitation sources besides the applied voltage, then $\Delta T_i^{exc} = 0$. Thus, assuming carriers thermalization, the linear dependence was used as a fitting function for the EL data, as indicated by the red dashed lines. In this approximation, T_L and κ_i are fitting parameters. The EL temperatures in panel (a) seem to follow the linear dependence with P_{el}, but the fitted lattice temperature, $T_L = 26.6$ K, lacks any physical sense since in the dark, at zero applied electrical power, the carriers are expected to thermalize with the lattice ($T_{eff}^{e\text{-}h} = T_L = 4$ K). Furthermore, the linear dependence cannot describe the PL1 temperatures, as displayed in figure 5.9 (b).

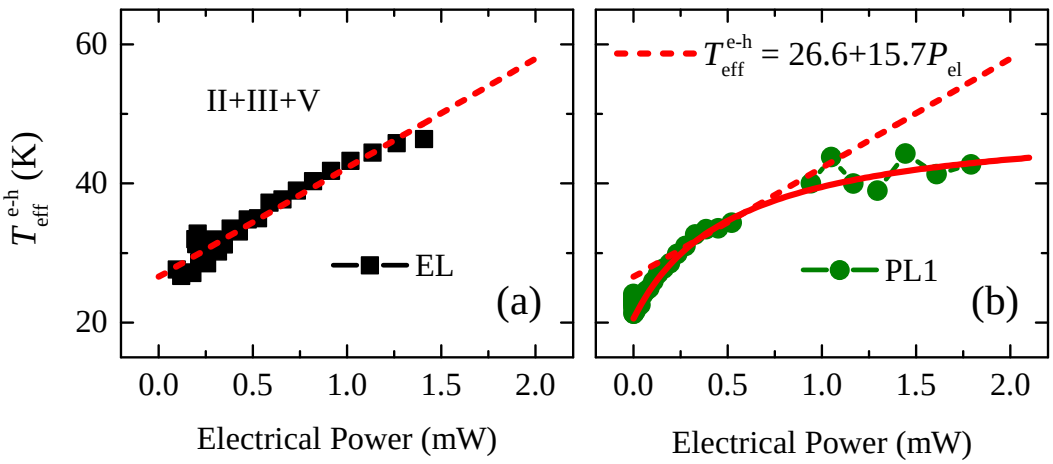

Figure 5.9 – $T_{eff}^{e\text{-}h}$ as a function of the applied electrical power for the (a) EL (black squares) and (b) PL1 (green dots) GaSb optical emissions. The data correspond to the spectral tails coming from regions II, III, and V. Red dashed lines correspond to a linear fit extrapolated to zero applied electrical power. The red solid line in (b) represents the best simulation, as described in figure 5.10 (b). Adapted from ref. [8].

These results are clear evidence that thermalization among electrons and holes is not satisfied as anticipated by Bonch-Bruevich and Kalashnikov in ref. [38]. Therein, the authors established that contrasting effective masses and scattering times between hot carriers are linked to differences in their effective temperatures leading to $T_e \neq T_h$. These

differences control the balance between the efficiency of the carrier-carrier scattering process and the strength of the coupling of the carriers with the lattice that leads to potential energy losses [30, 31, 40].

The non-thermalization of hot carriers implies that both electrons and holes contribute in a different way to the e-h pair effective temperature. This contribution is weighted by their effective masses, as established by eq. 1.62. According to that, fluctuations in holes temperature can also be detected by measuring $T_{\text{eff}}^{\text{e-h}}$, as long as T_{h} is lower than T_{e} (see figure 1.4). This is why the cooling process observed in figure 5.4 (b) can be ascribed to the evaporation of holes from the OW, under illumination. At this regime, the incoming light leads to hotter non-equilibrium electrons arriving at the OW so that the reduction in the local effective temperature of holes is better resolved.

The non-linear dependence of $T_{\text{eff}}^{\text{e-h}}$ with the applied electrical power is also a consequence of the non-thermalization between carriers. This can be verified by taking eqs. 1.60 and 5.3 to calculate $T_{\text{eff}}^{\text{e-h}}$ as a function of P_{el}. The results for the EL, PL1 and PL2 effective temperatures have been plotted in figures 5.10 (a)-(c), respectively, on a semi-logarithmic scale. Symbols represent the experimental data while color solid lines represent the best simulations keeping T_{h} constant. Color shaded bands indicate the possible responses by sweeping the holes temperature around the best value, T_{h}, with a deviation, ΔT_{h}. The best simulations show a good agreement with the experimental results in the whole range of the applied electrical power. It can be corroborated in figure 5.9 (b), where the best simulation for the PL1 temperatures is displayed as a solid red line.

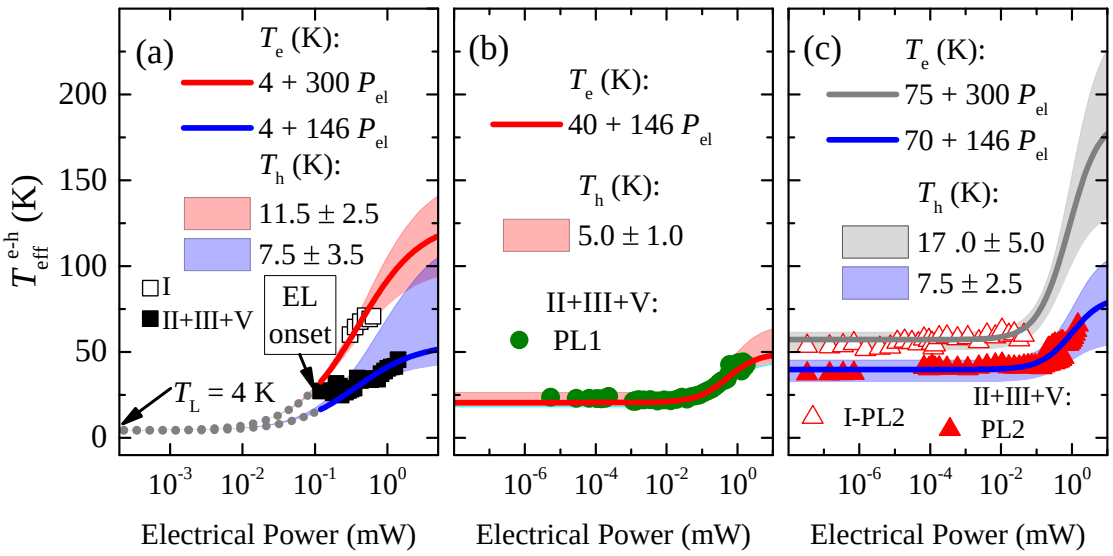

Figure 5.10 – Simulations of $T_{\text{eff}}^{\text{e-h}}$ as a function of the electrical power, for the data extracted from the GaSb (a) EL, (b) PL1, and (c) PL2 spectral tails. Symbols indicate the experimental data. Solid lines represent the best simulations. Color shaded regions correspond to simulations varying T_{h}. In (a), the mathematical extrapolations to zero electrical power are depicted as gray doted lines. The simulation for the PL1 data (red solid line) in (b) is also plotted in figure 5.9 (b) to show the good agreement with the experiment. Adapted from ref. [8].

In the simulations for the EL temperatures showed in panel (a), the lattice temperature and the variations of the electron temperature due to external sources besides the applied voltage were assumed as $T_L = 4$ K and $\Delta T_e^{exc} = 0$, respectively. The best results suggest that κ_e must be around 300 K mW^{-1} for the effective temperatures extracted from the I-tail (red line), which is almost twice the value of $\kappa_e = 146$ K mW^{-1} obtained for the effective temperatures extracted from the II+III+V-tail (blue line). Moreover, simulations indicate that hole temperatures must be close to 11.5 K in region I, and 7.5 K in regions II, III, and V. In contrast, electrons can reach temperatures of hundreds of Kelvin at these regions, and for the highest electrical powers. The extrapolation of the simulations to $P_{el} = 0$ (gray dotted lines) has just mathematical meaning because holes can only be created by impact ionization above the EL onset.

In the case of the simulations for the PL temperatures displayed in figures 5.10 (b) and (c), the same κ_e parameters obtained for T_e using the EL temperatures in panel (a) were employed for the calculations. These results demonstrate that under illumination, hole temperatures must be closer to the lattice temperature at regions II, III, and V, as pointed out by the red and blue bands in panels (b) and (c), where hole temperatures were found to be around 5.0 and 7.5 K, respectively. However, at region I, hole temperatures are expected to be close to 17.0 K, as indicated by the gray band in panel (c). By extrapolating the simulations to $P_{el} = 0$, it is found that $T_L + \Delta T_e^{exc}$ must be close to 40 K for the PL1 response and to 70 K for the PL2 emission, demonstrating that the low-energy laser (panel (c)) is more efficient for heating electrons in the GaSb layers than the high-energy laser, due to its greater penetration into the heterostructure. These results confirm that the non-thermalization between electrons and holes leads to a non-linear dependence of $T_{eff}^{e\text{-}h}$ with the applied electrical power.

Considering the effective temperatures extracted from the emission spectra for each region and taking into account the non-thermalization among electrons and holes, a gradient map of the carriers temperature throughout the heterostructure can be sketched as shown in figures 5.11 (a) and (b), for EL and EL+PL conditions, respectively. Color-gradient background represents the independent variations of the electrons (holes) temperature, T_e (T_h). Due to the weak coupling between the crystal lattice and electrons, T_e reaches higher values, of the order of hundreds of Kelvin (red-yellow gradient), than T_h (blue gradient), which is closer to the lattice temperature. When a forward bias voltage is applied, carriers are expected to reach the highest temperatures at region I and the OW (dark colors) due to the highly doping profiles, whereas at regions IV and V, electrons and holes attain the lowest temperatures (light colors).

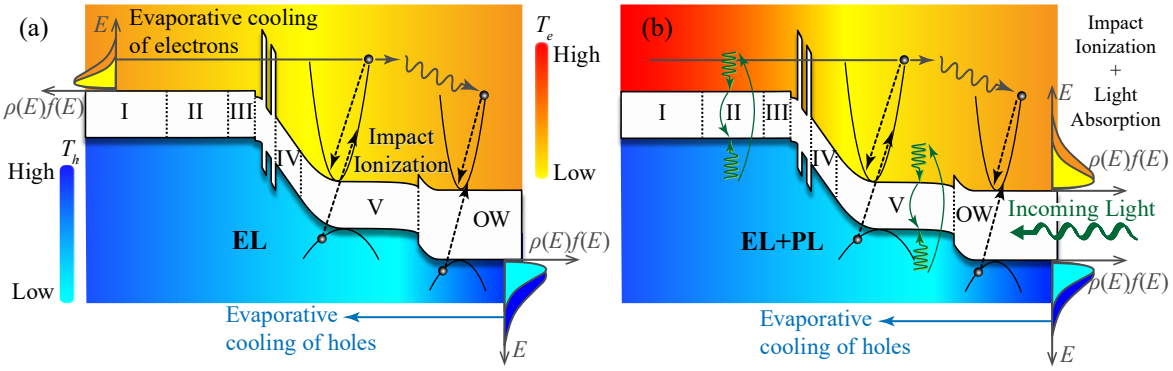

Figure 5.11 – Mapping of the non-equilibrium carriers effective temperature along the heterostructure for (a) EL and (b) EL+PL conditions under an applied forward voltage. Adapted from ref. [8].

This mapping of the local thermalization processes, obtained from the segmentation of the optical characterization of the semiconductor heterostructure, complements the non-trivial picture of the hot-carrier dynamics and their energy relaxation mechanisms. As presented here, these processes depend mainly on the difference between carriers effective masses and the carriers populations, as well as optical and electrical excitations, which prevent electrons and holes from thermalizing among them and with the lattice. Consequently, the effective temperature is affected by changes in holes temperature, especially when the difference with electrons temperature is prominent. In that case, holes temperature can produce noticeable fluctuations in the effective temperature, as well as a non-linear dependence of the carriers effective temperature with electrical power.

5.5 Time-Resolved Carrier Dynamics

Besides the voltage dependence of the carriers effective temperature presented in the last section, the modulation of the majority carrier flux through the DBS also affects the temporal evolution of the carrier dynamics in the quasi-bond states of the double-barrier quantum well. It enables the characterization of contrasting time scales correlated with different relaxation and recombination processes. In this way, the temporal evolution of the QW optical emission in RTD-C has been characterized via TRPL measurements, using the $\hbar\omega_2 = 1.15$ eV excitation laser in pulsed-wave mode, at an optical power density of 1.25×10^4 W/cm^2 and for $T = 4$ K, according to the experimental configuration presented in § 3.4.1. The observed RTD-C transient responses are presented in figure 5.12 (a) at the EL onset ($V = 1.50$ V, top panel), at resonance ($V = 2.10$ V, middle panel), and after resonance ($V = 3.30$ V, bottom panel), as indicated by vertical arrows in the $J(V)$ characteristic under illumination depicted in the inset. The intensity has been normalized, and the Instrument Response Function (IRF) is presented for reference as a gray curve.

At the peak of maximum intensity, after 2 ns, a shoulder-like emission emerges, hamper-

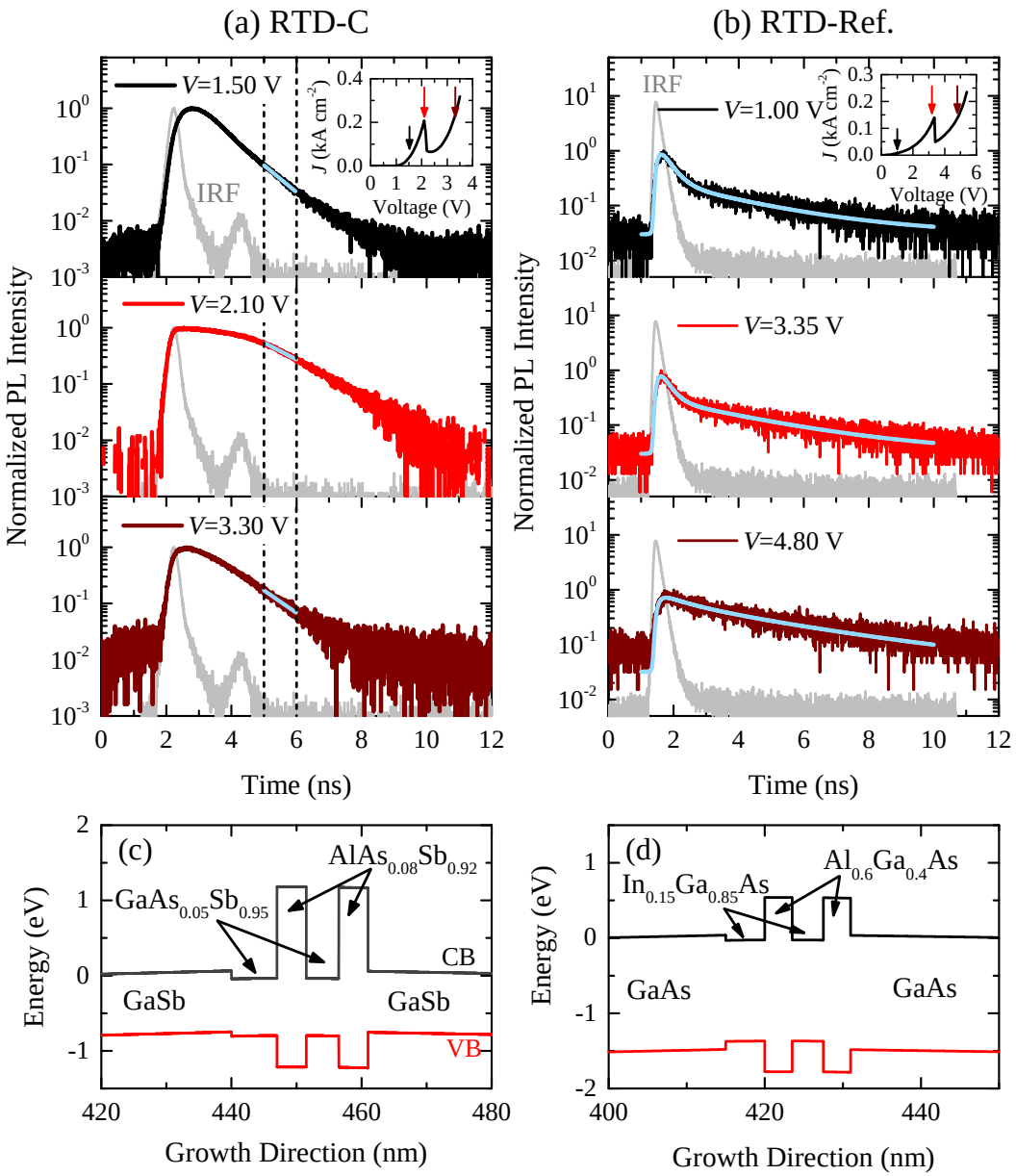

Figure 5.12 – Normalized transient response of the QW optical emission in (a) RTD-C and (b) RTD-Ref, before (top), on- (middle), and after resonance (bottom). The insets show the corresponding $J(V)$ characteristics pointing to the voltages where the transient curves were measured. The results of the fitting procedure to extract the effective lifetimes are shown by light-blue lines. The IRF (gray line) is also displayed. Simulated band profiles of the DBS for (c) RTD-C and (d) RTD-Ref.

ing the implementation of reconvolution models for the extraction of the effective lifetimes since these models are valid only for exponential decays. Close to the resonance, the slow intensity decay produces a plateau that extends up to $t \approx 5$ ns. With a mono-exponential fitting procedure, using a function of the form $\exp(-t/\tau_{\text{eff}})$, an effective lifetime of $\tau_{\text{eff}} = 6$ ns was estimated for the plateau at $V = 2.10$ V, close in value to the limit of radiative recombination reported for GaAsSb/GaAs QWs [41]. The same fitting procedure was performed to fit the decay spectra between 5 and 6 ns (framed within vertical dashed lines), as indicated by straight blue lines. Thus, the influence of the IRF, the plateau, and highly noisy regions

at longer temporal windows was avoided.

The RTD-C results were contrasted with the results obtained for the QW optical emission of a reference RTD (RTD-Ref), as presented in figure 5.12 (b), where the transient responses observed before (top panel), on- (middle panel), and after (bottom panel) resonance is displayed. RTD-Ref is composed of a DBS with an $In_{0.15}Ga_{0.85}As$ emitter prewell and QW. Their thicknesses are 5 and 4 nm, respectively. $Al_{0.6}Ga_{0.4}As$ barriers of 3.5 nm thick sandwich the QW, and n-type GaAs layers surround the structure. An n-type $Al_{0.2}Ga_{0.8}As$ optical window was also deposited on top of the heterostructure. This sample has been described in ref [42], where it was labeled as S-InGaAs. The resonance condition in RTD-Ref is achieved at $V = 3.20$ V, and the QW emission can be detected at 1.547 eV. The calculated band profiles of the DBS for RTD-C and RTD-Ref are displayed in figures 5.12 (c) and (d), respectively, for comparison. The temporal evolution of the QW PL intensity in RTD-Ref were acquired using an excitation laser with an energy of $\hbar\omega = 1.70$ eV and an optical power density of 2.29 kW/cm^2. Before and on-resonance conditions, the transient curves reveal a fast exponential decay followed by a slow one. At higher voltages, only the slow decay prevails. Since the fast decay is observed in the range of influence of the IRF, a reconvolution procedure [43] was performed to fit the decay curves. The resulting fitting curves are shown as blue lines in figure 5.12 (b).

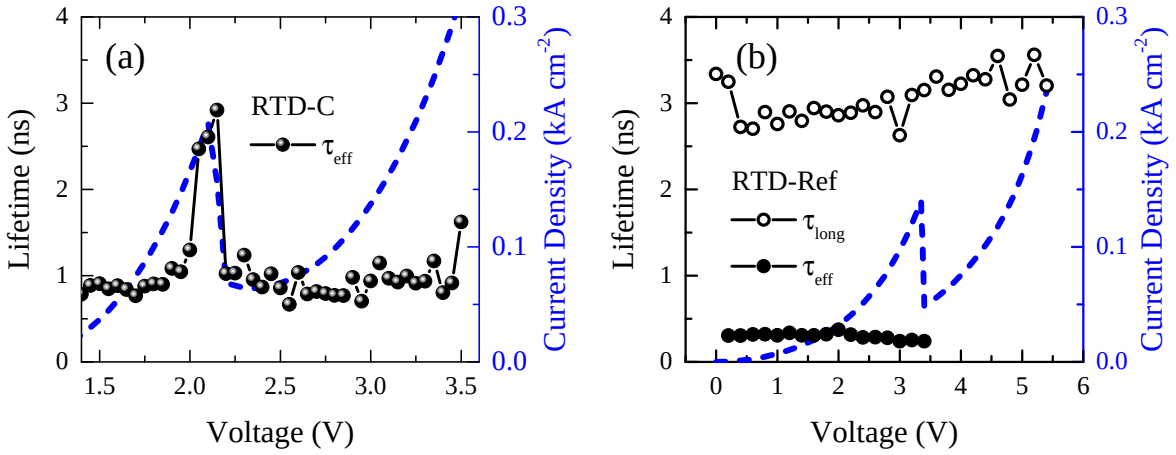

Figure 5.13 – Effective lifetimes as a function of the applied voltage for (a) RTD-C and (b) RTD-Ref. The corresponding $J(V)$ characteristics have been plotted as blue dashed lines.

Figures 5.13 (a) and (b) show the obtained effective lifetimes (as defined in § 1.5) as a function of the applied voltage for RTD-C and RTD-Ref, respectively. The corresponding $J(V)$ characteristics have also been plotted for reference (blue dashed lines). In the case of RTD-C, a remarkable non-monotonic voltage dependence of the effective lifetimes is observed: τ_{eff} shows an almost constant value of ~ 0.9 ns for out-of-resonance conditions, but at resonance, it increases with the current, peaking at ~ 3.0 ns. In contrast, both the fast and slow decays observed in RTD-Ref, keep constant effective lifetimes of $\tau_{\text{eff}} \approx$

0.3 ns and $\tau_{long} \approx 3.0$ ns, respectively, without any apparent correlation with the transport characteristic. τ_{long}, defined by eq. 1.68, can be attributed to accumulation at the prewell and the subsequent non-resonant tunneling of photogenerated carriers [44, 45], which can be also affected by recombination processes in the prewell.

Taking the ratio between τ_{eff} for RTD-C and RTD-Ref before resonance, one obtains a factor of $0.9/0.3 = 3.0$, indicating that effective lifetimes in the Sb-based DBS are three times longer than in the As-based DBS. This difference can be attributed to different factors. First of all, it has been observed that radiative lifetimes in bulk GaSb [46] can be higher than in bulk GaAs [47], depending on the temperature and donor concentrations. It can be assigned to the radiative lifetime (τ_0) dependence on the energy of the optical emission, $\hbar\omega$, as reported in ref. [48]. According to this work, $\tau_0 \propto (|\langle F_e|F_h\rangle|^2 E_p n\hbar\omega)^{-1}$, where $|\langle F_e|F_h\rangle|^2$ accounts for the overlapping between electron and hole wave functions, E_p is the Kane energy, and n is the refractive index in the material [49]. Then, the higher the emission energy, the shorter the radiative lifetime. In this sense, by taking the ratio between the QW emission energies of both samples, one gets a factor of $1.547/0.930 \approx 1.7$, which is almost half the factor obtained from the effective lifetimes. It means that τ_{eff} is not just determined by the recombination processes in the QWs, but other mechanisms must contribute.

In order to understand the discrepancies between the effective lifetimes in both systems, as well as their dependence on the current condition, a three-level rate equation model for the carrier dynamics inside the QW has been proposed. In this model, not only the radiative recombination but also the relaxation or escape processes of carriers play a fundamental role. The time evolution of the carriers population in the QW, after their injection by resonant or non-resonant channels, can be described by the following rate equations,

$$\frac{dn_E}{dt} = S_e - \frac{n_E}{\tau_e} - \frac{n_E}{\tau_T}\left(1 - \frac{n}{N_e}\right), \tag{5.4}$$

$$\frac{dn}{dt} = \frac{n_E}{\tau_T}\left(1 - \frac{n}{N_e}\right) - \frac{np}{\tau_0} - \frac{n}{\tau_e}, \tag{5.5}$$

$$\frac{dp}{dt} = S_h - \frac{np}{\tau_0} - \frac{p}{\tau_h}, \tag{5.6}$$

where n_E is the number of electrons at the emitter side, N_e is the electronic density of states, and $\tau_T \propto \mathcal{T}^{-1}$ is the electron tunneling time through the emitter barrier proportional to the transmission probability, $\mathcal{T}$. In turn, n and p are the number of electrons and holes in the ground quasi-bond state of the QW, and S_i and τ_i are respectively the current source and lifetime for electrons and holes (i =e,h). The optical recombination time is represented by τ_0, and the term $(1 - n/N_e)$ refers to the QW saturation process caused by the finite density of states [41]. The model, drawn in figure 5.14 (a), considers a constant source

of electrons S_e responsible for the injection of carriers from the emitter side into the QW, which depends on the electron tunneling time τ_T. At the resonance condition, the prewell acts as an electrons reservoir and the electron injection rate increases, saturating the QW ground state. This filling process generates the plateaus observed in the transient curves [41].

Carriers inside the QW can also escape or recombine at different time scales. The escape times, τ_i, can be estimated by considering a ping-pong model inside the QW. Classically, a carrier oscillates in the QW with a period, $\tau_{osc}(E)$, where E is the mechanical energy of the carrier in the well [50]. The semiclassical approximation of the escape frequency is then given by,

$$\frac{1}{\tau_i} = \mathcal{T}_i(E)\frac{1}{\tau_{osc,i}(E)}, \tag{5.7}$$

with the period of the classical oscillations as [50, 51],

$$\tau_{osc,i}(E) = 2\sqrt{\frac{2m_i^* E_i}{(eF)^2}}. \tag{5.8}$$

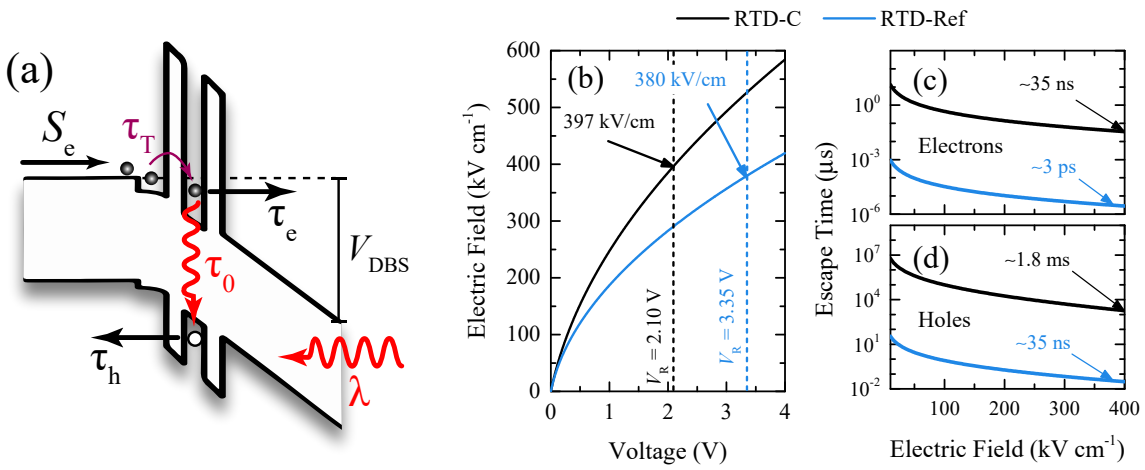

Figure 5.14 – (a) Sketch of the carrier relaxation dynamics in the double-barrier QW after optical excitation. (b) Calculated electric field at the DBS as a function of the applied voltage for RTD-C (black line) and RTD-Ref (blue line). Dashed lines indicate the resonance voltages and the corresponding electric field for each sample. Calculated escape times for (c) electrons and (d) holes in both samples. In each case, arrows point to the obtained escape times at the resonance condition.

In eq. 5.8, F is the local electric field, m_i^* is the carrier effective mass in the QW, and E_i is the carrier confinement energy in the QW. Assuming a triangular QW formed due to the applied voltage, E_i is given by [50],

$$E_i = \zeta_1 eFL_{QW}\left[\frac{\hbar^2}{2m_i^* eFL_{QW}^3}\right]^{1/3}, \tag{5.9}$$

where $\zeta_1 = -2.33$ corresponds to the first zero of the Airy Function ($\mathrm{Ai}(\zeta_1) = 0$), and L_{QW} is the thickness of the QW. The local electric field at the DBS, can be calculated as $F = |V_{DBS}|/l_{DBS}$, with V_{DBS} defined by eq. 2.11 and $l_{DBS} = 20$ nm as an effective DBS length. Figure 5.14 (b) shows the calculated electric field at the DBS as a function of the applied voltage, for RTD-C (black line) and RTD-Ref (blue line). Dashed lines indicate the resonance voltages and their corresponding electric fields. Then, electric fields of around 400 kV cm^{-1} can be expected at the DBSs under resonance conditions. For the calculations, effective permittivities of $\varepsilon = 15\varepsilon_0$ and $13\varepsilon_0$, and nominal donor densities of $N_D^+ = 5\times10^{17}$ cm^{-3} and 2×10^{17} cm^{-3}, were employed for RTD-C and RTD-Ref, respectively.

The transmission, $\mathcal{T}_i(E_i)$, through a thick enough rectangular barrier was considered approximately equal to [50, 51],

$$\mathcal{T}_i(E_i) = 16\left(\Upsilon_i + \frac{1}{\Upsilon_i}\right)^{-2}\exp(-2k_{b,i}L_b), \tag{5.10}$$

where L_b is the barrier thickness, $k_{b,i} = \sqrt{2m^*_{b,i}(U_{b,i}-E_i)}/\hbar$, $\Upsilon_i = k_i m^*_{b,i}/k_{b,i}m^*_i$, and $k_i = \sqrt{2m^*_i E_i}/\hbar$. Here, $m^*_{b,i}$ is the carrier effective mass at the barrier, and $U_{b,i}$ is the barrier height. According to this expressions and replacing eqs. 5.8-5.10 into eq. 5.7, the escape times for electrons and holes in both samples were calculated as a function of the electric field in the DBS, as presented in figures 5.14 (c) and (d), respectively. In these calculations, the nominal values of the barrier and QW thicknesses were used. The time escapes for electrons in RTD-C and RTD-Ref were obtained using QW effective masses of $0.041m_0$ and $0.057m_0$, barrier effective masses of $0.123m_0$ and $0.100m_0$ [26, 52], and barrier heights of 1.23 and 0.55 eV, respectively. In turn, the time escapes for holes in RTD-C and RTD-Ref were found using QW effective masses of $0.405m_0$ and $0.495m_0$, barrier effective masses of $0.919m_0$ and $0.600m_0$ [26, 52], and barrier heights of 0.47 and 0.40 eV, respectively. Barrier heights in both samples were determined by means of the calculated band profiles shown in figures 5.12 (c) and (d). These results suggest that, because of the high band offsets in the Sb-based DBS as compared with the As-based system (see figures 5.12 (c) and (d)), the tunneling probability is reduced and consequently, the escape times increase. Moreover, thicker barriers in RTD-C can also increase the escape times, as suggested by calculations using eq. 5.7 by varying the barrier thickness (not shown here). The reduction of the tunneling rates for thicker barriers have been also observed in different RTDs, as reported in refs. [53, 54].

It is worth noting that the escape times for electrons in RTD-C can be of the order of nanoseconds, similar to the optical recombination time obtained from the plateau of the transient curves, but shorter than the escape times for holes, which can present a slow relaxation dynamics. Taking this into consideration, for sake of simplicity, the analysis

starts by considering optical recombination processes with a recombination time larger than any other time-scales, such that $\tau_0 \to \infty$. As a consequence, the second term on the right side of eqs. 5.5 and 5.6 can be neglected. Taking also into account that the electrons are the majority carriers in the QW, changes produced in the number of holes due to a constant source S_h are also negligible ($S_h/S_e \to 0$). Under these assumptions, the solutions for the equation system depend on the initial number of electrons and holes produced by the laser pulse. These initial populations can be considered as $n_E(0) = n_E^0 + \Delta n_E$, $n(0) = n_0$, and $p(0) = \Delta p_0$ for electrons at the emitter side, and electrons and holes at the QW, respectively. The parameters Δn_E and Δp_0 correspond to variations in the initial carrier populations due to photocreation processes. Thus, in the stationary condition, when there is no laser exciting the sample, $\Delta n_E = \Delta p_0 = 0$.

Solving numerically eqs. 5.4-5.6 for n and p, and assuming $\tau_h/\tau_e = 10^2$ and $S_h/S_e = 0.1$, the optical recombination intensity was calculated as the product of the carrier populations, $\mathcal{I} = np$. Figures 5.15 (a) and (b) display the normalized optical intensity calculated as a function of time for $\tau_0 \to \infty$ and $\tau_0 \sim \tau_e$, respectively, and for different transmission probabilities (blue lines).

In figure 5.15 (a), three time scales for the carrier dynamics become explicit, similar to the transient response observed for RTD-C. These time scales are obtained at three different time ranges highlighted by gray shadow regions at short (light gray), intermediate (gray), and long (dark gray) temporal windows. The first decay is a slow decay, prominent when $\mathcal{T} \to 1$ or $\Delta n_E \to \infty$, and caused by the filling process of the quasi-bond states in the QW. The second decay is a fast decay, determined by the electron-hole pair relaxation process, characterized by $(\tau_{e\text{-}h})^{-1} \equiv (\tau_e)^{-1} + (\tau_h)^{-1}$. The last decay corresponds to a slower dynamics determined by the longer minority carrier lifetime, τ_h. For lower transmission probabilities, the intensity is low and the fast electron-hole pair relaxation dynamics prevail at shorter times. In contrast, at higher transmission probabilities, not only the filling process of the QW states is enhanced, but the intensity increases, leading to a larger amount of remnant carriers at long temporal windows, which can be associated with an increase in the EL background observed on the experiments (not shown here).

These results indicate that long radiative and escape lifetimes, as expected in Sb-based systems, can induce filling processes inside the QW, thus increasing the effective lifetimes at short temporal windows. Recalling that the estimated optical recombination time in the QW of RTD-C, obtained from the plateau observed at resonance, is around 6 ns, then the escape times for electrons in this system must be in the sub-nanosecond scale, which is lower than values obtained in figure 5.14 (c). This discrepancy can be ascribed to the contribution of faster escape channels from the Γ ground state. According to band profile simulations at $V = 0$ V and $T = 4$ K, the separation between Γ and L ground states at the

QW is of ~ 25 meV. Moreover, at the Γ minimum in GaSb-based materials, the density of states is much lower than in the L minimum while the electron effective mass is higher in the L states than in the Γ states [52, 55]. Consequently, a fraction of hot electrons can be scattered into L states at the QW, with $\Gamma \rightarrow L$ scattering times of the order of 10^2 fs [56–58]. This short lifetime can reduce τ_e with respect to τ_0.

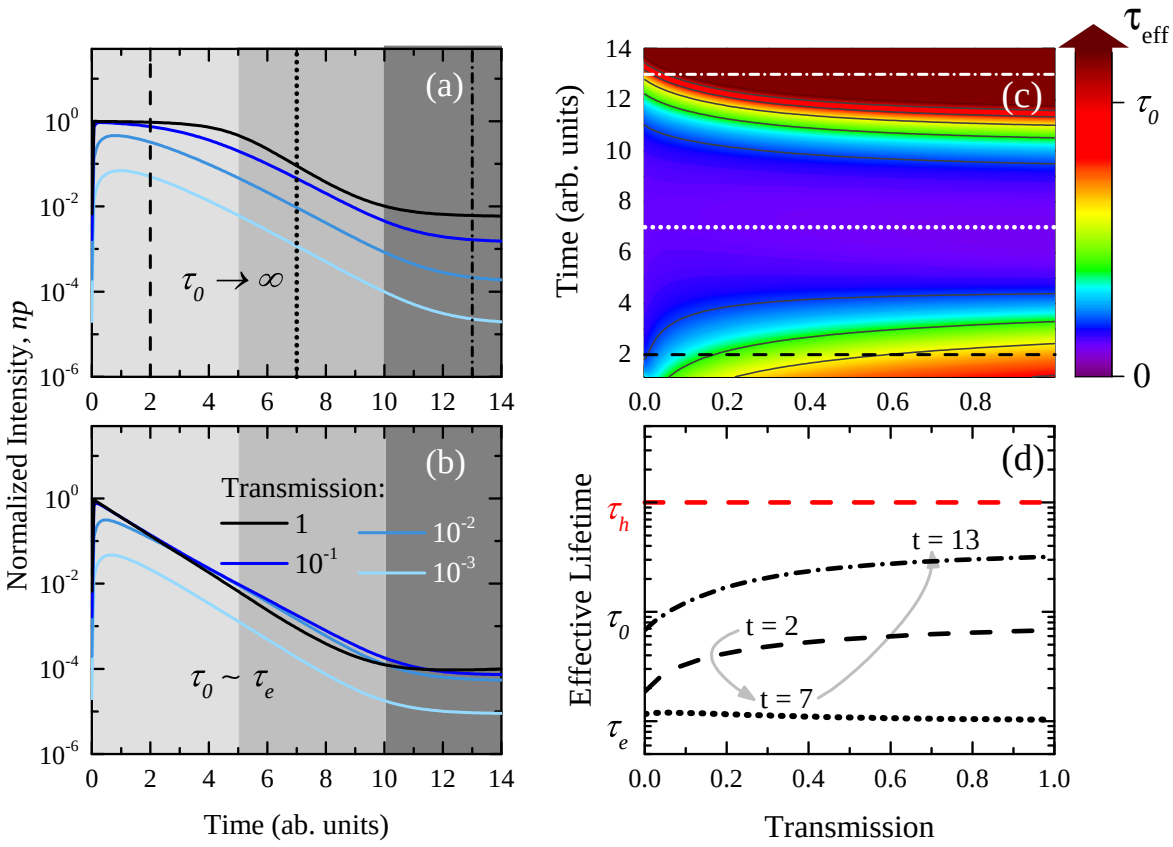

Figure 5.15 – Simulated transient curves for (a) $\tau_0 \rightarrow \infty$ and (b) $\tau_0 \sim \tau_e$, and for different values of the transmission coefficient (blue lines). Short, intermediate, and long temporal windows are indicated with light-gray, gray, and dark-gray shadow regions, respectively. (c) Color-gradient map showing the calculated effective lifetimes as a function of the transmission and time for $\tau_0 > \tau_e$. (b) Dependence of the calculated effective lifetime with the transmission extracted for $t = 2$ (dashed line), $t = 7$ (dotted line), and $t = 13$ (dot-dashed line), as also indicated in panels (a) and (c). At long temporal windows, the long lifetimes goes to the relaxation time for holes (red dashed line).

In contrast, if $\tau_0 \sim \tau_e$ as presented in figure 5.15 (b), only two time-scales can be observed. The first decay is a fast decay ruled by both, electron-hole pair relaxation mechanisms and fast optical recombinations, which hampers filling processes inside the QW. The second decay is again a slow decay at long temporal windows determined by the hole lifetimes. It corresponds to the case of RTD-Ref, where thinner and lower barriers in combination with higher QW optical emission energies reduce the escape times and the radiative lifetime in the QW, keeping the effective lifetime constant, with no modulation with the transmission. These differences between temporal windows in a transient response are crucial for the actual determination and characterization of the

lifetimes, which are unavoidably performed by fitting procedures within a finite temporal window. Under these conditions, the contribution of longer time scales that appear when the intensity is already very low is negligible.

If we consider the intensity transient as an exponential decrease, the effective lifetime can be defined by eq. 1.67, and its evolution with transmission and time can be obtained as shown in the color-map of figure 5.15 (c), where the contrast between short, intermediate, and long temporal windows can be seen. Here, $\tau_0/\tau_e = 10$ was assumed. At short ($t < 5$) and long ($t > 10$) temporal windows, τ_{eff} increases with the transmission, but at intermediate temporal windows, it remains constant at minimum values. To exemplify these situations, the line profiles of τ_{eff} for three times, $t = 2$ (dashed line), $t = 7$ (dotted line), and $t = 13$ (dot-dashed line), also indicated in panel (a), were extracted and plotted as a function of the transmission, as depicted in figure 5.15 (d). Changes in the transmission dependence of the effective lifetimes by modifying the temporal window produce three special cases. If the temporal window increases at short times, $\tau_{eff} \rightarrow \tau_0$ as indicated by the line for $t = 2$. If the temporal window increases at intermediate times, the electron-hole relaxation dynamics preponderate and $\tau_{eff} = \tau_{e\text{-}h}$. But, if the temporal window increases at long times, the slower minority carrier relaxation dynamics become more relevant. In this regime, the long lifetime as defined in eq. 1.68 corresponds to $\tau_{long} = \tau_h > \tau_{e\text{-}h}$ (red dashed line). Since the estimations of the experimental PL lifetimes are unavoidably performed within finite temporal windows, where $\tau_{eff} \neq \tau_{long}$, it would be impossible to prevent their dependence on the transmission, and consequently, on the density current of the majority carriers, according to figure 5.15 (d). However, this is not a drawback but rather an advantage of this procedure since three complementary dynamic conditions can be assessed under low and large currents.

The dependence of the effective lifetime on the applied voltage has been emulated in figures 5.16 (a)-(c) by assuming a Lorentzian function for the transmission as shown by the gray curves in the background and solving the rate equation system for $\tau_0/\tau_e = 1$, $\tau_0/\tau_e = 10$, and $\tau_0/\tau_e \rightarrow \infty$, respectively. The effective lifetimes were extracted at short temporal windows ($t = 2$). Dotted lines correspond to the calculation of the effective lifetime just for holes, τ_{eff}^{h}. Here, the influence of varying the ratio between the holes and electrons sources was also simulated for $S_h/S_e \rightarrow 0$ (black lines), $S_h/S_e = 0.5$ (red lines), and $S_h/S_e = 1$ (blue lines). In all cases, the effective lifetimes increase with S_h/S_e, once the minority relaxation dynamics become more important.

In these calculations, the large current condition at resonance leads to two opposite responses of the effective lifetimes with applied voltage. When $\tau_0/\tau_e = 1$, a dip in the effective lifetimes is obtained at the resonance condition, where τ_{eff} diminishes down to $\tau_{e\text{-}h}$, while very low currents of majority carriers (out of resonance condition) reveal little

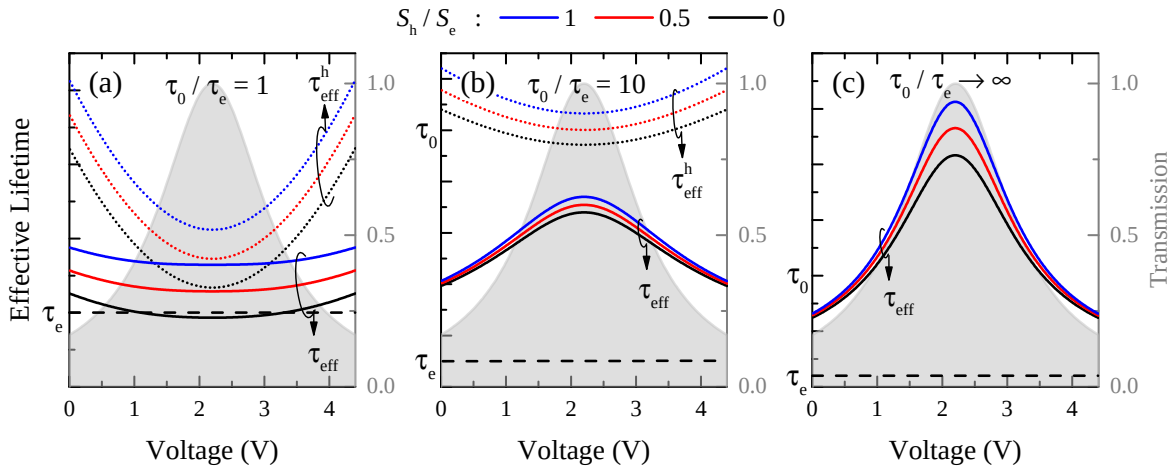

Figure 5.16 – Calculated effective lifetime as a function of the applied voltage for (a) $\tau_0/\tau_e = 1$, (b) $\tau_0/\tau_e = 10$, and (c) $\tau_0/\tau_e \to \infty$. The influence of $S_h/S_e \to 0$ (black lines), $S_h/S_e = 0.5$ (red lines), and $S_h/S_e = 1$ (blue lines) on the effective lifetimes is also depicted. A Lorentzian-like electronic transmission (gray) was assumed for the calculations.

longer effective lifetimes, close to τ_e. It has to do with the fact that filling-of-states processes in the QW are not efficient when radiative lifetimes are comparable with electrons escape times. As a consequence, the dynamics in the QW are ruled by electron-hole relaxation processes. On the other hand, when $\tau_0/\tau_e > 1$, large current conditions induce a peak in the effective lifetimes, which become closer to τ_0 for $\tau_0/\tau_e = 10$, as presented in panel (b), and to τ_h for $\tau_0/\tau_e \to \infty$, as indicated in panel (c). Out of resonance, the effective lifetimes drop due to the enhanced electron-hole pair relaxation dynamics or intervalley scattering processes. To complement the analysis presented here, the influence of changing the electrons escape time on the voltage dependence of the effective lifetimes was explored. Figure 5.17 (a) shows the results of these calculations for $\tau_e \to 0$ (black line), $\tau_e = 1$ (red line) and $\tau_e \to \infty$ (blue line). For the simulations, it was assumed that $S_h/S_e = 0.5$, $\tau_h \sim 10^2$, and $\tau_0 \sim 10$, and the effective lifetimes were extracted at short temporal windows ($t = 2$). Panels (b) and (c) show zooms of the plots for $\tau_e \to 0$ and $\tau_e \to \infty$, respectively, to reveal the voltage dependence in these limit cases.

According to these simulations, if $\tau_e \to \infty$, the optical recombination times prevail as mentioned before, and the effective lifetimes present a weak dependence with voltage, as shown in figure 5.17 (b), which could be undetectable. On the contrary, if the escape time for electrons is much faster than other lifetimes, $\tau_e \to 0$, then the extracted effective lifetimes are closer to τ_e and their dependence with the applied voltage, depicted in figure 5.17 (c), maybe also unnoticeable. This situation may correspond to the RTD-Ref, where electrons relaxation dynamics are expected to be faster than in RTD-C due to its lower and thinner barriers, corroborated by the observed short effective lifetimes plotted in figure 5.13 (b).

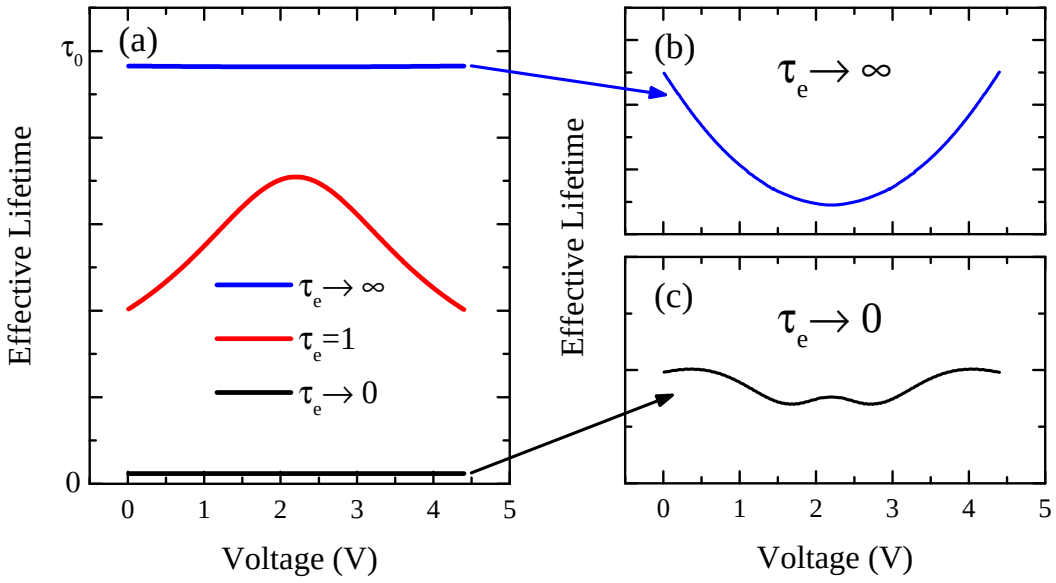

Figure 5.17 – (a) Calculated effective lifetime as a function of the applied voltage for $\tau_e \to 0$ (black line), $\tau_e = 1$ (red line), and $\tau_e \to \infty$ (blue line). Zooms of the limit cases are presented in panels (b) and (c), respectively.

These results account for the correlation between the lifetimes and the $J(V)$ characteristics presented in figure 5.13. Moreover, the lack of correlation of the experimental PL lifetimes and the current for voltages above the resonance indicates that the electrons source, S_e, that affects the electron-hole pair dynamics come essentially from the electronic coherent channel. In summary, the carrier dynamics in double-barrier QWs are ruled by three different time scales corresponding to radiative recombination processes, fast electron-hole pair and intervalley relaxation, and a slow minority carrier (heavy hole) relaxation mechanisms. The former time-scale is favored in Sb-based systems by high coherent currents (resonance condition), if $\tau_e < \tau_0 < \tau_h$, while the fast dynamics is enhanced by low coherent currents (out-of-resonance conditions). However, if $\tau_0 \to \infty$, the slow minority carrier relaxation prevails at resonance conditions, increasing the observed effective lifetimes. Thus, tuning the current through the RTD allows assessing these time scales almost independently.

References

[1] Y. Takeda, A. Ichiki, Y. Kusano, N. Sugimoto, and T. Motohiro, "Resonant tunneling diodes as energy-selective contacts used in hot-carrier solar cells," *J. Appl. Phys.*, vol. 118, no. 12, p. 124510, 2015.

[2] D. Suchet, Z. Jehl, Y. Okada, and J.-F. Guillemoles, "Influence of hot-carrier extraction from a photovoltaic absorber: An evaporative approach," *Phys. Rev. Appl.*, vol. 8, p. 034030, Sep 2017.

[3] T. P. Xiao, K. Chen, P. Santhanam, S. Fan, and E. Yablonovitch, "Electroluminescent refrigeration by ultra-efficient GaAs light-emitting diodes," *J. Appl. Phys.*, vol. 123, no. 17, p. 173104, 2018.

[4] I. Radevici, J. Tiira, T. Sadi, S. Ranta, A. Tukiainen, M. Guina, and J. Oksanen, "Thermophotonic cooling in GaAs based light emitters," *Appl. Phys. Lett.*, vol. 114, no. 5, p. 051101, 2019.

[5] T. Sadi, I. Radevici, and J. Oksanen, "Thermophotonic cooling with light-emitting diodes," *Nat. Photonics*, vol. 14, no. 4, pp. 205–214, 2020.

[6] H. Esmaielpour, V. R. Whiteside, L. C. Hirst, J. G. Tischler, C. T. Ellis, M. P. Lumb, D. V. Forbes, R. J. Walters, and I. R. Sellers, "Effect of occupation of the excited states and phonon broadening on the determination of the hot carrier temperature from continuous wave photoluminescence in InGaAsP quantum well absorbers," *Prog. Photovoltaics*, vol. 25, no. 9, pp. 782–790, 2017.

[7] H. Esmaielpour, M. Giteau, A. Delamarre, F. Gibelli, D.-T. Nguyen, N. Cavassilas, Y. Okada, J.-F. Guillemoles, L. Lombez, and D. Suchet, "Advanced analysis for hot-carriers photoluminescence spectrum," in *Physics, Simulation, and Photonic Engineering of Photovoltaic Devices IX* (A. Freundlich, M. Sugiyama, and S. Collin, eds.), vol. 11275, (San Francisco), pp. 30 – 37, International Society for Optics and Photonics, SPIE, 2020.

[8] E. D. Guarin Castro, A. Pfenning, F. Hartmann, G. Knebl, M. D. Teodoro, G. E. Marques, S. Höfling, G. Bastard, and V. Lopez-Richard, "Optical Mapping of Non-equilibrium Charge Carriers," *J. Phys. Chem. C*, vol. 125, no. 27, p. 14741–14750, 2021.

[9] A. Pfenning, G. Knebl, F. Hartmann, R. Weih, A. Bader, M. Emmerling, M. Kamp, S. Höfling, and L. Worschech, "Room temperature operation of GaSb-based resonant tunneling diodes by prewell injection," *Appl. Phys. Lett.*, vol. 110, no. 3, p. 033507, 2017.

[10] A. Pfenning, G. Knebl, F. Hartmann, R. Weih, M. Meyer, A. Bader, M. Emmerling, L. Worschech, and S. Höfling, "GaSb/AlAsSb resonant tunneling diodes with GaAsSb emitter prewells," *Appl. Phys. Lett.*, vol. 111, no. 17, p. 171104, 2017.

[11] S. Adachi, "Band gaps and refractive indices of AlGaAsSb, GaInAsSb, and InPAsSb: Key properties for a variety of the 2–4-μm optoelectronic device applications," *J. Appl. Phys.*, vol. 61, no. 10, pp. 4869–4876, 1987.

[12] K. Nakashima, "Electrical and optical studies in gallium antimonide," *Jpn. J. Appl. Phys.*, vol. 20, pp. 1085–1094, jun 1981.

[13] M. Wu and C. Chen, "Photoluminescence of liquid-phase epitaxial Te-doped GaSb," *J. Appl. Phys.*, vol. 73, no. 12, pp. 8495–8501, 1993.

[14] E. R. Cardozo de Oliveira, A. Pfenning, E. D. Guarin Castro, M. D. Teodoro, E. C. dos Santos, V. Lopez-Richard, G. E. Marques, L. Worschech, F. Hartmann, and S. Höfling, "Electroluminescence on-off ratio control of $n-i-n$ GaAs/AlGaAs-based resonant tunneling structures," *Phys. Rev. B*, vol. 98, p. 075302, Aug 2018.

[15] C. Van Hoof, J. Genoe, R. Mertens, G. Borghs, and E. Goovaerts, "Electroluminescence from bipolar resonant tunneling diodes," *Appl. Phys. Lett.*, vol. 60, no. 1, pp. 77–79, 1992.

[16] J. W. Cockburn, P. D. Buckle, M. S. Skolnick, D. M. Whittaker, W. I. E. Tagg, R. A. Hogg, R. Grey, G. Hill, and M. A. Pate, "Electroluminescence recombination from excited-state carrier populations in double-barrier resonant-tunneling structures," *Phys. Rev. B*, vol. 45, pp. 13757–13760, Jun 1992.

[17] J. Genoe, C. Van Hoof, K. Fobelets, R. Mertens, and G. Borghs, "pnp resonant tunneling light emitting transistor," *Appl. Phys. Lett.*, vol. 61, no. 9, pp. 1051–1053, 1992.

[18] H. T. Grahn, D. Bertram, H. Lage, K. V. Klitzing, and K. Ploog, "Electroluminescence spectroscopy of resonant tunnelling in GaAs-AlAs superlattices," *Semicond. Sci. Technol.*, vol. 9, pp. 537–539, may 1994.

[19] C. R. H. White, M. S. Skolnick, L. Eaves, and M. L. Leadbeater, "Electroluminescence and impact ionization phenomena in a double-barrier resonant tunneling structure," *Appl. Phys. Lett.*, vol. 58, no. 11, pp. 1164–1166, 1991.

[20] F. Hartmann, A. Pfenning, M. Rebello Sousa Dias, F. Langer, S. Höfling, M. Kamp, L. Worschech, L. K. Castelano, G. E. Marques, and V. Lopez-Richard, "Temperature tuning from direct to inverted bistable electroluminescence in resonant tunneling diodes," *J. Appl. Phys.*, vol. 122, no. 15, p. 154502, 2017.

[21] S. Sze and K. N. Kwok, *Physics of Semiconductor Devices.* New Jersey: John Wiley & Sons, Inc., 3rd ed., 2007.

[22] N. Yokoyama, K. Imamura, H. Ohnishi, T. Mori, S. Muto, and A. Shibatomi, "Resonant-tunneling hot electron transistor (RHET)," *Solid-State Electron.*, vol. 31, no. 3, pp. 577–582, 1988.

[23] M. Heiblum and M. V. Fischetti, "Ballistic hot-electron transistors," *IBM J. Res. Dev.*, vol. 34, no. 4, pp. 530–549, 1990.

[24] M. Dolginov, A. Drakin, L. Druzhinina, P. Eliseev, M. Mil'vidskii, B. Sverdlov, and V. Skripkin, "Injection lasers based on AlGaAsSb/GaSb and InGaAsSb/GaSb heterostructures," *J. Russ. Laser Res.*, vol. 5, no. 3, pp. 349–362, 1984.

[25] H. Zimmermann, "Basics of optical emission and absorption," in *Integrated Silicon Optoelectronics*, vol. 148 of *Springer Series in Optical Sciences*, pp. 1–9, Berlin: Springer, 2009.

[26] O. Madelung, *Semiconductors: Data Handbook*. Berlin: Springer, 3rd ed., 2004.

[27] S. Lyon, "Spectroscopy of hot carriers in semiconductors," *J. Lumin.*, vol. 35, no. 3, pp. 121–154, 1986.

[28] J. Tang, V. R. Whiteside, H. Esmaielpour, S. Vijeyaragunathan, T. D. Mishima, M. B. Santos, and I. R. Sellers, "Effects of localization on hot carriers in InAs/AlAs$_x$Sb$_{1-x}$ quantum wells," *Appl. Phys. Lett.*, vol. 106, no. 6, p. 061902, 2015.

[29] J. Shah, A. Pinczuk, A. C. Gossard, and W. Wiegmann, "Energy-loss rates for hot electrons and holes in GaAs quantum wells," *Phys. Rev. Lett.*, vol. 54, pp. 2045–2048, May 1985.

[30] R. A. Höpfel, J. Shah, and A. C. Gossard, "Nonequilibrium electron-hole plasma in GaAs quantum wells," *Phys. Rev. Lett.*, vol. 56, pp. 765–768, Feb 1986.

[31] H. M. van Driel, X. Zhou, W. W. Rühle, J. Kuhl, and K. Ploog, "Photoluminescence from hot carriers in low-temperature-grown gallium arsenide," *Appl. Phys. Lett.*, vol. 60, no. 18, pp. 2246–2248, 1992.

[32] H. Esmaielpour, L. Lombez, M. Giteau, A. Delamarre, D. Ory, A. Cattoni, S. Collin, J.-F. Guillemoles, and D. Suchet, "Investigation of the spatial distribution of hot carriers in quantum-well structures via hyperspectral luminescence imaging," *J. Appl. Phys.*, vol. 128, no. 16, p. 165704, 2020.

[33] J. R. Meyer, F. J. Bartoli, and M. R. Kruer, "Optical heating in semiconductors," *Phys. Rev. B*, vol. 21, pp. 1559–1568, Feb 1980.

[34] W. Ketterle and N. V. Druten, "Evaporative cooling of trapped atoms," in *Advances In Atomic, Molecular, and Optical Physics* (B. Bederson and H. Walther, eds.), vol. 37, (San Diego), pp. 181 – 236, Academic Press, 1996.

[35] A. Yangui, M. Bescond, T. Yan, N. Nagai, and K. Hirakawa, "Evaporative electron cooling in asymmetric double barrier semiconductor heterostructures," *Nat. Commun.*, vol. 10, no. 1, p. 4504, 2019.

[36] H. Heinrich and W. Jantsch, "Experimental determination of the electron temperature from Burstein-shift experiments in gallium antimonide," *Phys. Rev. B*, vol. 4, pp. 2504–2508, Oct 1971.

[37] B. Das, A. Basu, J. Das, and D. Bhattacharya, "Effective temperature of the non-equilibrium electrons in a degenerate semiconductor at low lattice temperature," *Phys. B*, vol. 474, pp. 21 – 26, 2015.

[38] V. L. Bonch-Bruevich and S. G. Kalashnikov, "XVI - Hot Electrons," in *The Physics of Semiconductors - Russian Edition*, (Moscow), pp. 523–524, Nauka, 1977.

[39] J. Shah, "IV.1 - Ultrafast luminescence studies of carrier relaxation and tunneling in semiconductor nanostructures," in *Hot Carriers in Semiconductor Nanostructures: Physics and Applications*, (San Diego), pp. 279–312, AT&T, Academic Press, 1992.

[40] H. L. Cui, X. L. Lei, and N. J. M. Horing, "Negative minority-electron mobility in a nonequilibrium electron-hole plasma," *Phys. Rev. B*, vol. 37, pp. 8223–8227, May 1988.

[41] M. Baranowski, M. Syperek, R. Kudrawiec, J. Misiewicz, J. A. Gupta, X. Wu, and R. Wang, "Carrier dynamics in type-II GaAsSb/GaAs quantum wells," *J. Phys.: Condens. Matter*, vol. 24, p. 185801, apr 2012.

[42] E. Cardozo de Oliveira, A. Naranjo, A. Pfenning, V. Lopez-Richard, G. Marques, L. Worschech, F. Hartmann, S. Höfling, and M. Teodoro, "Determination of Carrier Density and Dynamics via Magnetoelectroluminescence Spectroscopy in Resonant-Tunneling Diodes," *Phys. Rev. Applied*, vol. 15, p. 014042, Jan 2021.

[43] PicoQuant, *FluoFit: Global Fluorescence Decay Data Analysis Software - User's Manual and Technical Data*. PicoQuant GmbH, Berlin, Germany, 2018.

[44] H. Käß, W. Schuddinck, E. Goovaerts, C. Van Hoof, and G. Borghs, "Photoluminescence investigation of the tunnelling dynamics of holes and electrons in a p-type AlAs/GaAs resonant tunnelling structure," *Microelectron. Eng.*, vol. 43-44, pp. 355–361, 1998.

[45] I. Romandic, A. Bouwen, E. Goovaerts, C. V. Hoof, and G. Borghs, "Time-resolved photoluminescence spectroscopy of tunnelling processes in a bipolar AlAs/GaAs resonant-tunnelling structure," *Semicond. Sci. Technol.*, vol. 15, pp. 665–675, jun 2000.

[46] A. Y. Vul', "Ch. 6. gallium antimonide (gasb)," in *Handbook Series on Semiconductor Parameters* (M. Levinshtein, S. Rumyantsev, and M. Shur, eds.).

[47] G. W. 't Hooft and C. van Opdorp, "Temperature dependence of interface recombination and radiative recombination in (Al, Ga)As heterostructures," *Appl. Phys. Lett.*, vol. 42, no. 9, pp. 813–815, 1983.

[48] U. Bockelmann, "Exciton relaxation and radiative recombination in semiconductor quantum dots," *Phys. Rev. B*, vol. 48, pp. 17637–17640, Dec 1993.

[49] D. F. Cesar, M. D. Teodoro, V. Lopez-Richard, G. E. Marques, E. M. Jr., V. G. Dorogan, Y. I. Mazur, and G. J. Salamo, "Carrier transfer in the optical recombination of quantum dots," *Phys. Rev. B*, vol. 83, p. 195307, May 2011.

[50] G. Bastard, J. Brum, and R. Ferreira, "Electronic States in Semiconductor Heterostructures," in *Semiconductor Heterostructures and Nanostructures* (H. Ehrenreich and D. Turnbull, eds.), vol. 44 of *Solid State Physics*, pp. 229–415, Academic Press, 1991.

[51] G. Bastard, *Wave Mechanics Applied to Semiconductor Heterostructures*. Paris: les éditions de physique, 1990.

[52] I. Vurgaftman, J. R. Meyer, and L. R. Ram-Mohan, "Band parameters for III–V compound semiconductors and their alloys," *J. Appl. Phys.*, vol. 89, no. 11, pp. 5815–5875, 2001.

[53] M. Tsuchiya, T. Matsusue, and H. Sakaki, "Tunneling escape rate of electrons from quantum well in double-barrier heterostructures," *Phys. Rev. Lett.*, vol. 59, pp. 2356–2359, Nov 1987.

[54] C. Van Hoof, E. Goovaerts, and G. Borghs, "Sequential hole tunneling in n-type AlAs/GaAs resonant-tunneling structures from time-resolved photoluminescence," *Phys. Rev. B*, vol. 46, pp. 6982–6989, Sep 1992.

[55] P. Snow, D. Westland, J. Ryan, T. Kerr, H. Munekata, and L. Chang, "Hot carrier cooling in GaSb: Bulk and quantum wells," *Superlattices Microstruct.*, vol. 5, no. 4, pp. 595–598, 1989.

[56] W. S. Pelouch and L. A. Schlie, "Ultrafast carrier dynamics in GaSb," *Appl. Phys. Lett.*, vol. 66, no. 1, pp. 82–84, 1995.

[57] H. P. M. Pellemans, W. T. Wenckebach, and P. C. M. Planken, "Sub-Picosecond Far-Infrared Transient-Grating Measurements of Electron Cooling in InAs and GaSb," in

Ultrafast Phenomena X (P. F. Barbara, J. G. Fujimoto, W. H. Knox, and W. Zinth, eds.), (Berlin, Heidelberg), pp. 400–401, Springer Berlin Heidelberg, 1996.

[58] D. Smith, E. O'Sullivan, L. Rota, A. Maciel, and J. Ryan, "Ultrafast optical response and inter-valley scattering in GaSb/AlSb quantum wells," *Phys. E*, vol. 2, no. 1, pp. 156–160, 1998.

Chapter 6

Contrasting Magneto-transport and Magneto-optical Bistabilities

Besides the complex transport and optical properties of RTDs presented in previous chapters, the investigation of bistabilities close to the NDR region, as introduced in § 2.3.1, unveils peculiar optoelectronic responses that provide fundamental insights about the complex quantum transport physics in semiconductor heterostructures. The understanding of these dynamics linked to the emergence of a bistable conductive state, not only powers binary or multiple-valued logic applications [1–3] but also provides clues on how to modulate the optical emission with external factors such as temperature and applied electric and magnetic fields [4–7].

In this chapter, the temperature and magnetic-field dependence of the bistable transport properties and optical emission of unipolar resonant tunneling diodes are discussed. The unanticipated pinched hysteresis observed in the transport characteristic of the device has been ascribed to the intrinsic *magnetoresistance*, also responsible for the bistable optical emission of the sample. However, the bistable transport and optical characteristics seem to be detached since the qualitative shape of the optical bistability remains the same as the temperature and intrinsic resistance grow. The apparent disconnection between the transport and optical responses can be comprehended by taking into account the interplay among three independent tunneling transport channels. These channels are effective in generating electrons with energy enough to be involved in impact ionization processes. Particularly, the interband tunneling through the bandgap of the absorber that triggers the Zener tunneling breakdown also favors the production of holes at low temperatures. Considering these mechanisms, the pinched hysteresis in the $I(V)$ characteristics and the broadening of the optical hysteresis loop area has been unambiguously correlated to the intrinsic magnetoresistance, as demonstrated by magnetotransport experiments in a wide temperature range.

6.1 The Magneto-transport Bistability

The transport characteristics of RTD-D were studied in the temperature range from 4 up to 200 K and under applied magnetic fields up to 8 T parallel to the growth direction. The heterostructure layout was presented in figure 3.2 (d), and the $I(V)$ characteristics at zero applied magnetic fields ($B = 0$) are presented in figure 6.1 (a) for two different temperatures. After sweeping the applied voltage around the resonance condition, as represented by the color single-arrows, a bistable state is unveiled for each temperature. At T =200 K, the $I(V)$ characteristic exhibits a current peak of $I_p = 1.7$ mA, and a valley current of $I_v = 0.5$ mA with a PVCR of 3.4. These currents are observed, respectively, at the threshold voltages $V_u = 7.22$ V for the up-sweep, and $V_d = 6.76$ V for the down-sweep voltage direction. When the temperature is reduced, the bistability keeps its qualitative shape but suffers a shift to higher voltages [6]. Thus, at $T = 2$ K, peak and valley currents of $I_p = 2.5$ mA and $I_v = 1.3$ mA are detected at $V_u = 9.68$ V and $V_d = 9.50$ V, respectively, with a reduced PVCR of 1.9. The observed hysteresis can be ascribed to the presence of an intrinsic resistance, R, as discussed in § 2.3.1, whose value can be estimated according to eq. 2.19 for $R_{NDR} \to 0$. In other words, the ratio between the width and height of the hysteresis, taken as $\Delta V_h = V_u - V_d$ and $\Delta I_h = I_p - I_v$, respectively, as indicated by double arrows in figure 6.1 (a), provides the value of the intrinsic resistance, $R = \Delta V_h / \Delta I_h$. In this way, $R = 158\ \Omega$ at $T = 2$ K, and $R = 392\ \Omega$ at $T = 200$ K. Then, by reducing the temperature, the hysteresis not only is shifted to higher voltages but also its width is shrunk, a fact reflected in the decrease of the intrinsic resistance. The temperature-induced voltage shift of the bistable region in this RTD was already explored in ref. [6], where this response has been ascribed to an increasing charge buildup, close to the DBS, and the screening of the electric field as the temperature rises.

In the presence of an external magnetic field, the $I(V)$ characteristic exhibits a non-trivial magnetotransport response. Previous studies have documented the signatures of applied magnetic fields in the RTDs transport properties. They range from oscillations of the conductance [8, 9] produced by the magnetic field quantization of electronic states up to modulations of the intrinsic bistability in the current-voltage response induced by charge accumulation in the quantum well [10]. However, the magnetotransport characteristics presented here reveal an unanticipated response. Figures 6.1 (b) and (c) show the evolution of the bistability at T =2 and 200 K, respectively, when the applied magnetic field increases. The $I(V)$ characteristics have been shifted vertically in these figures for clarity. In both cases, the bistable state widens and twists into a pinched hysteresis loop by increasing the magnetic field. At cryogenic temperatures, the pinched hysteresis is obtained at lower magnetic fields. For example, at T =2 K, the pinched hysteresis is observed from $B = 3$ T

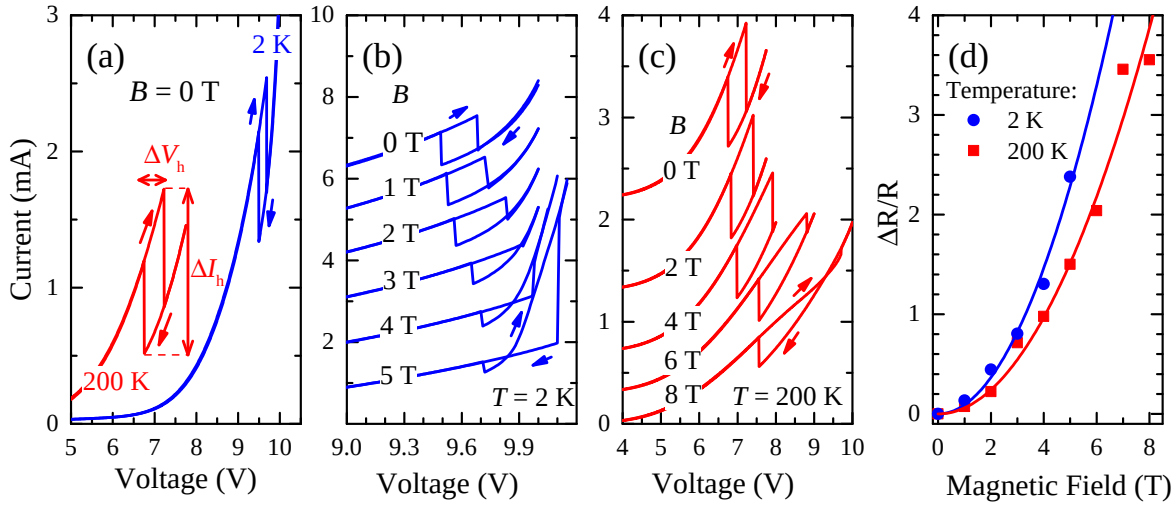

Figure 6.1 – (a) RTD-D $I(V)$ characteristics at zero applied magnetic fields for $T = 200$ K (red line) and $T = 4$ K (blue line). The width, ΔV_h, and height, ΔI_h, of the hysteresis are also indicated. Corresponding $I(V)$ characteristics at different applied magnetic fields for (b) $T = 200$ K (red) and (c) $T = 4$ K (blue). The curves have been shifted vertically for clarity. (d) Relative magnetoresistance for $T = 2$ K (blue circles) and $T = 200$ K (red squares) as a function of the magnetic field. The data points were obtained from the measured $I(V)$ characteristics, according to eq. 6.1. Solid lines represent the best parabolic fits.

while at T =200 K, it appears from $B = 8$ T. As mention before, the widening of the bistable region is evidence of an increasing intrinsic resistance, but, this time, caused by the applied magnetic field.

The magnetic field tuning of the intrinsic resistance, $R(B)$, has been characterized by its relative increase with respect to the value at $B = 0$ T, $R(0\text{ T})$, as

$$\frac{\Delta R}{R} = \frac{R(B) - R(0\text{ T})}{R(0\text{ T})} \tag{6.1}$$

The results corresponding to the experiments displayed in figures 6.1 (b) and (c) have been plotted in panel (d) as functions of the magnetic field for both $T = 2$ K (blue circles) and $T = 200$ K (red squares). A parabolic relation, $\Delta R/R = \beta B^2$, can be expected as reported in ref. [11], where β depends mainly on the geometry of the Fermi surfaces. The best fits of the experimental data using this expression are presented in figure 6.1 (d) as solid lines. They give as a result $\beta(2\text{ K}) = 0.091 \pm 0.003\text{ T}^{-2}$ and $\beta(200\text{ K}) = 0.061 \pm 0.002\text{ T}^{-2}$. Since β is also directly proportional to the scattering time [11], the reduction of its value by rising the temperature confirms that scattering processes in the heterostructure are faster at higher temperatures. It is also worth noting that the absolute value of the intrinsic resistance grows from a few hundreds of Ohms to almost 2 kΩ as the magnetic field increases.

The magnetotransport response of the diode can be simulated by assuming a current density, $J(V_{\text{RTD}})$, dependent on the voltage drop in the RTD, V_{RTD}, with the contribution of three transport channels for majority carriers (electrons), such that $J(V_{\text{RTD}}) =$

$J_{co}(V_{RTD}) + J_{inco}(V_{RTD}) + J_{ZTB}(V_{RTD})$. All of them have been illustrated in figure 6.2 (a), where a schematic representation of the RTD band profile under a high applied voltage has also been sketched. Here, $J_{co}(V_{RTD})$ (black arrow) corresponds to a resonant coherent channel through the DBS, as described by eq. 2.15. It can be simplified within the approximation proposed by Schulman et al. [12] for the transmission coefficient, assuming elastic, Γ_e, and inelastic, Γ_i, broadening of the transmission peak [6, 13], as

$$J_{co}(V_{RTD}) = \frac{e m^* k_B T \Gamma_e}{4\pi^2 \hbar^3} \ln\left[\frac{1+\exp\left(\frac{E_F - E_r + \zeta e V_{RTD}}{k_B T}\right)}{1+\exp\left(\frac{E_F - E_r - \zeta e V_{RTD}}{k_B T}\right)}\right]\left[\frac{\pi}{2} + \tan^{-1}\left(\frac{E_r - \zeta e V_{RTD}}{\Gamma_i/2}\right)\right] \tag{6.2}$$

where for $T = 200$ K, $m_e^* = 0.063 m_0$ is the effective electron mass at the GaAs quantum well, $E_F = 50$ meV is the Fermi level, $E_r = 150$ meV is the resonant energy level in the quantum well [6], $\Gamma_e = 0.07$ meV, $\Gamma_i = \Gamma_e + (2 \times 10^{-8})T$, and $\zeta = 0.024$. In turn, $J_{inco}(V_{RTD})$ (gray arrow) describes the incoherent transport of carriers characterized by eq. 2.16, using, $J_0 = 10^{-1}$ mA and $\eta = 10^{-3}$, in this case. The last contribution, J_{ZTB} (orange arrow), symbolizes the transport channel due to *Zener tunneling breakdown* (ZTB) observed when electrons in filled VB states tunnel through the bandgap of a narrow-gap semiconductor by the action of a high electric field. After tunneling, VB electrons reach conduction band levels, leaving holes at the VB [14, 15]. Zener tunneling can be described by the expression (see ref. [16], Ch. 8),

$$J_{ZTB}(V_{RTD}) = J_0^{ZTB} \exp\left[-\frac{4}{3}\frac{\sqrt{2m_{ng}^*}}{\hbar e F(V_{RTD})} E_{ng}^{3/2}\right] \tag{6.3}$$

In the case of RTD-D, this interband tunneling is ascribed to the $Ga_{0.89}In_{0.11}N_{0.04}As_{0.96}$ layer, since its high doping profile favors a pronounced depletion under high forward voltages. Moreover, this quaternary layer presents the lowest bandgap energy of the heterostructure (see figure 3.2 (d)), which implies a reduced potential barrier for Zener tunneling of electrons coming from the VB. In view of this, in eq. 6.3 we have: $J_0^{ZTB} = 0.25$ A, $m_{ng}^* \approx 0.1 m_0$, the effective electron mass in the narrow-gap GaInNAs layer [17, 18], with a bandgap energy of $E_{ng} \approx 1.00$ eV [19, 20], and $F = V_{RTD}/L_{eff}$, the local electric field defined by an effective length of $L_{eff} = 20$ nm. In addition, if the coherent and incoherent channels are assumed to coexist with the intrinsic resistance, R, then the total applied voltage, V, can be obtained according to eq. 2.18, by considering $I(V_{RTD}) = A[J_{co}(V_{RTD}) + J_{inco}(V_{RTD})]$, with $A = \pi r^2$ as the RTD-D's cross sectional area defined by a mesa radius of $r = 3$ μm.

The simulated total current as a function of V has been displayed in figure 6.2 (b) for $T = 200$ K and $B = 4$ T, which corresponds to an intrinsic resistance of $R = 775\ \Omega$, according to eq. 6.1 and the parabolic fitting presented in figure 6.1 (d). The contributions of each transport channel have also been plotted in figure 6.2 (c) for the coherent (black line),

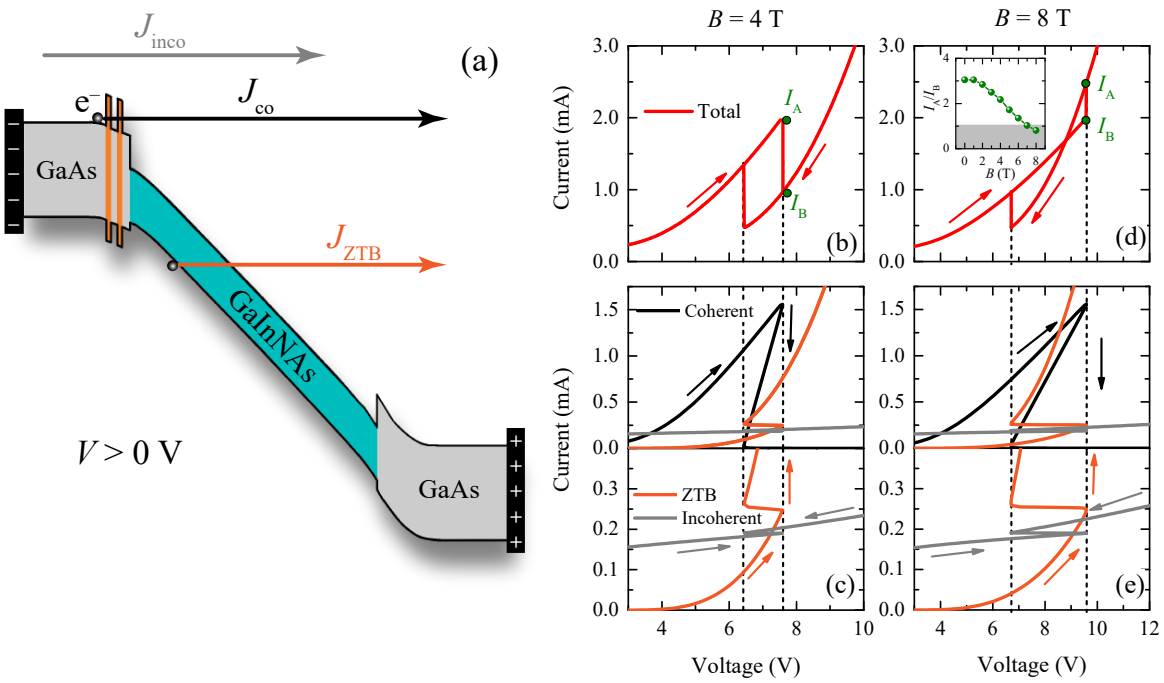

Figure 6.2 – (a) Sketch of the RTD-D band profile under a high applied forward voltage. Black, gray, and orange arrows indicate coherent, incoherent, and ZTB transport of electrons, respectively. (c) Total $I(V)$ characteristics calculated for T =200 K and a magnetoresistance of $R = 775\ \Omega$, corresponding to an applied magnetic field of B =4 T. (c) Simulated contribution of the coherent (black), incoherent (gray), and ZTB (orange) transport channels for the same magnetic field as in (b).Panels (d) and (f) present the same simulations as in (b) and (c), respectively, but for a resistance of $R = 1.9\ \text{k}\Omega$, equivalent to a magnetic field of B =8 T. The inset in (e) displays the current ratio, I_A/I_B as a function of the magnetic field, obtained from the currents at points A and B (green points) in the $I(V)$ characteristics. The gray region corresponds to the ratios obtained from pinched hysteresis.

incoherent (gray line), and ZTB (orange line) components. Panels (d) and (e) also present the simulations for the total current and the transport channels, respectively, for $B = 8$ T, corresponding to an intrinsic resistance of $R = 1.9\ \text{k}\Omega$. The obtained qualitative shapes of the hysteresis agree with the experimental hysteresis depicted in figure 6.1 (c). The simulations indicate that an increase in the intrinsic resistance caused by the increasing external magnetic field leads to the bistability twisting into a pinched hysteresis. The inset in figure 6.2 (d) shows the ratio, I_A/I_B, between the currents at points A and B (green points) of the simulated $I(V)$ characteristics as a function of the magnetic field. It reveals that the pinched hysteresis must emerge at magnetic fields above ~ 7 T (gray shadow region) for $T = 200$ K. Thus, the transition from a bistable to a pinched current-voltage response can be ascribed to the tuning of the magnetoresistance and the coexistence of the transport channels introduced above.

Note that two qualitatively different hysteretic patterns appear for each current component. During an up-sweep of the voltage, as indicated by arrows in figures 6.2 (c) and

(e), the current contribution through the coherent channel (top panels) sharply drops at the resonance voltage, leading to a clockwise bistability, while both, the incoherent and ZTB currents (bottom panels) increase at the same voltage condition, producing an anticlockwise loop. The magnetic field then modulates the intrinsic magnetoresistance, inducing a voltage shift of the transport channels to higher voltages and changing their relative contributions to the total current. In this way, at low voltages before the resonance condition, the incoherent channel is dominant. However, at higher voltages, the coherent and ZTB channels prevail, being the pinched hysteresis the result of their crossing, which is produced by the magnetoresistance voltage shift close to the resonance, as shown in the top panel of figure 6.2 (e). Consequently, the width of the bistable region and the induced pinched hysteresis can be modulated by an applied magnetic field.

6.2 The Bistable Optical Emission

Besides the singular transport properties of RTD-D, it also exhibits an EL emission that can be modulated not only by temperature, as reported in ref. [7] but also by external magnetic fields. The latter unveils peculiar traces that can be attributed separately to each transport channel, thus providing clues on how to tune the optical emission with external factors. In contrast to the reported conclusions in refs. [21, 22], where the light emission is assumed to be triggered just by cross-gap Zener transitions, we provide convincing evidence that holes are also generated through impact ionization processes. This has been already stated in ref. [7] by comparing the light emission of RTD-D with a reference sample where the collector region was removed. The present discussion addresses the relative contribution of the transport channels to the EL emission by exploiting its non-trivial magnetotransport response.

The EL spectra at $T = 5$ K for zero-applied magnetic fields have been depicted in figure 6.3 (a) for different voltage regimes. Two main emission bands with maximums at 1.52 eV and 1.69 eV can be identified corresponding to the light emitted from the GaAs collector region and within the double-barrier quantum well. As expected, the latter emission disappears beyond resonance (red and orange spectra) due to electron shortage. The integrated EL emission of the GaAs spectra as a function of voltage (red spheres) is displayed in figure 6.3 (b) for the same conditions as in panel (a). The corresponding $I(V)$ characteristic (black line) has also been plotted as a reference. The integrated EL emission also presents an optical bistability at the same voltage region of the transport bistability, but with an anticlockwise hysteresis contrary to the clockwise hysteresis of the $I(V)$ characteristic. When a magnetic field is applied, the $I(V)$ characteristic transits from a clockwise towards a pinched hysteresis, as discussed before, while the optical bistability keeps the anticlockwise hysteresis, just increasing its internal area. It can be evidenced in

figure 6.3 (c), where both the observed $I(V)$ characteristic and the integrated EL intensity have been plotted for a magnetic field of $B = 5$ T at $T = 5$ K.

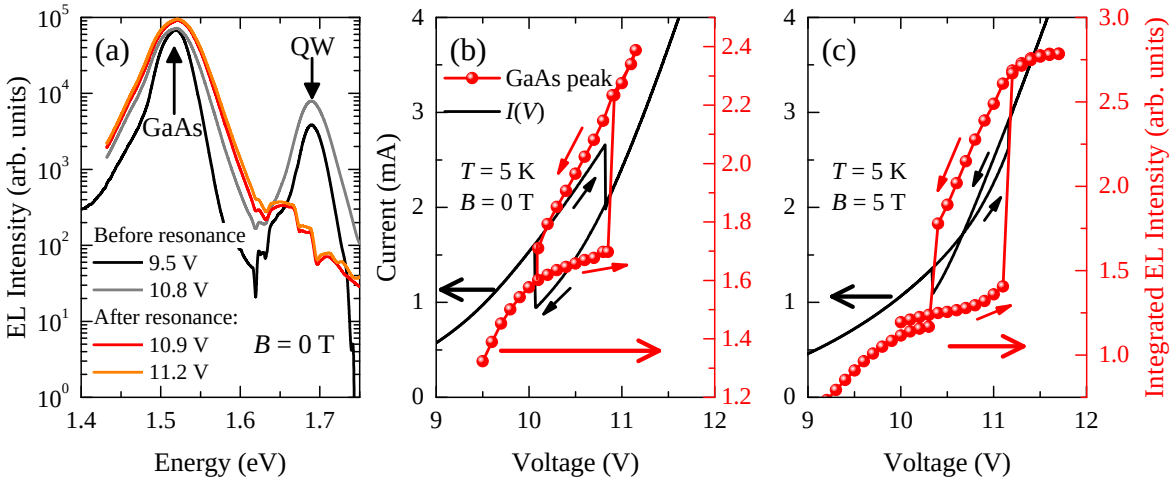

Figure 6.3 – (a) Electroluminescence spectra detected before (black and gray lines) and after (red and orange lines) resonance at $T = 5$ K. Correlation between the $I(V)$ characteristics (black lines) and the integrated intensity for the GaAs optical emissions (red dots) at $T = 5$ K for (b) $B = 0$ T and (c) $B = 5$ T.

In unipolar n-doped systems like RTD-D, two mechanisms can contribute to the generation of holes necessary for the EL emission. One mechanism has to do with the impact ionization process, induced by highly energetic electrons moving through the structure as discussed in the preceding chapter and refs. [4, 7, 23, 24]. This mechanism can, in principle, be associated with all the three transport channels detailed before. The other mechanism depends only on the Zener tunneling, triggered within the GaInNAs layer, as assumed in refs. [15, 21, 22]. The former mechanism has been sketched in the schematic band profile of figure 6.4 (a) with dashed arrows, whilst the latter has been represented by the orange solid arrow. Holes generated via these processes can subsequently be transported toward the inner regions of the heterostructure, as indicated by the horizontal blue arrow. Thus, photons can be emitted at different parts of the heterostructure where electrons and holes recombine as evinced in the EL spectra depicted in figure 6.3 (a).

Although the elucidation of the relative contribution of each transport channel to the hole generation and consequently, to the optical emission, is a puzzling task, as they are additively intertwined, it can be assumed that the amount of holes produced via impact ionization is proportional to the impact ionization rate (see eq. 1.48), given by [25],

$$\Pi(V_{\mathrm{RTD}}) = C\left(\frac{eV_{\mathrm{RTD}} - E_{\mathrm{th}}}{E_{\mathrm{th}}}\right)^{a}, \tag{6.4}$$

where, for GaAs, $C = 93.659 \times 10^{10}$ s^{-1}, $a = 4.743$ and $E_{\mathrm{th}} = (1 + 2m_{\mathrm{e}}^{*}/m_{\mathrm{h}}^{*})/(1 + m_{\mathrm{e}}^{*}/m_{\mathrm{h}}^{*})E_{\mathrm{g}}$, is the threshold energy above which the ionization process is triggered, being $m_{\mathrm{e}}^{*} = 0.063m_0$

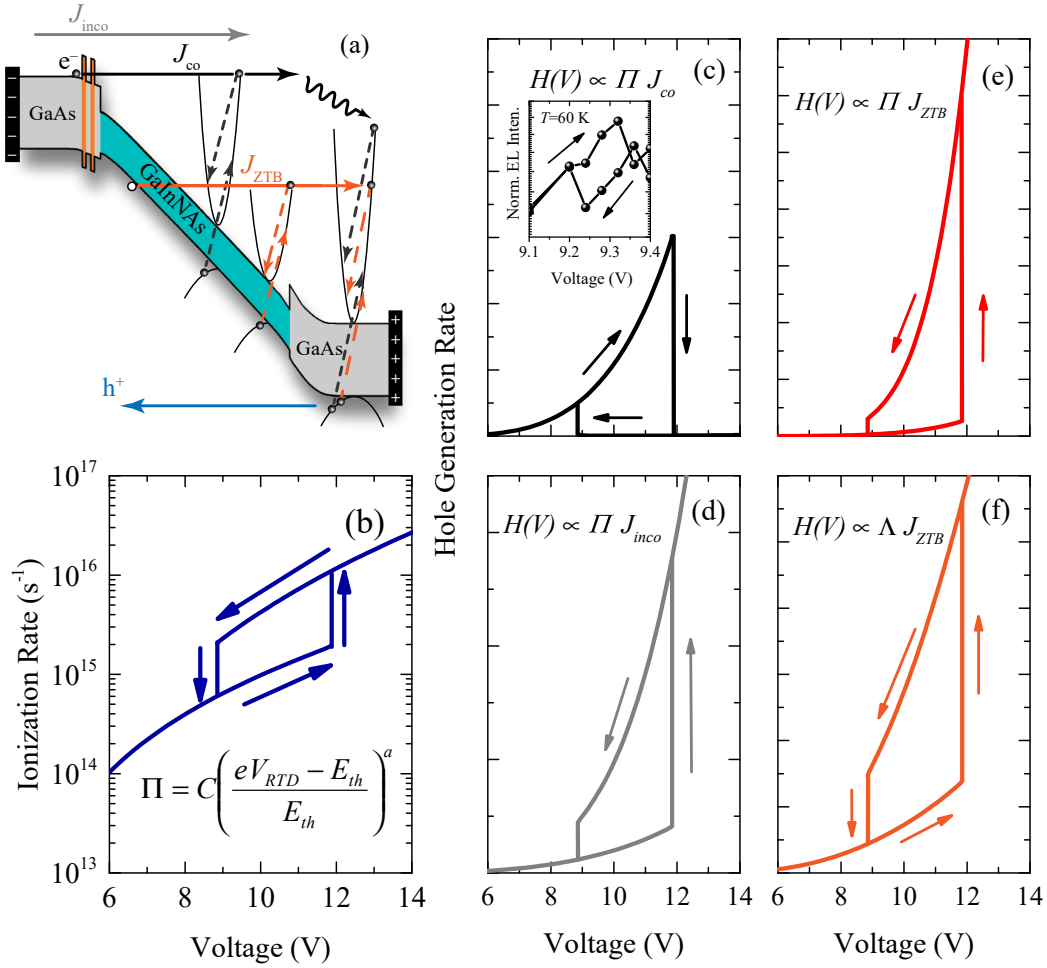

Figure 6.4 – (a) Sketch of the band profile illustrating the generation of holes via impact ionization from the coherent (black dashed arrows) and ZTB (orange dashed arrows) transport channels. The scattering of electrons is represented with a wavy arrow. The transport of the generated holes is symbolized with a blue solid arrow. (b) Calculated impact ionization rate, Π, as a function of the applied voltage for the GaAs layers. Calculated hole generation rate as a function of the applied voltage induced by impact ionization from the (b) coherent, (c) incoherent, and (d) ZTB channels, as well as by a (c) ZTB contribution independent of the ionization rate. Calculations were performed simulating the observed transport characteristics at $B = 5$ T and $T = 5$ K.

and $m_h^* = 0.53 m_0$, the electron and heavy-hole effective masses, respectively [25, 26]. Figure 6.4 (b) presents the calculated impact ionization rate using eq. 6.4, for a magnetoresistance corresponding to an applied magnetic field of $B = 5$ T at $T = 5$ K. The up- and down-sweep directions of voltage are indicated with arrows. Vertical lateral segments define the limits of the optical bistable region. According to the simulations, the calculated impact ionization rate displays an anticlockwise hysteresis as in the experiments, independently on the value of the intrinsic resistance. In this manner, the hole generation rate through impact ionization for each transport channel, J_j, can be calculated as, $H \propto \Pi J_j$ [23].

Figures 6.4 (c), (d) and (e) show the calculated hole generation rate assuming impact

ionization from the J_{co}, J_{inco}, and J_{ZTB} channels, respectively. Additionally, the hole generation induced by Zener tunneling has been considered as $H \propto \Lambda J_{ZTB}$, with Λ as a constant. The result of the calculation for this type of generation has been plotted in figure 6.4 (f). It is noteworthy that all but the coherent current produce anticlockwise hysteresis. It implies that under the considered conditions, the coherent channel plays a minor role in the hole generation process, bearing in mind the observed optical response displayed in figures 6.3 (b) and (c), where optical anticlockwise loops were found out. Yet, as reported in ref. [7] and exposed in the inset of figure 6.4 (c), the optical emission can be turned into a clockwise loop for temperatures around 60 K. In this case, the coherent channel can act as the main cause of such a response, highlighting that the actual response must be a combination of the transport channels.

To illustrate the relative role of each transport channel in the hole generation process and the way they shape the optical emission intensity as a function of voltage, the voltage dependence of the hole generation via impact ionization has been calculated as $H(V) \propto \Pi(J_{co} + \sigma J_{inco})$, adding a weight coefficient, σ, to tune the balance between the two current components. The result of this calculation is displayed in figure 6.5 (a) for three different values of σ. The on-off ratio H_A/H_B has been also obtained for each case by taking the quotient between the calculated hole generation rates at the first (point A) and second (point B) resonance states. It allows identifying transitions from clockwise ($H_A/H_B > 1$) to anticlockwise ($H_A/H_B < 1$) hysteresis. For $\sigma = 0.1$ (top panel), the coherent contribution prevails and a clockwise hysteresis is obtained. If $\sigma > 1.4$, the optical response must exhibit a pinched hysteresis (middle panel), similar to the one observed in the $I(V)$ characteristics at high magnetic fields. Greater values of σ generate anticlockwise bistabilities, as indicated in the bottom panel of figure 6.5 (a). The calculated total hole generation rate obtained as, $H \propto \Pi(J_{co} + J_{inco} + J_{ZTB}) + \Lambda J_{ZTB}$, is also shown in figure 6.5 (b), where a dominant ΛJ_{ZTB} term has been assumed. This leads to a response similar to the optical bistability presented in figures 6.3 (b) and (c), with an almost linear dependence on voltage inside the bistability for the down-sweep direction.

The experimental values of H_A/H_B as a function of temperature for $B = 0$ T are shown in figure 6.5 (c), pointing out to a temperature modulation of the contribution of each transport channel. The non-monotonic on-off ratio, H_A/H_B, indicates a transition toward a clockwise optical hysteresis ($H_A/H_B > 1$) for temperatures between 7 and 80 K. Based on the previous results, this transition can be explained by taking into account that at cryogenic temperatures, the resonance voltage shifts to higher values, increasing the electric field inside the heterostructure. Consequently, the ZTB channel is boosted under these conditions, inducing an anticlockwise bistability. Then, as the temperature increases toward 60 K, the weight of the coherent transport of electrons and the hole generation

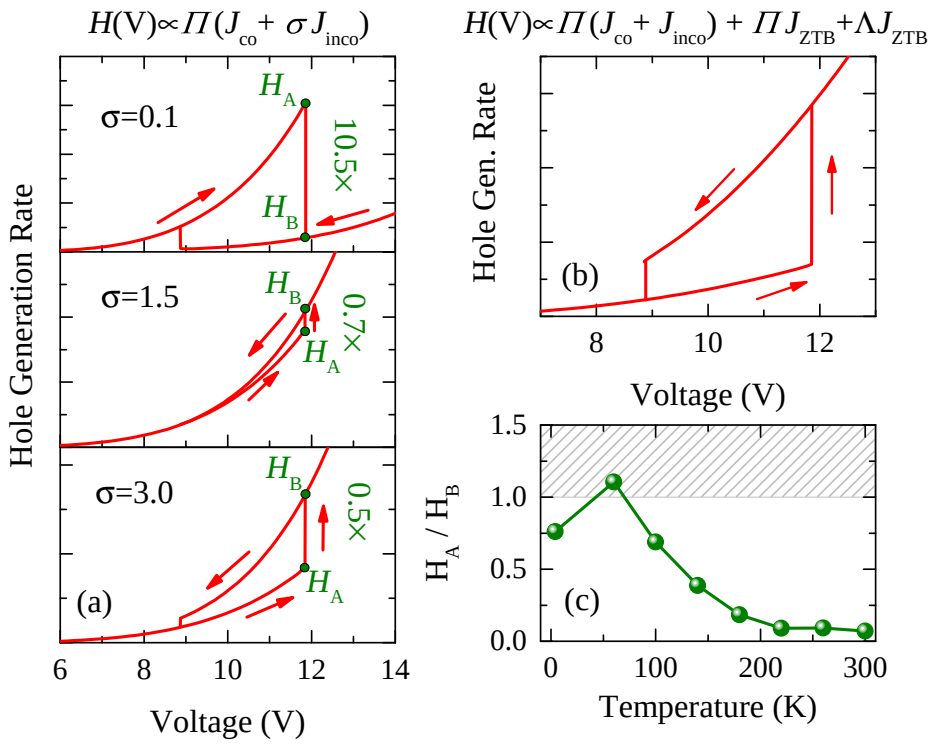

Figure 6.5 – (a) Calculated hole generation rate as a function of the applied voltage, considering impact ionization induced by the coherent and incoherent channels. The contribution of the incoherent channel was modulated varying the σ coefficient. The on-off ratio H_A/H_B has been obtained by taking the calculated hole generation rates at points A and B (green dots). The corresponding values are shown in green inside each panel. (b) Calculated total hole generation rate obtained as the sum of the different channel contributions. All the calculations were made for a magnetoresistance equivalent to an applied magnetic field of 5 T at 5 K. (c) Measured on-off ratio H_A/H_B as a function of temperature.

through impact ionization grows, inverting the bistability into a clockwise hysteresis. Further temperature increase drastically reduces the resonant voltage [7], weakening the contribution of the coherent and ZTB channels. It enhances the role of thermionic emissions, scattering, and other non-resonant processes, turning again the optical bistability into an anticlockwise hysteresis.

These results demonstrate that the interplay of three independent tunneling transport channels and the tuning of the magnetoresistance is responsible for the bistable current responses described here. All transport channels are effective in generating electrons with energy high enough to be involved in impact ionization processes. In addition, Zener tunneling can also contribute to the production of holes, especially at low temperatures. The generated holes can then recombine and produce the observed EL emission, whose dependence with the voltage can be modulated by temperature and magnetic fields applied along the growth direction. Under these conditions, the magnetoresistance of the system is tuned, inducing a pinched hysteresis in the $I(V)$ characteristics and a wide optical hysteresis at high magnetic fields. The observations are corroborated by the proposed

model, which enables explaining the different transport and optical bistabilities by considering changes in the magnetoresistance and the competition between hole generation channels. It allows understanding the seeming detachment between the current-voltage and light-voltage characteristics as the temperature and intrinsic resistance change during the voltage sweeps.

References

[1] P. Mazumder, S. Kulkarni, M. Bhattacharya, J. P. Sun, and G. Haddad, "Digital circuit applications of resonant tunneling devices," *Proc. IEEE*, vol. 86, no. 4, pp. 664–686, 1998.

[2] K. Narahara and K. Maezawa, "Large-amplitude voltage edge oscillating in a transmission line with regularly spaced series-connected resonant-tunneling diodes," *IEICE Electronics Express*, vol. 15, no. 17, pp. 20180678–20180678, 2018.

[3] M. Nagase, T. Takahashi, and M. Shimizu, "Switching characteristics of nonvolatile memory using GaN/AlN resonant tunneling diodes," *Jpn. J. Appl. Phys.*, vol. 58, p. 091001, jul 2019.

[4] C. R. H. White, M. S. Skolnick, L. Eaves, and M. L. Leadbeater, "Electroluminescence and impact ionization phenomena in a double-barrier resonant tunneling structure," *Appl. Phys. Lett.*, vol. 58, no. 11, pp. 1164–1166, 1991.

[5] F. Hartmann, F. Langer, D. Bisping, A. Musterer, S. Höfling, M. Kamp, A. Forchel, and L. Worschech, "GaAs/AlGaAs resonant tunneling diodes with a GaInNAs absorption layer for telecommunication light sensing," *Appl. Phys. Lett.*, vol. 100, no. 17, p. 172113, 2012.

[6] A. Pfenning, F. Hartmann, M. Rebello Sousa Dias, L. K. Castelano, C. Süßmeier, F. Langer, S. Höfling, M. Kamp, G. E. Marques, L. Worschech, and V. Lopez-Richard, "Nanothermometer Based on Resonant Tunneling Diodes: From Cryogenic to Room Temperatures," *ACS Nano*, vol. 9, no. 6, pp. 6271–6277, 2015. PMID: 26035628.

[7] F. Hartmann, A. Pfenning, M. Rebello Sousa Dias, F. Langer, S. Höfling, M. Kamp, L. Worschech, L. K. Castelano, G. E. Marques, and V. Lopez-Richard, "Temperature tuning from direct to inverted bistable electroluminescence in resonant tunneling diodes," *J. Appl. Phys.*, vol. 122, no. 15, p. 154502, 2017.

[8] V. J. Goldman, D. C. Tsui, and J. E. Cunningham, "Resonant tunneling in magnetic field: Evidence for space-charge buildup," *Phys. Rev. B*, vol. 35, pp. 9387–9390, Jun 1987.

[9] A. Zaslavsky, D. C. Tsui, M. Santos, and M. Shayegan, "Magnetotunneling in double-barrier heterostructures," *Phys. Rev. B*, vol. 40, pp. 9829–9833, Nov 1989.

[10] P. Orellana, F. Claro, E. Anda, and S. Makler, "Self-consistent calculation of resonant tunneling in asymmetric double barriers in a magnetic field," *Phys. Rev. B*, vol. 53, pp. 12967–12972, May 1996.

[11] H. Jones, C. Zener, and R. H. Fowler, "The theory of the change in resistance in a magnetic field," *Proceedings of the Royal Society of London. Series A, Containing Papers of a Mathematical and Physical Character*, vol. 145, no. 854, pp. 268–277, 1934.

[12] J. Schulman, H. De Los Santos, and D. Chow, "Physics-based RTD current-voltage equation," *IEEE Electron Device Lett.*, vol. 17, no. 5, pp. 220–222, 1996.

[13] M. Buttiker, "Coherent and sequential tunneling in series barriers," *IBM J. Res. Dev.*, vol. 32, no. 1, pp. 63–75, 1988.

[14] R. Sizmann and F. Koch, "The role of zener-tunneling in the subband structure of narrow-gap semiconductors," in *Resonant Tunneling in Semiconductors* (L. L. Chang, E. E. Mendez, and C. Tejedor, eds.), pp. 127–135, New York: Springer, 1991.

[15] D. Di Paola, M. Kesaria, O. Makarovsky, A. Velichko, L. Eaves, N. Mori, A. Krier, and A. Patanè, "Resonant Zener tunnelling via zero-dimensional states in a narrow gap diode," *Sci. Rep.*, vol. 6, p. 32039, 2016.

[16] S. Sze and K. N. Kwok, *Physics of Semiconductor Devices*. New Jersey: John Wiley & Sons, Inc., 3rd ed., 2007.

[17] E. D. Jones, N. A. Modine, A. A. Allerman, I. J. Fritz, S. R. Kurtz, A. F. Wright, S. T. Tozer, and X. Wei, "Optical properties of InGaAsN: a new 1-eV bandgap material system," in *Light-Emitting Diodes: Research, Manufacturing, and Applications III* (E. F. Schubert, I. T. Ferguson, and H. W. Yao, eds.), vol. 3621, pp. 52 – 63, International Society for Optics and Photonics, SPIE, 1999.

[18] G. Dumitras, *Optical and Electrical Characterization of InGaAsN used for 1.3 µm lasers*. PhD thesis, Technische Universität München, 2003.

[19] M. Kondow, K. Uomi, A. Niwa, T. Kitatani, S. Watahiki, and Y. Yazawa, "GaInNAs: A Novel Material for Long-Wavelength-Range Laser Diodes with Excellent High-Temperature Performance," *Jpn. J. Appl. Phys.*, vol. 35, pp. 1273–1275, feb 1996.

[20] S. Birner, T. Zibold, T. Andlauer, T. Kubis, M. Sabathil, A. Trellakis, and P. Vogl, "nextnano: General purpose 3-D simulations," *IEEE Trans. Electron Devices*, vol. 54, no. 9, pp. 2137–2142, 2007.

[21] T. A. Growden, W. Zhang, E. R. Brown, D. F. Storm, D. J. Meyer, and P. R. Berger, "Nea-UV electroluminescence in unipolar-doped, bipolar-tunneling GaN/AlN heterostructures," *Light: Sci. Appl.*, vol. 7, no. 2, pp. 17150–17150, 2018.

[22] T. A. Growden, W. Zhang, E. R. Brown, D. F. Storm, K. Hansen, P. Fakhimi, D. J. Meyer, and P. R. Berger, "431 kA/cm2 peak tunneling current density in GaN/AlN resonant tunneling diodes," *Appl. Phys. Lett.*, vol. 112, no. 3, p. 033508, 2018.

[23] E. R. Cardozo de Oliveira, A. Pfenning, E. D. Guarin Castro, M. D. Teodoro, E. C. dos Santos, V. Lopez-Richard, G. E. Marques, L. Worschech, F. Hartmann, and S. Höfling, "Electroluminescence on-off ratio control of $n-i-n$ GaAs/AlGaAs-based resonant tunneling structures," *Phys. Rev. B*, vol. 98, p. 075302, Aug 2018.

[24] E. D. Guarin Castro, A. Pfenning, F. Hartmann, G. Knebl, M. D. Teodoro, G. E. Marques, S. Höfling, G. Bastard, and V. Lopez-Richard, "Optical Mapping of Non-equilibrium Charge Carriers," *J. Phys. Chem. C*, vol. 125, no. 27, p. 14741–14750, 2021.

[25] R. Redmer, J. R. Madureira, N. Fitzer, S. M. Goodnick, W. Schattke, and E. Schöll, "Field effect on the impact ionization rate in semiconductors," *J. Appl. Phys.*, vol. 87, no. 2, pp. 781–788, 2000.

[26] I. Vurgaftman, J. R. Meyer, and L. R. Ram-Mohan, "Band parameters for III–V compound semiconductors and their alloys," *J. Appl. Phys.*, vol. 89, no. 11, pp. 5815–5875, 2001.

Conclusions

This thesis compiled a sequence of experimental and theoretical routes that were combined in order to unveil, describe, and explain the nature of various effects related to carrier dynamics in n-type resonant tunneling diodes (RTDs). The conclusions of many of these findings can also be extended to other semiconductor heterostructures without loss of generality when exploring the correlation between transport and optical properties. Some other results might contribute to enhancing the performance of optoelectronic devices based on this kind of heterostructures.

It has been demonstrated, by means of an extensive study on the optical and electrical properties of Sb-based double-barrier structures, that these systems present resonant tunneling of carriers, responsible for the modulation of the main electrical response, and its correlation with the optical emission. The optoelectronic response can be observed across a large temperature spectrum, from cryogenics up to room temperature, and for different illumination conditions. Resonant tunneling of majority carriers (electrons in this case) is produced by the presence of a coherent transport channel in the conduction band, which is more efficient at low temperatures thanks to the reduction of inelastic scattering processes. In turn, incoherent transport of majority carriers can be thermally activated when temperature increases.

The inclusion of a III-V narrow-gap quaternary layer at the collector region (top side) of the heterostructures improves the optical sensing capabilities of Sb- and As-based systems at the mid- and near-infrared spectral regions, respectively. In turn, the optical characterization indicates that these layers are direct-bandgap semiconductors with high crystal quality and no miscibility issues, as suggested by the low Urbach parameter (E_U = 10 meV) observed in some samples. The light absorption properties of quaternary layers, jointly with their enhanced type-I alignment at the heterojunctions with the double barrier structures and optical windows, permit controlling both, the selectivity and sensitivity of RTD photosensors, as well as their photoresponse as a function of the applied voltage. Experimental and theoretical results have provided unambiguous proofs pointing to a rich interplay of effects that combine creation, drift, trapping, and escape processes of photogenerated carriers that can be modulated with external bias voltages and incoming light.

Under illumination conditions, minority carriers (holes in this case) are generated by absorption of light which depending on the energy of the incoming photons, cannot be restricted just to the absorption layer, but may also appear in other regions of the het-

erostructure. Photogenerated holes can be transported by electric fields and recombine to produce the observed photoluminescence (PL) spectra, which are strongly dependent on the electrical response. In this way, the role of minority carriers in the overall dynamics of quantum tunneling devices has been correlated to their trapping efficiency and quantum transmission through the double barrier structures. Trapping of minority carriers at low voltages ($V \lesssim 1.00$ V) can hamper optical recombination processes in the vicinities due to Coulomb interaction with other holes, but enhances, for instance, the RTD sensor photoconductivity, as a consequence of the rise in the susceptibility. However, resonant (coherent) and non-resonant (incoherent) transport of holes reduce both the number of trapped carriers and the photoconductivity at higher voltages. From that point of view, an RTD sensor quality has been assessed in terms of the relative sensitivity, pointing to two different regimes that can be traced by varying the intensity of the photoexcitation. One regime emerges at high optical power densities, which induce a prominent photoresponse but narrow photosensitivity due to the steepness of the quantum efficiency onset. This regime is achieved by applying low voltages. The other regime corresponds to low optical power densities, where the photoconductivity and the screening of the threshold voltage of the quantum efficiency diminish. Then, the photosensitivity presents a broader voltage range of detection, but higher voltages are necessary to achieve this regime. In the case of Sb-based heterostructures, these photosensor characteristics boost the device photoresponse to the presence of gas molecules, such as H_2O at room temperature, as demonstrated in this work.

Due to the high doping profiles of the quaternary layers, applied electric fields can ionize and induce a considerable depletion at the absorber region that helps majority carriers, transported by coherent and incoherent channels to easily reach the threshold energy necessary to induce impact ionization processes. Thus, these transport channels become highly efficient in the generation of minority carriers through this mechanism. If the applied voltages are considerably high ($V \gtrsim 4.00$ V), transport channels induced by bandgap tunneling can also generate additional holes by their own, as well as contribute to the impact ionization processes. The generated holes can be then driven by the applied voltages to different regions of the heterostructures where they can recombine and produce the observed electroluminescence (EL) emission spectra. This dependence of the holes generation with the transport of majority carriers explains the observed correlation between the EL and the current conditions.

The segmentation of the EL and PL optical emissions of the heterostructures allowed mapping the local thermalization processes among majority and minority carriers, through the characterization of the effective temperature of non-equilibrium carriers. Thus, a non-trivial picture of carriers energy relaxation along the heterostructures has been constructed

by combining the contribution of different heating and cooling mechanisms. The difference in carrier effective masses, carrier populations, and optical and electrical excitations prevent majority and minority carriers from thermalizing among them and with the lattice. In this case, electron and hole populations must be considered as independent systems with independent temperatures at the conduction and valence band, respectively. Accordingly, electrons can reach higher temperatures than holes due to their weak coupling with the lattice, as compared with holes. Changes in the effective electron-hole pair temperature depend on the relation between the charge carrier effective masses and the ratio between the absolute carrier temperatures. In this sense, noticeable fluctuations in the effective temperature can be detected if the hole temperature is much lower than the electron temperature, as suggested by the exposed results. This imbalance on the carriers temperature produces the nonlinear dependence of the carrier effective temperature with applied electrical powers, as evinced in this work.

The relaxation mechanisms inside of the double-barrier quantum wells have also been assessed by exploring the correlation between the temporal evolution of the optical emission and the current conditions at the double barrier structure through the extraction of different effective lifetimes. This correlation is strongly dependent not only on the barrier width, which reduces the tunneling and escaping rates by increasing their thicknesses, but also on band parameters such as energy bandgaps, conduction and valence band offsets, and the separation between the ground states of the Γ and L valleys. In the case of double-barrier structures with low conduction band offsets and high energy bandgap and Γ-L separation, fast electron-hole pair relaxation processes at the sub-nanosecond scale can be detected. Low potential barriers favor the escape of majority and minority carriers and reduce the efficiency of the filling process of the density of states inside the quantum well. Then, slow relaxation processes in these systems can be attributed to the accumulation of carriers at the emitter side of the double barrier structure. As a result, the corresponding lifetimes do not show any correlation with the transport characteristics. In contrast, double-barrier structures with high conduction band offsets, and low energy bandgaps, in addition to a great proximity between Γ and L ground states, can present three different time scales: 1) a fast sub-nanosecond dynamics related to $\Gamma \rightarrow L$ intervalley scattering of hot majority carriers, 2) an electron-hole pair relaxation dynamics observed at nanosecond scales and ascribed to radiative recombination and escaping processes, and 3) a slow minority-carrier relaxation.

The fast relaxation mechanism is favored by low coherent currents, because hot electrons can be easily injected into the Γ-ground quasi-bond state, where they can quickly migrate to the L-ground quasi-bond state, thus reducing the probability of optical recombination and escape from the quantum well, once the electron effective masses are

greater in the L band than in the Γ band. In turn, electron-hole pair relaxation processes prevail for high coherent currents where the high injection of carriers enhances the filling process of the density of states at the Γ-ground state, making radiative recombination more likely since high potential barriers reduce the escaping rates of the majority carriers. The theoretical analysis presented here also suggests that if the optical recombination time increases several orders of magnitude, then the slow minority carriers relaxation dynamics dominate at resonance conditions. Consequently, different carrier relaxation dynamics, characterized with different time scales can be disclosed by modulating the coherent current of majority carriers through the double barrier structure.

Tuning of coherent and incoherent currents in quantum tunneling heterostructures presenting intrinsic resistance provides additional insights on the complex transport of carriers, which in this case, leads to bistable current responses, as described here. The intrinsic resistance shapes both the transport and optical bistability by varying temperature and applied magnetic fields. A pinched hysteresis can be induced in the transport characteristics due to the increase in the intrinsic resistance when the magnetic field rises along the growth direction. The strengthened magnetoresistance also widens the area of the optical hysteresis, conserving its shape. The proposed model corroborates that all conductive channels provide high energetic electrons that contribute to the EL emission via impact ionization. At the same time, the holes provided via Zener tunneling breakdown also contribute to the EL emission, particularly at low temperatures, where the resonance voltages are larger. Heating the sample favors the optical non-coherent channels, so the competition between the hole generation channels can be modulated by changing the temperature. It allows understanding the seeming detachment between the current-voltage and light-voltage characteristics as the temperature and intrinsic resistance change during the voltage sweeps.

Despite the good agreement between the experimental and theoretical results presented in this work, which unmasks the basic ingredients to understand the carrier dynamics and the correlation between optical and electronic properties in quantum tunneling heterostructures, further experimental observations and additional refinements to the models here-exposed can be performed, in order to reinforce their generalizations. In that regard, the bistability observed in Sb-based double-barrier structures can be better explored as a function of temperature and magnetic fields to corroborate or not the influence of the intrinsic resistance in the transport properties of this kind of system. The analysis can be complemented with spectroscopy measurements, which would also confirm whether or not EL emission can be detected in structures with narrow-gap absorption layers, such as RTDs A and B, which is a subject not explored yet. Moreover, the correlation between the optical emission and transport properties in these devices has not been studied before.

This could, for instance, allow for the characterization of the performance of the device as photodetectors at lower temperatures, as well as to provide indications on the origin of the observed asymmetrical transport response in symmetric RTDs. An in-detail area/perimeter study, ideally with smaller diameter diodes, can also offer clues on the effect of the shape and type of top contacts in the observed current-voltage characteristics of symmetric devices. In addition, the high quality of the quaternary layers can be advantageous to investigate band parameters such as effective masses in these semiconductors.

GaSb-based resonant tunneling diodes can offer additional evidence on the differences between Γ- and *L*-type resonant tunneling transport. Then, using n-type devices, these differences can be resolved by studying the transport of majority and minority carriers with higher current resonances at different temperatures. At the moment, there are some observations at room temperature that can be complemented with transport measurements at lower temperatures. The results would also be useful to understand the differences in the transport properties of p- and n-type RTDs. In the case of p-type GaSb-based structures, it would also be very interesting to study hole resonant tunneling processes and to explore impact ionization mechanisms from holes. Thus, the influence of the energy band structure of this type of double-barrier quantum wells on the carriers transport, relaxation, and even thermalization can be unfolded in these future studies.